JUSTUS-LIEBIG-
UNIVERSITÄT
GIESSEN

Institut für Theoretische Physik
Heinrich-Buff-Ring 16
35392 Gießen

Ab initio Modellierung ferroelektrischer Oxide unter Verspannungen und zweidimensionaler Kristalle

Ab initio modeling of ferroelectric oxides under strain and two-dimensional crystals

Dissertation

zur Erlangung des akademischen Grades
Doktor der Naturwissenschaften (Dr. rer. nat)

vorgelegt dem
Fachbereich 07
der
Justus-Liebig-Universität Gießen

verfasst von *Mike Nico Pionteck*

Gießen im Dezember 2025

Gießen, den 21. Februar 2026
Dem Fachbereich 07 der Justus-Liebig-Universität Gießen als Dissertation vorgelegt.

Eingereicht am: 12.12.2025
Tag der Disputation: 12.02.2026

Promotionskommission

Vorsitzender: Prof. Dr. Christian Heiliger
Erstgutachter: Prof. Dr. Simone Sanna
Zweitgutachter: Prof. Dr. Lukas M. Eng
Beisitzer: Prof. Dr. Nadine Leisgang

Acknowledgements

This thesis is dedicated to the memory of my grandfathers, **Hans-Jürgen Weber** and **Antonio Mastromattei**, whose care and support have accompanied me for as long as I can remember. I would also like to express my deep gratitude to my parents, siblings, and friends for their encouragement throughout the years. Their incredible support and patience during the preparation of this work were crucial for its success. In particular, I thank **Miguel Wiche** for his long-standing friendship and many vibrant moments.

I am deeply indebted to my supervisor, **Simone Sanna**, for his guidance, support, and patience throughout this work. I am very grateful to him for his continuous encouragement, and for the many opportunities he gave me to develop both scientifically and personally. I am also grateful to **Lukas M. Eng** for kindly serving as the second referee of this thesis. I also wish to thank the remaining members of the examination committee, **Christian Heiliger** and **Nadine Leisgang**, for their time.

Furthermore, I would like to acknowledge the fruitful collaborations that have influenced and enriched this work. I am grateful to the principal investigators of the experimental collaboration, **Lukas M. Eng** and **Michael Rüsing**, as well as to their students **Ekta Singh**, **Matthias Roeper**, and **Robin Buschbeck** for many constructive discussions and shared projects. In particular, I want to thank **Claudio Attaccalite** and **Myrta Grüning** for their collaboration. They were always available for discussions, during which I have learned a lot from them. I also thank Claudio Attaccalite for the opportunity to visit his group in Marseille, which was both scientifically and personally rewarding.

I also thank my fellow students **Felix Bernhardt**, **Kevin Eberheim**, **Ferdinand Ziese**, and **Ather Ahmad** for the good times we shared and for many stimulating discussions. I am particularly grateful to Felix Bernhardt for carefully proofreading this thesis and for his constructive comments and suggestions. I am also very grateful to all current and former members of our institute for creating a friendly working environment. The numerous discussions, lunch breaks, coffee breaks, and shared conference trips made the past years memorable. I would further like to thank the technical and administrative staff, whose often invisible work keeps research running smoothly.

I gratefully acknowledge the computing time granted on the Lichtenberg high-performance computer (HPC) of TU Darmstadt and on the supercomputers at the High-Performance Computing Center Stuttgart (HLRS). Furthermore, I acknowledge the computatinal resources provided by the HPC Core Facility and the HRZ of Justus-Liebig-Universität Gießen. Finally, I gratefully acknowledge financial support from the Deutsche Forschungsgemeinschaft through the research unit FOR5044.

Abstract

Ferroelectric oxides exhibit strong coupling between structural, electronic, and optical properties, which enables their use in photonic, optoelectronic, and quantum technologies. These couplings are investigated from first principles in two complementary directions. In the first part, a real-time formalism is developed to simulate nonlinear optical processes such as sum and difference frequency generation (SFG, DFG), enabling the calculation of coherent anti-Stokes Raman scattering (CARS). The approach extends the time-dependent Berry phase polarization method implemented in the Yambo code and allows the decomposition of the total polarization into distinct frequency components. This formalism is examplarily tested on hexagonal boron nitride (*h*-BN) and molybdenum disulfide (MoS_2), predicting their strong excitonic features. In the second part, the focus is on ferroelectric oxides, specifically lithium niobate ($LiNbO_3$, LN) and lithium tantalate ($LiTaO_3$, LT), under uniaxial stress. These materials are key components in nonlinear optical devices, where an application of strain strongly influences their optical response. Domain walls (DWs) play a crucial role in this context. In a first approximation, DWs in LN can be modeled as stressed bulk material. The structural, vibrational, electronic, and optical properties mostly of LN under uniaxial stress are studied using density functional theory (DFT). Phonon modes have a nearly linear dependence on strain, and the splitting of degenerate E modes under x and y compression directly reflects symmetry lowering. The computed strain-dependent nonlinear susceptibilities show that new tensor elements appear under uniaxial stress, consistent with observations of second-harmonic generation (SHG) contrast at DWs. Subsequently, the CARS spectra are calculated under stress applying the real-time approach from part one. Furthermore, the investigation of point defects show that the formation energies of Nb_{Li} antisites, small bound polarons, and bipolarons decrease under strain, offering a microscopic explanation for the enhanced conductivity observed at DWs. Overall, this work establishes a microscopic understanding of how strain and symmetry breaking influence the vibrational, optical, and electronic properties of ferroelectric oxides such as LN and LT.

Zusammenfassung

Ferroelektrische Oxide weisen eine reichhaltige Kopplung zwischen strukturellen, elektronischen und optischen Eigenschaften auf, was ihren Einsatz in photonischen, optoelektronischen und Quantentechnologien ermöglicht. Diese Kopplungen werden ausgehend von ersten Prinzipien in zwei komplementäre Richtungen untersucht. Im ersten Teil wird ein Echtzeitformalismus entwickelt, um nichtlineare optische Prozesse wie Summen- und Differenzfrequenzerzeugung (SFG, DFG) zu simulieren, wodurch die Berechnung der kohärenten Anti-Stokes-Raman-Streuung (CARS) ermöglicht wird. Der Ansatz erweitert die im Yambo-Code implementierte zeitabhängige Berry-Phasen-Polarisationsmethode und ermöglicht die Zerlegung der Gesamtpolarisation in einzelne Frequenzkomponenten. Dieser Formalismus wird auf hexagonales Bornitrid (h-BN) und Molybdändisulfid (MoS_2) angewendet und sagt deren starke Exzitonen-Eigenschaften voraus. Im zweiten Teil liegt der Fokus auf ferroelektrischen Oxiden, insbesondere Lithiumniobat ($LiNbO_3$, LN) und Lithiumtantalat ($LiTaO_3$, LT) unter mechanischer Spannung. Diese Materialien sind Schlüsselkomponenten in nichtlinearen optischen Bauelementen, in denen die Verspannung ihre Eigenschaften stark beeinflusst. Domänenwände (DWs) spielen in diesem Zusammenhang eine entscheidende Rolle. In einer ersten Näherung können DWs in LN als verspanntes Volumenmaterial modelliert werden. Die strukturellen, phononischen, elektronischen und optischen Eigenschaften von LN und LT unter Verformung werden mit Hilfe der Dichtefunktionaltheorie (DFT) untersucht. Phononenmoden haben eine nahezu lineare Abhängigkeit von der Verformung, und die Aufspaltung entarteter E-Moden unter x- und y-Kompression spiegelt direkt die Symmetrieverringerung wider. Die berechneten dehnungsabhängigen nichtlinearen Suszeptibilitäten zeigen, dass unter Spannung neue Tensorelemente auftauchen, was mit den Beobachtungen des Kontrasts der Frequenzverdopplung (SHG) an DWs übereinstimmt. Anschließend werden die CARS-Spektren unter Verspannung mit Hilfe des Echtzeitansatzes aus Teil Eins berechnet. Des Weiteren zeigt die Untersuchung von Punktdefekten, dass die Formationsenergien von Nb_{Li}-Antisites, kleinen gebundenen Polaronen und Bipolaronen unter Verformung abnehmen, was eine mikroskopische Erklärung für die an DWs beobachtete verbesserte Leitfähigkeit liefert. Insgesamt schafft diese Arbeit ein mikroskopisches Verständnis dafür, wie Verspannungen und Symmetriebrechung die phononischen, optischen und elektronischen Eigenschaften von ferroelektrischen Oxiden wie LN und LT.

Contents

1 Introduction 1

2 Electronic ground-state theory 5
- 2.1 The many-body problem . . . 5
- 2.2 Density functional theory . . . 6
  - 2.2.1 Hohenberg-Kohn theorems . . . 6
  - 2.2.2 Kohn-Sham formalism . . . 7
  - 2.2.3 Exchange-correlation functionals . . . 10
  - 2.2.4 Strongly correlated systems . . . 12
- 2.3 Basis set . . . 14
- 2.4 Pseudopotentials . . . 15
- 2.5 Hellman-Feynman theorem . . . 16
- 2.6 Frozen-phonon method . . . 16

3 Electronic excited-state theory 19
- 3.1 Nonlinear optics . . . 19
- 3.2 Band-structure theory . . . 21
- 3.3 Real-time approach . . . 24
  - 3.3.1 Dynamical Berry phase . . . 25
  - 3.3.2 Equation of motion . . . 28
  - 3.3.3 Computational scheme . . . 29
  - 3.3.4 Electron correlation . . . 30
  - 3.3.5 Real-time Bethe-Salpeter equation . . . 31

4 Frequency-mixing spectroscopy in two-dimensional crystals 37
- 4.1 Two-dimensional materials: *h*-BN & $\mathbf{MoS_2}$ . . . 37
- 4.2 Theoretical background . . . 38
  - 4.2.1 Nonlinear response from real-time simulations . . . 38
  - 4.2.2 Sum frequency generation . . . 40
  - 4.2.3 Field-induced second-harmonic generation . . . 41
- 4.3 Signal processing: two external monochromatic fields . . . 42
- 4.4 Computational details . . . 46
- 4.5 Results . . . 47
  - 4.5.1 SFG and DFG in monolayer *h*-BN . . . 48
  - 4.5.2 SFG and DFG in monolayer $\mathbf{MoS_2}$ . . . 49
  - 4.5.3 Field-induced second-harmonic generation in bilayer *h*-BN . . . 51
- 4.6 Conclusions . . . 51

5 Ferroelectric oxides under strain **53**
5.1 Ferroelectric oxides: $LiNbO_3$ & $LiTaO_3$ 53
5.2 Modeling uniaxial stress 53
5.3 Elastic Properties 56
  5.3.1 Computational details 56
  5.3.2 Results 57
5.4 Vibrational properties 57
  5.4.1 Theoretical background 57
  5.4.2 Computational details 59
  5.4.3 Results 60
5.5 Optical properties 66
  5.5.1 Theoretical background 66
  5.5.2 Computational details 68
  5.5.3 Results: Piezo-optic coefficients 69
  5.5.4 Results: Second-order nonlinear piezo-optic coefficients 73
5.6 Coherent anti-Stokes Raman spectroscopy 78
  5.6.1 Theoretical background 78
  5.6.2 Computational details 80
  5.6.3 Results 80
5.7 Polaronic properties 85
  5.7.1 Theoretical background 85
  5.7.2 Computational details 86
  5.7.3 Results 87
5.8 Conclusions 88

6 Summary & outlook **91**

Appendix **95**

Bibliography **115**

Publication list **131**

List of Figures

1.1 A schematic representation of the nonlinear processes studied in this work: sum frequency generation (SFG), difference frequency generation (DFG) and nonresonant background (NRB) in coherent anti-Stokes Raman spectroscopy (CARS). As indicated CARS can be considered as a combination of SFG and DFG processes. The resonant CARS signal is generated by the interaction of two laser beams exciting molecular vibrations, and a third beam generating a coherent anti-Stokes signal. 3

2.1 The enhancement factor of the PBE with $\kappa = 0.804$ and $\mu = 0.219$ (orange) and PBEsol with $\mu = 10/81$ (green) functionals. In case of LDAs the enhancement factor is one (blue). 10

3.1 A schematic representation of (a) second-harmonic generation (SHG), (b) third-harmonic generation (THG) 20

4.1 The strucuture of (a) *h*-BN monolayer (in-plane), (b) *h*-BN bilayer (out-of-plane), and (c) MoS_2 monolayer (in-plane) 38
4.2 In this workflow each box represents a separate run, executed by different codes/code run-levels. In the first step, the electronic structure is calculated. This is the input for the real-time simulation (blue box) and—in case of calculations beyond the independent particles—for the calculation of quasiparticle correction and the building-blocks for the self-energy operator, that are also input of the real-time simulation. The output from the real-time simulation is postprocessed to obtain, e.g. nonlinear spectral properties (with kind permission from M. Grüning). 39
4.3 A schematic representation of the nonlinear processes studied in this work: (a) sum frequency generation (SFG), (b) difference frequency generation (DFG) and (c) field-induced second-harmonic generation (FI-SHG). . . 40
4.4 SFG of *h*-BN with a pump frequency $\omega_2 = 3$ eV obtained at the IPA level using the full discrete Fourier transformation (FT) (blue solid line), singular value decomposition (SVD) (magenta dashed line), and the nonlinear least square fit (LSF) (yellow dotted line). Results obtained with different sampling times are shown. The discrete FT needs a sampling time (385 fs) about 26 times larger than the SVD and LSF (15 fs). Below is displayed the difference in logarithmic scales for SVD and LSF, respectively, with 5 fs less sampling time to show the convergence. . . . 43

4.5 The time-dependent polarization (purple solid line) of h-BN calculated at the independent particle level with two electric fields ($\omega_1 = 0.2$ eV, $\omega_2 = 3$ eV). The signal can be divided into two regions: an initial "equilibration" region (up to $t \gg \gamma_{\text{deph}}$, here $t = 50$ fs) during which the system's eigenfrequencies are suppressed by dephasing and a region where Eq. (4.13) holds. In the second region the polarization is logarithmically sampled (teal dots) within a converged time window of 15 fs, smaller than the fundamental period of 20.678 fs of the signal. This sampling time is sufficient to correctly determine the Fourier coefficients by the nonlinear least square fit (LSF) as verified by reconstructing the polarization (lavender dashed line) within the fundamental period using the Fourier coefficients and the truncated Eq. (4.13). 45

4.6 SFG/DFG spectra for h-BN in panels (a), (b) at the IPA and in panels (c), (d) at the TD-aGW level. The heatmaps have been generated using a frequency grid of $\omega_1 \times \omega_2 = 96 \times 96$ points. For each frequency pair a real-time simulation was run and the output signal processed. 47

4.7 Calculated imaginary dielectric function of (a) h-BN and (b) MoS_2 at the IPA (blue dashed line) and TD-aGW (orange solid line) level. The excitonic peaks E_1 and E_2 of h-BN are located at around 6.1 eV and 7 eV, respectively (panel (a)). The degenerate excitonic peak A/B as well as C can be seen at around 2.2 eV and 3 eV, respectively (panel (b)). 48

4.8 SFG/DFG spectra for MoS_2 in panels (a) and (b) at the IPA and in panels (c), (d) at the TD-aGW level. The heatmaps have been generated using a frequency grid of $\omega_1 \times \omega_2 = 96 \times 96$ points for the IPA and $\omega_1 \times \omega_2 = 72 \times 72$ for the TD-aGW. For each frequency pair a real-time simulation was run and the output signal processed. 50

4.9 Calculated THz field-induced second-harmonic generation of bilayer h-BN with ν=10 THz at the IPA level. Each curve consists of 192 frequency steps between $\omega = 1 - 6$ eV. 50

5.1 Top view of the LN crystal structure. Dotted lines show the x and y directions. The hexagonal unit cell is shown. 54

5.2 The calculated stress tensor elements as a function of uniaxial strain in x direction. The elastic stiffness tensor elements are obtained by the linear fits corresponding to Eqs. (5.6). 57

5.3 DFT calculated relative frequency shifts of the E(TO_4) mode of stoichiometric LN as a function of strain in z direction in (a) steps of 0.4 % and (b) steps of 0.02 %. The linear fit and the standard deviation for both are plotted and their fitting parameters displayed. The slopes for strain are defined as $(\Delta\omega)/(|\Delta\epsilon|)$ and displayed with the fitting error. 60

5.4 The DFT calculated relative frequency shifts of (a) E(TO_9) (first row), (b) E(TO_5) (second row) and (c) A_1(TO_2) (third row) modes of stoichiometric LN as a function of strain in steps of 0.4 % along the x, y and z direction. The slopes for strain are defined as $(\Delta\omega)/(|\Delta\epsilon|)$ and displayed with the fitting error. 61

5.5 The eigenvectors of the Raman active vibrations of unstrained stoichiometric LN and LT in the rhombohedral unit cell of the transversal phonon modes with A_1 and E symmetry. Thereby light grey is denoted as Li, dark grey as Nb/Ta, and red as O ion, while the green arrows represent the displacement direction. 63
5.6 Comparison of the experimental and theoretical frequency shift (at lower strains): (a)-(b) E(TO_6) phonon mode under compression along the x and y axes of stoichiometric LN. The shaded region around all the curves is the confidence interval of the linear fit. 65
5.7 Frequency shifts of (a) the E(TO_7) and (b) the A_1(TO_4) mode from the theoretical stoichiometric and experimental 5% Mg-doped LN sample when compressing along the z direction. The E(TO_7) mode shows a positive slope while the A_1(TO_4) shows a negative slope for z compression. 66
5.8 Calculated dispersion of (a) d_{15} and d_{24}, and (b) d_{31} and d_{32} with the sum of two-band contribution (non perturbative approach) and in a real-time approach (perturbative approach). In (b) the non pertubative approach yields the same result for d_{31} and d_{32}. 69
5.9 Calculated relative impermeability ΔB_i for 626 nm under uniaxial stress in (a) x, (b) y and (c) z direction and (d) shear stress. The POCs are determined by the slope of the linear fit. 70
5.10 DFT calculated dispersion of the (a) ordinary (dashed lines) and extraordinary (solid lines) refractive index and (b) birefringence for uniaxial stresses in z direction from -3 GPa to 3 GPa in steps of 1 GPa. 71
5.11 DFT computed (a) piezo-optic and (b) photoelastic coefficients as function of the excitation energy. 73
5.12 Calculated and measured SHG components with linear fits for 933 nm (theory) and 950 nm (experiment) under uniaxial stress in (a) x, (b) y and (c) z direction. The experimentally determined SHG components are normalized using Ref. [191]. (a) m point group symmetry with $d_{21} = d_{16}$. (b) m point group symmetry with $d_{21} = d_{16}$. (c) $3m$ point group symmetry with $d_{31} = d_{32}$ and $d_{22} = d_{21} = d_{16}$. 74
5.13 DFT computed dispersion of d_{31} and d_{32} under uniaxial stress in (a) x, (b) y and (c) z direction as well as (c) the dispersion of π_{311}, π_{322}, π_{321}, π_{312}, π_{313} and π_{321}. 77
5.14 A schematic representation of: (a) spontaneous Raman, (b) resonant coherent anti-Stokes Raman scattering (CARS) and (c) nonresonant background (NRB) in CARS. 79

5.15 (a) Real and imaginary part of the susceptibility component $\chi^{(3)}_{xxxx}$ of NRB in CARS of unstrained LN calculated with the approach of Sec. 4. The points indicate the calculated raw values. The solid lines correspond to an exponential fit to smooth the data in the range between 0.541 eV and 1.652 eV where the CARS measurements are performed. (b) Calculated (xxx, x) CARS spectrum of stoichimetric LN in comparison with experimental $y(xxx, x)y$ CARS spectrum of congruent LN. The calculated CARS spectrum is obtained by the absolute square of the sum of the resonant and nonresonant part which is obtained from the fit in the inset of (a). Since the absolute value of the resonant part is not known, the resonant and nonresonant part are normalized to the experimental data. 81

5.16 Calculated (zzz, z) resonant CARS spectrum of stoichiometric LN under uniaxial stress between -2 % and 2 % in x, y and z direction. The calculated intensities are drawn with an arbitrary Gaussian broadening of 10 cm^{-1}. The dotted lines indicate the $y(zzz, z)y$ experimental CARS spectrum of congruent LN off and on the domain wall (R. Buschbeck, private communication, 2025). 83

5.17 Calculated (xxx, z) resonant CARS spectrum of stoichiometric LN under uniaxial stress between -2 % and 2 % in x, y and z direction. The calculated intensities are drawn with an arbitrary Gaussian broadening of 10 cm^{-1}. The dotted lines indicate the $y(xxx, z)y$ experimental CARS spectrum of congruent LN off and on the domain wall. The dashed lines indicate the $y(xxx, z)y$ experimental phase-retrieval (PR) spectrum of congruent LN off and on the domain wall (R. Buschbeck, private communication, 2025). 84

5.18 Electronic band structures in (a) and (b) of the $\mathrm{Nb}_{\mathrm{Li}}^{4+}(4d^1)$ small bound polaron and (c) and (d) of the $\mathrm{Nb}_{\mathrm{Li}}^{4+}$–$\mathrm{Nb}_{\mathrm{Nb}}^{4+}(4d^1 - 4d^1)$ bipolaron in LN. The localized electronic state related to the polaron is plotted in blue (spin up channel in (a) and spin up and down channel in (c) and (d)). . 85

5.19 DFT calculated relative formation energy of the (a) $\mathrm{Nb}_{\mathrm{Li}}^{5+}(4d^0)$, (b) $\mathrm{Nb}_{\mathrm{Li}}^{4+}(4d^1)$ (c) $\mathrm{Nb}_{\mathrm{Li}}^{4+}$–$\mathrm{Nb}_{\mathrm{Nb}}^{4+}(4d^1 - 4d^1)$ antisites of LN under uniaxial strain in x, y and z direction, respectively. The lines are drawn for the eyes. The electronic charge density associated with the (d) $4d^1$ bound small polaron in the quasi-Jahn-Teller distortion and (e) $4d^1 - 4d^1$ bipolaron. Green and red balls represent the niobium and oxygen atoms, respectively. 87

A.1 The calculated stress tensor elements as a function of (a) ϵ_1, (b) ϵ_2, (c) ϵ_3, (d) ϵ_4, (e) ϵ_5 and (f) ϵ_6, while the rest of the strain tensor is set to zero in each case. 95

A.2 Calculated SHG components of unstrained LN obtained with sum of two-bands contributions (non perturbative approach) and real-time approach (perturbative approach). For (a) d_{11}, (b) d_{12}, (c) d_{13}, (d) d_{14}, (g) d_{23} and (i) d_{26}, the results of both approaches are identical. 102

A.3 Calculated SHG spectra of LN under uniaxial x stress between -3 and 3 GPa in steps of 1 GPa (1 GPa is omitted). Due to the symmetry reduction from $3m$ to m point group symmetry the d_{23} component appears (see (e)). The identities for the m point group symmetry from Table 5.8 apply to the SHG spectra under x stress. 103

A.4 Calculated SHG spectra of LN under uniaxial y stress between -3 and 3 GPa in steps of 1 GPa (-3 GPa and 1 GPa are omitted). Due to the symmetry reduction from $3m$ to m point group symmetry the d_{23} component appears (see (e)). The identities for the m point group symmetry from Table 5.8 apply to the SHG spectra under y stress. 104

A.5 Calculated SHG spectra of LN under uniaxial z stress between -3 and 3 GPa in steps of 1 GPa. Since the $3m$ point group symmetry is preserved ueder z stress, the d_{23} component is still zero (see (e)). The identities for the $3m$ point group symmetry from Table 5.8 apply to the SHG spectra under z stress. 105

A.6 Calculated spectra of the nonlinear piezo-optic coefficients of LN. Such coefficients, which are identical in the $3m$ point group, are shown together (see Table 5.8). Apart from minor deviations, the identies of Table 5.8 apply. Up to 1.5 eV the coefficients are nearly constant. 106

A.7 Calculated (xxx, x) resonant CARS spectrum of stoichiometric LN under uniaxial stress between -2 % and 2 % in x, y and z direction. The calculated intensities are drawn with an arbitrary Gaussian broadening of 10 cm^{-1}. The dotted lines indicate the $y(xxx, x)y$ experimental CARS spectrum of congruent LN off and on the domain wall. The dashed lines indicate the $y(xxx, x)y$ experimental phase-retrieval (PR) spectrum of congruent LN off and on the domain wall (R. Buschbeck, private communication, 2025). 107

A.8 Calculated (yyy, y) resonant CARS spectrum of stoichiometric LN under uniaxial stress between -2 % and 2 % in x, y and z direction. The calculated intensities are drawn with an arbitrary Gaussian broadening of 10 cm^{-1}. The dotted lines indicate the $z(yyy, y)z$ experimental CARS spectrum of congruent LN off and on the domain wall. The dashed lines indicate the $z(yyy, y)z$ experimental phase-retrieval (PR) spectrum of congruent LN off and on the domain wall (R. Buschbeck, private communication, 2025). 108

A.9 Calculated (xxx, z) resonant CARS spectrum of stoichiometric LN under uniaxial stress between -2 % and 2 % in x, y and z direction. The calculated intensities are drawn with an arbitrary Gaussian broadening of 10 cm^{-1}. The dotted lines indicate the $y(xxx, z)y$ experimental CARS spectrum of congruent LN off and on the domain wall. The dashed lines indicate the $y(xxx, z)y$ experimental phase-retrieval (PR) spectrum of congruent LN off and on the domain wall (R. Buschbeck, private communication, 2025). 109

A.10 Calculated (zzz, x) resonant CARS spectrum of stoichiometric LN under uniaxial stress between -2 % and 2 % in x, y and z direction. The calculated intensities are drawn with an arbitrary Gaussian broadening of 10 cm^{-1}. The dotted lines indicate the $y(zzz, x)y$ experimental CARS spectrum of congruent LN off and on the domain wall. The dashed lines indicate the $y(zzz, x)y$ experimental phase-retrieval (PR) spectrum of congruent LN off and on the domain wall (R. Buschbeck, private communication, 2025). 110

A.11 Calculated (xxx, y) resonant CARS spectrum of stoichiometric LN under uniaxial stress between -2 % and 2 % in x, y and z direction. The calculated intensities are drawn with an arbitrary Gaussian broadening of 10 cm^{-1}. The dotted lines indicate the $z(xxx, y)z$ experimental CARS spectrum of congruent LN off and on the domain wall. The dashed lines indicate the $z(xxx, y)z$ experimental phase-retrieval (PR) spectrum of congruent LN off and on the domain wall (R. Buschbeck, private communication, 2025). 111

A.12 Calculated (yyy, x) resonant CARS spectrum of stoichiometric LN under uniaxial stress between -2 % and 2 % in x, y and z direction. The calculated intensities are drawn with an arbitrary Gaussian broadening of 10 cm^{-1}. The dotted lines indicate the $z(yyy, x)z$ experimental CARS spectrum of congruent LN off and on the domain wall. The dashed lines indicate the $z(yyy, x)z$ experimental phase-retrieval (PR) spectrum of congruent LN off and on the domain wall (R. Buschbeck, private communication, 2025). 112

A.13 Calculated (zzz, z) resonant CARS spectrum of stoichiometric LN under uniaxial stress between -2 % and 2 % in x, y and z direction. The calculated intensities are drawn with an arbitrary Gaussian broadening of 10 cm^{-1}. The dotted lines indicate the $y(zzz, z)y$ experimental CARS spectrum of congruent LN off and on the domain wall. The dashed lines indicate the $y(zzz, z)y$ experimental phase-retrieval (PR) spectrum of congruent LN off and on the domain wall (R. Buschbeck, private communication, 2025). 113

List of Tables

3.1 Summary of several three- and four-wave mixing processes. The first column describes the wave mixing process with the relationship between the frequencies (ω_1, ω_2 and ω_3) of the incoming and outgoing (ω) photons. 21

4.1 All the parameters used in the nonlinear response calculations for both $\mathrm{MoS_2}$ and h-BN monolayers: the **k**-point sampling used in the IPA (TD-aGW in parentheses), the range of bands considered N_b, the cutoff, ϵ_cut, and the number of bands, ϵ_bands, used to converge the dielectric function $\epsilon_{\mathbf{G},\mathbf{G}'}$, the energetic shift ($\Delta E_\mathrm{so}$) for the scissor operator applied to the Kohn-Sham band structure, the height of the supercell L_z, and the effective layer thickness d_eff. The 2L-h-BN calculations are only at the IPA level, so no information about dielectric constant and scissor operator are reported. 46

5.1 The strain tensor corresponding to the applied uniaxial stress in x ($i = 1$), y ($i = 2$), and z ($i = 3$) direction, respectively. For all cases, $\epsilon_{13} = \epsilon_{12} = 0$. All calculations are done using the PBEsol exchange-correlation functional. 56

5.2 Comparison between the calculated elastic stiffness and compliance tensor elements with PBE, PBE+U ($U_\mathrm{eff} = 3.1\,\mathrm{eV}$), PBEsol and PBEsol+$U$ ($U_\mathrm{eff} = 3.1\,\mathrm{eV}$) and the experimental values of Warner *et al.* [6]. 58

5.3 Selection rules and Raman tensor elements for all investigated backscattering geometries for bulk LN with $R3c$ symmetry. x, y, z refer to the orthogonal reference system for tensor properties. TO and LO label transverse and longitudinal optical modes, respectively. 59

5.4 Calculated slopes of transversal $\mathrm{A_1}$ and E modes of stoichiometric LN under compressive and tensile strain, and stoichiometric LT under compressive strain in the x direction at higher strains in $\mathrm{cm^{-1}}/\%$. The slopes for strain are defined as $(\Delta\omega)/(|\Delta\epsilon|)$. 62

5.5 Comparison between the theoretical response at higher strains with the experimental response of stoichiometric LN stressed in y direction and 5 % Mg-doped LN stressed in z direction. Asterisks label modes that are Raman silent in the given scattering geometry and the E($\mathrm{TO_5}$) mode since experimentelly a disentanglement of the E($\mathrm{TO_5}$) and E($\mathrm{TO_6}$) mode is not possible. 64

5.6 Calculated POCs π_{im} (in Brewster, $1\,\mathrm{Br} = 10^{-12}\ \mathrm{m^2/N}$) for 626 nm in comparison with Ref. [186, 187] for 633 nm at room temperature averaged over different symmetry-equivalent sample geometries. 72

5.7 Calculated photoelastic coefficients p_{in} for 626 nm in comparison with Ref. [188, 189] for 633 nm at room temperature. 72
5.8 The relation between the uniaxial stress direction and the resulting crystal symmetry with its corresponding independent nonzero SHG and piezo-optic coefficients for $3m$ point group symmetry. The discussed tensor elements are represented as bold indices. All other tensor elements and identities are not discussed in this work but are expected to be nonzero. The nonlinear second-order susceptibility tensors for the m and $3m$ point group are expressed in detail in Appendix A.1.3. 75
5.9 Calculated and measured nonlinear POCs $\pi_{i\ell m}$ (in pmV^{-1}GPa^{-1}) for 933 nm and 950 nm obtained from the linear fit of Fig. 5.12. The experimental coefficients are normalized using Ref. [191]. Since d_{23} is zero in the unstressed case, the sign of π_{232} and π_{233} could not be experimentally determined and an alternative normalization procedure was performed. The corresponding values are marked with an asterisk. 76

A.1 Calculated frequencies of the Raman active phonon modes in unstrained LN in comparison with calculated and measured frequencies of Ref. [164]. 96
A.2 Calculated frequencies of the Raman active phonon modes in unstrained LT in comparison with calculated and measured frequencies of Ref. [164]. 97
A.3 Calculated slopes of transversal A$_1$ and E modes of LN under compressive and tensile strain in the x, y and z direction for strains in steps of 0.2 % in cm^{-1}/%. The slopes for strain are defined as $(\Delta\omega)/(|\Delta\epsilon|)$. 98
A.4 Calculated slopes of transversal A$_1$ and E modes of LT under compressive and tensile strain in the x, y and z direction for strains in steps of 0.4 % in cm^{-1}/%. The slopes for strain are defined as $(\Delta\omega)/(|\Delta\epsilon|)$. 99
A.5 Calculated SHG components of unstrained LN for an excitation wavelength of 933 nm in comparison with experimental literature values. The d_{15} component is not explicitly mentioned in the literature since $d_{15} = d_{32}$ for the considered laser wavelength in accordance to Kleinman symmetry. 101

1 Introduction

Ferroelectric oxides like lithium niobate ($LiNbO_3$, LN) and lithium tantalate ($LiTaO_3$, LT) are of central importance for technological applications in optics, photonics, and quantum technologies [1–4]. Due to their nonlinear optical and piezoelectric properties [5, 6], they are commonly used in devices such as frequency multipliers, modulators, waveguides [4, 7, 8], and thin-film integrated platforms [9–14].

Ferroelectric materials are characterized by domains with uniform polarization, which are separated by domain walls (DWs). DWs in LN can be created, displaced, or erased under moderate external fields, as demonstrated in poling experiments [15]. The atomic relaxations associated with DWs extend only over a few unit cells [16], leading to local symmetry breaking and modified bond lengths, and angles [17–20]. Especially, the local structural distortions at DWs are very similar to those caused by compressive stress in the bulk crystal, providing a relationship between stressed bulk and DW properties [15]. Moreover, the response of DWs to external electric fields is related to a complex redistribution of local stresses [15]. This interplay between polarization switching, mechanical deformation, and local strain fields emphasizes the need for a deeper understanding of LN properties under stress.

The aforementioned altered bond lengths and angles at DWs are mirrored by shifts in phonon frequencies [18]. While Raman spectra under hydrostatic pressure have been studied extensively [21], the case of uniaxial stress remains unexplored. To discriminate the influence of uniaxial stress fields from other factors, e.g. electrical fields [22] or compositional heterogeneity [23], and to quantify occurring stress markers, it is essential to gain fundamental knowledge on the relation of phonon properties and mechanical stress fields (see Ref. [P1]).

The nonlinear optical response can be described by the expansion of the polarization in powers of the electric field using Einstein summation convention [24]:

$$\mathcal{P}_i = \epsilon_0 \left(\chi^{(1)}_{ij} \mathcal{E}_j + \chi^{(2)}_{ijk} \mathcal{E}_j \mathcal{E}_k + \chi^{(3)}_{ijkl} \mathcal{E}_j \mathcal{E}_k \mathcal{E}_l + \dots \right). \tag{1.1}$$

The susceptibility $\chi^{(1)}_{ij}$ corresponds to linear optical properties, while higher-order susceptibilities describe nonlinear optical effects such as second-harmonic generation (SHG). In unstrained bulk LN, nonlinear effects have been sufficiently investigated [25]. However, recent experiments have demonstrated that at DWs, new nonlinear tensor elements appear that are forbidden by bulk symmetry [26, 27]. Since DWs are accompanied by local stress, this prompts the question of whether uniaxial stress in bulk LN can also activate otherwise symmetry-forbidden tensor components. Hence, investigating the linear and nonlinear piezo-optic effects, i.e., linear and nonlinear optical properties under stress, provides direct insight into how stress-induced symmetry breaking modifies the nonlinear susceptibility (see Refs. [P2, P3]). These effects are particularly important in quantum optical applications, such as broadband and tunable laser sources, optical amplifiers, frequency converters, single photon sources, or all-optical data processing [1–4]. In this context, stress also plays a relevant role in bulk-based applications, in particular in proton-exchanged or ion-diffused waveguides in the LN family, where stress is believed to cause the refractive index change [4, 7, 8].

Another key aspect concerns the microscopic origin of DW conductivity. Since in LN the spontaneous polarization is along the z axis, 180° walls are uncharged, while z walls are positively/negatively charged when polarization vectors of two neighboring domains point towards to/away from the wall (head-to-head/tail-to-tail wall) [19, 28]. Practically, tilted z walls exhibit strong wall-confined conductivity useful for nanoelectronic and photonic devices [19, 29]. Such conducting charged DWs (CDW) in LN exhibit conductivities orders of magnitude larger than the surrounding bulk [30–34], which makes them attractive for nanoelectronic applications [34–36]. The atomistic origin of the enhanced conductivity is not fully understood. First principles studies have shown that mechanisms such as local band bending cannot account alone for the observed conductivity [P4]. In addition, local defects such as $\mathrm{Nb_{Li}}$ antisites may play a decisive role for the CDW conductivity. These defects can host small bound polarons or bipolarons, which are well studied and understood for bulk systems [8, 37–41]. A systematic investigation of polaron formation energies under uniaxial stress provides a pathway to connect bulk defect physics with CDW transport phenomena.

In order to calculate the above mentioned properties of LN (and LT for the vibrational part) under uniaxial stress along all three crystallographic directions, density functional theory (DFT) as implemented in the Vienna Ab Initio Simulation Package (VASP) [42–44] and Quantum Espresso [45, 46] is employed. The refractive index and SHG response are calculated using a real-time approach based on the Berry phase formulation as implemented in Yambo [47–49]. For almost all of the properties, theoretical predictions are directly compared with experimental data, enabling quantitative validation.

Another feature, for which a methodological extension is neccessary, is also an objective of this work: Coherent anti-Stokes Raman spectroscopy (CARS) is a powerful nonlinear optical technique to probe vibrational modes within molecules or materials. In contrast to spontaneous Raman scattering, CARS provides highly resolved images with drastically increased scan speeds [50]. As a four-wave mixing (FWM) process (see Fig. 1.1), described by $\chi^{(3)}$, CARS involves two laser beams exciting atomic vibrations, and a third beam generating a coherent anti-Stokes signal, allowing for high resolution molecular imaging [51]. Primal applications are imaging of biological structures [52–55] as well as the characterization of two-dimensional (2D) materials, e.g. carbon nanotubes, graphene and hexagonal boron nitride (h-BN) [56–64]. However, recent studies have highlighted that also nonlinear optical single crystals are promising materials for CARS applications [65]. Advancements in *ab initio* approaches to calculate $\chi^{(3)}$ components could further refine the interpretation of CARS-based chemical fingerprints. Since the nonresonant background (NRB) in the CARS process (which is in principle accessible from first principles) is experimentally not directly available [65], the *ab initio* real-time simulation is a promising tool to support CARS measurements. Hence, the theoretical

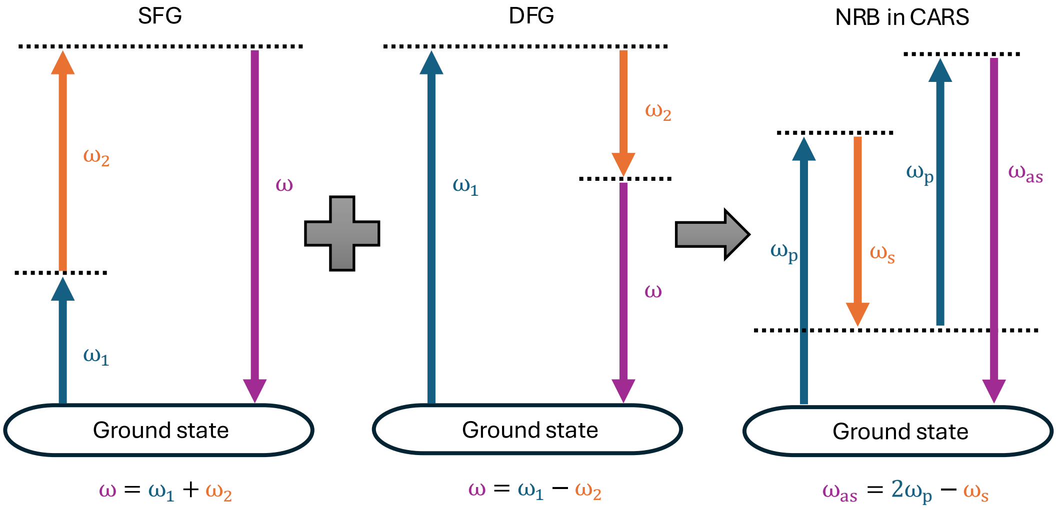

Figure 1.1: A schematic representation of the nonlinear processes studied in this work: sum frequency generation (SFG), difference frequency generation (DFG) and nonresonant background (NRB) in coherent anti-Stokes Raman spectroscopy (CARS). As indicated CARS can be considered as a combination of SFG and DFG processes. The resonant CARS signal is generated by the interaction of two laser beams exciting molecular vibrations, and a third beam generating a coherent anti-Stokes signal.

framework is extended to calculate CARS spectra of LN under uniaxial stress, making use of the calculated vibrational and nonlinear optical properties. With the implementation of real-time simulations available before the beginning of this work, only the study of harmonic processes such as SHG was possible. Considering CARS as a combination of sum frequency generation (SFG) and difference frequency generation (DFG) processes (see Fig. 1.1), an approach for SFG and DFG from first principles had to be developed to calculate the CARS response.

SFG and DFG spectroscopy are powerful experimental techniques in which the measured spectrum corresponds to the second-order nonlinear optical response $\chi^{(2)}$ arising from the interaction of two laser fields (see Fig. 1.1). These methods are highly sensitive to surfaces and interfaces [66–68]. Recently, there has been increasing interest in applying SFG and DFG to condensed matter systems. For example, SFG and DFG have been measured in layered molybdenum disulfide (MoS_2) and related heterostructures using either band-filtered supercontinuum illumination [69, 70] or wavelength-dependent spectroscopy [70–72]. Notably, SFG can be made dual resonant with excitons, leading to a strong enhancement of the response function, as recently shown in two-dimensional materials [73]. This enables SFG to probe exciton-exciton transitions, providing an alternative and complementary approach to pump-probe spectroscopy [74]. Designing and interpreting such experiments requires theoretical methods that can accurately describe both nonlinear light-matter interactions and the many-body physics of excitons in specific materials.

To date, only a few theoretical studies have addressed SFG and DFG in solids. Previous investigations of SFG have relied on simple two-band models [75] or first principles calculations using the Greenwood-Kubo formalism within the independent particle approximation (IPA) [73], thus neglecting excitonic effects.

A general method to extract SFG and DFG spectra from real-time simulations is introduced in Ref. [P5], which will be presented in this thesis. The implementation is based on the first principles framework of Ref. [49] as implemented in Yambo and YamboPy, which describes the coupling of electrons to external electric fields via the Berry phase formulation of the dynamical polarization [76], and incorporates many-body effects, including excitonic contributions, through an effective Hamiltonian [77]. Since this approach is restricted to the caluclation of harmonic responses, the present work generalizes the method to compute SFG and DFG as implemented in Yambo and YamboPy as an accessible open source code [P5, P6]. In order to test this method, SFG and DFG spectra are calculated for MoS_2 and h-BN monolayers, including excitonic effects using time-dependent adiabatic GW (TD-aGW). The results are compared with experimental data, demonstrating the method's reliability to accurately determine the nonlinear optical response of such materials.

The approach presented is not limited to the SFG and DFG but allows an efficient calculation of other response functions, such as field-induced second-harmonic generation (FI-SHG) [78, 79]. FI-SHG involves applying an electric field, such as laser pulses, direct current (DC), or an intense terahertz (THz) electric field, to a crystal and measuring the resulting second-harmonic intensity, which can provide important insights into the material properties. Centrosymmetric crystals, which have a null second-harmonic response (in the dipole approximation), are of particular interest because the applied field breaks the symmetry and produces even-order harmonic radiation. For a static electric field a real-time approach to study FI-SHG has been proposed in Ref. [80]. This work goes a step further, and puts forward a framework to simulate FI-SHG in the presence of time-dependent pump fields. For a h-BN bilayer, which is a centrosymmetric crystal, the second-harmonic response induced by a THz field breaking the inversion symmetry is calculated.

This thesis is structured as follows: First, the fundamental theory for treating electrons in a solid state in the electronic ground-state is summarized (see Sec. 2). This includes the introduction of the DFT approach and its extensions neccessary to determine the elastic, vibrational and polaronic properties of LN. Secondly, the theoretical framework for calculating electronic excited-state, i.e. linear and nonlinear optical properties is presented (see Sec. 3). Here, many-body perturbation theory, as well as the real-time approach based on the work of Attaccalite and Grüning [49] to calculate the nonlinear optical response, are introduced. Since the method development for SFG and DFG is required for the calculation of CARS spectra in LN, the implemented method and its results on h-BN and MoS_2 are presented in the third part as preparation for the fourth part (see Sec. 4). In the fourth part, the results on LN are shown, including the elastic, vibrational, optical and polaronic properties as well as, based on the approach for SFG and DFG, the CARS response under uniaxial stress (see Sec. 5). In the last part, the results are summarized and an outlook is given on how the presented methods and results can be extended. The results presented in this thesis are based on publications [P1–P15] prepared and submitted during the finalization of this work.

2 Electronic ground-state theory

2.1 The many-body problem

The solid-state problem is inherently a many-particle problem, requiring a quantum mechanical treatment. The study of multiple interacting particles is known as the many-body problem. The following is a brief overview of the many-body problem, presented based on Ref. [81].

For a system of N_e electrons and N_c nuclei, the time-independent Schrödinger equation is given by:

$$H\Psi(\mathbf{r},\mathbf{R}) = E\Psi(\mathbf{r},\mathbf{R}), \tag{2.1}$$

where H is the Hamiltonian operator, $\Psi(\mathbf{r},\mathbf{R})$ is the wavefunction, E is the total energy, $\mathbf{r} = \{\mathbf{r}_1, ..., \mathbf{r}_i, ..., \mathbf{r}_{N_\mathrm{e}}\}$ denotes the electronic coordinates, and $\mathbf{R} = \{\mathbf{R}_1, ..., \mathbf{R}_k, ..., \mathbf{R}_{N_\mathrm{c}}\}$ represents the nuclear coordinates. The wavefunction $\Psi(\mathbf{r},\mathbf{R})$ is a function of all electronic and nuclear coordinates, and the Hamilton operator H includes kinetic and potential energy terms for both electrons and nuclei [82]:

$$H = \underbrace{T_\mathrm{e} + V_\text{e-e} + V_\text{e-n}}_{H_e} + \underbrace{T_\mathrm{n} + V_\text{n-n}}_{H_\mathrm{n}}. \tag{2.2}$$

Here, T_c and T_e are the kinetic energy operators for nuclei and electrons, respectively, while $V_\text{c-c}$ and $V_\text{e-e}$ represent the Coulomb interactions between nuclei and electrons, and between electrons themselves. The final term $V_\text{e-c}$ denotes the interaction between electrons and nuclei.

Due to the vast number of particles on the order of 10^{23} in macroscopic systems [81], solving this equation exactly is infeasible, necessitating approximations.

A key simplification is the Born-Oppenheimer approximation based on Ref. [83], which exploits the large mass disparity between nuclei and electrons. Expressing the Hamiltonian in atomic units, the kinetic energy of the nuclei is proportional to m/M_k, where m is the electron mass and M_k the nuclear mass. Since $m/M_k \approx 10^{-4}$, nuclear motion is much slower than electronic motion. Such a seperation of the time scales of electron and nucleus motion allows to decouple Eq. (2.1) into an electronic Schrödinger equation [83]:

$$H_0\psi_\alpha(\mathbf{r},\mathbf{R}) = \epsilon_\alpha(\mathbf{R})\psi_\alpha(\mathbf{r},\mathbf{R}), \tag{2.3}$$

where the position of nuclei is fixed, and a Schrödinger equation for the nuclei [83]:

$$\left(\epsilon_\beta(\mathbf{R}) + T_\mathrm{n}\right)\chi_\beta(\mathbf{R}) = E\chi_\beta(\mathbf{R}), \tag{2.4}$$

where H_0 is the electronic Hamiltonian, ψ_α and ϵ_α are the wave function and energy of the electrons, respectively, and χ_β and ϵ_β are the wave function and energy of the nuclei, respectively. Here, α and β denote a complete set of quantum states. For each configuration $\mathbf{R}$, the electrons are considered to move in a fixed lattice. In this way, the dynamics of nuclei are decoupled from those of electrons. The ground-state of the electrons in each configuration $\mathbf{R}$ can be calculated and inserted into the differential equation for the nuclei motion. As a result, the ground-state of a solid can be calculated in a self-consistent way. This approximation supports modern electronic structure methods, particularly DFT, which further simplifies the many-particle problem by replacing explicit electronic interactions with an effective potential.

2.2 Density functional theory

As a consequence of the Born-Oppenheimer approximation, the electrons can be described independently from the nuclei by (2.3). Hence, a theory is required for determining the ground-state of the electrons within a fixed lattice configuration. This corresponds to a many-body problem, where the interaction between N_e electrons needs to be considered.

Various theories have been developed to describe electron-electron interactions in a many-body system, e.g., Hartree-Fock and Thomas-Fermi theory [82]. These approaches have in common that they are mean field theories, where the electron-electron interaction is described by noninteracting identical electrons in an average field. However, such theories are not sufficient to describe the complex electron-electron interactions in solids. The Hartree-Fock method, for instance, neglects correlation effects, leading to a systematic underestimation of the electronic band gap [82]. Although, the Hartree-Fock method can be extended via configuration interaction to include correlation effects, this significantly increases the computational cost as well as the storage requirements. The Thomas-Fermi theory is a semiclassical model to describe atomic systems, where the kinetic energy of the electrons is described by a classical kinetic energy term. This theory is not sufficient to describe the electronic structure of solids, as it neglects quantum mechanical effects [82]. However, an important feature of the Thomas-Fermi theory is that it introduces the concept of the electron density to express the ground-state energy of the system instead of the many-particle wave function like in the Hartree-Fock method. This is the fundamental idea of the DFT which describes the electronic structure of many-body systems in terms of the electron density exploiting the Hohenberg-Kohn theorems. In the next section, the Hohenberg-Kohn theorems are presented on the basis of Ref. [84].

2.2.1 Hohenberg-Kohn theorems

The Hohenberg-Kohn theorems provide the formal basis of DFT, establishing energy functionals that depend only on the electron density. The electron density is defined as:

$$\rho(\mathbf{r}) = N \int |\Psi(\mathbf{r}_1, \mathbf{r}_2, ..., \mathbf{r}_N)|^2 \mathrm{d}\mathbf{r}_2 ... \mathrm{d}\mathbf{r}_{N_\mathrm{e}}. \tag{2.5}$$

The theorems state:

1. **First theorem:** The ground-state electron density $\rho(\mathbf{r})$ uniquely determines the external potential $v_{\text{ext}}(\mathbf{r})$ given by the nuclei up to an additive constant. This implies that the external potential is a functional of the density, $v_{\text{ext}}(\mathbf{r}) = v_{\text{ext}}[\rho(\mathbf{r})]$.

2. **Second theorem:** The ground-state energy is a unique functional of the electron density, given by:
$$E[\rho] = F[\rho] + \int v_{\text{ext}}(\mathbf{r})\rho(\mathbf{r})\mathrm{d}^3 r, \tag{2.6}$$
where $F[\rho]$ is the universal energy functional that depends only on the electron density, and $v_{\text{ext}}(\mathbf{r})$ is the external potential. The exact, and only the exact ground-state density minimizes this energy functional.

Both theorems are consequences of the variational principle, which states that the ground-state energy is the minimum of the energy functional $E[\rho]$ over all possible electron densities. An important benefit of introducing functionals of the electron density is that the number of independent variables is reduced from $3N_\text{e}$ to three in comparison to Hartree-Fock theory, where the wave function depends on $3N_\text{e}$ variables. This reduction in the number of variables makes DFT computationally more memory efficient than Hartree-Fock theory.
The Hohenberg-Kohn theorems establish DFT as a formally exact theory for ground-state properties, though the functional $F[\rho]$ is not explicitly known and must be approximated in practice. The universal functional contains the non-classical terms for exchange and correlation, which are the most computationally challenging aspects of DFT. The exchange term accounts for the indistinguishability of particles, which manifests in the Pauli exclusion principle for electrons. The correlation term accounts for electron-electron interactions that are not captured by the exchange term or the bare Coulomb interaction. The next section will discuss the Kohn-Sham formalism based on Ref. [85], which providing a framework for solving the many-body problem.

2.2.2 Kohn-Sham formalism

The idea of the Kohn-Sham formalism is to replace the interacting many-electron system with a system of non-interacting electrons that yield the same ground-state density, making DFT a mean-field theory [85]. In the Kohn-Sham formalism, the electron density is expressed as a sum of the squared Kohn-Sham orbitals $\Phi_i(\mathbf{r})$ [85]:

$$\rho(\mathbf{r}) = \sum_i |\Phi_i(\mathbf{r})|^2. \tag{2.7}$$

With this ansatz, the unknown universal functional $F[\rho]$ can be described as a sum of the kinetic energy $T_\text{s}[\rho]$, the Hartree energy $E_\text{H}[\rho]$, and the exchange-correlation energy $E_\text{xc}[\rho]$ [85]:

$$F[\rho] = T_\text{s}[\rho] + E_\text{H}[\rho] + E_\text{xc}[\rho]. \tag{2.8}$$

The kinetic energy term $T_\text{s}[\rho]$ is the kinetic energy of non-interacting electrons with the density $\rho(\mathbf{r})$. The Hartree energy $E_\text{H}[\rho]$ describes the Coulomb electron-electron repulsion, and the exchange-correlation energy $E_\text{xc}[\rho]$ accounts for the quantum mechanical effects of electron-electron interactions. The terms are described by the following equations [85]:

$$T_\mathrm{s}[\rho] = -\frac{\hbar^2}{2m}\sum_i \int \Phi_i^*(\mathbf{r})\nabla^2\Phi_i(\mathbf{r})\mathrm{d}^3r, \tag{2.9}$$

$$E_\mathrm{H}[\rho] = \frac{1}{2}\int\int \frac{\rho(\mathbf{r})\rho(\mathbf{r}')}{|\mathbf{r}-\mathbf{r}'|}\mathrm{d}^3r\mathrm{d}^3r', \tag{2.10}$$

$$E_\mathrm{xc}[\rho] = \int \epsilon_\mathrm{xc}(\rho(\mathbf{r}))\rho(\mathbf{r})\mathrm{d}^3r. \tag{2.11}$$

As a result, the total energy functional can be expressed as:

$$E[\rho] = T_\mathrm{s}[\rho] + E_\mathrm{H}[\rho] + E_\mathrm{xc}[\rho] + \int v_\mathrm{ext}(\mathbf{r})\rho(\mathbf{r})\mathrm{d}^3r. \tag{2.12}$$

The variation of this energy functional with respect to the electronic density yields the Kohn-Sham equations:

$$\left(-\frac{\hbar^2}{2m}\nabla^2 + v_\mathrm{eff}(\mathbf{r})\right)\Phi_i(\mathbf{r}) = \epsilon_i\Phi_i(\mathbf{r}), \tag{2.13}$$

where $v_\mathrm{eff}(\mathbf{r})$ is the effective potential given by:

$$v_\mathrm{eff}(\mathbf{r}) = v_\mathrm{ext}(\mathbf{r}) + v_\mathrm{H}(\mathbf{r}) + v_\mathrm{xc}(\mathbf{r}). \tag{2.14}$$

Here, $v_\mathrm{H}(\mathbf{r})$ is the Hartree potential and $v_\mathrm{xc}(\mathbf{r})$ is the exchange-correlation potential with

$$v_\mathrm{H}(\mathbf{r}) = \int \frac{\rho(\mathbf{r}')}{|\mathbf{r}-\mathbf{r}'|}\mathrm{d}^3r', \tag{2.15}$$

$$v_\mathrm{xc}(\mathbf{r}) = \frac{\delta E_\mathrm{xc}[\rho]}{\delta\rho(\mathbf{r})}. \tag{2.16}$$

With the Kohn-Sham equations, the many-body problem is reduced to a set of N_e non-interacting single-particle Schrödinger equations. The single-particle wave functions $\Phi_i(\mathbf{r})$ and eigenvalues ϵ_i are called Kohn-Sham orbitals and energies, respectively, which do not correspond to the wavefunctions and eigenvalues of the true many-body system, i.e., the electrons. However, from the Kohn-Sham orbitals, the true ground-state density of the system can be calculated from which the ground-state properties can be derived. The Kohn-Sham eigenvalues qualitatively represent the electronic band structure of the system. While the energy levels themselves have no physical meaning, the band gap is a physical quantity that can be calculated from the Kohn-Sham eigenvalues. However, the Kohn-Sham band gap systematically underestimates the true band gap of semiconductors depending on the choice of the exchange-correlation functional.

The DFT framework can also be expressed in spin polarized form, where the electron density is split into spin-up and spin-down components [86]:

$$\rho_\sigma(\mathbf{r}) = \sum_{i\in\sigma}|\Phi_i^\sigma(\mathbf{r})|^2, \tag{2.17}$$

where $\sigma = \uparrow, \downarrow$ denotes the spin component and $i \in \sigma$ indicates that the sum is taken over the Kohn-Sham orbitals of a specific spin channel. The total electron density is then given by [86]:

$$\rho(\mathbf{r}) = \rho_{\uparrow}(\mathbf{r}) + \rho_{\downarrow}(\mathbf{r}). \tag{2.18}$$

This only influences only the exchange-correlation potential, which is now a function of the spin density [86]:

$$v_{\mathrm{xc}}^{\sigma}(\mathbf{r}) = \frac{\delta E_{\mathrm{xc}}[\rho_{\uparrow}, \rho_{\downarrow}]}{\delta \rho_{\sigma}(\mathbf{r})}, \tag{2.19}$$

where σ denotes the spin component. The Kohn-Sham equations are then solved for each spin channel separately, leading to two sets of Kohn-Sham orbitals and eigenvalues [86]:

$$\left(-\frac{\hbar^2}{2m}\nabla^2 + v_{\mathrm{eff}}^{\sigma}(\mathbf{r})\right)\Phi_i^{\sigma}(\mathbf{r}) = \epsilon_i^{\sigma}\Phi_i^{\sigma}(\mathbf{r}), \tag{2.20}$$

The Kohn-Sham formalism provides a practical framework for solving the many-body problem in DFT, enabling the calculation of electronic structure properties for a wide range of materials. If the exchange-correlation functional $E_{\mathrm{xc}}[\rho]$ is given, the Kohn-Sham equations can be solved self-consistently to obtain the ground-state density and energy of the system. The following scheme outlines the steps involved in the self-consistent formulation of DFT [82]:

1. **Initialization:** Choose an initial guess for the electron density $\rho(\mathbf{r})$.
2. **Determine the effective potential:** Calculate the effective potential $v_{\mathrm{eff}}(\mathbf{r})$ from the electron density $\rho(\mathbf{r})$.
3. **Solve the Kohn-Sham equations:** Solve the Kohn-Sham equations to obtain the Kohn-Sham orbitals $\Phi_i(\mathbf{r})$ and energies ϵ_i.
4. **Update the electron density:** Construct the new electron density $\rho'(\mathbf{r})$ from the Kohn-Sham orbitals.
5. **Compare densities:** Compare the new electron density $\rho'(\mathbf{r})$ with the previous density $\rho(\mathbf{r})$. Distinguish between two cases:
    (a) If the difference between $\rho'(\mathbf{r})$ and $\rho(\mathbf{r})$ is below a predefined threshold, the calculation is converged. The last density and the corresponding total energy are considered as the ground-state density and energy.
    (b) If the difference between $\rho'(\mathbf{r})$ and $\rho(\mathbf{r})$ is above a predefined threshold, update the electron density $\rho(\mathbf{r})$ with $\rho'(\mathbf{r})$ and repeat steps 2-5 until convergence is reached.

This self-consistent procedure exploits the fact that the electron density of the ground-state minimizes the total energy functional as stated by the second Hohenberg-Kohn theorem. The total energy of the system is minimized with respect to the electron density, which is achieved by iteratively updating the electron density until self-consistency is reached. The DFT is formally exact, but the accuracy of the method depends on the choice of the exchange-correlation functional $E_{\mathrm{xc}}[\rho]$. Several approximations have been developed for the exchange-correlation functional, which will be discussed in the next section.

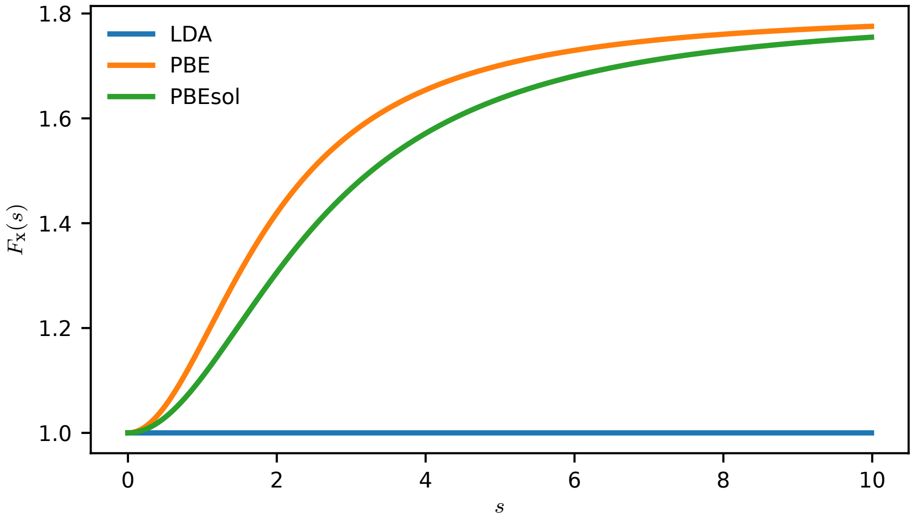

Figure 2.1: The enhancement factor of the PBE with $\kappa = 0.804$ and $\mu = 0.219$ (orange) and PBEsol with $\mu = 10/81$ (green) functionals. In case of LDAs the enhancement factor is one (blue).

2.2.3 Exchange-correlation functionals

The most challenging aspect of DFT is the approximation of the exchange-correlation functional $E_{\mathrm{xc}}[\rho]$, which collects (i) the difference between the exact many-body kinetic energy and the non-interacting kinetic energy and (ii) the non-classical part of the electron-electron interaction, comprising exchange from the indistinguishability of electrons and Coulomb correlation. On the one hand, the Thomas-Fermi theory provides a simple approximation for the kinetic energy [81]:

$$T_{\mathrm{TF}}[\rho] = \frac{3}{10}(3\pi^2)^{2/3} \int \rho^{5/3}(\mathbf{r})\mathrm{d}^3r, \tag{2.21}$$

which is a local approximation that depends only on the electron density at a given point of a homogeneous electron gas. On the other hand, the model of Thomas-Fermi theory is not sufficient to describe the kinetic energy of non-interacting electrons in a solid, as it neglects exchange and correlation effects, and lacks band structure. Although Paul Dirac has extended the Thomas-Fermi theory to include exchange effects:

$$E_{\mathrm{x}}[\rho] = -\frac{3}{4}\left(\frac{3}{\pi}\right)^{1/3} \int \rho^{4/3}(\mathbf{r})\mathrm{d}^3r, \tag{2.22}$$

the Dirac exchange functional is still not sufficient to describe the exchange-correlation energy of electrons in a solid. However, based on these models, exchange-correlation functionals have been developed that are used in practical DFT calculations even today:

- **Local density approximation (LDA):** Assumes that the exchange-correlation energy at each point in space depends only on the local density, modeled after the uniform electron gas [85, 86]:

$$E_{\mathrm{xc}}^{\mathrm{LDA}}[\rho] = \int \epsilon_{\mathrm{xc}}^{\mathrm{hom}}(\rho(\mathbf{r}))\rho(\mathbf{r})\mathrm{d}^3r. \tag{2.23}$$

The exchange-correlation energy is merged from the exchange and correlation energy, where the exchange energy is calculated from the Dirac exchange functional for a homogeneous electron gas and the correlation energy is determined by empirical parametrizations. Since a homogeneous electron gas is used in this approximation, the LDA works well for conducting systems like metals which behave similar to a homogeneous electron gas. Nevertheless, the LDA has been shown to be sufficient also for insulating systems. However, the price for the simplified model of an electron gas is that the LDA underestimates the band gap and lattice constants of semiconductors and insulators.

- **Generalized gradient approximation (GGA):** In order to take into account inhomogeneities in the ansatz of the LDA, the GGA approximates the exchange-correlation energy as a functional of the electron density and its gradient [87–89]:

$$E_{\mathrm{xc}}^{\mathrm{GGA}}[\rho] = \int \epsilon_{\mathrm{xc}}^{\mathrm{GGA}}(\rho(\mathbf{r}), \nabla\rho(\mathbf{r}))\rho(\mathbf{r})\mathrm{d}^3r. \tag{2.24}$$

The exchange term

$$E_{\mathrm{x}}^{\mathrm{GGA}}[\rho] = \int \epsilon_{\mathrm{x}}^{\mathrm{hom}}(\rho(\mathbf{r}))\rho(\mathbf{r})F_{\mathrm{x}}(s)\mathrm{d}^3r, \tag{2.25}$$

introduces an exchange enhancement factor F_{x}, which is a function of the electron density and its gradient:

$$s = \frac{|\nabla\rho|}{2(3\pi^2)^{1/3}\rho^{4/3}}, \tag{2.26}$$

and can be considered as a correction with respect to the LDA. On the basis of GGA, different functionals have been developed, e.g., the Perdew-Burke-Ernzerhof (PBE) functional which is one of the most widely used functionals in DFT calculations. The enhancement factor of the PBE functional is given by [89]:

$$F_{\mathrm{x}}^{\mathrm{PBE}}(s) = 1 + \kappa - \kappa/(1 + \frac{\mu s^2}{\kappa}), \tag{2.27}$$

where κ and μ are empirical parameters. This means that the enhancement factor is one if the gradient of the electron density is zero, which corresponds to the LDA. In Fig. 2.1 the enhancement factor for LDA and PBE with $\kappa = 0.804$ and $\mu = 0.219$ (values for the PBE functional) is shown. The enhancement factor of the PBE functional is larger than one for small values of s and smaller than one for large values of s. This means that the PBE functional enhances the exchange energy for small values of s and reduces the exchange energy for large values of s.

A disadvantage of the PBE functional is, however, that it overestimates the lattice constants of solids by about 2% [90]. In order to correct this, the revised PBE functional (PBEsol) has been developed, which is more accurate with respect to structural properties of solids [90]. For structural properties, small gradients of the electron density are important, which are not well described by the PBE functional. Therefore, in PBEsol $\mu = \frac{10}{81}$ is chosen, which leads to a better description of the structural properties of solids. In Fig. 2.1 the enhancement factor of the PBEsol functional is shown in comparison to LDA and PBE. For small gradients the enhancement factor of the PBEsol functional approaches the LDA enhancement factor, while for large gradients it approaches the PBE enhancement factor. This means that the PBEsol functional is a compromise between the LDA, which describes structural properties more accurately than the PBE functional, and the PBE functional, which describes electronic properties more accurately than the LDA [90].

2.2.4 Strongly correlated systems

While LDA and GGA are sufficient to describe delocalized s- and p-electrons, for localized d- and f-electrons the LDA and GGA functionals are not suited. In order to describe also localized electrons, a so called Hubbard Hamiltonian has been introduced based on the tight-binding method. The Hubbard Hamiltonian describes the interaction of localized electrons on a lattice, where the hopping term describes the kinetic energy of the electrons, and the on-site term describes the electron-electron interaction. In the second quantization, the Hubbard Hamiltonian is given by:

$$H = -t \sum_{\langle i,j \rangle} \left(c_i^\dagger c_j + c_j^\dagger c_i \right) + U \sum_i n_i (n_i - 1), \tag{2.28}$$

where t is the hopping parameter, U is the on-site interaction (also called Hubbard parameter), and $c_i^\dagger$ and c_i are the creation and annihilation operators for an electron at site i, respectively. The Hubbard Hamiltonian can be used to derive a functional for the exchange-correlation energy of localized electrons. This means that the total exchange-correlation energy contains the exchange-correlation energy of the LDA or GGA functional and an additional term that describes the interaction of localized electrons:

$$E_{\text{xc}}[\rho] = E_{\text{xc}}^{\text{LDA}}[\rho] + E_{\text{xc}}^{\text{Hubbard}}[\rho] - E_{\text{xc}}^{\text{dc}}[\rho], \tag{2.29}$$

where $E_{\text{xc}}^{\text{LDA}}[\rho]$ is the exchange-correlation energy of the LDA functional, $E_{\text{xc}}^{\text{Hubbard}}[\rho]$ is the exchange-correlation energy of the Hubbard Hamiltonian, and $E_{\text{xc}}^{\text{dc}}[\rho]$ is the double counting correction. The double counting correction is necessary to avoid double counting of the electron-electron interaction, which is already included in the LDA or GGA functional. This results in the following expression for the exchange-correlation energy [91, 92]:

$$E_{\text{xc}}^{\text{LDA+U}}[\rho] = E_{\text{xc}}^{\text{LDA}}[\rho] - \sum_I \left[\frac{U^I}{2} \sum_{m \neq m'} n_m^I n_{m'}^I - \frac{U^I}{2} \sum_{m,m'} n_m^I n_{m'}^I \right], \tag{2.30}$$

where U^I is the Hubbard parameter for atom I, and n_m^I is the occupation number of the m-th orbital of atom I. The detailed derivation can be found in the literature [91, 92].

The Hubbard parameter can be determined empirically by altering the value of U until calculated properties, e.g., lattice constants, match experimental values. However, this approach can lead to overcorrection of other properties which can be underestimated or overestimated depending on the choice of U. Therefore, another way is to determine it in a self-consistent way by converging the linear response with respect to the Hubbard parameter.

To determine the Hubbard parameter in a self-consistent way, a small perturbation α^I is added to the potential of the atomic sites I [92]. The response of the electron density defines the linear response function χ_{IJ} [92]:

$$\chi_{IJ} = \frac{\partial n^I}{\partial \alpha^J}. \tag{2.31}$$

The Hubbard parameter can then be determined from the linear response function where the difference between the inverse of the perturbed and a bare response function is taken into account [92]:

$$U^I = (\chi_0 - \chi)^{-1}_{II}, \tag{2.32}$$

where χ_0 is the bare response function and χ is the perturbed response function. The Hubbard parameter can be determined in a self-consistent way by iteratively updating the effective potential and the electron density until convergence is reached:

1. **Determine unperturbed ground-state:** Calculate the electronic density of the unperturbed ground-state from the self-consistent Kohn-Sham formalism.
2. **Perturbation:** Add a small perturbation α^I to the effective potential of the atomic site I and determine the on-site density n^I within a non-self-consistent calculation of the ground-state. Using finite differences and Eq. (2.31) yields the bare response function χ_0.
3. **Non-self-consistent calculation:** Calculate the perturbed effective potential and occupation n^I from the non-self-consistent Kohn-Sham formalism at the fixed ground-state density. Using finite differences and Eq. (2.31) yields the perturbed response function χ_0.
4. **Self-consistent calculation:** Repeat step 3, but now within a self-consistent calculation of the ground-state. This means that the electron density is updated in each iteration until convergence is reached. Using finite differences and Eq. (2.31) yields the perturbed response function χ.
5. **Update Hubbard parameter:** Calculate the Hubbard parameter U^I from the linear response function χ and the bare response function χ_0 using Eq. (2.32).
6. **Convergence check:** Compare the updated and previous Hubbard parameter. Distinguish between two cases:
   (a) If the difference between updated and previous Hubbard parameters is below a predefined threshold, the calculation is converged. The last Hubbard parameter is considered as the final Hubbard parameter.

(b) If the difference updated and previous Hubbard parameters is above a predefined threshold, repeat steps 2-6 until convergence is reached.

This approach allows for a more accurate description of the electronic structure of materials with strong electron-electron interactions, such as transition metal oxides and heavy fermion systems, as it takes into account the self-consistent response of the electron density to the effective potential.

2.3 Basis set

Many ansatzes for the wavefunction exist and can be applied to solve the Kohn-Sham equations, e.g. superposition of atomic orbitals (LCAO), plane waves, or Gaussian-type orbitals [81]. The choice of the ansatz depends on the system under consideration and the computational resources available. In this work, we use plane waves as basis functions to solve the Kohn-Sham equations. The plane wave basis set is defined as [81]:

$$\Phi_i(\mathbf{r}) = \frac{1}{\sqrt{V}} \sum_{\mathbf{G}} c_{\mathbf{G}} e^{i\mathbf{G}\cdot\mathbf{r}}, \tag{2.33}$$

where $\mathbf{G}$ is a reciprocal lattice vector, $c_{\mathbf{G}}$ are the coefficients of the plane wave expansion, and $\mathbf{r}$ is the position vector. The plane wave basis set is a complete set of orthonormal functions that can be used to represent any wavefunction in a periodic system. The coefficients $c_{\mathbf{G}}$ are determined by solving the Kohn-Sham equations self-consistently. The plane wave basis set is defined in reciprocal space, which is the Fourier transform of the real space. The reciprocal lattice vectors $\mathbf{G}$ are defined as:

$$\mathbf{G} = \frac{2\pi}{a}(h, k, l), \tag{2.34}$$

where a is the lattice constant, and h, k, and l are integers that define the reciprocal lattice vectors. The plane wave basis set is defined in a box with periodic boundary conditions, which means that the wavefunction is periodic in all three dimensions. The plane wave basis set is a complete set of orthonormal functions that can be used to represent any wavefunction in a periodic system. The coefficients $c_{\mathbf{G}}$ are determined by solving the Kohn-Sham equations self-consistently.

As they have the periodicity of the lattice, the advantage of using plane waves as basis functions is that they are computationally efficient and can be easily parallelized. The disadvantage of using plane waves as basis functions is that they formally require an infinite number of plane waves for accurate representation of the wavefunction. Hence, the plane wave basis set is truncated at a cutoff energy E_{cut}, which defines the maximum kinetic energy of the plane waves included in the basis set. The cutoff energy is defined as:

$$\frac{\hbar^2}{2m}|\mathbf{G}|^2 \leq E_{\text{cut}}. \tag{2.35}$$

A higher cutoff energy allows more plane waves to be included in the basis set, improving the accuracy of the results [93]. However, this also increases computational demands, as the number of plane waves grows with the cutoff energy. Thus, it is necessary to balance accuracy and computational efficiency. Additionally, the k-point mesh determines how the Brillouin zone is sampled. A finer k-point mesh yields more precise results, but also raises computational cost due to the increased number of k-points required for the calculation.

Another limiting factor are the number of electrons in the system. In all-electron models, all electrons are treated explicitly in the self-consistent calculation of the Kohn-Sham equations. The number of plane waves required to converge the results is proportional to the number of electrons in the system. For heavy elements with many core electrons, this leads to a large number of plane waves required to converge the results, which increases the computational cost significantly. Hence, instead of all-electron models, pseudopotentials are used to reduce the number of plane waves required to converge the results.

2.4 Pseudopotentials

In this concept two types of electrons are distinguished: valence and core electrons [81]. On the one hand, the valence electrons are the electrons that are involved in chemical bonding and determine the electronic properties of the material. Therefore, the valence electrons are treated explicitly when solving the Kohn-Sham equations to caluclate the electron density. On the other hand, the core electrons are the electrons that are not involved in chemical bonding and are tightly bound to the nucleus. The core electrons are treated implicitly by using pseudopotentials, which are effective potentials that replace the core electrons and their interactions with the valence electrons. The interaction of the valence electrons with ionic core (frozen core electrons plus nucleus) is represented by an effective potential, which is called pseudopotential [81]. The pseudopotential $v_{\text{ps}}(\mathbf{r})$ is given by a superposition of pseudopotentials of single atoms:

$$v_{\text{ps}}(\mathbf{r}) = \sum_I v_{\text{ps}}^I(\mathbf{r} - \mathbf{R}_I), \tag{2.36}$$

where $v_{\text{ps}}^I(\mathbf{r} - \mathbf{R}_I)$ is the pseudopotential of atom I at position $\mathbf{R}_I$. The pseudopotential is constructed such that it reproduces the scattering properties of the core electrons and their interactions with the valence electrons. The effective potential $v_{\text{eff}}(\mathbf{r})$ is then given by:

$$v_{\text{eff}}(\mathbf{r}) = v_{\text{ps}}(\mathbf{r}) + v_{\text{H}}(\mathbf{r}) + v_{\text{xc}}(\mathbf{r}). \tag{2.37}$$

By defining a cutoff radius R_c, the pseudopotential is constructed such that the wavefunction of the core electrons is replaced by a smooth function outside the cutoff radius. The pseudopotential is then used to calculate the effective potential $v_{\text{eff}}(\mathbf{r})$, which is used to solve the Kohn-Sham equations. The pseudopotential method allows to reduce the number of plane waves required to converge the results, as the core electrons are not treated explicitly [81].

Several pseudopotentials have been developed, e.g., norm-conserving pseudopotentials, ultrasoft pseudopotentials, and the projector augmented wave (PAW) method. The norm-conserving pseudopotentials are the simplest and most widely used pseudopotentials [94]. They are constructed such that the norm of the wavefunction is conserved when the core electrons are replaced by the pseudopotential. The ultrasoft pseudopotentials are a generalization of the norm-conserving pseudopotentials, which allow for a larger cutoff radius and a smaller number of plane waves to converge the results. The PAW method combines the benefits of both norm-conserving and ultrasoft pseudopotentials [95]. It describes the core electrons and their interactions with the valence electrons more accurately, while still reducing the computational cost.

2.5 Hellman-Feynman theorem

The forces acting on the nuclei are given by the Hellman-Feynman theorem [96], which states that the force acting on the nucleus I is given by the derivative of the total energy with respect to the position of the nucleus [96]:

$$\begin{aligned}\mathbf{F}_I &= -\frac{\partial E}{\partial \mathbf{R}_I} = -\frac{\partial E_{\mathrm{xc}}}{\partial \mathbf{R}_I} - \frac{\partial E_{\mathrm{H}}}{\partial \mathbf{R}_I} - \frac{\partial E_{\mathrm{ext}}}{\partial \mathbf{R}_I} \\ &= e^2 \int \sum_{i=1}^{N_{\mathrm{e}}} Z_i \frac{\mathbf{r}-\mathbf{R}_I}{|\mathbf{r}-\mathbf{R}_I|^3} \rho(\mathbf{r}) \mathrm{d}^3 r + e^2 \sum_{j=1}^{N_{\mathrm{c}}} Z_i Z_j \frac{\mathbf{R}_I - \mathbf{R}_j}{|\mathbf{R}_I - \mathbf{R}_j|^3},\end{aligned} \tag{2.38}$$

The first term describes the interaction of the nucleus with the electron density, while the second term describes the interaction of the nucleus with other nuclei. An important fact is that the Hellmann-Feynman forces are also functionals of the electron density, which makes them suitable for DFT calculations. The forces acting on the nuclei are calculated from the Hellmann-Feynman theorem, and the atomic positions are updated using a steepest descent or conjugate gradient method. After each iteration the Hellmann-Feynman forces are calculated and the atomic positions are updated until convergence is reached. The convergence criterion is usually set to a force threshold, which defines the maximum force acting on the nuclei. If the maximum force acting on the nuclei is below the force threshold, the calculation is considered converged. The Hellmann-Feynman theorem allows to calculate the forces acting on the nuclei in a self-consistent way, which is important for geometry optimization and molecular dynamics simulations [96]. Another important application of the Hellmann-Feynman forces are the calculation of phonon frequencies at the Γ-point within the so called frozen-phonon method.

2.6 Frozen-phonon method

There are several methods to calculate phonons, such as the linear response method and the frozen-phonon method. In this work, the frozen-phonon method is employed to determine the phonon frequencies at the Γ-point. The following description is based on Ref. [81]. It is assumed that a given Bravais lattice defines the crystal structure, leading to periodic boundary conditions due to translational invariance. The lattice vector $\mathbf{R}_n^0$ of the n-th unit cell corresponds to the equilibrium configuration, i.e., the energetically minimized state of the solid. Translational invariance holds between the lattice vectors $\mathbf{R}_n^0 - \mathbf{R}_m^0$ of any two unit cells. The position of the μ-th atom within the unit cell is given by $\mathbf{R}_\mu$, so the equilibrium position of the μ-th atom in the n-th unit cell is $\mathbf{R}_n^0 + \mathbf{R}_\mu$. To describe phonons, atomic displacements from equilibrium must be considered. The time-dependent displacement of the μ-th atom in the n-th unit cell is denoted by $\mathbf{u}_{n\mu}$. When atoms oscillate around their equilibrium positions, their time-dependent positions are given by [81]:

$$\mathbf{R}_{n\mu} = \mathbf{R}_n^0 + \mathbf{R}_\mu + \mathbf{u}_{n\mu} \tag{2.39}$$

Subsequently, the Taylor series of the effective potential $V_{\text{eff}}(\mathbf{R})$ around the equilibrium position $\mathbf{R}^0 = \mathbf{R}_n^0 + \mathbf{R}_\mu$ up to the second order is considered within the harmonic approximation [81]:

$$\begin{aligned}
V_{\text{eff}}(\mathbf{R}) \approx & \underbrace{V(\mathbf{R}^0)}_{=0} + \sum_{n=1}^{\frac{N_c}{r}} \sum_{\mu=1}^{r} \sum_{\alpha=1}^{d} \underbrace{\left.\frac{\partial V(\mathbf{R})}{\partial R_{n\mu\alpha}}\right|_{\mathbf{R}^0}}_{=0} \cdot u_{n\mu\alpha} \\
& + \frac{1}{2} \sum_{n,m=1}^{\frac{N_c}{r}} \sum_{\mu,\nu=1}^{r} \sum_{\alpha,\beta=1}^{d} \underbrace{\left.\frac{\partial^2 V(\mathbf{R})}{\partial R_{n\mu\alpha} \partial R_{m\nu\beta}}\right|_{\mathbf{R}^0}}_{=:\Phi_{n\mu\alpha,m\nu\beta}} \cdot u_{n\mu\alpha} u_{m\nu\beta} \\
= & \frac{1}{2} \sum_{n,m=1}^{\frac{N_c}{r}} \sum_{\mu,\nu=1}^{r} \sum_{\alpha,\beta=1}^{d} \Phi_{n\mu\alpha,m\nu\beta} u_{n\mu\alpha} u_{m\nu\beta}.
\end{aligned} \tag{2.40}$$

Here α and β denote the direction of the displacement, e.g. in Cartesian coordinates, with $d = 3$ and the spatial operator $\mathbf{R}_{n\mu} = (R_{n\mu 1}, R_{n\mu 2}, R_{n\mu 3})^T$. The number of atoms per unit cell is described with r. The first two terms vanish, as the effective potential is minimized at the equilibrium position of the nuclei. The third term describes the harmonic approximation of the effective potential, which is used to calculate the phonon frequencies. The Hessian matrix gives the forces when the nuclei are displaced from their equilibrium positions [81]:

$$F_{n\mu\alpha} = -\sum_{m=1}^{\frac{N_c}{r}} \sum_{\nu=1}^{r} \sum_{\beta=1}^{d} \Phi_{n\mu\alpha,m\nu\beta} u_{m\nu\beta} \tag{2.41}$$

For the time-dependent atomic displacement $u_{n\mu\alpha}(t) = \mathbf{R}_{n\mu}(t) - \mathbf{R}_{n\mu}^0$ the following ansatz is used:

$$u_{n\mu\alpha}(t) = \frac{1}{\sqrt{M_\mu}} \tilde{u}_{n\mu\alpha} e^{-i\omega t} \tag{2.42}$$

where M_μ is the mass of the nucleus μ, and $\tilde{u}_{n\mu\alpha}$ is the amplitude of the atomic displacement. After Fourier transformation, the equation of motion (EOM) is given by [81]:

$$\sum_{\nu=1}^{r} \sum_{\beta=1}^{d} \left[\left(\underline{\underline{D}} \right)_{\mu\alpha,\nu\beta} (\mathbf{q}) - \omega^2 \delta_{\mu\alpha} \delta_{\nu\beta} \right] w_{\nu\beta} = 0 \tag{2.43}$$

where $\mathbf{q}$ is the wave vector, and $w_{\nu\beta}$ is the amplitude of displacement:

$$\tilde{u}_{n\mu\alpha} = w_{\mu\alpha} e^{i\mathbf{q}\cdot\mathbf{R}_n^0}. \tag{2.44}$$

The dynamical matrix $\underline{\underline{D}}(\mathbf{q})$ is defined as:

$$D_{\mu\alpha,\nu\beta} = \frac{1}{\sqrt{M_\mu M_\nu}} \Phi_{\mu\alpha,\nu\beta}. \tag{2.45}$$

The dynamical matrix describes the interaction of the nuclei with each other and their interactions with the electron density. The eigenvalues of the dynamical matrix give the phonon frequencies. In order to determine the phonon frequencies, the dynamical matrix is diagonalized. The phonon frequencies at the Γ-point are given by the square root of the eigenvalues of the dynamical matrix:

$$\omega_n^2 = \langle e_n | D | e_n \rangle \, , \tag{2.46}$$

where e_n are the eigenvectors of the dynamical matrix, and ω_n are the frequencies of phonon mode n.

In order to solve Eq. (2.43) and obtain the phonon frequencies, the dynamical matrix needs to be calculated. In the framework of the frozen-phonon method, the dynamical matrix is calculated by displacing the nuclei from their equilibrium positions. In this state the system is considered as frozen, and the forces acting on the nuclei are calculated using the Hellmann-Feynman theorem in combination with the electron density yielded by the Kohn-Sham equations. The forces acting on the nuclei are calculated for different displacements of the nuclei, and the dynamical matrix is constructed from the forces acting on the nuclei. The dynamical matrix is then diagonalized to obtain the phonon frequencies. The frozen-phonon method is a powerful tool to calculate phonon frequencies, as it allows to calculate the phonon frequencies at the Γ-point without the need for a supercell calculation. However, it is limited to small displacements of the nuclei, as large displacements can lead to anharmonic effects, which are not taken into account by Eq. (2.40). Nevertheless, in this work the frozen-phonon method is sufficient to calculate the phonon frequencies at the Γ-point, as the displacements of the nuclei are small and the anharmonic effects are negligible.

3 Electronic excitated-state theory

3.1 Nonlinear optics

If a solid, e.g. an insulator or a semiconductor, immersed in an electric field $\boldsymbol{\mathcal{E}}$, the dipoles inside the solid will generate a polarization field $\boldsymbol{\mathcal{P}}$ against the applied field. The sum of the applied field and the polarization field is the total field inside the solid also called displacement field $\boldsymbol{\mathcal{D}}$ [24]:

$$\boldsymbol{\mathcal{D}} = \epsilon_0 \boldsymbol{\mathcal{E}} + \boldsymbol{\mathcal{P}}, \tag{3.1}$$

where ϵ_0 is the permittivity of free space. The relation between the external field $\boldsymbol{\mathcal{E}}$ and displacement field $\boldsymbol{\mathcal{D}}$ is given by the constitutive relation:

$$\boldsymbol{\mathcal{D}} = \epsilon_0 \epsilon_r \boldsymbol{\mathcal{E}}, \tag{3.2}$$

where ϵ_r is the relative permittivity of the solid. In a first approximation, the polarization field $\boldsymbol{\mathcal{P}}$ can be expressed as:

$$\boldsymbol{\mathcal{P}} = \epsilon_0 (\epsilon_r - 1) \boldsymbol{\mathcal{E}} = \epsilon_0 \chi \boldsymbol{\mathcal{E}}, \tag{3.3}$$

where χ is the electric susceptibility of the solid. The electric susceptibility is a measure of how easily the dipoles inside the solid can be polarized by an external field. For an isotropic solid, the electric susceptibility is a scalar. In the case of large electric fields (10^5 volts/cm), the relation between the time-dependent polarization field $\boldsymbol{\mathcal{P}}(t)$ and the electric field $\boldsymbol{\mathcal{E}}(t)$ is given by the following expansion [24]:

$$\mathcal{P}_i(t) = \chi_{ij}^{(1)} \mathcal{E}_j(t) + \chi_{ijk}^{(2)} \mathcal{E}_j(t) \mathcal{E}_k(t) + \chi_{ijkl}^{(3)} \mathcal{E}_j(t) \mathcal{E}_k(t) \mathcal{E}_l(t) + ..., \tag{3.4}$$

where i, j, k, l are the indices of the Cartesian coordinates, and Gaussian units as well as Einstein summation convention are used. The first term is the linear response of the solid to the applied field. All terms behind the first term are nonlinear responses. In fact, Eq. 3.4 describes an instantaneous response of a solid to an applied field. However, in reality, the response of a solid to an applied field is not instantaneous. The polarization field $\boldsymbol{\mathcal{P}}(t)$ depends on the history of the applied field $\boldsymbol{\mathcal{E}}(t)$ and the response of the solid is delayed. This delay is described by a convolution integral [24]:

$$\begin{aligned} \mathcal{P}_i(t) = & \int \chi_{ij}^{(1)}(t - t_1) \mathcal{E}_j(t_1) \mathrm{d}t_1 + \iint \chi_{ijk}^{(2)}(t - t_1, t - t_2) \mathcal{E}_j(t_1) \mathcal{E}_k(t_2) \mathrm{d}t_1 \mathrm{d}t_2 \\ & + \iiint \chi_{ijkl}(t - t_1, t - t_2, t - t_3) \mathcal{E}_j(t_1) \mathcal{E}_k(t_2) \mathcal{E}_l(t_3) \mathrm{d}t_1 \mathrm{d}t_2 \mathrm{d}t_3 + ..., \end{aligned} \tag{3.5}$$

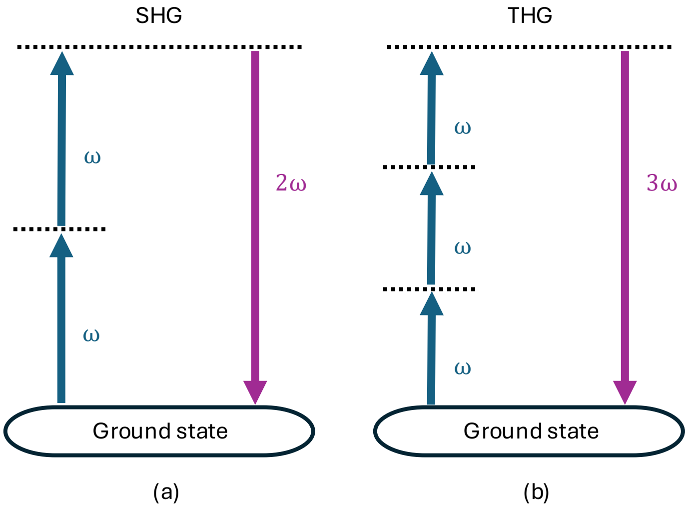

Figure 3.1: A schematic representation of (a) second-harmonic generation (SHG), (b) third-harmonic generation (THG)

Here, $\chi^{(1)}_{ij}(t-t_1)$, $\chi^{(2)}_{ijk}(t-t_1, t-t_2)$, and $\chi^{(3)}_{ijkl}(t-t_1, t-t_2, t-t_3)$ are the linear, second-order, and third-order response functions, respectively. These tensors characterize the material's response to one, two, or three incident photons, and thus encode a wide range of nonlinear optical phenomena. To analyze which processes are described by each response function, it is useful to transform the polarization field $\boldsymbol{\mathcal{P}}(t)$ into the frequency domain. The Fourier transform of $\boldsymbol{\mathcal{P}}(t)$ is given by [24]:

$$\begin{aligned}\mathcal{P}_i(\omega) &= \chi^{(1)}_{ij}(\omega;\omega_1)\mathcal{E}_j(\omega_1) + \iint \chi^{(2)}_{ijk}(\omega;\omega_1,\omega_2)\mathcal{E}_j(\omega_1)\mathcal{E}_k(\omega_2)d\omega_1 d\omega_2 \\ &\qquad + \iiint \chi^{(3)}_{ijkl}(\omega;\omega_1,\omega_2,\omega_3)\mathcal{E}_j(\omega_1)\mathcal{E}_k(\omega_2)\mathcal{E}_l(\omega_3)d\omega_1 d\omega_2 d\omega_3 + \dots \\ &= \chi^{(1)}_{ij}(\omega;\omega_1)\mathcal{E}_j(\omega_1) + \chi^{(2)}_{ijk}(\omega;\omega_1,\omega_2)\mathcal{E}_j(\omega_1)\mathcal{E}_k(\omega_2) \\ &\qquad + \chi^{(3)}_{ijkl}(\omega;\omega_1,\omega_2,\omega_3)\mathcal{E}_j(\omega_1)\mathcal{E}_k(\omega_2)\mathcal{E}_l(\omega_3) + \dots, \end{aligned} \tag{3.6}$$

where $\omega_1, \omega_2, \omega_3$ are the frequencies of the electric field $\boldsymbol{\mathcal{E}}(\omega)$ and $\omega = \sum_i \omega_i$ is the frequency of the polarization field $\boldsymbol{\mathcal{P}}(\omega)$. The last conversion is only valid for monochromatic fields, e.g., with sinusoidal time-dependence. For different configurations of the electric fields, the response functions describe different optical phenomena. The first-order response function $\chi^{(1)}_{ij}(\omega;\omega_1)$ describes linear optics. The nonlinear terms describe various optical phenomena such as second-harmonic generation (SHG) and third-harmonic generation (THG) (see Fig. 3.1). For SHG, two photons with the same frequency $\omega_1 = \omega_2$ are mixed to generate a photon with frequency $\omega = 2\omega_1$. For THG, three photons with the same frequency $\omega_1 = \omega_2 = \omega_3$ are mixed to generate a photon with frequency $\omega = 3\omega_1$. Other processes described by the nonlinear response functions include sum frequency generation (SFG), difference frequency generation (DFG), two-photon absorption (TPA), etc. Table 3.1 summarizes the most important nonlinear optical processes.

How large are nonlinear effects? Assuming an atomic electric field $\mathcal{E} = \mathcal{E}_{at} \sim 10^{11}$ V/m and linear susceptibility $\chi^{(1)}$ of the order of unity, the second-order susceptibility $\chi^{(2)} = \chi^{(1)}/\mathcal{E}_{at}$ is of the order of 10^{-12} m/V. Similarly, the third-order susceptibility $\chi^{(3)} =$

Table 3.1: Summary of several three- and four-wave mixing processes. The first column describes the wave mixing process with the relationship between the frequencies (ω_1, ω_2 and ω_3) of the incoming and outgoing (ω) photons.

Wave mixing process	ω_1, ω_2, ω_3	ω
Second-harmonic generation	$\omega_1 = \omega_2$	$2\omega_1$
Sum frequency generation	$\omega_1 \neq \omega_2$	$\omega_1 + \omega_2$
Difference frequency generation	$\omega_1 \neq \omega_2$	$\omega_1 - \omega_2$
Pockels effect	$\omega_2 \to 0$	ω_1
Optical rectification	$\omega_1 = \omega_2$	0
Third-harmonic generation	$\omega_1 = \omega_2 = \omega_3$	$3\omega_1$
Two photon absorption	$\omega_1 = \omega_2 = -\omega_3$	ω_1
DC Kerr effect	$\omega_1 = \omega_2 = 0$	ω_3
Optical Kerr effect	$\omega_2 = -\omega_3$; $\omega_1 \neq \omega_2$	ω_1
Intensity-dependent refractive index	$\omega_2 = -\omega_3$; $\omega_1 = \omega_2$	ω_1

$\chi^{(1)}/\mathcal{E}_{at}^2$ is of the order of 10^{-24} m/V [24]. Hence, the linear response term is the dominating factor in the electric polarization since the nonlinear susceptibilities are very small compared to the linear susceptibility. The study of nonlinear optical processes is challenging on both fronts: Computationally, double precision is needed because the nonlinear signals are tiny differences of large quantities accumulated over long time evolutions. Experimentally, the signals are weak and demand high-intensity, precisely controlled lasers and careful alignment to detect. Electric fields of an order of 10^5 volts/cm are required to observe nonlinear optical effects. This was first achived by Franken *et al.* in 1961, who observed SHG in quartz [97]. By now, such electric fields can be achieved by using commercial high-power lasers as well as exploiting phase matching conditions. How can the nonlinear susceptibilities be calculated? In this work two different approaches are discussed. The first approach is the sum over states approach based on time-dependent perturbation theory. The second approach is a real-time approach.

3.2 Band-structure theory

Based on pertubation theory, an analytical expression for the optical response functions are derived by Leitsmann *et al.* [98]. The interaction between electrons and an external electromagnetic field with the vector potential $\mathbf{A}(\mathbf{r}, t)$ and the scalar potential $\Phi(\mathbf{r}, t)$ can be described by the Hamiltonian H in the interaction picture. The interaction Hamiltonian is given by:

$$H = \frac{1}{2m} \sum_{i=1}^{N} (\mathbf{p}_i - e\mathbf{A}(\mathbf{r}_i, t))^2 + V(\mathbf{r}), \tag{3.7}$$

where $\mathbf{p}_i$ is the momentum operator of the i-th electron, e is the charge of the electron, $V(\mathbf{r})$ is the potential energy of the system and $\mathbf{r}_i$ is the position operator of the i-th electron. The Hamiltonian can be rewritten in a more convenient form:

$$H = \sum_{i=1}^{N} \left[\frac{\mathbf{p}_i^2}{2m} + \frac{e}{2m} (\mathbf{p}_i \cdot \mathbf{A}(\mathbf{r}_i, t) + \mathbf{A}(\mathbf{r}_i, t) \cdot \mathbf{p}_i) + \frac{e^2}{2m} \mathbf{A}^2(\mathbf{r}_i, t) \right] + V(\mathbf{r}), \tag{3.8}$$

The first term is the kinetic energy of the unperturbed system. The second term indicates the time-dependent response of the electon's wave function to the external field and yields the so called dynamical current density (in some literature also called the paramagnetic current density) [98]:

$$\mathbf{j}_{\text{dyn}}(\mathbf{r}, t) = \frac{e}{2m} \left(\psi^*(\mathbf{r}, t) \nabla \psi(\mathbf{r}, t) - \psi(\mathbf{r}, t) \nabla \psi^*(\mathbf{r}, t) \right), \tag{3.9}$$

using the continuous equation:

$$\frac{\partial \rho(\mathbf{r}, t)}{\partial t} + \nabla \cdot \mathbf{j}(\mathbf{r}, t) = 0, \tag{3.10}$$

and the Heisenberg equation:

$$\frac{\partial \rho(\mathbf{r}, t)}{\partial t} = \frac{i}{\hbar} \left[H, \rho(\mathbf{r}, t) \right]. \tag{3.11}$$

The third term in Eq. (3.8) describes an instantaneous response of the system to the external field. This term and the dynamical current density give together the total current density $\mathbf{j}(\mathbf{r}, t)$ [98]:

$$\mathbf{j}(\mathbf{r}, t) = \mathbf{j}_{\text{dyn}}(\mathbf{r}, t) - \frac{e^2}{mc} \rho(\mathbf{r}, t) \mathbf{A}(\mathbf{r}, t), \tag{3.12}$$

where c is the speed of light. In the interaction picture, the time evolution operator $U(t)$ is given by [98]:

$$\begin{aligned} U(t) = & -\frac{i}{\hbar} \int_{-\infty}^{t} H(t') U(t') \mathrm{d}t' \\ & -\frac{i}{\hbar} \int_{-\infty}^{t} H(t') \mathrm{d}t' + \left(-\frac{i}{\hbar} \right)^2 \int_{-\infty}^{t} \mathrm{d}t' \int_{-\infty}^{t'} H(t') H(t'') U(t'') \mathrm{d}t'' + \dots, \end{aligned} \tag{3.13}$$

which can be expanded recursively to any order. Using this the induced current density $\mathbf{j}_{\text{ind}}(\mathbf{r}, t)$ can be expressed as:

$$\mathbf{j}_{\text{ind}}(\mathbf{r}, t) = U^\dagger(t) \mathbf{j}(\mathbf{r}, t) U(t) - \mathbf{j}_{\text{dyn}}(\mathbf{r}, t). \tag{3.14}$$

The induced current density $\mathbf{j}_{\text{ind}}(\mathbf{r}, t)$ is the response of the system to the external field which can be expressed by the expansion:

$$\mathbf{j}_{\text{ind}}(\mathbf{r}, t) = \sum_{i}^{\infty} \mathbf{j}_{\text{ind}}^{(i)}(\mathbf{r}, t), \tag{3.15}$$

where $\mathbf{j}^{(i)}_{\text{ind}}(\mathbf{r},t)$ is the i-th order response function. The first-order induced current density is given by:

$$j^{(1)}_{\text{ind},\alpha}(\mathbf{r},t) = -\frac{i}{\hbar c}\int d\mathbf{r}' \int_{-\infty}^{t} \mathrm{d}t' \left[j_{\text{dyn},\beta}(\mathbf{r}',t'), j_{\text{dyn},\alpha}(\mathbf{r},t)\right] A_\beta(\mathbf{r}',t'), \tag{3.16}$$

and the second-order:

$$\begin{aligned} j^{(2)}_{\text{ind},\alpha}(\mathbf{r},t) = &- \frac{1}{\hbar^2 c^2}\int d\mathbf{r}' \int d\mathbf{r}'' \int_{-\infty}^{t} \mathrm{d}t' \int_{-\infty}^{t'} \mathrm{d}t'' \\ &\cdot \left[j_{\text{dyn},\beta}(\mathbf{r}'',t''), \left[j_{\text{dyn},\beta}(\mathbf{r}',t'), j_{\text{dyn},\alpha}(\mathbf{r},t)\right]\right] A_\beta(\mathbf{r}',t') \end{aligned} \tag{3.17}$$

where α, β are the indices of the Cartesian coordinates. The induced current density $\mathbf{j}_{\text{ind}}(\mathbf{r},t)$ can be expressed in terms of the polarization field $\boldsymbol{\mathcal{P}}(\mathbf{r},t)$ [98]:

$$\mathbf{j}_{\text{ind}}(\mathbf{r},t) = \frac{\partial \boldsymbol{\mathcal{P}}(\mathbf{r},t)}{\partial t}. \tag{3.18}$$

This leads in combination with Eq. (3.16) to the following expression for the linear response function $\epsilon_{\alpha\beta}(\omega;\omega)$ [98]:

$$\epsilon_{\alpha\beta}(-\omega;\omega) = \delta_{\alpha\beta} + \frac{8\pi e^2}{\hbar m^2 \tilde{\omega}^2 V}\sum_{nm\mathbf{k}} f_{nm}(\mathbf{k})\frac{p^\alpha_{nm}(\mathbf{k})p^\beta_{mn}(\mathbf{k})}{\omega_{mn}(\mathbf{k}) - \tilde{\omega}}, \tag{3.19}$$

and the second-order response function $\chi^{(2)}_{\alpha\beta\gamma}(-2\omega;\omega,\omega)$ [98]:

$$\begin{aligned} \chi^{(2)}_{\alpha\beta\gamma}(-2\omega;\omega,\omega) =& \frac{-ie^3}{\hbar^2 m^3 \tilde{\omega}^3 V}\sum_{nml\mathbf{k}} \frac{1}{\omega_{mn}(\mathbf{k}) - 2\tilde{\omega}} \\ &\cdot \left[\frac{f_{nl}(\mathbf{k})p^\alpha_{nm}\left\{p^\beta_{ml}p^\gamma_{ln}\right\}}{\omega_{ln}(\mathbf{k}) - \tilde{\omega}} + \frac{f_{ml}(\mathbf{k})p^\alpha_{nm}\left\{p^\beta_{ml}p^\gamma_{ln}\right\}}{\omega_{ml}(\mathbf{k}) - \tilde{\omega}}\right], \end{aligned} \tag{3.20}$$

with $f_{nm}(\mathbf{k}) = f(\epsilon_n(\mathbf{k})) - f(\epsilon_m(\mathbf{k}))$ the difference of the Fermi-Dirac distribution function of eigenstates n and m, $\tilde{\omega} = \omega + i\eta$ with η a small positive number, V the volume of the system, $p^\alpha_{nm}(\mathbf{k}) = \langle\psi_n(\mathbf{k})|p_\alpha|\psi_m(\mathbf{k})\rangle$ the matrix element of the momentum operator between the eigenstates n and m, and $\omega_{mn}(\mathbf{k}) = \epsilon_m(\mathbf{k}) - \epsilon_n(\mathbf{k})$ the energy difference between the eigenstates n and m. The notation $\{...\}$ means:

$$\left\{p^\beta_{ml}p^\gamma_{ln}\right\} = \frac{1}{2}\left(p^\beta_{ml}p^\gamma_{ln} + p^\gamma_{ln}p^\beta_{ml}\right). \tag{3.21}$$

Equation (3.20) can be split into two-band contributions [98]:

$$\begin{aligned} \chi^{(2),\text{two}}_{\alpha\beta\gamma}(-2\omega;\omega,\omega) =& \frac{-ie^3}{\hbar^2 m^3 V}\sum_{nm\mathbf{k}}\left[\frac{16 f_{nm}(\mathbf{k})p^\alpha_{nm}\left\{\Delta^\beta_{mn}p^\gamma_{mn}\right\}}{\omega_{mn}(\mathbf{k})^4(\omega_{mn}(\mathbf{k}) - 2\tilde{\omega})}\right. \\ &\left. - \frac{f_{nm}(\mathbf{k})p^\alpha_{nm}\left\{\Delta^\beta_{mn}p^\gamma_{mn}\right\}}{\omega_{mn}(\mathbf{k})^4(\omega_{mn}(\mathbf{k}) - \tilde{\omega})}\right], \end{aligned} \tag{3.22}$$

and a three-band contribution [98]:

$$\begin{aligned}\chi^{(2),\text{three}}_{\alpha\beta\gamma}(-2\omega;\omega,\omega) = & \frac{-ie^3}{\hbar^2 m^3 V} \sum_{n\neq m\neq l\mathbf{k}} \frac{p^{\alpha}_{nm}\left\{p^{\beta}_{ml}p^{\gamma}_{ln}\right\}}{\omega_{ln}(\mathbf{k}) - 2\omega_{mn}(\mathbf{k})} \\ & \cdot \left[\frac{16 f_{nm}(\mathbf{k})}{\omega_{mn}(\mathbf{k})^3(\omega_{mn}(\mathbf{k}) - \tilde{\omega})} + \frac{f_{ml}(\mathbf{k})}{\omega_{ml}(\mathbf{k})^3(\omega_{ml}(\mathbf{k}) - \tilde{\omega})} \right. \\ & \left. + \frac{f_{ln}(\mathbf{k})}{\omega_{ln}(\mathbf{k})^3(\omega_{ln}(\mathbf{k}) - \tilde{\omega})}\right]. \end{aligned} \tag{3.23}$$

As a result, the optical response functions are obtained by summation over states, which can be calculated in the framework of DFT. Here this theory is described in the IPA. This means that the electrons are treated as non-interacting particles. This is a good approximation for undoped nonmagnetic semiconductors and insulators at 0 K. However, it is possible to use this approach within the *GW* approximation to include self-energy effects. In addition, Bethe-Salpeter equations (BSE) can be solved in order to account for excitionic and local field effects [98]. In order to save computational time, only the two-band contribution can be calculated since in practice the three-band contribution is very small. Also the sum over states can be limited to a certain number of bands which need to be converged.

An issue of the sum over states approach is that the formalism derived in a perturbative approach and thus the sum itself become more complex as the order of the response function increases. To avoid this problem, another ansatz is presented in the following section. This ansatz is based on the real-time propagation of the wave function in the presence of an external field. This approach allows to calculate the nonlinear response functions of in principle any order in a more efficient way.

3.3 Real-time approach

The idea of the real-time approach is that if the external electric field, on the one hand, and the dynamical polarization, on the other hand, are known, the optical response can be derived from Eq. (3.4). For this the dynamical polarization is calculated in the time-domain from real-time simulations.

How to define the polarization in periodic systems? This question was a problem for many years. In order to understand why this problem is so difficult, let's first consider an isolated system, i.e. a system with open boundary conditions. The polarization is defined as the dipole moment per unit volume:

$$\boldsymbol{\mathcal{P}} = \frac{1}{V}\int \mathbf{r}\rho(\mathbf{r})\mathrm{d}\mathbf{r}, \tag{3.24}$$

where V is the volume of the system and $\rho(\mathbf{r})$ is the charge density at the position $\mathbf{r}$. In this case, the polarization is a well-defined quantity. However, in periodic systems, the situation is different. A naive way to define the polarization is to use the same definition as for isolated systems and generalize it to periodic systems. In doing so, two approaches are thinkable.

Firstly, the dipole moment could be averaged over the whole sample. In this case, the contributions of the dipole moments inside the sample cancel each other. The only contribution to the dipole moment is the dipole moment at the surface of the sample

resulting from charge accumulations at the surface [99]. As a result, the polarization is in this definition not a bulk property but a surface property. Another issue is that the whole sample needs to be treated in the calculations which is, assuming a system with 10^{23} particles, not feasible.
Secondly, the dipole moment could be averaged over the unit cell. In this case, the polarization is a bulk property. However, the problem is that the dipole moment is not a well-defined quantity in periodic systems since the unit cell is not unambiguously defined. Depending on the choice of the unit cell, the dipole moment can be different. As the polarization needs to be a well-defined quantity, this approach is not feasible either.
Another proposal might be to derive the macroscopic polarization from the macroscopic average of the microscopic polarization:

$$\nabla \cdot \boldsymbol{\mathcal{P}}_{\text{micro}} = -\rho(\mathbf{r}), \tag{3.25}$$

where $\boldsymbol{\mathcal{P}}_{\text{micro}}$ is the microscopic polarization. However, also in this approach the macroscopic polarization is not a well-defined, since the microscopic polarization is defined up to a constant.
After all proposals failed to well-define the polarization, in the next section the modern approach to define the polarization in periodic systems is presented, which was introduced by King-Smith and Vanderbilt [100].

3.3.1 Dynamical Berry phase

In the theory of polarization in periodic systems, King-Smith and Vanderbilt make use of the concept of the Berry phase [101, 102]. In order to understand this concept let's first consider a system which is described by a Hamiltonian $H(\mathbf{R})$:

$$H(\mathbf{R}) \left|\psi_n(\mathbf{R})\right\rangle = E_n(\mathbf{R}) \left|\psi_n(\mathbf{R})\right\rangle , \tag{3.26}$$

which depends on a set of parameters $\mathbf{R}$ that parameterize an arbitrary process. The eigenstates of the Hamiltonian are denoted by $|\psi_n(\mathbf{R})\rangle$ and the corresponding eigenenergies are denoted by $E_n(\mathbf{R})$. If the parameters $\mathbf{R}$ are changed adiabatically, and the system is in the eigenstate $|\psi_n(\mathbf{R})\rangle$, the wave function acquires a phase factor γ_n:

$$e^{-i\gamma_n} = \frac{\langle\psi_n(\mathbf{R}_1)|\psi_n(\mathbf{R}_2)\rangle}{|\langle\psi_n(\mathbf{R}_1)|\psi_n(\mathbf{R}_2)\rangle|}, \tag{3.27}$$

given by:

$$\gamma_n = -\operatorname{Im}\ln \langle\psi_n(\mathbf{R}_1)|\psi_n(\mathbf{R}_2)\rangle . \tag{3.28}$$

Since the phase of the wave function is defined up to a constant, it has no physical meaning. However, if the wave fuction is changed adiabatically around a closed path in parameter space with several parameters $\mathbf{R}$, the phase factor γ_n becomes:

$$\gamma_n = -\operatorname{Im}\ln \left(\langle\psi_n(\mathbf{R}_1)|\psi_n(\mathbf{R}_2)\rangle \langle\psi_n(\mathbf{R}_2)|\psi_n(\mathbf{R}_3)\rangle \langle\psi_n(\mathbf{R}_3)|\psi_n(\mathbf{R}_1)\rangle\right) . \tag{3.29}$$

Now each wave function appears with its complex conjugated complement. As a result, constant phase shifts cancel each other out, yielding a gauge-invariant phase factor γ_n, also called the Berry phase. The Berry phase can be generalized to a closed path C in parameter space with several parameters $\mathbf{R}$:

$$\gamma_n = i \oint_C \left\langle \psi_n(\mathbf{R}) \middle| \frac{\partial}{\partial \mathbf{R}} \psi_n(\mathbf{R}) \right\rangle d\mathbf{R}. \tag{3.30}$$

After introducing the Berry phase for an abstract problem, the theory of King-Smith and Vanderbilt is presented, which exploits the Berry phase to define the change of the polarization in periodic systems [100]. From the flow of the polarization currents, the change of the polarization $\Delta\boldsymbol{\mathcal{P}}$ can be expressed as:

$$\Delta\boldsymbol{\mathcal{P}} = \int_0^1 \frac{\partial \boldsymbol{\mathcal{P}}}{\partial \lambda} \mathrm{d}\lambda, \tag{3.31}$$

where λ parameterizes the process. The derivative $\frac{\partial \boldsymbol{\mathcal{P}}}{\partial \lambda}$ can be described using perturbation theory:

$$\frac{\partial \mathcal{P}_\alpha}{\partial \lambda} = -\frac{ife\hbar}{N\Omega m} \sum_{nm\mathbf{k}} \frac{\langle \psi_{n,\mathbf{k}}(\lambda) | p_\alpha | \psi_{m,\mathbf{k}}(\lambda) \rangle \left\langle \psi_{m,\mathbf{k}}(\lambda) \middle| \frac{\partial V_{KS}(\lambda)}{\partial \lambda} \psi_{n,\mathbf{k}}(\lambda) \right\rangle}{\left(\epsilon_{n,\mathbf{k}}(\lambda) - \epsilon_{m,\mathbf{k}}(\lambda)\right)^2} + \text{c.c.}, \tag{3.32}$$

where N is the number of unit cells in the system, Ω is the volume of the unit cell, $V_{KS}(\lambda)$ is the Kohn-Sham potential, and $\epsilon_{n,\mathbf{k}}(\lambda)$ is the Kohn-Sham eigenvalue. In a periodic system, the Schrödinger equation is given by:

$$\left[\frac{p^2}{2m} + V_{KS}(\mathbf{r})\right] |\psi_{n,\mathbf{k}}(\mathbf{r})\rangle = \epsilon_{n,\mathbf{k}} |\psi_{n,\mathbf{k}}(\mathbf{r})\rangle . \tag{3.33}$$

The wave function $|\psi_{n,\mathbf{k}}(\mathbf{r})\rangle$, obeying Born-von Karman boundary conditions, can be expressed as:

$$|\psi_{n,\mathbf{k}}(\mathbf{r})\rangle = e^{i\mathbf{k}\cdot\mathbf{r}} |u_{n,\mathbf{k}}(\mathbf{r})\rangle , \tag{3.34}$$

according to Bloch's theorem [103], where $|u_{n,\mathbf{k}}(\mathbf{r})\rangle$ is the periodic part of the wave function. Inserting this into Eq. (3.33) yields:

$$\left[\frac{1}{2m}(p + \hbar\mathbf{k})^2 + V(\mathbf{r})\right] |u_{n,\mathbf{k}}(\mathbf{r})\rangle = \epsilon_{n,\mathbf{k}} |u_{n,\mathbf{k}}(\mathbf{r})\rangle . \tag{3.35}$$

Equation (3.35) has now a periodic Hamiltonian parameterized by the wave vector $\mathbf{k}$. This gives rise to the expectation value of the momentum operator p and the Kohn-Sham potential $V_{KS}(\mathbf{r})$ resulting in the following expression for the change of the polarization:

$$\Delta\mathcal{P}_\alpha = \frac{2ie}{(2\pi)^3} \int_{BZ} \mathrm{d}\mathbf{k} \sum_n \langle \psi_{n,\mathbf{k}} | \frac{\partial}{\partial \mathbf{k}} | \psi_{n,\mathbf{k}} \rangle , \tag{3.36}$$

by integrating λ from 0 to 1, exploitig $V_{KS}(0) = V_{KS}(1)$, setting $f = 2$ for spin-degenerate bands, and choosing a gauge where the wave function is periodic in $\mathbf{k}$-space, i.e. $|\psi_{n,\mathbf{k}}\rangle = |\psi_{n,\mathbf{k}+\mathbf{G}}\rangle$ and

$$|u_{n,\mathbf{k}}(\mathbf{r})\rangle = e^{i\mathbf{G}\cdot\mathbf{r}} |u_{n,\mathbf{k}+\mathbf{G}}(\mathbf{r})\rangle , \tag{3.37}$$

with $\mathbf{G}$ a reciprocal lattice vector, which is in 1D given by $G = 2\pi n/L$ with n an integer and L the length of the system. Equation (3.36) has the form of a Berry phase with the closed path in parameter space being the Brillouin zone.

While the King-Smith-Vanderbilt (KSV) formulation of the polarization expresses the change of the polarization in terms of the Berry phase of Bloch states, it is strictly defined for non-interacting systems and relies on the representation of the wave function in reciprocal space. A generalized formulation in real space is given by Resta who reformulated in terms of ground state many-body wave functions $|\Psi_0\rangle$ via the Berry phase [104–106]:

$$\Delta\boldsymbol{\mathcal{P}}_\alpha = \frac{eN_{\mathbf{k}_\alpha}\mathbf{a}_\alpha}{2\pi V}\operatorname{Im}\ln\left\langle\Psi_0\middle|e^{i\mathbf{q}_\alpha\cdot\mathbf{R}}\middle|\Psi_0\right\rangle, \tag{3.38}$$

where $\mathbf{q}_\alpha = \frac{\mathbf{b}_\alpha}{N_{\mathbf{k}_\alpha}}$ is the smallest distance in reciprocal space between the two points along the direction α with the reciprocal lattice vector $\mathbf{b}_\alpha$ and $N_{\mathbf{k}_\alpha}$ the number of $\mathbf{k}$-points in the direction α, and $\mathbf{a}_\alpha$ is the lattice vector in the direction α. The operator $\mathbf{R} = \sum_{i=1}^{N}\mathbf{r}_i$ is the total position operator of the system. Considering the many-body wave function $|\Psi_0\rangle$ as a Slater determinant of the single-particle wave functions $|\psi_{n,\mathbf{k}}\rangle$, the polarization can be expressed in terms of the Berry phase of the single-particle wave functions. This can be expressed as the determinant of an overlap matrix $S_{\mathbf{k}m,\mathbf{k}'n}$:

$$S_{\mathbf{k}m,\mathbf{k}'m'} = \left\langle\psi_{m,\mathbf{k}}\middle|e^{i\mathbf{q}_\alpha\cdot\mathbf{R}}\middle|\psi_{m',\mathbf{k}'}\right\rangle, \tag{3.39}$$

where m and m' are the band indices. As a result, the change in polarization can be expressed as:

$$\Delta\boldsymbol{\mathcal{P}}_\alpha = -\frac{ef\mathbf{a}_\alpha}{2\pi N_{\mathbf{k}_\alpha^\perp}v}\operatorname{Im}\ln\det S, \tag{3.40}$$

where $N_{\mathbf{k}_\alpha^\perp}$ is the number of $\mathbf{k}$-points in the direction perpendicular to $\mathbf{b}_\alpha$ and $f = 2$ for spin-degenerate bands. From the periodic gauge it folllows that the overlap matrix $S_{\mathbf{k}m,\mathbf{k}'n}$ is only non-zero if $\mathbf{k}' - \mathbf{k} = \mathbf{q}_\alpha$. As a result, the overlap matrix reduces to:

$$S_{mn}(\mathbf{k},\mathbf{k}+\mathbf{q}_\alpha) = \left\langle v_{m,\mathbf{k}}\middle|v_{n,\mathbf{k}+\mathbf{q}_\alpha}\right\rangle, \tag{3.41}$$

where $v_{m,\mathbf{k}}$ is the periodic part of the wave function. The polarization is then expressed as a product of $N_{\mathbf{k}_\alpha}$ overlap matrices $S_{mn}(\mathbf{k},\mathbf{k}+\mathbf{q}_\alpha)$:

$$\Delta\boldsymbol{\mathcal{P}}_\alpha = -\frac{ef}{2\pi v}\frac{\mathbf{a}_\alpha}{N_{\mathbf{k}_\alpha^\perp}}\sum_{\mathbf{k}_\alpha^\perp}\operatorname{Im}\ln\prod_{i=1}^{N_{\mathbf{k}_\alpha}-1}\det S(\mathbf{k}_i,\mathbf{k}_i+\mathbf{q}_\alpha), \tag{3.42}$$

where v is the volume of the unit cell. Exploiting matrix properties, the product of the determinants can be rewritten as the trace of the logarithm of the overlap matrices:

$$\Delta\boldsymbol{\mathcal{P}}_\alpha = -\frac{ef}{2\pi v}\frac{\mathbf{a}_\alpha}{N_{\mathbf{k}_\alpha^\perp}}\sum_{\mathbf{k}_\alpha^\perp}\operatorname{Im}\sum_{i=1}^{N_{\mathbf{k}_\alpha}-1}\operatorname{tr}\ln S(\mathbf{k}_i,\mathbf{k}_i+\mathbf{q}_\alpha). \tag{3.43}$$

3.3.2 Equation of motion

Following the scheme of Souza *et al.* [76], a Lagrangian formalism is applied to a Hamiltonian of the form:

$$H = H^0 + H^{\boldsymbol{\mathcal{E}}}(t), \tag{3.44}$$

where H^0 is the unperturbed single-particle Hamiltonian and $H^{\boldsymbol{\mathcal{E}}}(t)$ is the time-dependent perturbed Hamiltonian describing the coupling with an external electric field $\boldsymbol{\mathcal{E}}(t)$. According to Ref. [76] the Lagrangian is given by:

$$\mathcal{L} = \frac{i\hbar}{N_{\mathbf{k}}} \sum_{n\mathbf{k}} \left\langle v_{n,\mathbf{k}} \middle| \frac{\partial}{\partial t} v_{n,\mathbf{k}} \right\rangle - E^0 - v\boldsymbol{\mathcal{E}} \cdot P, \tag{3.45}$$

where E^0 is the unperturbed energy:

$$E^0 = \frac{1}{N_{\mathbf{k}}} \sum_{n\mathbf{k}} \left\langle v_{n,\mathbf{k}} \middle| H^0_{\mathbf{k}} \middle| v_{n,\mathbf{k}} \right\rangle, \tag{3.46}$$

using $H^0_{\mathbf{k}} = e^{-\mathbf{k}\cdot\mathbf{r}'} H^0 e^{\mathbf{k}\cdot\mathbf{r}}$. The last term in Eq. (3.45) describes the coupling of the external electric field $\boldsymbol{\mathcal{E}}$ to the polarization $\boldsymbol{\mathcal{P}}$ of the system. In order to derive the equation of motion from the Lagrangian, the Euler-Lagrange equation is used:

$$\frac{\mathrm{d}}{\mathrm{d}t}\left(\frac{\partial \mathcal{L}}{\partial \dot{q}_i}\right) - \frac{\partial \mathcal{L}}{\partial q_i} = 0, \tag{3.47}$$

where q_i are the generalized coordinates and $\dot{q}_i$ their time derivatives. The generalized coordinates are given by the periodic part of the wave function $v_{n,\mathbf{k}}$ and the generalized momenta are given by the time derivative of the periodic part of the wave function $\dot{v}_{n,\mathbf{k}}$. The equation of motion can be expressed as:

$$\begin{aligned} \frac{\mathrm{d}}{\mathrm{d}t} \frac{\delta \mathcal{L}}{\langle \delta \dot{v}_{n,\mathbf{k}} |} - \frac{\delta \mathcal{L}}{\langle \delta v_{n,\mathbf{k}} |} &= 0, & (3.48)\\ i\hbar \frac{\mathrm{d}}{\mathrm{d}t} | v_{n,\mathbf{k}} \rangle - H^0_{\mathbf{k}} | v_{n,\mathbf{k}} \rangle - N_{\mathbf{k}} v \boldsymbol{\mathcal{E}} \cdot \frac{\delta \boldsymbol{\mathcal{P}}}{\langle \delta v_{n,\mathbf{k}} |} &= 0, & (3.49) \end{aligned}$$

where $\delta\mathcal{L}$ is the variation of the Lagrangian and $\delta v_{n,\mathbf{k}}$ is the variation of the periodic part of the wave function. The variation of the polarization can be expressed as [76]:

$$\frac{\delta \boldsymbol{\mathcal{P}}_\alpha}{\langle \delta v_{n,\mathbf{k}} |} = -\frac{ief}{2\pi} \frac{\mathbf{a}_\alpha}{w N_{\mathbf{k}^\perp_\alpha} v} \left(\left| \tilde{v}^+_{n,\mathbf{k}} \right\rangle - \left| \tilde{v}^-_{n,\mathbf{k}} \right\rangle \right), \tag{3.50}$$

with

$$\left| \tilde{v}^\pm_{n,\mathbf{k}} \right\rangle = \sum_m (S(\mathbf{k}), \mathbf{k}^\pm_\alpha)^{-1}_{mn} \left| v^\pm_{m,\mathbf{k}_\alpha} \right\rangle, \tag{3.51}$$

where $\mathbf{k}^\pm_\alpha = \mathbf{k} \pm \Delta\mathbf{k}_\alpha$ with $\Delta\mathbf{k}_\alpha$ the distance in reciprocal space between the two points along the direction α with the reciprocal lattice vector $\mathbf{b}_\alpha$. Inserting this into the equation of motion yields:

$$i\hbar \frac{\mathrm{d}}{\mathrm{d}t} | v_{m,\mathbf{k}} \rangle = \left(H^0_{\mathbf{k}} + w_{\mathbf{k}}(\boldsymbol{\mathcal{E}}) + w^\dagger_{\mathbf{k}}(\boldsymbol{\mathcal{E}}) \right) | v_{m,\mathbf{k}} \rangle, \tag{3.52}$$

where $w_{\mathbf{k}}(\boldsymbol{\mathcal{E}})$ is the coupling operator of the external electric field $\boldsymbol{\mathcal{E}}$ to the polarization $\boldsymbol{\mathcal{P}}$ resulting from the variation of the polarization:

$$w_{\mathbf{k}}(\boldsymbol{\mathcal{E}}) = \frac{ief}{4\pi} \sum_{m\alpha} (\mathbf{a}_\alpha \cdot \boldsymbol{\mathcal{E}}) N_{\mathbf{k}_\alpha} \sum_{\sigma=\pm} \sigma \left| \tilde{v}^{\sigma}_{m,\mathbf{k}_\alpha} \right\rangle \langle v_{m,\mathbf{k}} | \, . \tag{3.53}$$

Since the coupling operator is not hermitian, $w^{\dagger}_{\mathbf{k}}(\boldsymbol{\mathcal{E}})$ is added to ensure a well-defined hermitian operator. This is possible since at any time $w^{\dagger}_{\mathbf{k}}(\boldsymbol{\mathcal{E}}) \, |v_{m,\mathbf{k}}\rangle = 0$ [76].

3.3.3 Computational scheme

To calculate the optical response of a system from the real-time propagation of the wave function, the following computational scheme, implemented in the Yambo code [47–49], is used:

1. The Kohn-Sham eigenstates $|\psi_{n,\mathbf{k}}\rangle$ and the corresponding eigenenergies $\epsilon_{n,\mathbf{k}}$ are computed. This part of the calculation is done using a plane wave based DFT code. If needed, the quasiparticle correction within the $\mathrm{G}_0 W_0$ approximation. Based on these quantities, the single-particle Hamiltonian H^0 is constructed.
2. According to the algorithm of Ref. [107], the EOM (Eq. (3.52)) is integrated for an applied external electric field $\boldsymbol{\mathcal{E}}(t)$, yielding the time-dependent periodic part of the wave function $v_{n,\mathbf{k}}(t)$. As a result, the dynamical polarization $P(t)$ is obtained from the overlap matrix $S_{mn}(\mathbf{k}, \mathbf{k}+\mathbf{q}_\alpha)$ of the Berry phase.
3. The dynamical polarization $\boldsymbol{\mathcal{P}}(t)$ is Fourier transformed to the frequency domain yielding the nonlinear response function of any order.

Unlike the sum over states approach, the real-time method is flexible with respect to the form of the external electric field. Various field profiles can be applied, such as a delta-like pulse $\boldsymbol{\mathcal{E}}(t) = \boldsymbol{\mathcal{E}}_0 \delta(t - t_0)$, a monochromatic sinusoidal field $\boldsymbol{\mathcal{E}}(t) = \boldsymbol{\mathcal{E}}_0 \sin(\omega_L t)$, or a quasi-monochromatic field $\boldsymbol{\mathcal{E}}(t) = \boldsymbol{\mathcal{E}}_0 \sin(\omega_L t) \exp(-\delta^2 (t - t_0)^2 / 2)$, where $\boldsymbol{\mathcal{E}}_0$ is the field amplitude, ω_L is the frequency, and δ characterizes the pulse width. The delta-like pulse is typically used for linear response calculations, while the monochromatic and quasi-monochromatic fields are suited for nonlinear response. The computational scheme accommodates any of these field types without modification [49].
To avoid spurious contributions from the system's eigenfrequencies which are excited by the sudden application of the electric field at t_0, a finite dephasing is introduced by adding an imaginary term to the Hamiltonian [49]:

$$\Gamma = -\frac{i}{\gamma_{\text{deph}}} \sum_{l} \left(|v_{l,\mathbf{k}}\rangle \langle v_{l,\mathbf{k}}| + \left| v^0_{l,\mathbf{k}} \right\rangle \left\langle v^0_{l,\mathbf{k}} \right| \right) , \tag{3.54}$$

where γ_{deph} is the dephasing rate and $\left| v^0_{l,\mathbf{k}} \right\rangle$ are the Bloch functions of the unperturbed Hamiltonian H^0. The dephasing rate determines the lifetime of the excited states and is chosen such that the eigenfrequency contributions to the nonlinear response are suppressed.

The dynamical polarization $\boldsymbol{\mathcal{P}}(t)$ is evaluated for a simulation time significantly exceeding the dephasing time. Beginning from an initial equilibrium state, the polarization is analyzed by expanding it in a Fourier series [49]:

$$\boldsymbol{\mathcal{P}}(t) = \sum_{n=-\infty}^{\infty} \mathbf{C}^{(n)} \exp\left[-i\omega^{(n)} t\right], \tag{3.55}$$

where $\mathrm{p}^{(n)}$ are the Fourier coefficients and $\omega^{(n)} = n\omega_L$ is the frequency of the n^{th} harmonic. The coefficients $\mathrm{p}^{(n)}$ are obtained by truncating the series at order S and sampling $2S+1$ values $\boldsymbol{\mathcal{P}}_i \equiv \boldsymbol{\mathcal{P}}(t_i)$ over one period $T_L = 2\pi/\omega_L$. For each Cartesian direction α, this yields the linear system [49]:

$$\sum_{n=-S}^{S} \mathcal{F}_i^{(n)} C_\alpha^{(n)} = \mathcal{P}_{\alpha,i}, \quad i = 1, \ldots, 2S+1, \tag{3.56}$$

where $\mathcal{F}_i^{(n)} \equiv \exp\left[-i\omega^{(n)} t_i\right]$ defines the Fourier matrix. Solving this system for $C_\alpha^{(n)}$ allows extraction of the n^{th}-order susceptibility by dividing by the n^{th} power of the α component of $\mathcal{E}_0$.

The nonlinear susceptibilities exhibit rapid convergence with S: for instance, Ref. [49] demonstrates that second-order susceptibilities converge with $S = 4$, while third-order susceptibilities converge with $S = 6$.

3.3.4 Electron correlation

Different correlation effects can be accounted for by constructing the corresponding effective Hamiltonian in Eq. (3.52). The simplest approximation for the effective Hamiltonian we consider in this work is the IPA describing the unperturbed (zero-field) Kohn-Sham system [85]:

$$h = -\frac{\hbar^2}{2m}\sum_i \nabla_i^2 + V_{\mathrm{eI}} + V_{\mathrm{H}}[\rho^0] + V_{\mathrm{xc}} = \sum_i \varepsilon_{n,\mathbf{k}} \left|u_{n,\mathbf{k}}\right\rangle \left\langle u_{n,\mathbf{k}}\right| [\rho^0], \tag{3.57}$$

where $\hat{V}_{\mathrm{eI}}$ is the electron-ion interaction, $\hat{V}_{\mathrm{H}}[\rho^0]$ and $\hat{V}_{\mathrm{xc}}[\rho^0]$ are respectively the Hartree and exchange-correlation potentials evaluated at the unperturbed ground-state electron density ρ^0, $\varepsilon_{n,\mathbf{k}}$ the Kohn-Sham energies (eigenvalues) and $|u_{n,\mathbf{k}}\rangle$ the periodic part of the Kohn-Sham wavefunctions. The Hamiltonian in Eq. (3.57) has two main shortcomings. First, the band gaps obtained from the Kohn-Sham energies are systematically underestimated—yielding to an overall underestimation of the optical gap. Second, the response of the density-functional potentials to the change in the density is missing and so are local-field effects and quasi-particle excitations. The former shortcoming is corrected by introducing a state-dependent scissor operator term,

$$\Delta\hat{H}_{\mathbf{k}} = \sum_n \Delta_{n\mathbf{k}} \left|u_{n,\mathbf{k}}\right\rangle \left\langle u_{n,\mathbf{k}}\right|, \tag{3.58}$$

where state-dependent $\Delta_{n\mathbf{k}}$ is the scissor operator. That is, considering the Kohn-Sham energies as the zero-order approximation to quasiparticle energies, the scissor operator introduces a first order correction. Such correction can be obtained from first-principles within the so-called GW approximation derived from many-body perturbation theory [108] (a simpler approach is to have a single scissor operator chosen to reproduce e.g. the experimental fundamental band gap). To address the second shortcoming, one can introduce the fluctuation of the Hartree potential (Eq. (3.57)) generated by the variation of the electron density induced by the external fields [49], and the screened-exchange self-energy term [107]. This latter term is a nonlocal operator which accounts for the screened electron-hole attraction and introduces excitonic effects. This approximation is explained in more detail presented in the next section based on Ref. [107].

3.3.5 Real-time Bethe-Salpeter equation

The time-dependent Bethe-Salpeter equation is a method to include excitonic effects in the optical response of a system which will be presented following Refs. [102, 107, 109]. The Hamiltonian of the system is given by:

$$H = h + H^{\mathrm{mb}} + H^{\boldsymbol{\mathcal{E}}}, \tag{3.59}$$

where h is the single-particle Hamiltonian given by Eq. (3.57) with density ρ, H^{mb} is the many-body Hamiltonian and $H^{\boldsymbol{\mathcal{E}}}$ is the time-dependent perturbation Hamiltonian with an external electric field $\boldsymbol{\mathcal{E}}(t)$. In the so called non-equilibrium Green's function (NEGF) formalism, Kadanoff and Baym introduced the time-dependent Green's function $G(\mathbf{r}, t; \mathbf{r}', t')$ which describes the time evolution of the system. The Green's function is defined for a fixed momentum $\mathbf{k}$ and is given by [110]:

$$G_{n_1 n_2, \mathbf{k}}(t_1, t_2) = \int \phi^*_{n_1, \mathbf{k}}(\mathbf{r}) G(\mathbf{r}, t_1; \mathbf{r}', t_2) \phi_{n_2, \mathbf{k}}(\mathbf{r}') \mathrm{d}\mathbf{r}\mathrm{d}\mathbf{r}', \tag{3.60}$$

where $\phi_{n,\mathbf{k}}(\mathbf{r})$ are the eigenstates of the single-particle Hamiltonian h and n_1 and n_2 are the band indices. In the EOMs for the Green's function in Eq. (3.60) is obtained from creation and destruction operators in the framework of the second quantization. However, the EOMs is a recursive dependence of two, three etc. particle Green's function. In order to truncate this recursive chain, a self-energy operator $\Sigma_{\mathbf{k}}(t_1, t_2)$, holding information of all higher order Green's functions is introduced. Since the two-particle Green's functions as well as the self-energy terms depent explicitly on t_1 and t_2 due to the missing time-translation invariance for non-equilibrium situations, one defines an advanced $\Sigma^{\mathrm{a}}_{\mathbf{k}}(\mathbf{G}^{\mathrm{a}}_{\mathbf{k}})$, a retarded $\Sigma^{\mathrm{r}}_{\mathbf{k}}(\mathbf{G}^{\mathrm{r}}_{\mathbf{k}})$, as well as a greater and a lesser $\Sigma^{>}_{\mathbf{k}}\Sigma^{<}_{\mathbf{k}}(\mathbf{G}^{>}_{\mathbf{k}}\mathbf{G}^{<}_{\mathbf{k}})$ self-energy operator (Green's function). This results in the following EOM [109]:

$$\begin{aligned} i\hbar \frac{\partial}{\partial t_1} G^{<}_{n_1 n_2 \mathbf{k}}(t_1, t_2) = {} & \delta(t_1 - t_2)\delta_{n_1 n_2} \\ & + h_{n_1 n_2 \mathbf{k}}(t_1) G^{<}_{n_1 n_2 \mathbf{k}}(t_1, t_2) + \sum_{n_3} U_{n_1 n_3 \mathbf{k}}(t_1) G^{<}_{n_3 n_2 \mathbf{k}}(t_1, t_2) \\ & + \sum_{n_3} \int \mathrm{d}t_3 \, [\Sigma^{\mathrm{r}}_{n_1 n_3 \mathbf{k}}(t_1, t_3) G_{n_3 n_2 \mathbf{k}}(t_3, t_2) \\ & + \Sigma^{<}_{n_1 n_3 \mathbf{k}}(t_1, t_3) G^{\mathrm{a}}_{n_3 n_2 \mathbf{k}}(t_3, t_2)]. \end{aligned} \tag{3.61}$$

Together with the adjoint equation for $\frac{\partial}{\partial t_2} G^{<}_{n_1 n_2 \mathbf{k}}(t_1, t_2)$, the equation of motion for the Green's function $G^{<}_{n_1 n_2 \mathbf{k}}(t_1, t_2)$ and analogously for $G^{>}_{n_1 n_2 \mathbf{k}}(t_1, t_2)$ can be derived. These coupled equations are called the Kadanoff-Baym equations (KBEs).

In the static limit, Eq. (3.61) can be simplified by adopting a static retarded approximation for the self-energy operator:

$$\Sigma^{\mathrm{r}}(t_1,t_2) = \left[\Sigma^{\mathrm{COHSEX}}(t_1) - V_{\mathrm{xc}}\right]\delta(t_1-t_2), \tag{3.62}$$

$$\Sigma^{<}(t_1,t_2) = 0, \tag{3.63}$$

where $\Sigma^{\mathrm{COHSEX}}(t_1)$ is the Coulomb-hole plus screened-exchange (COHSEX) self-energy operator [111]. Correlation effects already present in the single-particle Hamiltonian h are subtracted from the COHSEX self-energy. The COHSEX self-energy is composed as $\Sigma^{\mathrm{COHSEX}}(t_1) = \Sigma^{\mathrm{SEX}}(t_1) + \Sigma^{\mathrm{COH}}(t_1)$, with

$$\Sigma^{\mathrm{SEX}}(\mathbf{r},\mathbf{r}',t) = iW(\mathbf{r},\mathbf{r}',G^{<})G^{<}(\mathbf{r}',\mathbf{r},t), \tag{3.64}$$

$$\Sigma^{\mathrm{COH}}(\mathbf{r},\mathbf{r}',t) = -W(\mathbf{r},\mathbf{r}',G^{<})\frac{1}{2}\delta(\mathbf{r}-\mathbf{r}'), \tag{3.65}$$

where $W(\mathbf{r},\mathbf{r}',G^{<})$ is the dynamically screened Coulomb interaction in the RPA. The first term represents the screened-exchange interaction, while the second term accounts for the Coulomb-hole contribution. Both are obtained from the static limit of the GW self-energy [109, 111]. With this approximation, Eq. (3.61) decouples from $\Sigma^{>}$ and becomes diagonal in time:

$$\begin{aligned} i\hbar\frac{\partial}{\partial t_1}G^{<}_{n_1n_2\mathbf{k}}(t) = \big[&h_{\mathbf{k}} + H^{\boldsymbol{\mathcal{E}}}(t) + V^{\mathrm{H}}[\rho] - V^{\mathrm{H}}[\tilde{\rho}] \\ &+ (\Sigma^{\mathrm{COHSEX}}(t) - V_{\mathrm{xc}}[\tilde{\rho}]), G^{<}_{\mathbf{k}}(t)\big]_{n_1n_2}, \end{aligned} \tag{3.66}$$

where $\tilde{\rho}$ is the ground-state density of the fully interacting system, given by:

$$\tilde{\rho}(\mathbf{r}) = \sum_{n\mathbf{k}} f_{n\mathbf{k}}\left|\phi_{n\mathbf{k}}(\mathbf{r})\right|^2, \tag{3.67}$$

with $f_{n\mathbf{k}}$ the Fermi-Dirac occupation number. The time-dependent electron density $\rho(\mathbf{r},t)$ reads:

$$\rho(\mathbf{r},t) = \frac{i}{\hbar}\sum_{n_1n_2\mathbf{k}}\phi_{n_1\mathbf{k}}(\mathbf{r})\phi^{*}_{n_2\mathbf{k}}(\mathbf{r})G^{<}_{n_2n_1\mathbf{k}}(t). \tag{3.68}$$

In order to apply the G_0W_0+BSE approach, Eq. (3.66) is rewritten as:

$$\begin{aligned} i\hbar\frac{\partial}{\partial t_1}G^{<}_{n_1n_2\mathbf{k}}(t) = \big[&h_{\mathbf{k}} + \Delta h_{\mathbf{k}} + H^{\boldsymbol{\mathcal{E}}}(t) + V^{\mathrm{H}}[\rho] - V^{\mathrm{H}}[\tilde{\rho}] \\ &+ (\Sigma^{\mathrm{COHSEX}}[G^{<}] - \Sigma^{\mathrm{COHSEX}}[\tilde{G}^{<}]), G^{<}_{\mathbf{k}}(t)\big]_{n_1n_2}, \end{aligned} \tag{3.69}$$

where $\Delta h_{\mathbf{k}}$ is the scissor operator which is added to the single-particle Hamiltonian $h_{\mathbf{k}}$ in order to correct for the underestimation of the optical band gap [112]. The Kohn-Sham exchange-correlation potential $V_{\mathrm{xc}}[\tilde{\rho}]$ disappears as it is independent of $G^{<}(t)$. The solution for the unperturbed Hamiltonian $h_{\mathbf{k}}$ is given by:

$$\tilde{G}^{<}_{n_1n_2\mathbf{k}} = i\hbar f_{n_1\mathbf{k}}\delta_{n_1n_2}, \tag{3.70}$$

under the assumption that the Fermi-Dirac distribution function of the independent particle system is not affected by the introduction of the G_0W_0 correction.

When switching on an external electric field, a variation in the Green's function $G^{<}(t)$ is expected and, in turn, also a variation in the self-energy as well as Hartree potential. For a strong external electric field, the change of these quantities depends on all orders of the electric filed. However, assuming a weak external electric field, the linear term in the electric field is sufficient to describe the change of the Green's function. In this linear response limit, Eq. (3.69) reduces to the G_0W_0+BSE approach as will be shown in the following [113]. The linear response is expressed in the retarded correlation function $\chi^{\mathrm{r}}(\mathbf{r},t;\mathbf{r}',t')$ which is defined as [114]:

$$\chi^{\mathrm{r}}(\mathbf{r},t;\mathbf{r}',t') = \left.\frac{\delta\langle\rho(\mathbf{r},t)\rangle}{\delta H^{\boldsymbol{\mathcal{E}}}(\mathbf{r}',t')}\right|_{\boldsymbol{\mathcal{E}}=0}, \tag{3.71}$$

which can be expressed as an expansion in terms of independent particle wave functions $\phi_{i\mathbf{k}}(\mathbf{r})$:

$$\chi^{\mathrm{r}}(\mathbf{r},t;\mathbf{r}',t';\mathbf{q}) = \sum_{ij,\mathbf{k}}\sum_{lm,\mathbf{k}'}\chi^{\mathrm{r}}_{ij,\mathbf{k};lm,\mathbf{k}'}(t,t';\mathbf{q})\phi_{i,\mathbf{k}}(\mathbf{r})\phi'_{j,\mathbf{k}+\mathbf{q}}(\mathbf{r})\phi^{*}_{l,\mathbf{k}'}(\mathbf{r}')\phi^{*}_{m,\mathbf{k}'+\mathbf{q}}(\mathbf{r}'), \tag{3.72}$$

where $\mathbf{q}$ is the momentum of the incoming photon. The matrix elements of the retarded correlation function $\chi^{\mathrm{r}}_{ij,\mathbf{k};lm,\mathbf{k}'}(t,t';\mathbf{q})$ are given by:

$$\chi^{\mathrm{r}}_{ij,\mathbf{k};lm,\mathbf{k}'}(t,t';\mathbf{q}) = \iint d\mathbf{r}d\mathbf{r}'\phi^{*}_{i,\mathbf{k}}(\mathbf{r})\phi^{*}_{m,\mathbf{k}'+\mathbf{q}}(\mathbf{r}')\phi_{j,\mathbf{k}+\mathbf{q}}(\mathbf{r})\phi_{l,\mathbf{k}'}(\mathbf{r}'). \tag{3.73}$$

The caluclation of momentum transfer $\mathbf{q}$ is in principle possible, but here the focus is on the pure optical response. Hence, the momentum is set to zero, i.e. $\mathbf{q}=0$ [115].
In combination with Eq. (3.68) and (3.72), Eq. (3.71) can be rewritten in terms of the matrix elements of the retarded correlation function $\chi^{\mathrm{r}}_{ij,\mathbf{k};lm,\mathbf{k}'}(t,t')$:

$$\chi^{\mathrm{r}}_{ij,\mathbf{k};lm,\mathbf{k}'}(t,t') = \left.\frac{\delta\left\langle iG^{<}_{ij,\mathbf{k}}(t)\right\rangle}{\delta H^{\boldsymbol{\mathcal{E}}}_{lm,\mathbf{p}}(t')}\right|_{\boldsymbol{\mathcal{E}}=0}. \tag{3.74}$$

Inserting this into Eq. (3.69) yields a new equation of motion for the retarded correlation function $\chi^{\mathrm{r}}_{ij,\mathbf{k};lm,\mathbf{p}}(t,t')$:

$$\begin{aligned} i\hbar\frac{\partial}{\partial t}\chi^{\mathrm{r}}_{ij,\mathbf{k};lm,\mathbf{p}}(t,t') = \frac{\delta}{\delta H^{\boldsymbol{\mathcal{E}}}_{lm,\mathbf{p}}(t')}\big[&h_{\mathbf{k}} + \Delta h_{\mathbf{k}} + H^{\boldsymbol{\mathcal{E}}}(t) + V^{\mathrm{H}}[\rho(t)] - V^{\mathrm{H}}[\tilde{\rho}] \\ &+ \Sigma_{\mathbf{k}}[G^{<}(t)] - \Sigma_{\mathbf{k}}[\tilde{G}^{<}], G^{<}_{\mathbf{k}}(t)\big]_{ji}. \end{aligned} \tag{3.75}$$

Now let's derive the variation for the scissor operator, Hartree potential and the self-energy operator with respect to pertubation $H^{\boldsymbol{\mathcal{E}}}(t)$. From Eq. (3.75) in combination with Eq. (3.74) and the scissor operator $\Delta h_{\mathbf{k}} = (\epsilon^{G_0W_0}_{n_1\mathbf{k}} - \epsilon^{KS}_{n_2\mathbf{k}})\delta_{n_1n_2}$ the variation of the single-particle Hamiltonian, scissor operator and pertubation Hamiltonian with respect to the perturbation $H^{\boldsymbol{\mathcal{E}}}(t)$ is given by:

$$\begin{aligned} \frac{\delta}{\delta H^{\boldsymbol{\mathcal{E}}}_{lm,\mathbf{p}}(t')}\big[h_{\mathbf{k}} + \Delta h_{\mathbf{k}} + H^{\boldsymbol{\mathcal{E}}}(t), G^{<}_{\mathbf{k}}(t)\big]_{ji} = (\epsilon^{G_0W_0}_{j\mathbf{k}} - \epsilon^{G_0W_0}_{i\mathbf{k}})\chi^{\mathrm{r}}_{ji,\mathbf{k};lm,\mathbf{p}}(t-t') \\ + i(f_{i\mathbf{k}} - f_{j\mathbf{k}})\delta_{jl}\delta_{im}\delta_{\mathbf{k},\mathbf{p}}, \end{aligned} \tag{3.76}$$

where $\epsilon_{i\mathbf{k}}^{G_0W_0}$ is the G_0W_0 correction to the Kohn-Sham eigenvalue $\epsilon_{i\mathbf{k}}^{KS}$. Since the system is invariant under time translation for weak external electric fields, the retarded correlation function depends only on the time difference $t - t'$.

The variation of the Hartree potential is obtained from Eq. (3.74) and the derivative chain rule:

$$\delta V^{\mathrm{H}}[\rho(t)] = \sum_{nn',\mathbf{p}} \sum_{lm,\mathbf{k}'} \iint \mathrm{d}t'\mathrm{d}t'' \frac{\delta V^{\mathrm{H}}_{ij,\mathbf{k}}[\rho(t)]}{\delta G^{<}_{nn',\mathbf{p}}(t')} \chi^{\mathrm{r}}_{nn',\mathbf{p};lm,\mathbf{k}'}(t', t'') \delta H^{\boldsymbol{\mathcal{E}}}_{lm,\mathbf{k}'}(t''). \tag{3.77}$$

Similarly the variation of the self-energy operator can be derived. The Hartree potential and the self-energy operator can be expressed in terms of the screened interaction W and the long range part of the Coulomb potential $v^{\mathbf{q}=0}$ responsible for local field effects:

$$V^{\mathrm{H}}_{mn,\mathbf{k}}(t) = -2i \sum_{ij} G^{<}_{ij,\mathbf{k}}(t) v^{\mathbf{q}=0}_{mn,\mathbf{k};ij,\mathbf{k}}, \tag{3.78}$$

$$\Sigma^{\mathrm{COHSEX}}_{mn,\mathbf{k}}(t) = i \sum_{ij,\mathbf{q}} G^{<}_{ji,(\mathbf{k}-\mathbf{q})}(t) W_{m\mathbf{k},i(\mathbf{k}-\mathbf{q});n\mathbf{k},j(\mathbf{k}-\mathbf{q})}(t), \tag{3.79}$$

Inserting Eq. (3.78) into Eq. (3.77) yields the variation of the Hartree potential with respect to the perturbation $H^{\boldsymbol{\mathcal{E}}}(t)$:

$$\begin{aligned} &\frac{\delta}{\delta H^{\boldsymbol{\mathcal{E}}}_{lm,\mathbf{p}}(t')} \left[V^{\mathrm{H}}_{\mathbf{k}}[\rho(t)] - V^{\mathrm{H}}_{\mathbf{k}}[\tilde{\rho}], G^{<}_{\mathbf{k}(t)} \right]_{ji} \Bigg|_{\boldsymbol{\mathcal{E}}=0} \\ &= -2(f_{i\mathbf{k}} - f_{j\mathbf{k}}) \sum_{st} v^{\mathbf{q}=0}_{ji,\mathbf{k};st,\mathbf{k}} \chi^{\mathrm{r}}_{st,\mathbf{k};lm,\mathbf{p}}(t - t'). \end{aligned} \tag{3.80}$$

Analogously, the variation of the self-energy operator with respect to the perturbation $H^{\boldsymbol{\mathcal{E}}}(t)$ is given by:

$$\begin{aligned} &\frac{\delta}{\delta H^{\boldsymbol{\mathcal{E}}}_{lm,\mathbf{p}}(t')} \left[\Sigma_{\mathbf{k}}[G^{<}(t)] - \Sigma_{\mathbf{k}}[\tilde{G}^{<}], G^{<}_{\mathbf{k}(t)} \right]_{ji} \Bigg|_{\boldsymbol{\mathcal{E}}=0} \\ &= (f_{i\mathbf{k}} - f_{j\mathbf{k}}) \sum_{st,\mathbf{q}} W_{j\mathbf{k},s(\mathbf{k}-\mathbf{q});i\mathbf{k},t(\mathbf{k}-\mathbf{q})} \chi^{\mathrm{r}}_{st,(\mathbf{k}-\mathbf{q});lm,\mathbf{p}}(t - t'), \end{aligned} \tag{3.81}$$

where the variation of the screened interaction with respect to the perturbation is neglected. As a result, the variations of scissor operator, Hartree potential and self-energy operator with respect to the perturbation $H^{\boldsymbol{\mathcal{E}}}(t)$ can be inserted into the equation of motion for the retarded correlation function:

$$\begin{aligned} &\left[\hbar\omega - \left(\epsilon^{G_0W_0}_{j\mathbf{k}} - \epsilon^{G_0W_0}_{i\mathbf{k}} \right) \right] \chi^{\mathrm{r}}_{ij,\mathbf{k};lm,\mathbf{p}}(\omega) = i(f_{i\mathbf{k}} - f_{j\mathbf{k}}) \delta_{jl} \\ &\cdot \left[\delta_{jl}\delta_{im}\delta_{\mathbf{k},\mathbf{p}} + i \sum_{st,\mathbf{q}} \left(W_{j\mathbf{k},s(\mathbf{k}-\mathbf{q});i\mathbf{k},t(\mathbf{k}-\mathbf{q})} - 2v^{\mathbf{q}=0}_{ji,\mathbf{k};st,\mathbf{k}} \right) \chi^{\mathrm{r}}_{st,(\mathbf{k}-\mathbf{q});lm,\mathbf{p}}(\omega) \right], \end{aligned} \tag{3.82}$$

whereby also a Fourier tranformation with respect to the time difference $t - t'$ is performed. This equation has finally the form of the BSE.

Starting from a single-particle Hamiltonian h with its eigenstates and eigenvalues and the scissor correction Δh, obtained from previous DFT and G_0W_0 calculations, respectively, a time-dependent pertubation in form of an external electric field in a shape like in Sec. 3.3.3 is switched on. This yields the equation of motion as expressed in Eq. (3.69) which can be integrated in the scheme of second-order Runge-Kutta for the diagonal part of $G^<$ [116, 117]. Similarly, to the the TDDFT approach from Sec. 3.3.3, the optical response of the system is obtained from the time-dependent polarization by Fourier transformation. In terms of non-equilibrium Green's functions, the polarization is given by:

$$\boldsymbol{\mathcal{P}}(t) = -\frac{1}{V} \sum_{n,m,\mathbf{k}} r_{nm,\mathbf{k}} G^<_{nm,\mathbf{k}}(t), \tag{3.83}$$

where V is the volume of the unit cell and $r_{nm,\mathbf{k}}$ is the dipole matrix element between the two states n and m with momentum $\mathbf{k}$. The computational scheme is implemented in the Yambo code [47, 48, 107].

4 Frequency-mixing spectroscopy in two-dimensional crystals

4.1 Two-dimensional materials: *h*-BN & MoS$_2$

Two-dimensional materials have attracted significant attention over the past decade due to their exceptional electronic and optical properties, arising from reduced dimensionality and quantum confinement [118, 119]. Among them, h-BN and MoS$_2$ represent two paradigmatic cases. Although both share a layered hexagonal lattice structure, they differ fundamentally in their electronic nature. While h-BN is a wide band gap insulator (about 6 eV) [120], MoS$_2$ is a transition-metal dichalcogenide (TMD) [121, 122]. Their contrasting band structures and dielectric screening make them ideal prototypes for exploring excitonic effects and nonlinear optical phenomena in 2D systems.

Hexagonal boron nitride crystallizes in a honeycomb lattice with alternating boron and nitrogen atoms, which break inversion symmetry (see Fig. 4.1(a)). The combination of strong in-plane covalent bonding and weak van der Waals interlayer coupling leads to flat monolayers [123]. Despite its large gap, h-BN monolayer exhibits pronounced excitonic effects. The reduced dielectric screening in two dimensions enhances the Coulomb interaction between electrons and holes [124]. These excitons dominate the optical absorption and give rise to distinct peaks in the linear and nonlinear spectra [77, 125], providing a proper test case of many-body interactions in this otherwise wide gap material.

The bilayer h-BN symmetry depends on stacking. In the usual AA' antiparallel stacking (see Fig. 4.1(b)), the two sheets are related by inversion, so their second-order polarizations (all even-order as well) cancel and SHG vanishes [126, 127]. If the bilayer is perturbed, e.g., by a small twist, lateral shift, strain, the inversion symmetry is lifted and second-order polarization reappears [126, 128]. The mentioned ways of breaking symmetry are computationally demanding as they require large supercells. However, the application of an out-of-plane electric field in form of FI-SHG is an efficient way to break inversion symmetry in bilayer h-BN and induce a second-order response. In contrast to monolayer h-BN, an interlayer hybridization between the bands of the two layers, crossing at the K point, occurs in bilayer h-BN. This leads to a dark exciton below the bright exciton, which is absent in the monolayer case [129].

Monolayer MoS$_2$ (see Fig. 4.1(c)) belongs to the family of TMDs characterized by direct band gaps in the visible range and strong spin-orbit coupling [121, 130]. The absence of inversion symmetry and the presence of inequivalent K and K' valleys in the Brillouin zone cause spin-valley locking [131], enabling valley-selective optical excitation with

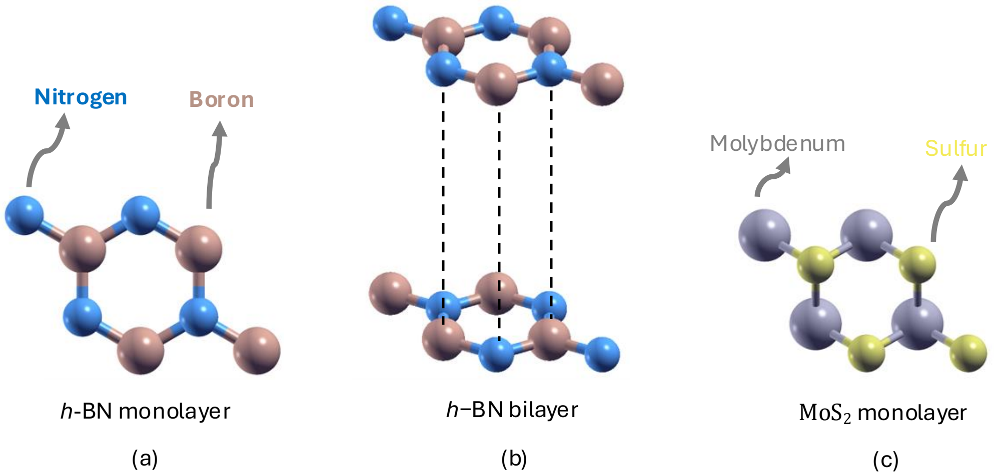

Figure 4.1: The strucuture of (a) *h*-BN monolayer (in-plane), (b) *h*-BN bilayer (out-of-plane), and (c) MoS$_2$ monolayer (in-plane)

circularly polarized light [132–136]. The lowest-energy excitonic transitions, labeled A and B, originate from spin-split valence bands at the K point [137–143]. A more dominating excitonic transition along the $K-\Gamma$ high-symmetry axis is labeled as C exciton [77, 144]. These excitons are responsible for the strong photoluminescence of monolayer MoS$_2$ and contribute substantially to its nonlinear optical response [70, 77, 145].

Both, *h*-BN and MoS$_2$ serve as model systems to study excitonic phenomena in 2D materials. Their contrasting electronic structures enable to understand the influence of dimensionality, screening, and spin-orbit coupling on the linear and nonlinear optical response. The following approach and the corresponding results are based on Ref. [P5].

4.2 Theoretical background

4.2.1 Nonlinear response from real-time simulations

The nonlinear optical susceptibilities are obtained from the time evolution of Bloch electrons in a uniform time-dependent electric field (see the corresponding workflow in Fig. 4.2) [49]. The approach developed in Ref. [49], limited to a single monochromatic field as presented in Sec. 3.3, is extended. This extension enables access to a wide range of nonlinear phenomena. In this chapter, attention is given to SFG and DFG (Sec. 4.2.2) as well as FI-SHG (Sec. 4.2.3)[1].

As outlined in Sec. 3.3, the time evolution of the electronic system under the influence of two monochromatic homogeneous fields $\boldsymbol{\mathcal{E}}_1(t)$ and $\boldsymbol{\mathcal{E}}_2(t)$ is governed by the following EOMs for the valence Bloch states (see Fig. 4.2):

$$i\hbar\frac{\mathrm{d}}{\mathrm{d}t}|v_{m\mathbf{k}}\rangle = \left\{H_{\mathbf{k}}^{\mathrm{MB}} + ie\left[\boldsymbol{\mathcal{E}}_1(t) + \boldsymbol{\mathcal{E}}_2(t)\right]\cdot\tilde{\partial}_{\mathbf{k}}\right\}|v_{m\mathbf{k}}\rangle\,, \tag{4.1}$$

where $|v_{m\mathbf{k}}\rangle = |v_{m\mathbf{k}}(t)\rangle$ denotes the periodic part of the time-dependent Bloch states.

---

[1] During the finalization of this work, a new study has been published proposing an alternative approach by Ono [146] to the one developed in Ref. [P5].

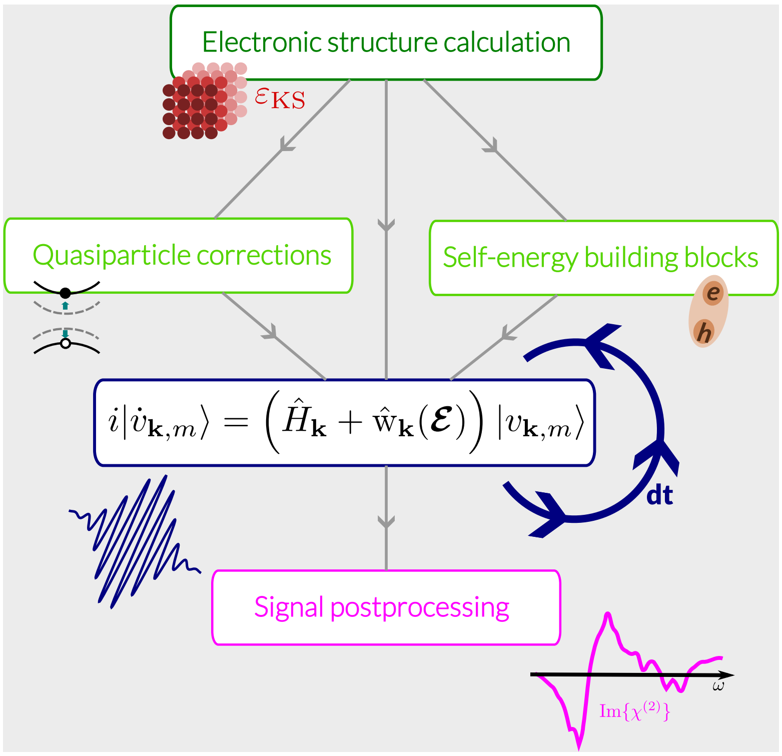

Figure 4.2: In this workflow each box represents a separate run, executed by different codes/code run-levels. In the first step, the electronic structure is calculated. This is the input for the real-time simulation (blue box) and—in case of calculations beyond the independent particles—for the calculation of quasiparticle correction and the building-blocks for the self-energy operator, that are also input of the real-time simulation. The output from the real-time simulation is postprocessed to obtain, e.g. nonlinear spectral properties (with kind permission from M. Grüning).

On the right-hand side of Eq. (4.1), the second term represents the coupling with the external field in the dipole approximation. This coupling is expressed as a **k**-derivative operator. The tilde indicates that the operator is gauge covariant, meaning the solutions of Eq. (4.1) remain unchanged under unitary rotations at **k** (see Ref. [76] for further details). $H^{\mathrm{MB}}_{\mathbf{k}}$ denotes the effective many-body Hamiltonian. Various correlation effects can be included by constructing the corresponding effective Hamiltonian (see Fig. 4.2). The most sophisticated effective Hamiltonian considered in this work is the TD-aGW[2] approximation [107] (see Sec. 3.3.5), which incorporates electron-hole interaction and local field effects:

$$H^{\mathrm{MB}}_{\mathbf{k}} \equiv H^{\mathrm{KS}}_{\mathbf{k}} + \Delta H_{\mathbf{k}} + V_{\mathrm{h}}(\mathbf{r})[\Delta\rho] + \Sigma_{\mathrm{SEX}}[\Delta\gamma]\ , \tag{4.2}$$

where $H^{\mathrm{KS}}_{\mathbf{k}}$ is the Hamiltonian of the unperturbed Kohn-Sham system [85], $\Delta H_{\mathbf{k}}$ is the scissors operator applied to the Kohn-Sham eigenvalues, and $V_{\mathrm{h}}(\mathbf{r})[\Delta\rho]$ is the real-time Hartree potential [49], which accounts for local field effects [113] arising from system inhomogeneities. The term Σ_{SEX} is the screened-exchange self-energy that describes the electron-hole interaction [107]. $\Delta\rho$ and $\Delta\gamma$ are, respectively, the variations of the density

---

[2] Notice that the TD-aGW approximation was called TD-BSE, TD-SEX or TD-HSEX in previous publications [47, 74, 107].

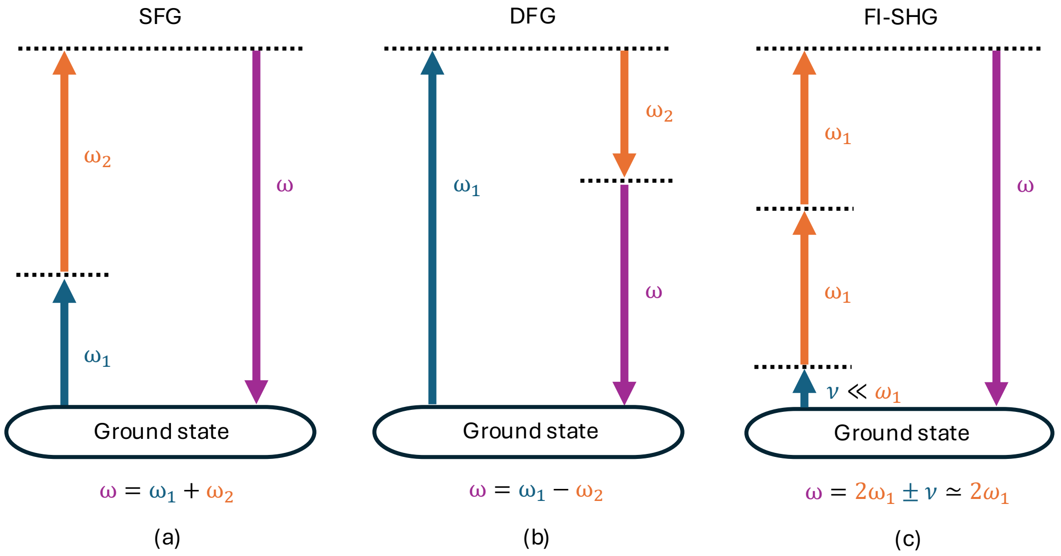

Figure 4.3: A schematic representation of the nonlinear processes studied in this work: (a) sum frequency generation (SFG), (b) difference frequency generation (DFG) and (c) field-induced second-harmonic generation (FI-SHG).

and the density matrix induced by the external fields. In the limit of small perturbations, Eqs. (4.1) and Eq. (4.2) reproduce the optical absorption calculated with the GW+BSE approach [113] as demonstrated both analytically and numerically in Ref. [107]. The other approximation considered is the IPA, which corresponds to $H^{\mathrm{MB}} \equiv H^{\mathrm{KS}}$.
The real-time polarization along the lattice vector $\mathbf{a}$ is obtained from the solutions $|v_{m\mathbf{k}}\rangle$ of Eq. (4.1) as [76]:

$$\mathcal{P}_{\parallel}(t) = -\frac{ef|\mathbf{a}|}{2\pi V}\mathrm{Im}\,\log\prod_{\mathbf{k}}^{N_{\mathbf{k}}-1}\det S\left(\mathbf{k},\mathbf{k}+\mathbf{q};t\right), \tag{4.3}$$

where $S(\mathbf{k},\mathbf{k}+\mathbf{q};t)$ denotes the overlap matrix between the time-dependent valence states $|v_{n\mathbf{k}}\rangle$ and $|v_{m\mathbf{k}+\mathbf{q}}\rangle$, V is the unit cell volume, f is the spin degeneracy, $N_{\mathbf{k}}$ is the number of $\mathbf{k}$-points along the polarization direction, and $\mathbf{q} = 2\pi/(N_{\mathbf{k}}\mathbf{a})$. The n-order susceptibilities $\chi^{(n)}$ are then extracted from the frequency-dependent polarization, which is expanded in a power series of the two incident fields as:

$$\begin{aligned}\mathcal{P}_\alpha(\omega) = &\sum_{\beta=1}^{3}\sum_{i=1}^{2}\chi^{(1)}_{\alpha\beta}(\omega;\omega_i)\mathcal{E}_\beta(\omega_i) + \sum_{\beta,\gamma=1}^{3}\sum_{i,j=1}^{2}\chi^{(2)}_{\alpha\beta\gamma}(\omega;\omega_i,\omega_j)\mathcal{E}_\beta(\omega_i)\mathcal{E}_\gamma(\omega_j)\\ &+\sum_{\beta,\gamma,\delta=1}^{3}\sum_{i,j,k=1}^{2}\chi^{(3)}_{\alpha\beta\gamma\delta}(\omega;\omega_i,\omega_j,\omega_j)\mathcal{E}_\beta(\omega_i)\mathcal{E}_\gamma(\omega_j)\mathcal{E}_\delta(\omega_k) + O(\mathcal{E}^4)\,,\end{aligned} \tag{4.4}$$

where ω_i, ω_j are the frequencies of the perturbing fields $\mathcal{E}_\beta$ and $\mathcal{E}_\gamma$, and ω is the frequency of the outgoing polarization, with α, β, γ denoting the Cartesian directions.

4.2.2 Sum frequency generation

A schematic representation of the SFG and DFG response functions considered in this work is shown in Fig. 4.3(a),(b). These correspond to $\chi^{(2)}(\omega,\omega_i,\omega_j)$ in Eq. (4.4), where

$\omega = \omega_i \pm \omega_j$. The procedure for deriving SFG and DFG from the time-dependent polarization is described in Sec. 4.3. Here, their Lehmann representation is discussed, as it is useful for interpreting the results.

The general form of the second-order susceptibility, $\chi^{(2)}_{\alpha\beta\gamma}(\omega_3;\omega_1,\omega_2)$ in the Lehmann representation, obtained through second-order perturbation theory [24], reads:

$$\begin{aligned}\chi^{(2)}_{\alpha\beta\gamma}(\omega_3;\omega_1,\omega_2) = \frac{-ie^3}{m^3\tilde{\omega}_3\tilde{\omega}_1\tilde{\omega}_2}\sum_{\lambda\lambda'}\Bigg[&\frac{\alpha_{0\lambda}\beta_{\lambda\lambda'}\gamma_{\lambda'0}}{(\tilde{\omega}_2-\Omega_{\lambda'})(\tilde{\omega}_3-\Omega_\lambda)} + \frac{\beta_{0\lambda}\gamma_{\lambda\lambda'}\alpha_{\lambda'0}}{(\tilde{\omega}_1+\Omega_\lambda)(\tilde{\omega}_3+\Omega_{\lambda'})} \\ &- \frac{\gamma_{0\lambda}\alpha_{\lambda\lambda'}\beta_{\lambda'0}}{(\tilde{\omega}_1-\Omega_{\lambda'})(\tilde{\omega}_2+\Omega_\lambda)} + \frac{\alpha_{0\lambda}\gamma_{\lambda\lambda'}\beta_{\lambda'0}}{(\tilde{\omega}_1-\Omega_{\lambda'})(\tilde{\omega}_3-\Omega_\lambda)} \\ &+ \frac{\gamma_{0\lambda}\beta_{\lambda\lambda'}\alpha_{\lambda'0}}{(\tilde{\omega}_2+\Omega_\lambda)(\tilde{\omega}_3+\Omega_{\lambda'})} - \frac{\beta_{0\lambda}\alpha_{\lambda\lambda'}\gamma_{\lambda'0}}{(\tilde{\omega}_2-\Omega_{\lambda'})(\tilde{\omega}_1+\Omega_\lambda)}\Bigg],\end{aligned} \tag{4.5}$$

where Ω_λ denote the excitation energies of the system, and $\alpha_{\lambda\lambda'}$ represents the momentum matrix elements $\langle\lambda|P_\alpha|\lambda'\rangle$ between excited states, with analogous definitions for $\beta_{\lambda\lambda'}$ and $\gamma_{\lambda\lambda'}$. The quantities $\tilde{\omega}_1 = \omega_1 + i\eta$, $\tilde{\omega}_2 = \omega_2 + i\eta$, and $\tilde{\omega}_3 = \tilde{\omega_1} + \tilde{\omega}_2$ are used, where η is a small positive parameter introducing dephasing. The many-body momentum operator is given by $\mathbf{P} = \sum_i \mathbf{p}_i$, with $\mathbf{p}_i$ acting on particle i.

An approximation to Eq. (4.5) can be obtained by substituting many-body states and energies with excitonic ones [113]: $|\lambda\rangle \simeq |\Psi^{\rm exc}_\lambda\rangle$ and $\Omega_\lambda \simeq E_\lambda$. For the SFG case, where $\omega_3 = \omega_1 + \omega_2$, only positive contributions to $\chi^{(2)}$ are retained, yielding:

$$\begin{aligned}\chi^{(2)}_{\alpha\beta\gamma}(\omega_1+\omega_2;\omega_1,\omega_2) \approx \sum_{\lambda\lambda'}\Bigg[&\frac{P_{\alpha,0\lambda}P_{\beta,\lambda\lambda'}P_{\gamma,\lambda'0}}{(\tilde{\omega}_2-E_{\lambda'})(\tilde{\omega}_1+\tilde{\omega}_2-E_\lambda)} - \frac{P_{\gamma,0\lambda}P_{\alpha,\lambda\lambda'}P_{\beta,\lambda'0}}{(\tilde{\omega}_1-E_{\lambda'})(\tilde{\omega}_2+E_\lambda)} \\ &+ \frac{P_{\alpha,0\lambda}P_{\gamma,\lambda\lambda'}P_{\beta,\lambda'0}}{(\tilde{\omega}_1-E_{\lambda'})(\tilde{\omega}_1+\tilde{\omega}_2-E_\lambda)} - \frac{P_{\beta,0\lambda}P_{\alpha,\lambda\lambda'}P_{\gamma,\lambda'0}}{(\tilde{\omega}_2-E_{\lambda'})(\tilde{\omega}_1+E_\lambda)}\Bigg],\end{aligned} \tag{4.6}$$

where $P_{\alpha,\lambda\lambda'} = \langle\Psi^{\rm exc}_\lambda|p_\alpha|\Psi^{\rm exc}_{\lambda'}\rangle$ as defined in Ref. [74]. A similar approach has been adopted in the literature for the SHG case [98, 147]. According to this expression, strong peaks are expected when $\omega_1 + \omega_2$ is resonant with an excitonic energy or when the individual laser frequencies ω_1, ω_2 are resonant with an exciton. It should be noted that the first and third terms exhibit poles at both one-photon (i.e., ω_1, ω_2) and two-photon ($\omega_1 + \omega_2$) resonances. Furthermore, if $P_{\alpha,\lambda\lambda'}$ is nonzero for $\lambda \neq \lambda'$, resonances involving two distinct excitonic energies may also occur.

4.2.3 Field-induced second-harmonic generation

Among the higher-order responses that can be extracted from Eq. (4.4), the FI-SHG is considered (see Fig. 4.3(c)). In a system with inversion symmetry all even-order susceptibilities vanish. For instance, the second-order polarization:

$$\mathcal{P}^{(2)}_i = \sum_{jk}\chi^{(2)}_{ijk}(-2\omega;\omega,\omega)\mathcal{E}_j(\omega)\mathcal{E}_k(\omega), \tag{4.7}$$

is zero if the system is centrosymmetric, as is the case for h-BN bilayer shown in Fig. 4.1(b). However, when an external field $\mathcal{E}_l$ is applied, an additional contribution to the second-order polarization:

$$\mathcal{P}_i^{(2)} = \sum_{jk} \left[\chi_{ijk}^{(2)}(-2\omega;\omega,\omega) + \frac{\mathrm{d}\chi_{ijk}^{(2)}(\mathbf{R}(\boldsymbol{\mathcal{E}}),\boldsymbol{\mathcal{E}})}{\mathrm{d}\mathcal{E}_l}\mathcal{E}_l(\nu) \right] \mathcal{E}_j(\omega)\mathcal{E}_k(\omega), \tag{4.8}$$

arises, where $\mathbf{R}(\boldsymbol{\mathcal{E}})$ indicates the dependence of the crystal structure on the applied field. The term $\mathrm{d}\chi_{ijk}^{(2)}(\mathbf{R}(\boldsymbol{\mathcal{E}}),\boldsymbol{\mathcal{E}})/\mathrm{d}\mathcal{E}_l$ is nonzero in centrosymmetric systems, leading to a finite second-order polarization. This effect is known as FI-SHG. The derivative of the second-order susceptibility with respect to the external field can be split into two contributions:

$$\frac{\mathrm{d}\chi_{ijk}^{(2)}(\mathbf{R}(\boldsymbol{\mathcal{E}}),\boldsymbol{\mathcal{E}})}{\mathrm{d}\mathcal{E}_l} = \left.\frac{\partial\chi_{ijk}^{(2)}(\mathbf{R}_0,\boldsymbol{\mathcal{E}})}{\partial\boldsymbol{\mathcal{E}}}\right|_{\mathcal{E}_l=0} + \sum_{n\alpha} \left.\frac{\partial\chi_{ijk}^{(2)}(\mathbf{R},\boldsymbol{\mathcal{E}}=0)}{\partial\tau_{n\alpha}}\right|_{\mathbf{R}=\mathbf{R}_0} \frac{\partial\tau_{n\alpha}}{\partial\mathcal{E}_l}, \tag{4.9}$$

where $\tau_{n\alpha}$ are the atomic displacements induced by the external field and $\mathbf{R}_0$ is the equilibrium crystal structure. The first term represents the electronic contribution, while the second term accounts for the ionic contribution to the FI-SHG. According to Grillo *et al.* [80] the ionic contribution is neglectable. If $\mathcal{E}_l$ is static, i.e. $\nu = 0$, the electronic contribution to the FI-SHG can be expressed as:

$$\left.\frac{\partial\chi_{ijk}^{(2)}(\mathbf{R}_0,\mathcal{E})}{\partial\mathcal{E}}\right|_{\mathcal{E}_l=0} = \chi_{ijkl}^{(3)}(-2\omega;\omega,\omega,0), \tag{4.10}$$

Similarly, if $\nu \ll \omega$, i.e., $\mathcal{E}_l$ is in the THz range (see Fig. 4.3(c)), it follows that $2\omega\pm\nu \approx 2\omega$ and Eq. (4.8) can be rewritten as

$$\mathcal{P}_i^{(2)}(2\omega^{\pm}) \approx \sum_{jk} \chi_{ijkl}^{(3)}(2\omega;\omega,\omega,\nu)\mathcal{E}_j(\omega)\mathcal{E}_k(\omega)\mathcal{E}_l(\nu). \tag{4.11}$$

In this context, the additional electric field in the THz range can be considered as small perturbation that breaks the symmetry. Extracting the $\chi^{(3)}$ values from $\mathcal{P}_i^{(2)}(2\omega^+)$ and $\mathcal{P}_i^{(2)}(2\omega^-)$, the corresponding FI-SHG for low-frequency time-dependent pump fields is obtained.

4.3 Signal processing: two external monochromatic fields

The signal processing of the polarization $\boldsymbol{\mathcal{P}}(t)$ is based on the discrete Fourier transform (FT), similar to the approach of Attaccalite and Grüning [49] discussed in Sec. 3.3. Extending this formalism to include an additional field, as in Eq. (4.1), is straightforward. The main challenge addressed in this work is to develop practical and accurate methods for extracting the relevant nonlinear susceptibilities from the resulting polarization $\boldsymbol{\mathcal{P}}(t)$. While a discrete FT-based strategy is used in Ref. [49] (Sec. (4.1)) for a single external monochromatic field, this analysis can be generalized to multiple external fields. The method proposed in this section is quite general and could be applied to Hamiltonians that differ from the one used in this work. Examples include tight-binding and other lattice models.

However, the common period for two or more commensurate frequencies can be several hundred femtoseconds, leading to very long and computationally expensive simulations.

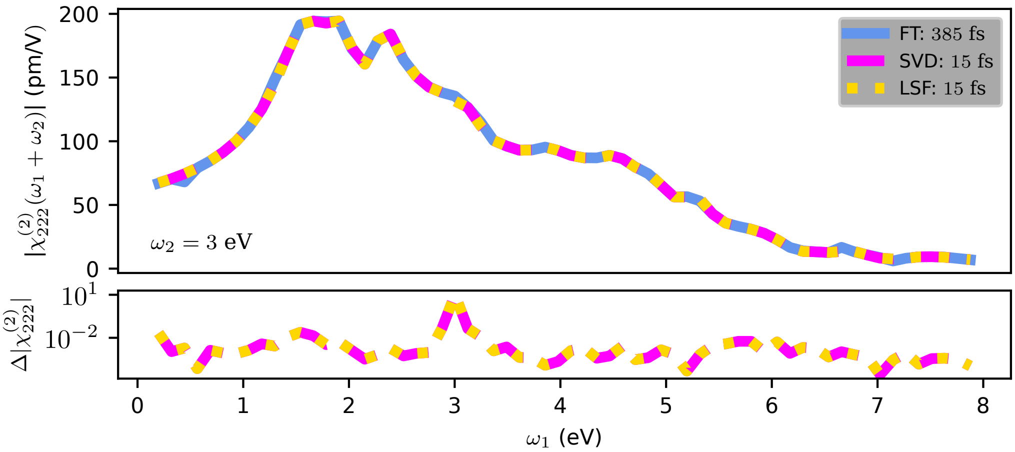

Figure 4.4: SFG of *h*-BN with a pump frequency $\omega_2 = 3$ eV obtained at the IPA level using the full discrete Fourier transformation (FT) (blue solid line), singular value decomposition (SVD) (magenta dashed line), and the nonlinear least square fit (LSF) (yellow dotted line). Results obtained with different sampling times are shown. The discrete FT needs a sampling time (385 fs) about 26 times larger than the SVD and LSF (15 fs). Below is displayed the difference in logarithmic scales for SVD and LSF, respectively, with 5 fs less sampling time to show the convergence.

Two monochromatic fields with commensurate frequencies, ω_1 and ω_2, are considered. Frequencies are commensurate as long as they are rational numbers (i.e., $\omega_1, \omega_2 \in \mathbf{Q}$). The fundamental frequency is obtained from the greatest common divisor of ω_1 and ω_2:

$$\omega_0 = \frac{\gcd(\lfloor 10^m \omega_1 \rceil, \lfloor 10^m \omega_2 \rceil)}{10^m}, \tag{4.12}$$

where $m = \max(n_1, n_2)$ and n_1, n_2 are the number of decimals in ω_1 and ω_2, respectively. The resulting polarization $\boldsymbol{\mathcal{P}}(t)$ is periodic with period $T = 2\pi/\omega_0$ and can thus be expressed as a Fourier series as in Eq. (3.55), in terms of the harmonics of ω_0. Since the frequencies of the external fields are multiples of the fundamental frequency, $\omega_1 = M\omega_0$ and $\omega_2 = N\omega_0$, the $|M \pm N|$ harmonics correspond to SFG and DFG. When the system of linear equations in Eq. (3.56) is set up, the sum over harmonics must be truncated at a suitable S to include these processes (i.e., $S \gtrapprox M + N$). Compared to the case of a single external field, the dimension of the system of linear equations is significantly increased. More importantly, T can become very large for frequency pairs with more than one decimal (see Fig. 4.4). Depending on the ratio of ω_1 and ω_2, T may be orders of magnitude larger than typical laser periods in the near-infrared to near-UV range ($\approx 1-5$ fs). As computational expense increases linearly with simulation time, processing the polarization signal from two monochromatic fields using these approaches can result in computationally demanding simulations.

Alternatively, the polarization $\boldsymbol{\mathcal{P}}(t)$ can be expanded as a product of two Fourier series, one in the harmonics of ω_1 and the other in the harmonics of ω_2:

$$\boldsymbol{\mathcal{P}}(t) = \sum_{n,m=-\infty}^{\infty} \mathbf{C}^{(n,m)} \exp\left[-i(n\omega_1 + m\omega_2)t\right], \tag{4.13}$$

where the matrix of Fourier coefficients is denoted by $\mathbf{C}^{(n,m)}$. The Fourier coefficients are obtained by solving a system of $(2S_1+1)(2S_2+1)$ linear equations:

$$\sum_{n=-S_1}^{S_1} \sum_{m=-S_2}^{S_2} \mathcal{F}_i^{(n,m)} \mathbf{C}_\alpha^{(n,m)} = \mathcal{P}_{\alpha,i}, \tag{4.14}$$

where $\mathcal{F}_i^{(n,m)} \equiv \exp[-i(n\omega_1 + m\omega_2)t_i]$ and S_1, S_2 are the maximum number of harmonics considered for each external field. Compared to the discrete FT with a single external field, the relevant coefficients can be directly identified; for example, $n = 1, m = 1$ yields the SFG and $n = 2, m = \pm 1$ yields the FI-SHG (with $\omega_2 = \Omega$). However, the system of linear equations in Eq. (4.14) is generally ill-conditioned. To solve Eq. (4.14), the Moore-Penrose inverse [148, 149], also known as the pseudoinverse, of $\mathcal{F}_i^{(n,m)}$ is computed using singular value decomposition (SVD). With this approach (referred to as SVD), a much shorter sampling time than T can be used, which significantly reduces the simulation time compared to the discrete FT.

A further approach for obtaining the Fourier coefficients is to solve a least squares problem (LSF) [150]. In this method, the set of $\mathbf{C}_\alpha^{(n,m)}$ is determined by minimizing:

$$\sum_{i=1}^{N} |\mathcal{P}_\alpha(t_i) - \bar{\mathcal{P}}_\alpha(t_i)|^2, \tag{4.15}$$

where N denotes the number of sampling points and $\bar{\mathcal{P}}$ is the truncated Fourier series of Eq. (4.13) up to order S. As with the SVD-based approach, the main advantage of the LSF over the discrete FT is that only a portion of the period T needs to be sampled to accurately determine the Fourier coefficients. For example, in the case of h-BN, Fig. 4.5 shows the polarization from the simulation compared with that reconstructed from Eq. (4.13) using coefficients obtained via LSF. Although only 15 fs are sampled, accurate results are achieved.

The accuracy and performance of the three approaches are compared in Fig. 4.4 for the SFG of h-BN. By employing the SVD- and LSF-based approaches, the required simulation time can be reduced by a factor of 26 compared to the discrete FT.

For the LSF to be accurate, one must carefully sample the key features of the signal, e.g. minima, maxima, and turning points. This implies that, in general, the LSF needs more sampling points $\mathcal{P}_{\alpha,i}$ (that is a higher sampling rate) than the discrete FT. This does not impact the cost of the simulations since a small time step is needed to integrate the equation of motion in Eq. (4.1). Non-uniform sampling (logarithmic or randomized) is more effective—thus reducing the sampling rate—than uniform sampling in capturing the key features of the signal, especially for high-frequency signals. An example of logarithmic sampling for LSF is shown in Fig.. 4.5.

Another aspect to be considered is the choice of the susceptibility tensor element to be calculated. Depending on the crystal symmetry, certain tensor elements are equivalent; however, directions in which the linear response is non-zero tend to be less precise and more unstable. This is attributed to two factors. First, the spurious signal resulting from the sudden switch-on is stronger. Second, the fitting procedure is less accurate since the linear response coefficient is about 6 orders of magnitude larger than the SHG,

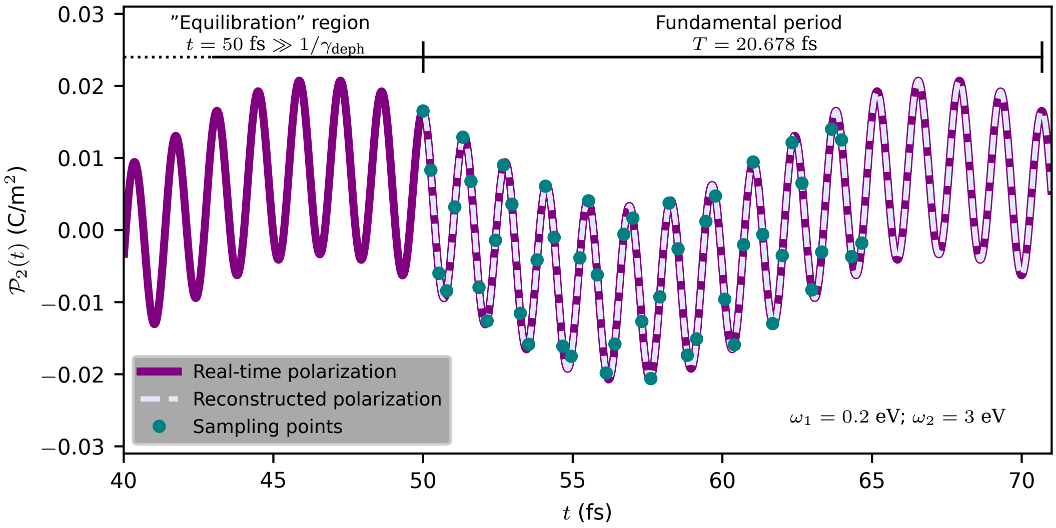

Figure 4.5: The time-dependent polarization (purple solid line) of h-BN calculated at the independent particle level with two electric fields ($\omega_1 = 0.2$ eV, $\omega_2 = 3$ eV). The signal can be divided into two regions: an initial "equilibration" region (up to $t \gg \gamma_{\mathrm{deph}}$, here $t = 50$ fs) during which the system's eigenfrequencies are suppressed by dephasing and a region where Eq. (4.13) holds. In the second region the polarization is logarithmically sampled (teal dots) within a converged time window of 15 fs, smaller than the fundamental period of 20.678 fs of the signal. This sampling time is sufficient to correctly determine the Fourier coefficients by the nonlinear least square fit (LSF) as verified by reconstructing the polarization (lavender dashed line) within the fundamental period using the Fourier coefficients and the truncated Eq. (4.13).

SFG, and DFG coefficients. Therefore, if possible, directions where the linear response is absent should be selected. For instance, in the case of the second-order response for 2D hexagonal systems such as those studied here, it is preferable to consider the off-diagonal elements, e.g., $\chi^{(2)}_{122}$, given that $\chi^{(2)}_{122} = \chi^{(2)}_{222}$ by crystal symmetry.

Furthermore, the LSF approach encounters its most challenging scenario when $\omega_1 \approxeq \omega_2$. When the frequencies are exactly equal, the least squares problem becomes ill-posed. For instance, considering the first term of the second-order polarization:

$$\begin{aligned}\mathcal{P}^{(2)} &= \chi^{(2)}(2\omega_1;\omega_1,\omega_1)\mathcal{E}^2(\omega_1) + \chi^{(2)}(2\omega_2;\omega_2,\omega_2)\mathcal{E}^2(\omega_2) \\ &+ \chi^{(2)}(\omega_1+\omega_2;\omega_1,\omega_2)\mathcal{E}(\omega_1)\mathcal{E}(\omega_2) + \dots \end{aligned} \tag{4.16}$$

If $\omega_1 \approxeq \omega_2$, the SHG and SFG terms become indistinguishable, and their coefficients cannot be uniquely determined by least squares optimization. Similar difficulties are encountered when one frequency is an integer multiple of the other.

In such cases, several strategies can be adopted. The repeated terms in the fitting function may be removed, starting values for the optimization can be taken from the closest already computed frequencies, or the results can be interpolated from neighbouring frequencies.

It should be noted that the quasi-degenerate case also presents difficulties for the discrete FT approach, as closely spaced frequencies lead to rapid beats in the signal. Accurately

Table 4.1: All the parameters used in the nonlinear response calculations for both MoS_2 and *h*-BN monolayers: the **k**-point sampling used in the IPA (TD-aGW in parentheses), the range of bands considered N_b, the cutoff, ϵ_{cut}, and the number of bands, ϵ_{bands}, used to converge the dielectric function $\epsilon_{\mathbf{G},\mathbf{G}'}$, the energetic shift ($\Delta E_{so}$) for the scissor operator applied to the Kohn-Sham band structure, the height of the supercell L_z, and the effective layer thickness d_{eff}. The 2L-*h*-BN calculations are only at the IPA level, so no information about dielectric constant and scissor operator are reported.

System	**k**-points	N_b	ϵ_{cut} (Ha)	ϵ_{bands}	ΔE_{so} (eV)	L_z (Å)	d_{eff} (Å)
MoS_2	30×30 (21×21)	4–13	5	200	0.72	10.88	6.15
h-BN	30×30 (18×18)	3–7	5	200	3.35	10.58	3.33
2L-*h*-BN	30×30	5–14	–	–	–	10.58	6.66

resolving these beats requires a very long sampling interval to capture the beat frequency $(\omega_1 - \omega_2)$.

However, cases involving degenerate or nearly degenerate frequencies are of limited theoretical and experimental relevance. Theoretically, for degenerate frequencies, the procedures described in Ref. [49] (see Sec. 3.3.3) can be used to extract the second-harmonic, while experimentally, interest is typically focused on distinct frequencies resonant with different electron-hole excitations [73].

4.4 Computational details

Ground-state properties of the *h*-BN mono- and bilayer and the MoS_2 monolayer were obtained within discrete FT using the Quantum Espresso code [45, 46]. The PBE functional [89] was adopted together with scalar-relativistic optimized norm-conserving pseudopotentials from the PseudoDojo repository (v0.4) [151] for *h*-BN and from the Fritz Haber Institute (FHI) [152] for MoS_2. The Kohn-Sham Hamiltonian was diagonalized for a specified number of states (see **k**-points and bands N_b in Table 4.1), which were then used as the basis set to represent all operators entering Eq. (4.1). All real-time simulations were carried out using the Yambo code [47]. The EOMs [Eq. (4.1)] were propagated using the Crank-Nicolson integrator with a time-step of 0.01 fs. Dephasing was included by sampling between 50-200 fs in all simulations. The static dielectric function $\epsilon_{\mathbf{G},\mathbf{G}'}$ required for the screened-exchange self-energy, Σ_{SEX} in Eq. (4.2), was computed within the random-phase approximation (see Ref. [47] for more details). All calculations were performed in a supercell, and for each system, the susceptibility extracted from the time-dependent polarization was rescaled to the effective thickness, d_{eff}, resulting in $\chi_{rescaled}(\omega) = L_z/d_{eff} \cdot \chi(\omega)$, where L_z denotes the z dimension of the supercell. The SFG and DFG spectra were obtained by performing simulations for all frequency pairs, ω_i, ω_j, within the chosen energy ranges. The relevant susceptibilities were extracted from the resulting polarizations [Eq. (4.4)] using the YamboPy code [P6], as described in Sec. 4.3. All simulation parameters are summarized in Table 4.1.

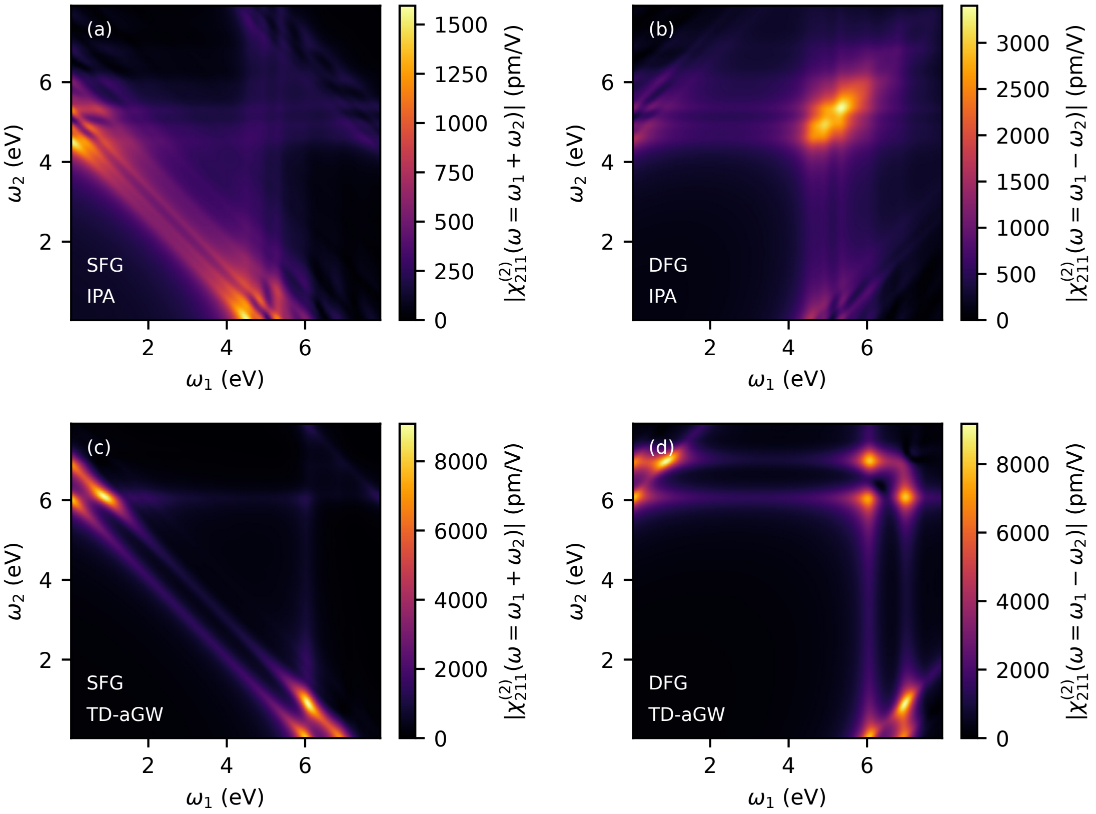

Figure 4.6: SFG/DFG spectra for *h*-BN in panels (a), (b) at the IPA and in panels (c), (d) at the TD-aGW level. The heatmaps have been generated using a frequency grid of $\omega_1 \times \omega_2 = 96 \times 96$ points. For each frequency pair a real-time simulation was run and the output signal processed.

4.5 Results

The approach outlined in Secs. 4.2-4.3 is applied to the SFG and DFG in *h*-BN and MoS_2 monolayers. *h*-BN monolayer is a wide band gap insulator with strong excitonic features and provides a clear example of the need for an accurate inclusion of excitonic effects. MoS_2 monolayer is one of the most widely studied 2D material, including its SFG and DFG [69, 72]. Since the *h*-BN and MoS_2 monolayers belong to the D_{3h} point group [153], they have only one non-vanishing second-order susceptibility tensor element with $\chi^{(2)}_{222} = -\chi^{(2)}_{211} = -\chi^{(2)}_{112} = -\chi^{(2)}_{121} \equiv \chi^{(2)}$[3] For SFG and DFG, results are shown in a heatmap, in which each point has been obtained by a separate real-time simulation. As a guide to reading such heatmaps (see, e.g., Fig. 4.6), reference can be made to Eqs. (4.5)-(4.6). The susceptibilities corresponding to SFG/DFG have poles both at one-photon ($\omega_{1,2} = \Omega_\lambda$) and at two-photon ($\omega_1 \pm \omega_2 = \Omega_\lambda$) resonances with single-particle transitions (or with excitons) in the system. The one-photon resonances correspond to vertical (ω_1) and horizontal (ω_2) lines in the SFG and DFG heatmaps. In the SFG heatmap, the two-photon resonances correspond to negative slope lines running from $\omega_2 = \Omega_\lambda$ to

---

[3] For MoS_2 the orientation of the x aligned along an armchair direction following the conventions of Ref. [154] has been chosen.

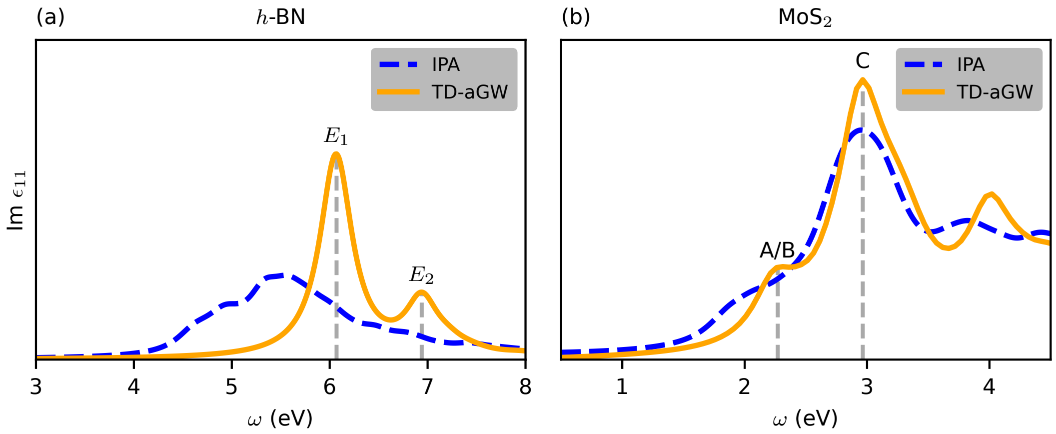

Figure 4.7: Calculated imaginary dielectric function of (a) h-BN and (b) MoS$_2$ at the IPA (blue dashed line) and TD-aGW (orange solid line) level. The excitonic peaks E_1 and E_2 of h-BN are located at around 6.1 eV and 7 eV, respectively (panel (a)). The degenerate excitonic peak A/B as well as C can be seen at around 2.2 eV and 3 eV, respectively (panel (b)).

$\omega_1 = \Omega_\lambda$, while in DFG they correspond to positive slope lines starting at $\omega_2 = \Omega_\lambda$ and $\omega_1 = \Omega_\lambda$. Further, the diagonal $\omega_1 = \omega_2$ corresponds to the SHG in the SFG and the optical rectification in the DFG heatmap. In Sec. 4.5.3, THz-induced second-harmonic generation in 2L-h-BN is considered. This system has inversion symmetry and thus has zero SHG at zero-field.

4.5.1 SFG and DFG in monolayer *h*-BN

In Fig. 4.6, the SFG and DFG spectra for h-BN at the IPA and TD-aGW levels are reported. At the IPA level, the SFG spectrum (Fig 4.6(a)) of h-BN is dominated by two-photon resonances with single-particle transitions between 4-6 eV (negative slope bands). In particular, the lowest-energy band corresponds to the transition from the valence band minimum to the conduction band maximum. The one-photon transitions (vertical and horizontal bands) are much weaker though a significant enhancement is observed for part of the spectra both resonant with one- and two-photon absrption. In particular, this portion of the SFG spectrum is twice as intense as the SHG (the $\omega_1 = \omega_2$ diagonal). The DFG spectrum (Fig 4.6(b)) is dominated by the resonant optical rectification between 4-6 eV ($\omega_1 = \omega_2$). Further, one-photon resonances (vertical and horizontal bands) are visible, again enhanced when two-photon resonances are also present. These results can be straightforwardly related to the IPA absorption spectrum (see e.g. Ref. [77], which presents a broad peak between 4-6 eV). This broad peak can be found in the calculated absorption spectrum in Fig.4.7(a).

As expected, the addition of the electron-hole interaction drastically changes the SFG/DFG spectra[4]. Sharper and much stronger (note the different color scale) features appear in the TD-aGW spectra, corresponding to the E_1, E_2 excitonic peaks at around 6.1 eV and 7 eV [125]. These two excitonic peaks can also be identified in the calculated absorption

---

[4] Note that the shift of the onset is due to the addition of the scissor operator in Table 4.1 partially compensated by the exciton binding energy.

spectrum at TD-aGW level in Fig. 4.7(a). Two-photon resonances with the two excitons are clearly visible in the SFG spectrum (negative slope lines in Fig 4.6(c)) and DFG spectrum (positive slope lines starting at the exciton energy in Fig 4.6(d)). One-photon resonances are also visible (as vertical/horizontal lines). The responses are significantly enhanced in the SFG (DFG) when one laser is resonant with E_1 (E_2) and the second laser with $E_2 - E_1$. These spectral features correspond to the first and third terms in Eq. (4.6) and provide a measure of the strength of exciton-exciton transitions. In the DFG spectrum, strong features are visible as well on the diagonal, corresponding to the exciton-resonant optical rectification, as well as when one laser is resonant with one exciton and the second with the other (corresponding to the second and fourth term in Eq. (4.6)).

4.5.2 SFG and DFG in monolayer MoS$_2$

In Fig. 4.8, the SFG and DFG spectra for monolayer MoS$_2$ at both the IPA and TD-aGW levels are presented. When compared with *h*-BN, the differences between the IPA and TD-aGW spectra are less striking, as already observed for the absorption [143] and SHG [77]. Similarly to what was observed for the SHG [77, 145, 155], a significant enhancement is seen at resonances with the C exciton (≈ 3 eV), while the weaker A and B excitons (≈ 2.2 eV, as spin-orbit coupling is not included the peaks are degenerate) show minimal excitonic enhancement. These excitonic peaks are also visible in the linear absorption spectrum as shown in Fig. 4.7(b).

The SFG spectrum shows a strong two-photon resonance with the C exciton (negative slope line) while the DFG spectrum shows a strong one-photon resonance (vertical/horizontal line) and a strong exciton resonant optical rectification. Though less evident than for *h*-BN, there is an enhancement in the intensity in correspondence of exciton-exciton transitions. In the SFG (Fig 4.8(c)), the signal is enhanced when one laser is resonant with the A/B exciton (about 2.2 eV) while the frequency of the second matches the energy difference between the C and A/B excitons. In the DFG (Fig 4.8(d)), the signal is enhanced when one laser is resonant with the C exciton (about 3 eV) while the frequency of the second corresponds to the energy difference between the C and A/B excitons. SFG and DFG were measured in mono- [70, 72, 156, 157] and few-layers [69] MoS$_2$. In the presence of metal substrates [156], excitonic resonances were shown to be strongly attenuated, and their position shifted due to gap renormalization. These effects are beyond the methodology presented in this manuscript. Other measurements are performed in a pump-probe configuration with a delay between the pump and probe [156], which in our case requires the inclusion of dephasing effects that are beyond the scope of the present work. Finally, for insulating substrates and synchronized pump and probe, our simulation results are in agreement with existing measurements. In particular, SFG has been observed [157] at 2.9 eV when laser fields at 1.2 eV and 1.9 eV were injected. The DFG was observed [72] by fixing one laser at 3.06 eV and varying the second between 0.79 and 0.95 eV, showing an enhancement of the signal between 2.1-2.2 eV, which the authors attributed to excitonic effects in this region. Our results support this interpretation.

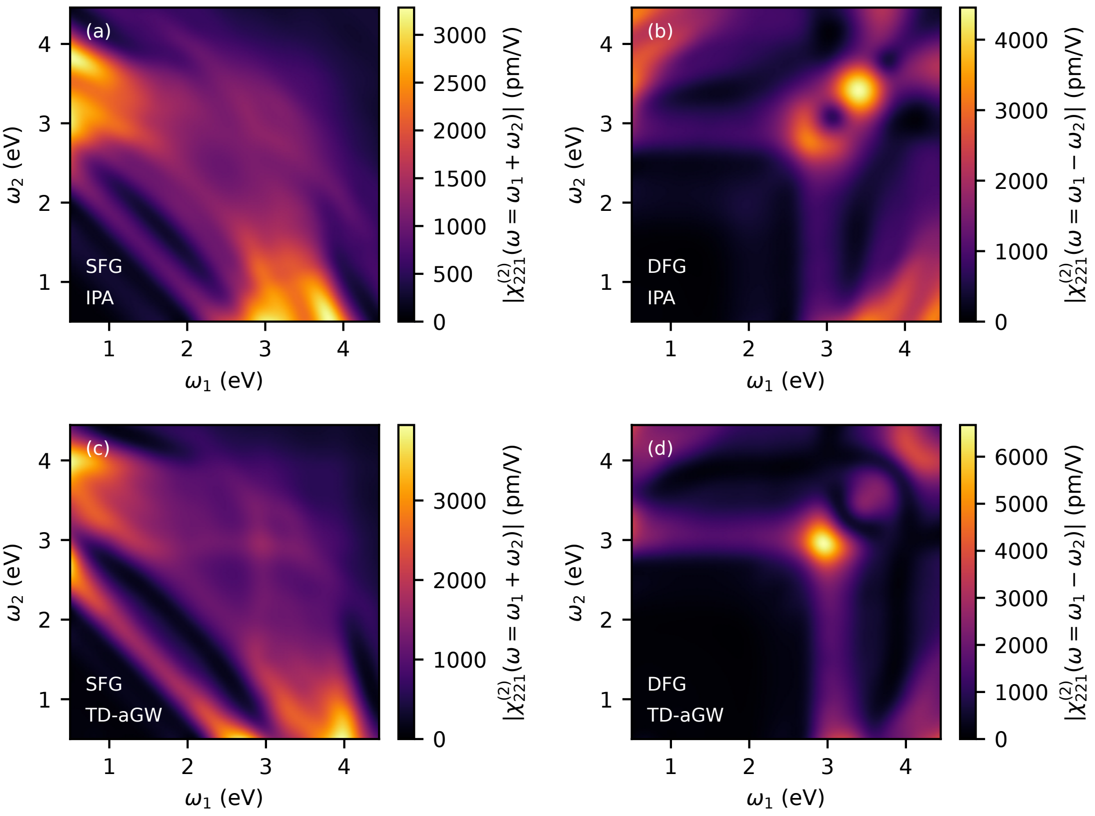

Figure 4.8: SFG/DFG spectra for MoS_2 in panels (a) and (b) at the IPA and in panels (c), (d) at the TD-aGW level. The heatmaps have been generated using a frequency grid of $\omega_1 \times \omega_2 = 96 \times 96$ points for the IPA and $\omega_1 \times \omega_2 = 72 \times 72$ for the TD-aGW. For each frequency pair a real-time simulation was run and the output signal processed.

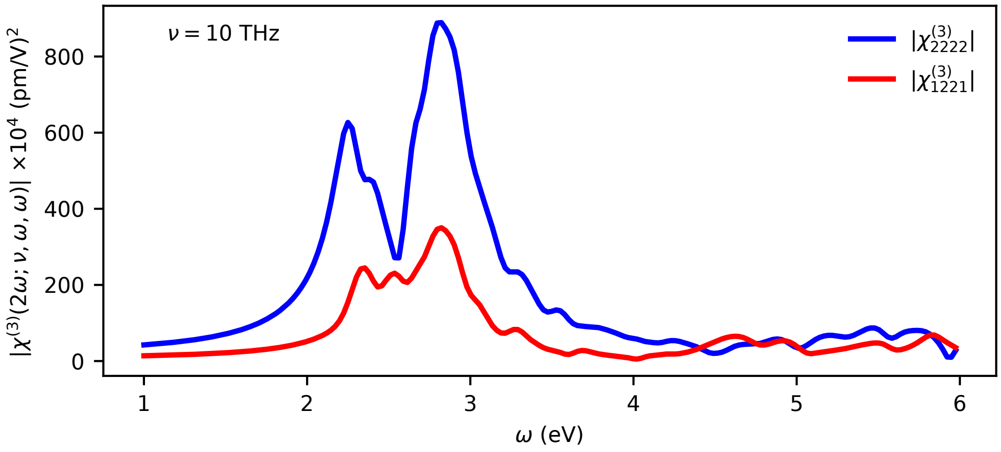

Figure 4.9: Calculated THz field-induced second-harmonic generation of bilayer h-BN with ν=10 THz at the IPA level. Each curve consists of 192 frequency steps between $\omega = 1 - 6$ eV.

4.5.3 Field-induced second-harmonic generation in bilayer *h*-BN

In Fig. 4.9, the third-order susceptibility corresponding to FI-SHG in bilayer h-BN at the IPA level is shown. For each frequency ω, a real-time simulation was performed in the presence of a THz pump ($\nu = 10$ THz). The response functions in the figure correspond to two configurations: both pump and probe along the y direction ($\chi^{(3)}_{2222}$), and pump along x with probe along y ($\chi^{(3)}_{1221}$). In both cases, a strong resonance is observed at approximately half the electronic band gap, around $2-3$ eV, similar to the SHG in monolayer h-BN [77]. It can be seen that the response intensity is higher when pump and probe are parallel compared to the perpendicular configuration. The magnitude of $\chi^{(3)}$ is comparable to that of bulk ferroelectric oxides, which are recognized for their excellent nonlinear properties [25]. These results indicate that two-dimensional crystals may be employed as detectors for THz radiation [158].

4.6 Conclusions

In this chapter, a computational framework is presented to study sum and difference frequency generation by means of real-time simulations in presence of multiple laser fields. With multiple fields, the signal processing required to extract the nonlinear susceptibilities is numerically challenging. In particular, using a discrete Fourier transform approach may need very long and thus computationallly costly simulations. The approaches based either on the singular value decomposition or on the least squares optimization give accurate results with short sampling time, allowing to significantly reduce the simulation time. These approaches enable the calculation of second-order response functions, as SFG/DFG, and higher nonlinear response functions, as FI-SHG, including excitonic effects within many-body theory.

For the systems studied, monolayer h-BN and MoS$_2$, including excitonic effects in SFG and DFG spectra is critical. In both materials, strong features corresponding to exciton transitions, as recently experimentally observed for another layered material [73], are predicted. Further, the results on FI-SHG for a h-BN bilayer demonstrate that the approach can be used to compute and interpret nonlinear terahertz spectroscopy of solids [159]. Finally, the approach presented can be coupled to atomic vibrations by using finite displacement methods [160, 161], opening the way to simulate other spectroscopic techniques such as CARS. Since the pure NRB in CARS is not directly available experimentally [65], the *ab initio* real-time simulation is a promising feature to support CARS measurements. This is applied on ferroelectric oxides such as LN, which is part of the investigation in the next chapter.

5 Ferroelectric oxides under strain

5.1 Ferroelectric oxides: $LiNbO_3$ & $LiTaO_3$

LN is an uniaxial ferroelectric oxide that crystallizes in the trigonal space group $R3c$, belonging to the point group $3m$. It has a Curie temperature of about 1480 K. In its ferroelectric phase, oxygen atoms form a distorted hexagonal close-packed lattice. The resulting oxygen octahedral cages are alternately occupied by lithium ions, niobium ions, or left vacant in a periodic arrangement along the z axis. These ions inside are slightly shifted with respect to the center of the oxygen cages causing a spontaneous polarization of approximately 0.7 Cm^{-2} along the z axis [5]. The noncentrosymmetric structure is responsible for the strong second-order nonlinear optical response [25].

In contrast to the z axis of LN, the x and y directions are non-polar. Although optically equivalent, they differ structurally in their atomic stacking sequence: along x axis, the crystal consists of repeating $-O_9 - Li_6Nb_6 - O_9$ layers, while along the y axis it is built from stacked $Li_2Nb_2O_6$ layers [5, 162, 163] (see Fig. 5.1). This anisotropy implies that compressive and tensile stress applied along x and y axes will affect the atomic arrangement, and consequently the linear and nonlinear optical response, in distinct ways.

LT has a similar structure and properties, with tantalum ions replacing niobium ions, and shares the same $R3c$ space group as well as many physical properties with LN, but exhibits slight differences due to the heavier Ta atom and its slightly larger ionic radius [5]. For instance, the elastic and vibrational properties of LT closely mirror those of LN [164]. Because of their structural similarity, comparative studies of LN and LT allow to understand the role of chemical substitution from strain-induced vibrational properties.

5.2 Modeling uniaxial stress

In order to model stress in a crystal, it is neccessary to understand how the crystal responds to an applied stress in terms of the deformation of the crystal lattice. Such mechanical properties are described by the fourth rank elastic stiffness tensor c_{ijkl} and the elastic compliance tensor s_{ijkl} whereby s_{ijkl} is the inverse of the elastic stiffness tensor (c_{ijkl}), i.e. $s_{ijkl} = c_{ijkl}^{-1}$. Both these tensors connect the symmetric and second rank strain ϵ_{ij} and stress σ_{ij} tensors to each other. The stress tensor σ_{ij} is defined by force applied to an unit area of a material, while the strain tensor ϵ_{ij} is the relative change of length in a material. In the elastic regime, stress and strain are connected

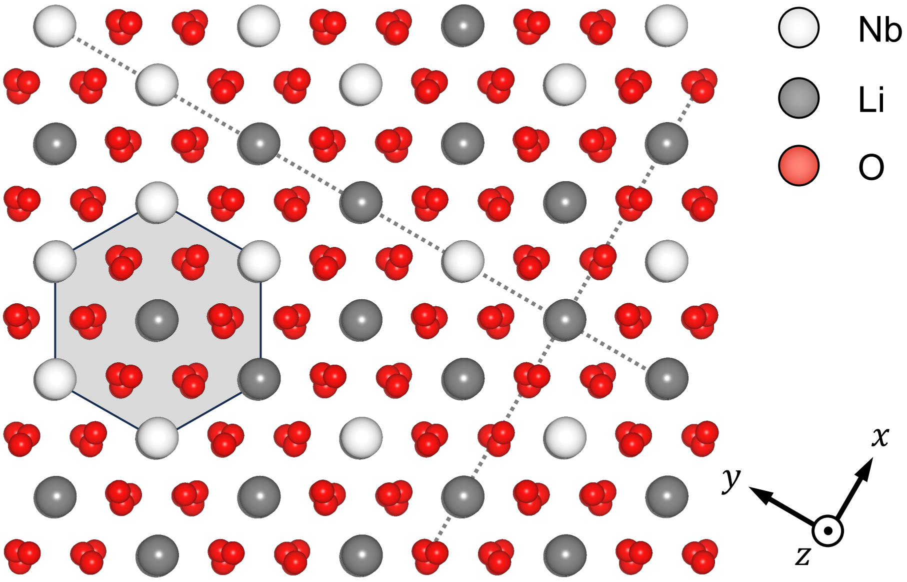

Figure 5.1: Top view of the LN crystal structure. Dotted lines show the x and y directions. The hexagonal unit cell is shown.

by both the elastic stiffness tensor and the elastic compliance tensor via Hooke's law, which can be written as:

$$\begin{aligned} \epsilon_{ij} &= s_{ijkl}\sigma_{kl}, \\ \sigma_{ij} &= c_{ijkl}\epsilon_{kl}. \end{aligned} \tag{5.1}$$

Equation (5.1) can be simplified by using Voigt notation:

$$\begin{array}{ccc} 11 \rightarrow 1 & 12 \rightarrow 6 & 13 \rightarrow 5 \\ 22 \rightarrow 2 & 21 \rightarrow 6 & 23 \rightarrow 4 \\ 33 \rightarrow 3 & 31 \rightarrow 5 & 32 \rightarrow 4, \end{array}$$

reducing the number of independent components to 36. As the components of the stiffness tensor are the second-order derivatives of the mechanical energy density with respect to strain components, stiffness and compliance tensor are further reduced to 21 independent components with Schwarz's theorem [165].

As a result, the strain-stress relationship can be expressed in a more compact form [5, 165]:

$$\begin{aligned} \sigma_m &= c_{mn}\epsilon_n, \\ \epsilon_m &= s_{mn}\sigma_n. \end{aligned} \tag{5.2}$$

In the case of ferroelectric LN crystal, which belongs to the trigonal crystal system and $3m$ point group, the elastic compliance and stiffness tensors can be written in the following form [5, 165]:

$$[s_{nm}] = \begin{pmatrix} s_{11} & s_{12} & s_{13} & s_{14} & 0 & 0 \\ s_{12} & s_{11} & s_{13} & -s_{14} & 0 & 0 \\ s_{13} & s_{13} & s_{33} & 0 & 0 & 0 \\ s_{14} & -s_{14} & 0 & s_{44} & 0 & 0 \\ 0 & 0 & 0 & 0 & s_{44} & 2s_{14} \\ 0 & 0 & 0 & 0 & 2s_{14} & s_{66} \end{pmatrix}, \tag{5.3}$$

$$[c_{mn}] = \begin{pmatrix} c_{11} & c_{12} & c_{13} & c_{14} & 0 & 0 \\ c_{12} & c_{11} & c_{13} & -c_{14} & 0 & 0 \\ c_{13} & c_{13} & c_{33} & 0 & 0 & 0 \\ c_{14} & -c_{14} & 0 & c_{44} & 0 & 0 \\ 0 & 0 & 0 & 0 & c_{44} & c_{14} \\ 0 & 0 & 0 & 0 & c_{14} & c_{66} \end{pmatrix}. \tag{5.4}$$

The elastic compliance tensor is given in the Cartesian basis whose orientation related to the rhombohedral unit cell is defined by the standard orientation by Weis *et al.* [5]. In this work a rhombohedral unit cell is applied which is also oriented according to this standard orientation. However, the orientation is not yet unambiguously defined by this convention. In accordance to the standard orientation, the basis vector of the rhombohedral unit cell can point in either the Cartesian $+y$ or -y direction. The former is the general case for the rhombohedral unit cell and the latter for the basis of the elastic compliance tensor. Hence, the basis of the elastic compliance tensor was rotated by 180° about the z axis by a basis transformation according to Ref. [166]. This basis transformation results in the same tensor elements, except from a sign change of $s_{14} \rightarrow -s_{14}$ and $c_{14} \rightarrow -c_{14}$.

To model uniaxial stress, the following procedure is applied as described in Refs. [P1–P3]. The lattice vectors of the rhombohedral unit cell $\boldsymbol{a}_q(\epsilon)$ $[q = 1, .., 3]$ are adjusted after the application of a strain tensor ϵ according to:

$$\boldsymbol{a}_q(\epsilon) = (\boldsymbol{I} + \epsilon)\, \boldsymbol{a}_q(0), \tag{5.5}$$

where $\boldsymbol{I}$ is denoted as the identity matrix. The corresponding strain tensor under uniaxial stress can be derived by the elastic compliance tensor and Eq. (5.19). In order to calculate uniaxial stress in the Cartesian directions, one of the first three components (the uniaxial stress components) of the stress tensor is set to a nonzero value, while the remaining components are set to zero. This leads with Eq. (5.19) to a strain tensor which can be used to obtain the lattice vectors that arise under uniaxial stress. After adjusting the lattice vectors of the rhombohedral unit cell according to the stress, the atomic positions are relaxed within DFT with fixed lattice vectors. In this procedure, uniaxial stress is modeled with explicit consideration of Poisson ratios and shear strain effects. Since the corresponding strain tensor under uniaxial stress is derived from the elastic compliance tensor, it is neccessary to investigate the elastic properties of LN crystals first which will be presented in the following section (see Sec. 5.3) based on the results of Ref. [P2]. The corresponding strain tensor for various uniaxial stress values is shown in Table 5.1 compiled from the results of the DFT calculations using the PBEsol exchange-correlation functional.

Table 5.1: The strain tensor corresponding to the applied uniaxial stress in x ($i = 1$), y ($i = 2$), and z ($i = 3$) direction, respectively. For all cases, $\epsilon_{13} = \epsilon_{12} = 0$. All calculations are done using the PBEsol exchange-correlation functional.

	x stress			y stress			z stress		
σ_{ii} [GPa]	1	2	3	1	2	3	1	2	3
ϵ_{11} [%]	0.603	1.206	1.809	-0.140	-0.280	-0.420	-0.135	-0.270	-0.405
ϵ_{22} [%]	-0.140	-0.280	-0.420	0.603	1.206	1.809	-0.135	-0.270	-0.405
ϵ_{33} [%]	-0.135	-0.270	-0.405	-0.135	-0.270	-0.405	0.508	1.016	1.524
ϵ_{23} [%]	-0.064	-0.128	-0.192	0.064	0.128	0.192	0.000	0.000	0.000

5.3 Elastic Properties

5.3.1 Computational details

The electronic ground state calculations are performed within DFT using the GGA [88] as implemented in the Quantum Espresso package [45, 46]. Optimized norm-conserving Vanderbilt pseudopotentials [151, 167] are used, with projectors up to $l = 2$ for Li and O and $l = 3$ for Nb. The electronic wave functions are expanded in a plane-wave basis with a kinetic energy cutoff of 85 Ry. Brillouin zone sampling is carried out with an $8 \times 8 \times 8$ k-point mesh. Atomic positions are relaxed until the Hellmann-Feynman forces and total energy converge below 10^{-4} a.u. and 10^{-5} a.u., respectively.

If uniaxial strain is applied, e.g. in the x direction, i.e. $\epsilon_1 \neq 0 = \epsilon_2 = \epsilon_3 = \epsilon_4 = \epsilon_5 = \epsilon_6$, four linear equations between the corresponding stress tensor elements and the nonzero strain tensor element result

$$\sigma_1 = c_{11}\epsilon_1, \tag{5.6a}$$

$$\sigma_2 = c_{12}\epsilon_1, \tag{5.6b}$$

$$\sigma_3 = c_{13}\epsilon_1, \tag{5.6c}$$

$$\sigma_4 = c_{14}\epsilon_1. \tag{5.6d}$$

The stress tensor for various uniaxial strain values is calculated within DFT, ranging from $-1\,\%$ to $1\,\%$ in increments of $0.2\,\%$, ensuring the strain remains within the linear elastic regime. By applying Eqs. (5.6) to the computed stress tensor elements at each strain, the elastic constants are extracted via linear fitting. The elastic compliance tensor components are then obtained as the inverse of the stiffness tensor as expressed in Eq. (5.2).

In this work, this procedure is implemented using both the PBE [89] and the revised PBEsol [90] exchange-correlation functionals, each with and without the DFT+U correction in the formalism of Cococcioni and de Gironcoli [92]. The effective Hubbard potential for Nb is determined to be 3.1 eV from linear response calculations in Quantum Espresso, as described in Sec. 2.2.4, consistent with literature values [168, 169]. The following results are shown from Ref. [P2].

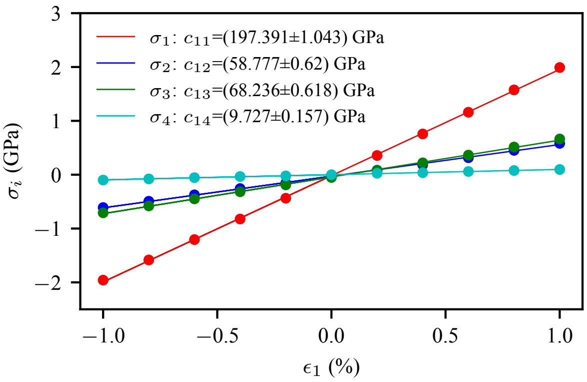

Figure 5.2: The calculated stress tensor elements as a function of uniaxial strain in x direction. The elastic stiffness tensor elements are obtained by the linear fits corresponding to Eqs. (5.6).

5.3.2 Results

For uniaxial strain applied in the x direction, the stress tensor is computed for various strain values and fitted according to Eqs. (5.6), yielding the elastic constants from the slope as shown in Fig. 5.2. All other possible configurations of uniaxial strain can be found in the Appendix A.1.1. The elastic constants obtained from these linear stress-strain relationships are averaged and summarized in Table 5.2. The elastic compliance tensor, calculated as the inverse of the elastic stiffness tensor, is also included in Table 5.2. The results show good agreement with Warner *et al.* [6], with the PBEsol functional providing the closest match to experiment. While tuning the Hubbard potential slightly improves the agreement, applying the Hubbard correction to PBEsol worsens the agreement for c_{14} and c_{44}. This is consistent with the work of Weck and Kim [170], who showed that different elastic tensor elements respond differently to the effective Hubbard potential. As the Hubbard correction increases computational cost and does not consistently improve accuracy, all subsequent calculations use the PBEsol functional without Hubbard corrections.

5.4 Vibrational properties

5.4.1 Theoretical background

At the zone center of bulk LN, the vibrational modes can be classified into A_1, A_2 and E symmetry classes, each with distinct characteristics and optical activity. Bulk LN possesses four A_1, five A_2 and nine twofold-degenerate E modes. The A_1 and E modes are both Raman and infrared active. These modes are characterized by specific symmetry properties [164]: A_1 modes involve vibrations that preserve the threefold rotational symmetry of the crystal and exhibit atomic displacement aligned primarily along the z direction. E modes are twofold-degenerate and involve vibrations in the x-y plane. These displacements break rotational symmetry, particularly, through oxygen atom motion. In contrast, A_2 modes are not optically active, as they lack changes in polarizability or dipole moment necessary for Raman or infrared activity. Instead, A_2

Table 5.2: Comparison between the calculated elastic stiffness and compliance tensor elements with PBE, PBE+U ($U_{\text{eff}} = 3.1\,\text{eV}$), PBEsol and PBEsol+$U$ ($U_{\text{eff}} = 3.1\,\text{eV}$) and the experimental values of Warner *et al.* [6].

Elastic constants	PBE	PBE+U	PBEsol	PBEsol+U	Warner *et al.* [6]
c_{11} [GPa]	182	192	197	206	203
c_{12} [GPa]	57	57	59	57	53
c_{13} [GPa]	58	62	68	72	75
c_{14} [GPa]	13	8	10	4	9
c_{33} [GPa]	215	223	233	240	245
c_{44} [GPa]	47	57	58	69	60
c_{66} [GPa]	63	68	69	74	75
s_{11} [TPa^{-1}]	6.65	6.10	6.03	5.64	5.78
s_{12} [TPa^{-1}]	-1.84	-1.44	-1.40	-1.09	-1.01
s_{13} [TPa^{-1}]	-1.30	-1.30	-1.35	-1.36	-1.47
s_{14} [TPa^{-1}]	-2.35	-1.06	-1.28	-0.39	-1.02
s_{33} [TPa^{-1}]	5.35	5.20	5.08	4.99	5.02
s_{44} [TPa^{-1}]	22.58	17.84	17.68	14.54	17.0
s_{66} [TPa^{-1}]	16.83	14.95	14.86	13.56	13.6

modes involve atomic displacements that are antisymmetric and do not couple with electromagnetic fields, rendering them silent in optical spectra. This symmetry-based distinction plays a critical role in determining the optical properties and selection rules for vibrational modes in bulk LN. The Raman tensors for irreducible representations for the $R3c$ symmetry are [171]

$$A_1(z) = \begin{pmatrix} a & 0 & 0 \\ 0 & a & 0 \\ 0 & 0 & b \end{pmatrix}, \tag{5.7}$$

$$E(y) = \begin{pmatrix} c & 0 & 0 \\ 0 & -c & d \\ 0 & d & 0 \end{pmatrix}, \tag{5.8}$$

$$E(-x) = \begin{pmatrix} 0 & -c & -d \\ -c & 0 & 0 \\ -d & 0 & 0 \end{pmatrix}. \tag{5.9}$$

All possible scattering geometries in back-scattering Raman spectroscopy are compiled in Table 5.3. In the $R3c$ symmetry of LN, certain modes are expected for specific polarization configurations within Porto notation $\boldsymbol{k}_0(\boldsymbol{e}_0, \boldsymbol{e}_S)\boldsymbol{k}_S$ where $\boldsymbol{k}_0, \boldsymbol{k}_S$ are the propagation directions of incoming and scattered photons and $\boldsymbol{e}_0, \boldsymbol{e}_S$ are their polarization. According to the selection rules A$_1$ and E modes are visible in (x, x) and (y, y) geometries, while in (x, z) and (y, z) configurations E modes are nonzero only. Due to the crystal

Table 5.3: Selection rules and Raman tensor elements for all investigated backscattering geometries for bulk LN with $R3c$ symmetry. x, y, z refer to the orthogonal reference system for tensor properties. TO and LO label transverse and longitudinal optical modes, respectively.

Configuration	Symmetry	Eff. TO	Eff. LO
$x(y,y)\bar{x}$	A_1 TO, E TO	a^2+c^2	
$x(y,z)\bar{x}$	E TO	d^2	
$x(z,y)\bar{x}$	E TO	d^2	
$x(z,z)\bar{x}$	A_1 TO	b^2	
$y(x,x)\bar{y}$	A_1 TO, E LO	a^2	c^2
$y(x,z)\bar{y}$	E TO	d^2	
$y(z,x)\bar{y}$	E TO	d^2	
$y(z,z)\bar{y}$	A_1 TO	b^2	
$z(x,x)\bar{z}$	A_1 LO, E TO	c^2	a^2
$z(x,y)\bar{z}$	E TO	c^2	
$z(y,x)\bar{z}$	E TO	c^2	
$z(y,y)\bar{z}$	A_1 LO, E TO	c^2	a^2

symmetry and since the theoretical study does not involve longitudinal optical (LO) modes, the spectra for the (x,x) and (y,y) as well as for the (x,z) and (y,z) spectra are equal in theoretical spectra. Additionally, the (z,z) and (x,y) configuration show only A_1 and E modes, respectively [164].

In the following the computational details and the corresponding results from Ref. [P1] are presented.

5.4.2 Computational details

The DFT calculations are carried out within the GGA [172] using the PBE functional [89] as implemented in VASP [44]. PAW [95] potentials are employed, with projectors up to $l = 3$ for Nb and Ta, and $l = 2$ for Li and O, as validated in previous work [164]. The electronic wave functions are expanded in a plane-wave basis with a kinetic energy cutoff of 475 eV. To model uniaxial stress, the lattice constants of the rhombohedral unit cell are adjusted as described in Sec. 5.2. Experimental lattice constants ($a_{\mathrm{R}}^{\mathrm{LN}} = 5.494$ Å, $\alpha^{\mathrm{LN}} = 55.867\,°$ and $a_{\mathrm{R}}^{\mathrm{LT}} = 5.474$ Å, $\alpha^{\mathrm{LT}} = 56.171\,°$) [164] and elastic constants from Warner *et al.* [6] are used in this section, as vibrational properties are sensitive to the choice of lattice parameters.

Previous investigations have shown that the vibrational properties of stoichiometric LN and LT are slightly affected by the doping of 5% MgO, as shown in Refs. [164]. Hence, the calculations for stoichiometric LN and LT are compared with µ-Raman spectroscopy measurements in combination with a uniaxially stressed cell [32] of stoichiometric as well as of 5% MgO-doped LN, which is a common doping level in experiments [173].

The calculations were performed in two ranges for LN and LT: First, the effects of strain, i.e. compressive as well as tensile strain, on the phonon frequencies have been calculated

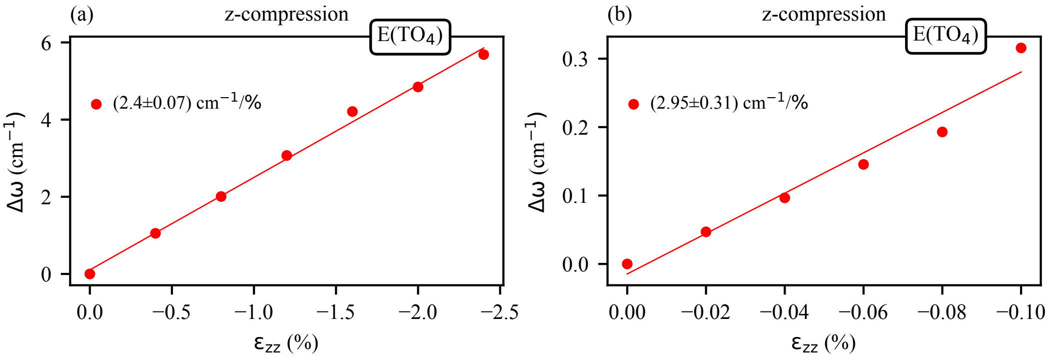

Figure 5.3: DFT calculated relative frequency shifts of the E(TO_4) mode of stoichiometric LN as a function of strain in z direction in (a) steps of 0.4 % and (b) steps of 0.02 %. The linear fit and the standard deviation for both are plotted and their fitting parameters displayed. The slopes for strain are defined as $(\Delta\omega)/(|\Delta\epsilon|)$ and displayed with the fitting error.

in fine increments up to values reachable in the experiments. Second, calculations for higher values of strains, but larger increments, were performed. For LN and LT this procedure has been performed for lower strains up to 0.10 %, as well as for higher values up to 2.4 %. Here, increments of 0.02 % and 0.4 % have been chosen, respectively. The Hellmann-Feynman forces are minimized under a threshold value of 0.005 eV/Å by relaxation of the atomic positions.

The Γ-centered phonon frequencies and eigenvectors are derived by the frozen-phonon method [174] without symmetry constraints. For the calculation of the Hessian matrix, atomic displacements of 0.015 Å in each Cartesian direction are considered. Since the approach does not take into account the long-range electric fields accompanying the longitudinal-optical (LO) phonons, the calculations are restricted to transversal-optical (TO) phonons. An 8 × 8 × 8 k-point mesh is used to sample the first Brillouin-zone corresponding to the rhombohedral unit cell, which yields 192 irreducible points.

5.4.3 Results

In order to benchmark the accuracy of the present models, the calculated phonon frequencies for unstrained stoichiometric LN and LT are compared with previous studies [164] (see Appendix A.1.2 for full data). Relative to the experimental results of Ref. [P1], the largest discrepancy for LN and LT is found for the $A_1(TO_4)$ mode, with deviations of 20 cm^{-1} and 22 cm^{-1}, respectively. The average deviation from experiment is approximately 8.7 cm^{-1} for LN and 8.4 cm^{-1} for LT. These values are comparable to the mean deviations reported in Ref. [164] (10.7 cm^{-1} for LN and 10.8 cm^{-1} for LT), indicating good agreement with both prior theoretical and experimental data. The typical deviations are also consistent with those found in other literature, such as Refs. [173, 175].

To illustrate the calculated dependence of phonon frequencies, the E(TO_4) mode of LN is shown in Fig. 5.3. Figures 5.3(a) and (b) display the results for larger and smaller strain increments, respectively. The frequency shift of the E(TO_4) mode exhibits an

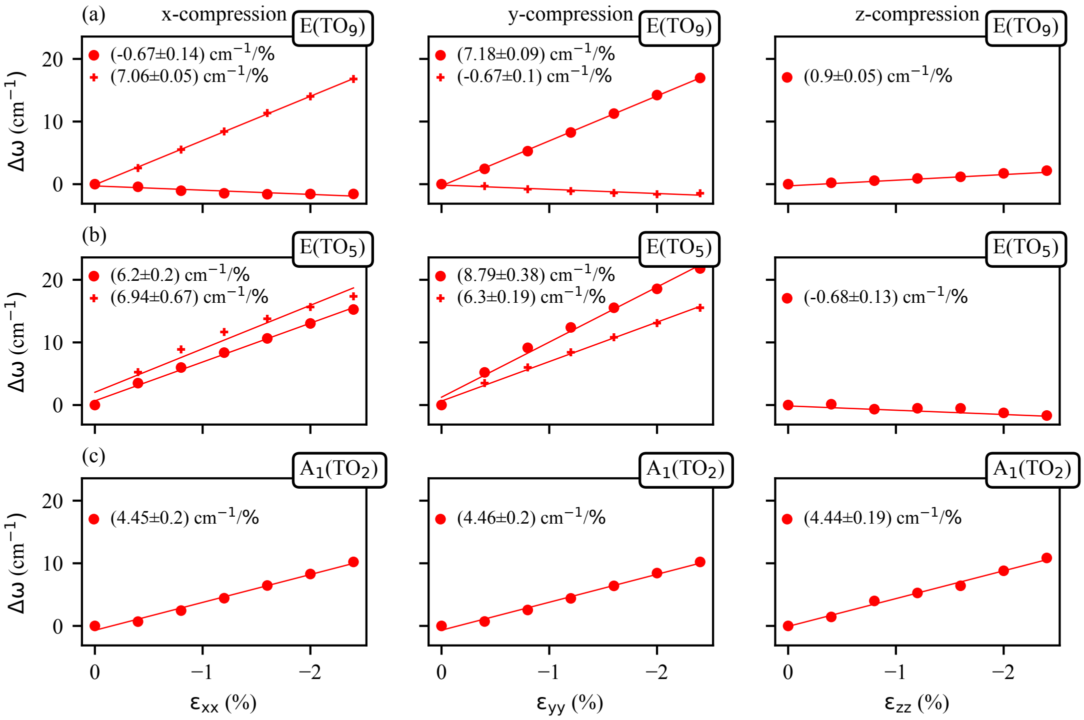

Figure 5.4: The DFT calculated relative frequency shifts of (a) E(TO$_9$) (first row), (b) E(TO$_5$) (second row) and (c) A$_1$(TO$_2$) (third row) modes of stoichiometric LN as a function of strain in steps of 0.4 % along the x, y and z direction. The slopes for strain are defined as $(\Delta\omega)/(|\Delta\epsilon|)$ and displayed with the fitting error.

approximately linear relationship with the applied compressive strain. This linear trend is observed for all calculated modes under both compressive and tensile strain in stoichiometric LN and LT, consistent with previous results for LN and LT under hydrostatic pressure as presented by Mendes-Filho *et al.* [21]. In Fig. 5.3(a), the frequency increases by up to 6 cm^{-1}, while in (b) the increase is up to 0.3 cm^{-1}.

The calculations show that in stoichiometric LN and LT, the degeneracy of the E modes is lifted when strain is applied along the x or y direction, due to the reduction of the threefold symmetry. This results in splitting into two branches, consistent with previous studies on various 2D materials that reported mode splitting under symmetry reduction by strain [176, 177]. Therefore, for strain along x and y, all E modes are treated individually. For instance, the E(TO$_9$) mode exhibits pronounced splitting under compression along x and y (see Fig. 5.4(a)). In contrast, for z compression, the E(TO$_9$) mode remains degenerate, as strain along z does not reduce the symmetry. This behavior holds for all E modes of LN and LT under strain.

Since the slopes for strain along the x and y directions in both LN and LT are very similar due to the crystal symmetry (see Appendix A.1.2), Table 5.4 reports only the slopes for strain along the x direction. With the exception of the A$_1$(TO$_1$) and A$_1$(TO$_4$) modes, compressive strain results in an increase in frequency, while tensile strain leads to a decrease, consistent with previous studies on other materials [178, 179]. For LN, the slopes under compressive and tensile strain are nearly identical for each mode, differing

Table 5.4: Calculated slopes of transversal A_1 and E modes of stoichiometric LN under compressive and tensile strain, and stoichiometric LT under compressive strain in the x direction at higher strains in $\text{cm}^{-1}/\%$. The slopes for strain are defined as $(\Delta\omega)/(|\Delta\epsilon|)$.

Phonon mode	LN comp. $[\text{cm}^{-1}/\%]$	LN tens. $[\text{cm}^{-1}/\%]$	LT comp. $[\text{cm}^{-1}/\%]$
$A_1(TO_1)$	0.22	-4.49	3.46
$A_1(TO_2)$	4.45	-3.03	5.08
$A_1(TO_3)$	4.82	-7.18	4.69
$A_1(TO_4)$	6.35	-1.03	3.74
$E(TO_1)$	0.48/4.24	-0.61/-2.81	2.25/1.03
$E(TO_2)$	1.74/-0.14	-2.11/-0.11	0.46/3.59
$E(TO_3)$	1.48/3.27	-3.67/-1.05	3.05/2.82
$E(TO_4)$	4.28/-0.11	-4.49/-0.12	2.58/2.90
$E(TO_5)$	6.20/6.94	-8.90/-13.24	10.76/8.61
$E(TO_6)$	12.80/11.03	-7.62/-4.45	13.64/14.27
$E(TO_7)$	4.18/2.40	0.11/0.15	2.00/1.42
$E(TO_8)$	2.87/-0.55	-7.08/0.70	5.30/3.25
$E(TO_9)$	-0.67/7.06	2.98/-7.02	4.77/4.79

mainly in sign. While this behavior is expected, it is not universal, as shown for a 2D material by Pak *et al.* [178]. Although both $E(TO_5)$ and $E(TO_6)$ modes exhibit the largest frequency shifts under compressive and tensile strain, under compression the $E(TO_6)$ mode has a larger slope than $E(TO_5)$, whereas under tension this order is reversed, as seen in Table 5.4. This trend holds for strain along both x and y directions in LN and LT (see Appenidx A.1.2).

Additionally, Table 5.4 lists the results for LT under compression for the same modes. Direct comparison with LN shows that the values are very similar in both directions and magnitude, consistent with Mendes-Filho *et al.* [21] and expected since LN and LT are isostructural materials. However, some minor differences are present. Notably, the degeneracy lifting is less pronounced in LT compared to LN. For example, the upper branch of the $E(TO_1)$ mode has a much smaller slope in LT. The $E(TO_9)$ mode also shows a much weaker degeneracy lift in LT under compression than in LN. These differences can be understood by considering the eigenvectors shown in Fig. 5.5 for $A_1(TO_{1-4})$ and $E(TO_{1-9})$ modes in the rhombohedral unit cell [164, 173]. Modes with significant vibrational contributions from Nb and Ta ions, such as $E(TO_1)$, display slightly different behavior between LN and LT [164]. In contrast, modes with minimal Nb/Ta contributions in their eigenvectors behave similarly under compression in both materials. For the $E(TO_9)$ mode, where O atom displacements dominate over Nb/Ta, the difference between LN and LT may be attributed to the nature of the Nb/Ta-O bond, as discussed in Refs. [164, 173]. The average Nb-O bond length (2.02 Å) is slightly longer than Ta-O (2.00 Å). Stronger bonding with the oxygen atoms, and thus larger deformation of the oxygen octahedron, may be the reason for differences between

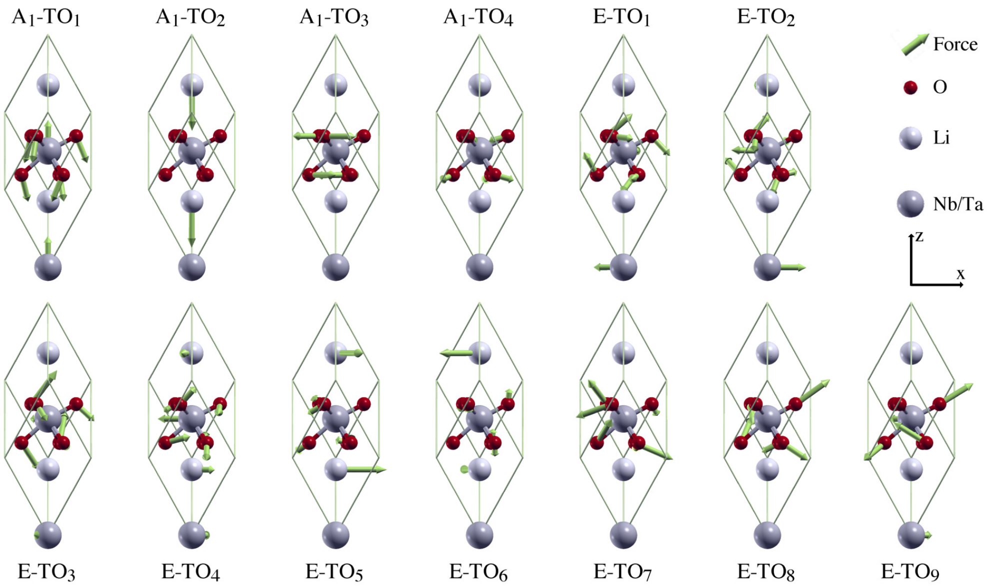

Figure 5.5: The eigenvectors of the Raman active vibrations of unstrained stoichiometric LN and LT in the rhombohedral unit cell of the transversal phonon modes with A_1 and E symmetry. Thereby light grey is denoted as Li, dark grey as Nb/Ta, and red as O ion, while the green arrows represent the displacement direction.

LN and LT concerning the E(TO_9) mode. Similarly, small differences in E(TO_7) and E(TO_8), which are pure oxygen octahedron distortions, may also be related to the different Nb/Ta-O bonding.

For x compression, the theoretical results show that the E(TO_6) mode exhibits a lifting of degeneracy, consistent with Sec. 5.4.3. For a more precise comparison, Table 5.5 lists the slopes for higher strains under y and z compression. The theoretical prediction of degeneracy lifting provides a new perspective for interpreting the experimental data. Specifically, for x compression, the measured $\overline{\mathrm{Z}}$(YY)Z data aligns with the calculated upper branch, while the $\overline{\mathrm{Z}}$(XY)Z and $\overline{\mathrm{Z}}$(XX)Z measurements correspond to the lower branch. For y compression, the situation is reversed: the $\overline{\mathrm{Z}}$(XY)Z and $\overline{\mathrm{Z}}$(XX)Z geometries show the higher slope, and $\overline{\mathrm{Z}}$(YY)Z the lower slope. Thus, by employing different scattering geometries, the experimental data can reproduce the theoretically predicted lifting of degeneracy under x and y compression.

Based on this interpretation, it can be concluded that the experimental and theoretical data fit very well. For a more accurate comparison, the slopes for higher strains for y and z compression are listed in Table 5.5.

Interpreting the experimental data as lifting the degenerate E modes on x and y compression can also help characterize compressed LN. From the data, it can be implied that one has x compressed LN when the $\overline{\mathrm{Z}}$(YY)Z geometry measures a higher slope than for the $\overline{\mathrm{Z}}$(XY)Z and $\overline{\mathrm{Z}}$(XX)Z geometries. If, on the other hand, one has y compressed LN, this argument just reverts. In contrast, if no splitting of E modes is observed in different scattering geometries, it can be concluded that the LN under investigation must be a z-compressed sample. Furthermore, the experimental comparison in Fig. 5.6 and Table 5.5, confirms the prediction that the E(TO_6) mode is the mode with the highest slope for x and y compression.

Table 5.5: Comparison between the theoretical response at higher strains with the experimental response of stoichiometric LN stressed in y direction and 5 % Mg-doped LN stressed in z direction. Asterisks label modes that are Raman silent in the given scattering geometry and the E(TO$_5$) mode since experimentelly a disentanglement of the E(TO$_5$) and E(TO$_6$) mode is not possible.

	sLN-y (cm^{-1}/%)				5Mg-LN-z (cm^{-1}/%)			
Modes	$\overline{\mathrm{Z}}$(XX)Z	$\overline{\mathrm{Z}}$(XY)Z	$\overline{\mathrm{Z}}$(YY)Z	Theory	$\overline{\mathrm{X}}$(ZZ)X	$\overline{\mathrm{X}}$(YZ)X	$\overline{\mathrm{X}}$(YY)X	Theory
A$_1$(TO$_1$)	*	*	*	-0.09	-4.97 ± 0.93	*	-5.10 ± 5.63	-2.97
A$_1$(TO$_2$)	*	*	*	4.46	7.49 ± 1.08	*	5.98 ± 4.73	4.44
A$_1$(TO$_3$)	*	*	*	4.13	4.54 ± 1.24	*	-0.19 ± 1.4	0.65
A$_1$(TO$_4$)	*	*	*	5.70	-4.94 ± 0.65	*	-6.94 ± 0.60	-4.91
E(TO$_1$)	6.27 ± 0.63	5.97 ± 0.63	4.41 ± 0.60	4.05/ 1.48	*	0.40 ± 0.44	-0.15 ± 0.54	-0.61
E(TO$_2$)	5.48 ± 0.35	4.84 ± 0.35	1.56 ± 0.34	-1.30/ 2.55	*	0.61 ± 0.53	1.08 ± 1.51	-2.55
E(TO$_3$)	7.56 ± 1.04	5.81 ± 1.04	4.68 ± 1.07	1.50/ 3.93	*	1.46 ± 1.75	1.44 ± 7.44	0.50
E(TO$_4$)	4.5 ± 0.69	4.44 ± 0.69	2.42± 0.68	0.22/ 3.80	*	5.43 ± 0.92	-3.84 ± 11.74	2.40
E(TO$_5$)	*	*	*	8.79/ 6.30	*	*	*	-0.68
E(TO$_6$)	12.9 ± 1.85	11.13 ± 1.85	9.16 ± 2.02	11.51/ 10.08	*	0.72 ± 2.31	1.90 ± 1.9	-0.94
E(TO$_7$)	3.41 ± 0.68	1.64 ± 0.68	1.23 ± 0.82	4.37/ 1.98	*	7.21 ± 2.64	7.69 ± 0.59	4.75
E(TO$_8$)	8.56 ± 0.48	6.72 ± 0.48	3.27 ± 0.70	-0.61/ 4.83	*	6.73 ± 0.62	6.20 ± 5.94	3.35
E(TO$_9$)	-	-	-	7.18/ -0.67	-	-	-7.95 ± 13.41	0.90

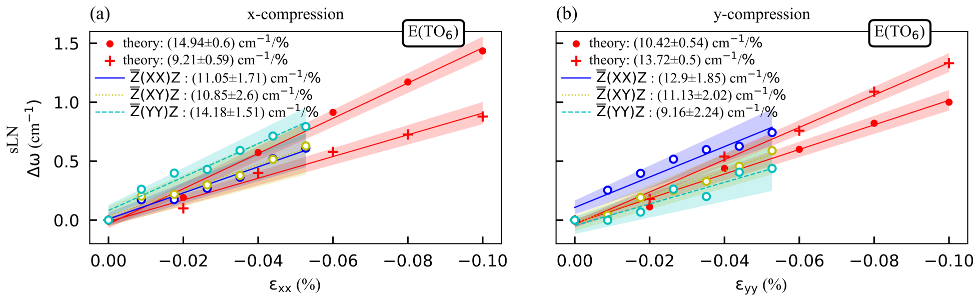

Figure 5.6: Comparison of the experimental and theoretical frequency shift (at lower strains): (a)-(b) E(TO_6) phonon mode under compression along the x and y axes of stoichiometric LN. The shaded region around all the curves is the confidence interval of the linear fit.

As discussed, most phonon mode frequencies increase linearly with increasing compression. However, for certain modes and strain directions such as A_1(TO_4) under z stress, the opposite trend is observed. Both theory and experiment reveal a linear decrease in frequency with increasing z compression (see Fig. 5.7(b)). This unusual behavior can also be explained by the eigenvectors. Figure 5.5 shows that the oxygen ions move toward and then away from the positively charged niobium ions. Under z compression, the reduced cation-cation distance means that, as the oxygen ions move away from niobium, the restoring force from niobium is weakened due to the closer proximity of lithium ions, which also exert a Coulomb force on the oxygen ions. Consequently, the frequency decreases under z compression. A similar argument applies to the A_1(TO_1) mode. Additional results for other modes under z compression are summarized in Table 5.5.

Furthermore, calculations have shown that the degeneracy of the E modes is lifted for x and y compression upon symmetry reduction. The splitting has also been observed in experiments when measured under different scattering geometries. Based on the theoretical and experimental investigations three rules can be formulated to characterize the direction of uniaxial compression of a LN sample using different scattering geometries. This only concerns the E modes. The sample is x compressed if higher frequency shifts are observed for the $\overline{Z}$(YY)Z geometry than for the $\overline{Z}$(XY)Z and $\overline{Z}$(XX)Z geometries when applying the same compressive stress. For y compression, the opposite is the case. In contrast, when no differences are observed between the frequency shift of the E modes for various scattering geometries, it can be concluded that the sample under investigation must be z compressed. Accordingly, the extracted slopes serve as reference values for the observed peak shifts. Using these slopes, one can identify the type of compression in LN crystals, which contributes to understanding the nature of DWs and improves the application of waveguides.

Since LN is an optically nonlinear materials, it is expectable that their nonlinear optical properties depend on strain. Therefore, further studies of strained LN regarding its linear and nonlinear optical responses, could provide deeper insight into the characterization of ferroelectric DWs and piezoelectric devices. For this reason, the following sections will focus on the optical response of these materials as a function of strain.

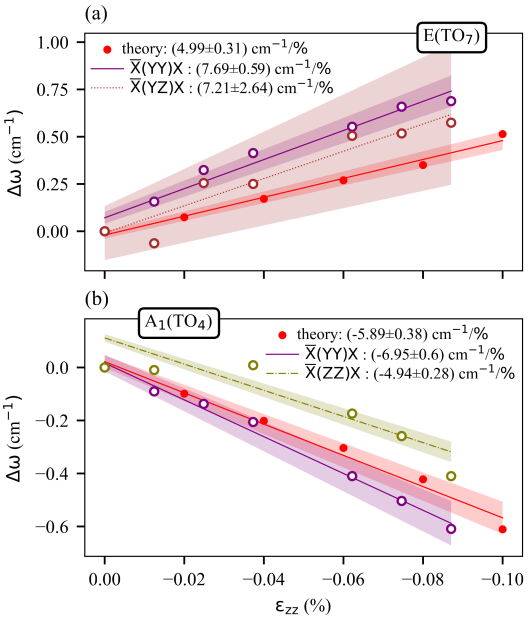

Figure 5.7: Frequency shifts of (a) the E(TO$_7$) and (b) the A$_1$(TO$_4$) mode from the theoretical stoichiometric and experimental 5% Mg-doped LN sample when compressing along the z direction. The E(TO$_7$) mode shows a positive slope while the A$_1$(TO$_4$) shows a negative slope for z compression.

5.5 Optical properties

5.5.1 Theoretical background

The piezo-optic tensor with its piezo-optic coefficients (POCs) π_{im} $[i = 1, ..., 6; m = 1, ..., 6]$ describes the change in the refractive indices with the applied stress on a crystal. This relationship is expressed in the linear regime via

$$\Delta B_i = \pi_{im}\sigma_m, \tag{5.10}$$

whereby $\Delta B_i = \Delta(n_i^{-2})$ with the refractive index n_i is the relative change of the impermeability with applied stress. In turn, the photoelastic tensor p_{in} $[i = 1, ..., 6; n = 1, ..., 6]$ characterizes the change in the refractive indices with the internal strain in a crystal with

$$\Delta B_i = p_{in}\epsilon_n. \tag{5.11}$$

However, since the internal strain is difficult to determine, it is often more convenient to quantify the POCs for experimental measurements [180]. If the piezo-optic and elastic stiffness tensor are known, the photoelastic tensor can be calculated by

$$p_{in} = \pi_{im}c_{mn}. \tag{5.12}$$

For crystals of the $R3c$ space group, the piezo-optic and photoelastic tensor have the following form [5, 165]

$$[\pi_{im}] = \begin{pmatrix} \pi_{11} & \pi_{12} & \pi_{13} & \pi_{14} & 0 & 0 \\ \pi_{12} & \pi_{11} & \pi_{13} & -\pi_{14} & 0 & 0 \\ \pi_{31} & \pi_{31} & \pi_{33} & 0 & 0 & 0 \\ \pi_{41} & -\pi_{41} & 0 & \pi_{44} & 0 & 0 \\ 0 & 0 & 0 & 0 & \pi_{44} & 2\pi_{41} \\ 0 & 0 & 0 & 0 & 2\pi_{14} & \pi_{11}-\pi_{12} \end{pmatrix}, \tag{5.13}$$

$$[p_{in}] = \begin{pmatrix} p_{11} & p_{12} & p_{13} & p_{14} & 0 & 0 \\ p_{12} & p_{11} & p_{13} & -p_{14} & 0 & 0 \\ p_{31} & p_{31} & p_{33} & 0 & 0 & 0 \\ p_{41} & -p_{41} & 0 & p_{44} & 0 & 0 \\ 0 & 0 & 0 & 0 & p_{44} & p_{41} \\ 0 & 0 & 0 & 0 & p_{14} & \frac{p_{11}-p_{12}}{2} \end{pmatrix}. \tag{5.14}$$

In this work, the calculated dispersion of the dielectric function is used to determine the dispersion of the refractive indices under stress and a complete set of piezo-optic. Using Eq. (5.12), as well as the calculated elastic constants in Tab. 5.2 and the POCs, the dispersion of the full set of photoelastic coefficients is predicted.

To describe the change of the second-order nonlinear optical response as a function of stress, the nonlinear photoelastic tensor is introduced. Its definition is given in analogy to the linear optical photoelastic tensor, which quantifies the coupling between the linear optical response and strain. The linear photoelastic effect is expressed by a second-rank tensor [5, 165].

Similarly, the strain-induced contribution to the total nonlinear polarization $\mathcal{P}_i(2\omega)$ $[i = 1, .., 3]$

$$\mathcal{P}_i(2\omega) = \chi^{(2)}_{ijk}(-2\omega; \omega, \omega)\mathcal{E}_j(\omega)\mathcal{E}_k(\omega), \tag{5.15}$$

in the presence of external electric fields $\mathcal{E}_j$ and $\mathcal{E}_k$ $[j, k = 1, .., 3]$ with frequency ω, can be described, to first order, by an additional term in the nonlinear optical susceptibility $\chi^{(2)}_{ijk}$. This additional term is a second-order nonlinear fifth-rank photoelastic tensor $p_{ijkgh} = p_{ijkgh}(-2\omega; \omega, \omega)$ $[i = 1, .., 3; j = 1, .., 3; k = 1, .., 3; g = 1, .., 3; h = 1, .., 3]$. Thus,

$$\chi^{(2)}_{ijk} = \chi^{(2,0)}_{ijk} + p_{ijkgh}\epsilon_{gh}, \tag{5.16}$$

where $\chi^{(2,0)}_{ijk}$ and $\chi^{(2)}_{ijk}$ $[i = 1, .., 3; j = 1, .., 3; k = 1, .., 3]$ denote the second-order susceptibility tensor of the unstrained and strained crystal, respectively [181, 182]. Since both the strain $\epsilon_n = \epsilon_{gh}$ $[n = 1, ..., 6]$ and the second-order susceptibility tensor $d_{i\ell} = \frac{1}{2}\chi^{(2)}_{ijk}$ $[i = 1, ..., 3; \ell = 1, ..., 6]$ can be expressed in contracted notation, the nonlinear photoelastic tensor for SHG is represented as a third-rank tensor $p_{i\ell n}$ $[i = 1, ..., 3; \ell = 1, ..., 6; n = 1, ..., 6]$, such that

$$d_{i\ell} = d^{(0)}_{i\ell} + \frac{1}{2}p_{i\ell n}\epsilon_n. \tag{5.17}$$

Again in analogy to the linear case, a second-order nonlinear piezo-optic tensor of third-rank $\pi_{i\ell m}$ $[i = 1, ..., 3; \ell = 1, ..., 6; m = 1, ..., 6]$ can be introduced to describe the coupling of the nonlinear optical response to the stress tensor σ_m $[m = 1, ..., 6]$, i.e., for the description of the stress-induced SHG:

$$d_{i\ell} = d_{i\ell}^{(0)} + \frac{1}{2}\pi_{i\ell m}\sigma_m, \tag{5.18}$$

by inserting

$$\epsilon_n = s_{nm}\sigma_m, \tag{5.19}$$

where s_{nm} $[n = 1, ..., 6; m = 1, ..., 6]$ is the elastic compliance tensor, and using the definition

$$\pi_{i\ell m} = p_{i\ell n}s_{nm}. \tag{5.20}$$

5.5.2 Computational details

The electronic ground state calculations are performed within DFT using the Quantum Espresso package [45, 46] applying the same setup as in Sec. 5.3. The GGA functional [88] with the PBEsol modification [90] is used to accurately describe structural and mechanical properties. The resulting lattice constants show excellent agreement with Ref. [5], with deviations of 0.255 % in the rhombohedral lattice constant and 0.007 % in the angle.

To model the linear and nonlinear optical response of the strained crystals, uniaxial stress is applied from −3 GPa to 3 GPa in steps of 1 GPa in all Cartesian directions, respectively. The corresponding strain tensor for the stress values is indicated in Table 5.1. With the additional calculation of the linear optical response under shear stress, i.e. for $\sigma_4 \neq 0 = \sigma_1 = \sigma_2 = \sigma_3 = \sigma_5 = \sigma_6$, the complete photoelastic properties are obtained. As the linear regime for shear stress is an order of magnitude smaller than for uniaxial stress, shear stresses of −0.1 GPa and 0.1 GPa are applied.

The optical response, i.e., $\mathrm{Re}[\epsilon]$ and $\mathrm{Im}[\epsilon]$ as well as $\mathrm{Re}\left[\chi^{(2)}\right]$ and $\mathrm{Im}\left[\chi^{(2)}\right]$, is calculated in a real-time approach as implemented in Yambo [47–49], in which the dynamical polarization is defined in the Berry-phase formulation as described in Sec. 3.3. This method has already been successfully applied to unstrained stoichiometric LN [25]. All optical calculations are done with a $13 \times 13 \times 13$ k-point mesh without symmetry constraints, ensuring well-converged optical spectra. To obtain the optical spectrum, a series of 64 simulations of 47 fs each for a monochromatic electric field at the pump wavelength in a photon energy range from 0.2 eV to 4 eV (6200 nm to 310 nm) is carried out. Since all optical calculations are performed within the IPA, the band gap is underestimated, resulting in a red-shift of the optical spectra. In this work, only the electronic contributions to the susceptibility are considered. Although this introduces some inaccuracies in the low-energy region of the spectra, the relative changes in susceptibility remain reliable. For SHG, the absolute values of the real and imaginary parts of the susceptibility are discussed.

Since LN belongs to the $3m$ point group, it has four independent SHG components with $d_{15} = d_{24}$, $d_{31} = d_{32}$, d_{33}, and $d_{22} = d_{21} = d_{16}$ [24]. In fact, the calculations for unstrained LN show four independent SHG components. Yet non vanishing values (although generally small) for d_{34}, d_{35}, d_{36}, d_{32} and d_{25} are calculated. Moreover, d_{24} is

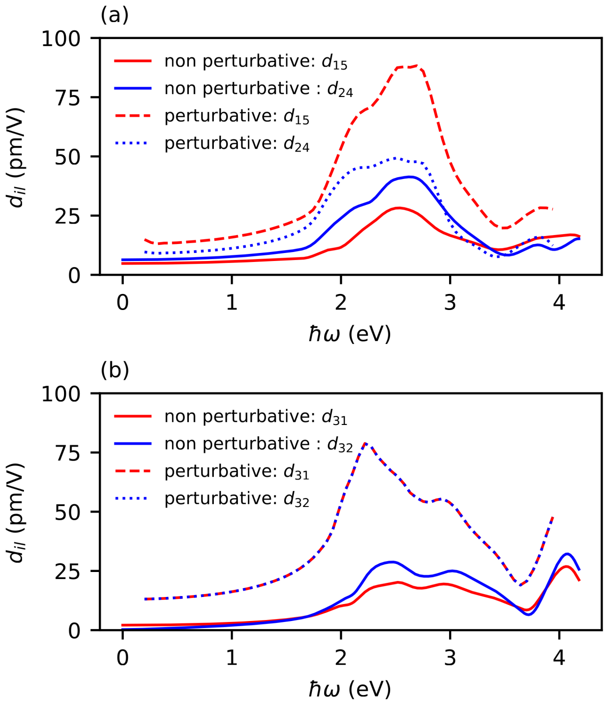

Figure 5.8: Calculated dispersion of (a) d_{15} and d_{24}, and (b) d_{31} and d_{32} with the sum of two-band contribution (non perturbative approach) and in a real-time approach (perturbative approach). In (b) the non pertubative approach yields the same result for d_{31} and d_{32}.

not equal to d_{15} and seems to be damped (see Fig. 5.8 and Fig. A.2). In order to check this issue, optical nonlinearities are also calculated using the perturbative approach of Riefer *et al.* [183] (see Appendix A.1.3). In this approach, the wave functions and eigenvalues, calculated in the VASP code [44], are postprocessed. The computational details for the calculation of these wave functions are described in the Appendix A.1.3. The SHG is obtained from the two-band contribution from Eq. (3.22) in the framwork of the pertubtaive approach from Sec. 3.2 derived from Refs. [98, 184, 185]. The absolute SHG values determined by VASP are somewhat smaller than those of Yambo as can be seen in Fig. 5.8. However, the nonvanishing SHG components calculated with the real-time, non perturbative approach are also non-vanishing in the calculations performed with the frequency based, perturbative approach, excluding issues in the code implementation (see Fig. 5.8 and Appendix A.1.3). Hence, the real-time approach as implemented in Yambo is used for the investigation of the SHG under stress and is considered as reliable. The inconsistent SHG components can be attributed to numerical issues caused by the missing phononic contributions in the applied IPA caluclations, and are not further discussed in this work. In the next sections the results of the optical properties under uniaxial stress from Refs. [P2, P3] are summarized.

5.5.3 Results: Piezo-optic coefficients

Based on the calculated dielectric function, the refractive indices are determined as a function of the excitation energy under uniaxial stress in the Cartesian directions

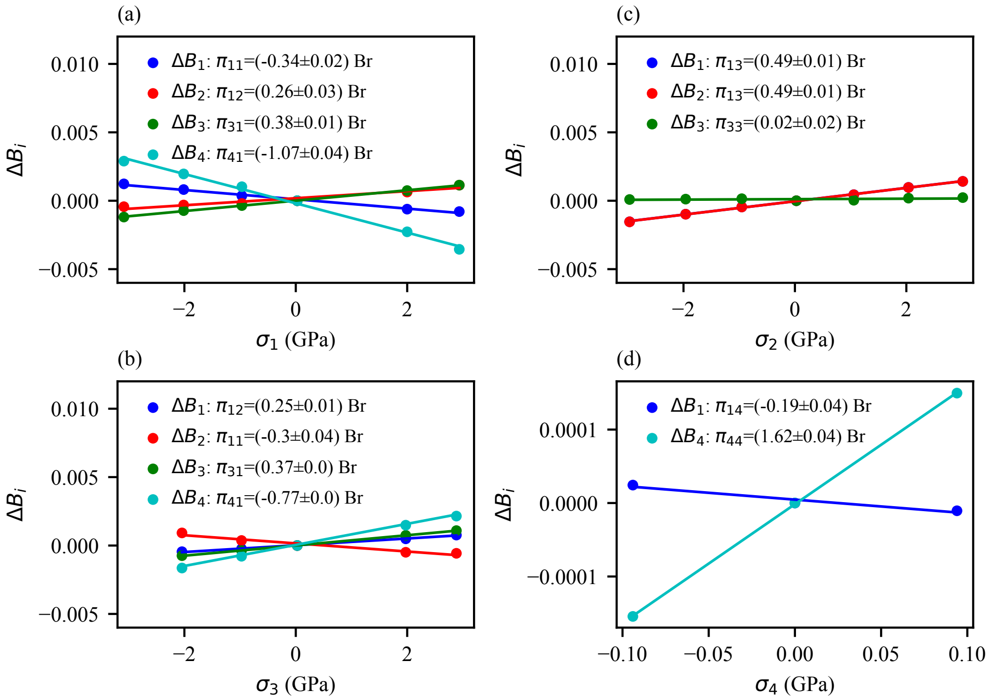

Figure 5.9: Calculated relative impermeability ΔB_i for 626 nm under uniaxial stress in (a) x, (b) y and (c) z direction and (d) shear stress. The POCs are determined by the slope of the linear fit.

and shear stress. Typically, the refractive indices and birefringence are measured at an excitation wavelength of 633 nm. Therefore, for the verification of the calculated results, the optical properties are discussed for a wavelength of 626 nm from the calculated series as it is closest to the experimental wavelengths. The calculated refractive indices and birefringence of unstrained LN at 626 nm are $n_\mathrm{o} = 2.390$, $n_\mathrm{e} = 2.264$ and $\Delta n = -0.126$, and in reasonable agreement with the experimental values at 633 nm at room temperature ($n_\mathrm{o}^\mathrm{exp} = 2.2910$, $n_\mathrm{e}^\mathrm{exp} = 2.2005$, $\Delta n^\mathrm{exp} = -0.0905$) [5].

Figure 5.9 shows the impermeabilities as a function of uniaxial stress in the respective Cartesian directions and shear stress for 626 nm. The impermeabilities change roughly linearly for both compressive and tensile stress. The POCs are obtained via the impermeabilities under uniaxial stress and Eq. (5.10) [see Fig. 5.9]. As already shown in Ref. [P1] by the lifting of the degeneracy of the E modes of LN, the threefold rotational symmetry of the crystal is broken by stress in x or y direction. In linear optics, the symmetry lowering results in the lifting of the degenerate ordinary dielectric function under x and y stress. Due to the anistropy of x and y axis (see Sec. 5.1), LN is transformed by x and y stress from a uniaxial to a biaxial crystal in the xy-plane. This is also mirrored by $\pi_{11} \neq \pi_{12}$. The B_1 decreases under x stress and B_2 decreases under y stress by approximately the same amount. In addition, B_2 increases under x stress and B_1 increases under y stress by a similar amount. The reason for this is that LN belongs to the $R3c$ space group [5], which is why $\pi_{12} = \pi_{21}$ applies to the piezo-optic coefficients. For the same reason, it holds $\pi_{31} = \pi_{23}$. Thus, B_3 increases by the same amount for uniaxial stress in x and y direction.

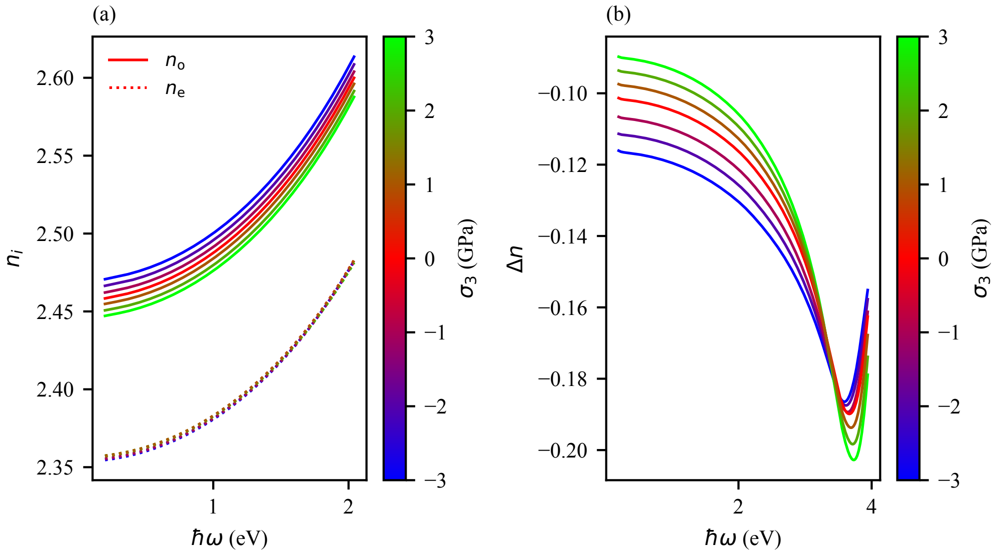

Figure 5.10: DFT calculated dispersion of the (a) ordinary (dashed lines) and extraordinary (solid lines) refractive index and (b) birefringence for uniaxial stresses in z direction from $-3\,\text{GPa}$ to $3\,\text{GPa}$ in steps of $1\,\text{GPa}$.

It is also shown in Ref. [P1] that stress in the z direction does not lower the symmetry of LN, and does not lift the degeneracy of phonon modes with E symmetry. This is also in agreement with the results of this study, as the ordinary refractive index remains degenerate under stress in z direction and, therefore, LN remains a uniaxial crystal, as can be seen in Fig. 5.9(c). Under stress in z direction, the ordinary refractive index decreases, while the extraordinary refractive index barely changes. In turn, this implies that the change in birefringence is mainly determined by the change in the ordinary refractive index, except for the sign, as can be seen from the slopes in Figs. 5.9(c) and 5.10(a) and (b). Figure 5.10(a) shows the dispersion of the two refractive indices under z stress. Again, it can be seen that it is mainly the ordinary refractive index that changes with applied z stress. Figure 5.10(b) demonstrates the dispersion of birefringence. Since the birefringence is mainly determined by the change in the ordinary refractive index, it increases at excitation energies of up to $3.3\,\text{eV}$ with the application of uniaxial stress in z direction. Close to the minimum, which is slightly blue-shifted with z stress, this behavior reverses.

The resulting POCs at 626 nm are summarized in Tab. 5.6 alongside values from Refs. [186, 187]. Since the error in the slope from the linear fit to B_2 in Figs. 5.9(a) and (b) is significantly larger than for B_1, only the π_{11} and π_{12} values obtained from the B_1 fit are discussed in Tab. 5.6 and hereafter. Similarly, the magnitude of π_{41} from Fig. 5.9(b) is reported in Tab. 5.6. The larger deviation from linearity for B_2 may be due to the approximate validity of the linear relationship between B_2 and σ_1/σ_2 up to $3\,\text{GPa}$ or $-3\,\text{GPa}$. Aside from this, the error bars in Fig. 5.9 indicate that all other impermeability and stress tensor components exhibit a strictly linear relationship. Using the calculated POCs and the elastic stiffness tensor from Tabs. 5.2 and 5.6, the photoelastic tensor is obtained via Eq. (5.12). The resulting photoelastic coefficients are compared with Refs. [188, 189] in Tab. 5.7. Both the calculated piezo-optic and photoelastic co-

Table 5.6: Calculated POCs π_{im} (in Brewster, 1 Br= 10^{-12} m^2/N) for 626 nm in comparison with Ref. [186, 187] for 633 nm at room temperature averaged over different symmetry-equivalent sample geometries.

π_{im} [Br]	This work	Ref. [186]	Ref. [187]
π_{11}	-0.34	-0.38	-0.47
π_{12}	0.25	0.09	0.11
π_{13}	0.49	0.80	2.00
π_{31}	0.37	0.50	0.47
π_{33}	0.02	0.20	1.60
π_{14}	-0.19	-0.81	0.70
π_{41}	-0.77	-0.88	-1.90
π_{44}	1.62	2.25	0.21

Table 5.7: Calculated photoelastic coefficients p_{in} for 626 nm in comparison with Ref. [188, 189] for 633 nm at room temperature.

p_{in}	This work	Ref. [188]	Ref. [189]
p_{11}	-0.021	-0.021	0.036
p_{12}	0.064	0.060	0.072
p_{13}	0.108	0.172	0.092
p_{31}	0.097	0.142	0.178
p_{33}	0.055	0.118	0.088
p_{14}	-0.017	-0.052	-
p_{41}	-0.090	-0.109	0.155
p_{44}	0.078	0.121	-

efficients show good agreement with literature. The present results confirm the POCs from Ref. [186], except for π_{12} and π_{33}, which show larger deviations. Nevertheless, π_{33} is also much smaller than π_{13} in Ref. [186], indicating that the birefringence change is mainly governed by the ordinary refractive index, which must decrease under z stress since $0 < \pi_{13}$. Thus, the ratio $0 < \pi_{13} - \pi_{33}$ reflects the increase in birefringence with z stress, consistent with the behavior shown in Fig. 5.10.

The photoelastic coefficients are determined directly by the Dixon-Cohen method [190] in Ref. [189] and by piezo-optic measurements using Eq. (5.12) in Ref. [188]. The main difference between Ref. [188] and Ref. [189] is the sign of p_{11} and p_{41} as ultrasonic methods like the Dixon-Cohen technique are ambiguous in the determination of the sign of the photoelastic coefficients. The photoelastic coefficients calculated in this work confirm the negative sign of p_{11}, p_{14} and p_{41}.

The piezo-optic and photoelastic coefficients are calculated not only for an excitation wavelength of 626 nm, but also their dispersion in the step size explained in Sec. 5.5.2. These are displayed in Fig. 5.11. The component p_{13} has a saddle point between 3.4 eV and 3.6 eV. All other components have an extremum between 3.5 eV and 3.8 eV, which

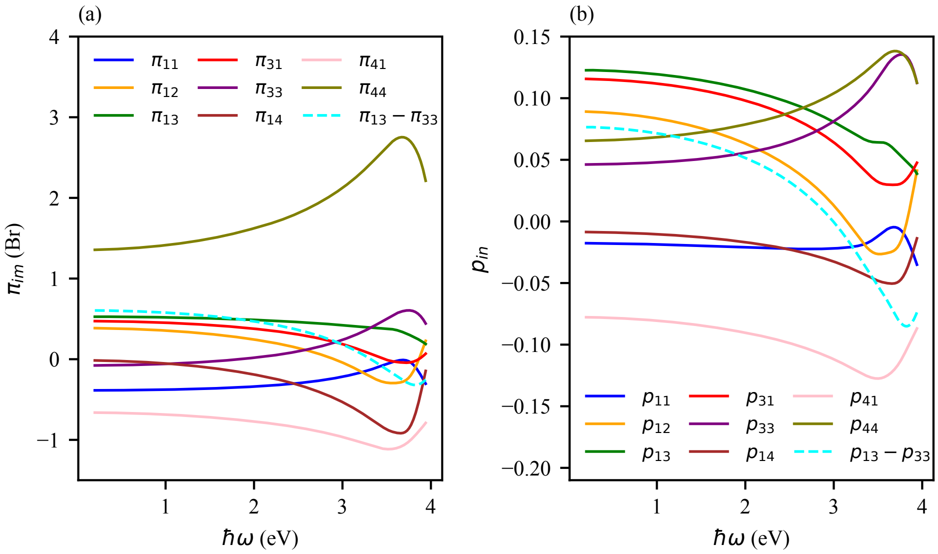

Figure 5.11: DFT computed (a) piezo-optic and (b) photoelastic coefficients as function of the excitation energy.

is related to the electronic band gap of 3.5 eV that has been reproduced using IPA. Since the change in birefringence is indicated by $\pi_{13} - \pi_{33}$ and $p_{13} - p_{33}$, these are additionally plotted in Fig. 5.11. On the one hand, up to an excitation energy of about 3 eV respectively 3.3 eV under uniaxial strain respectively stress, the birefringence increases. On the other hand, its change decreases in this range. In turn, from 3.0 eV respectively 3.3 eV, the birefringence decreases under uniaxial strain respectively stress in z direction. Its change has a maximum at around 3.8 eV. This behavior under z stress for different excitation energies corresponds to the calculated dispersion of the birefringence for different z stresses in Fig. 5.10.

5.5.4 Results: Second-order nonlinear piezo-optic coefficients

Figure 5.12 shows the calculated dependence of the different SHG components on the applied strain and compares it with the measured values from a colaboration as published in Ref. [P3]. In the experiment, the same apparatus as in Ref. [P1] is used, which allows the measurement of the SHG components under uniaxial stress. For the measurements, a LN thin film of 600 nm is used. Since the surface effects of such a thin film containing several hundreds of unit cells is minimal, comparison with theoretical results obtained for pure LN bulk crystals is reasonable. For more details on the experimental setup, see Refs. [P1, P3]. The SHG components change linearly for small stresses, in accordance to Refs. [181, 182, 192, 193]. In Fig. 5.12 the calculated SHG components for an excitation wavelength of 933 nm is shown, which is the calculated excitation closest to the experimental laser (950 nm). The measured components are extrapolated by a linear fit, and plotted as a function of the stress in each Cartesian direction as well. The extrapolated linear fits of the experimental data show the same stress dependence of the calculated data, although the magnitude of the components shows some deviation.
The calculated absolute values of the SHG tensor components for the unstrained crystal

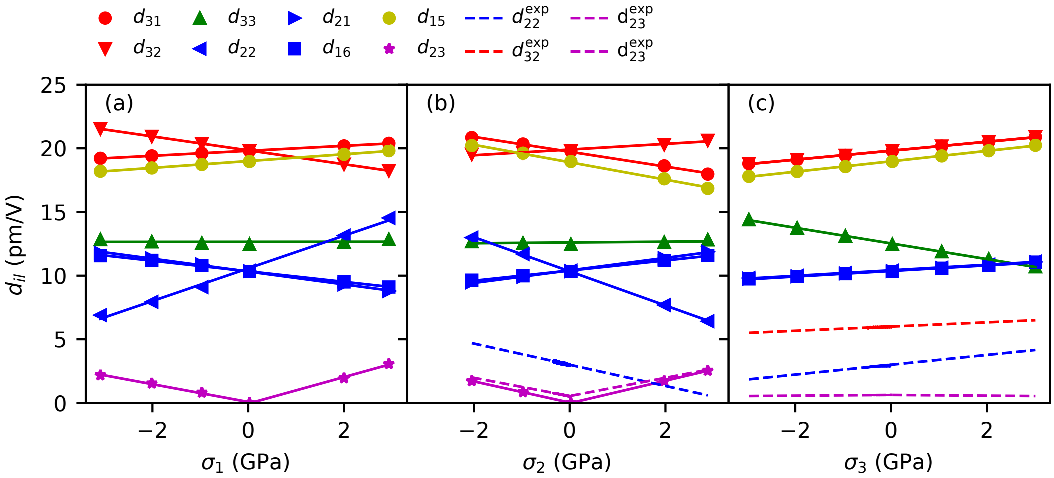

Figure 5.12: Calculated and measured SHG components with linear fits for 933 nm (theory) and 950 nm (experiment) under uniaxial stress in (a) x, (b) y and (c) z direction. The experimentally determined SHG components are normalized using Ref. [191]. (a) m point group symmetry with $d_{21} = d_{16}$. (b) m point group symmetry with $d_{21} = d_{16}$. (c) $3m$ point group symmetry with $d_{31} = d_{32}$ and $d_{22} = d_{21} = d_{16}$.

differ somewhat from literature values [191, 194–197] (see Appendix A.1.3). While the ratio between d_{22} and d_{31} is in reasonable agreement with reported values, the calculated d_{33} component does not exhibit the largest magnitude, in contrast to experiment, as shown in Fig. 5.12. Notably, Riefer *et al.* [183] also found a similar ratio of d_{33} to the other components in their IPA calculations. Since this work focuses on the relative changes in SHG under uniaxial stress, more advanced computational methods beyond the IPA are not applied.

As shown in previous studies [P1–P3] (see Sec. 5.4.3 and 5.5.3), applying stress along the z direction maintains the crystal symmetry. Consequently, four independent SHG components are observed, as illustrated in Fig. 5.12(c). The identities for $\pi_{i\ell 3}$ listed in Table 5.8 follow from the symmetry properties of the crystal under uniaxial z stress, consistent with Ref. [182]. The d_{24} component is not discussed in detail here, but it is expected that d_{24} and d_{15} remain equal under uniaxial z stress, i.e., $\pi_{243} = \pi_{153}$, due to the preserved symmetry [182].

In contrast, the C_{3v} symmetry is reduced by stress in x and y direction, again in agreement with previous investigations, which reported a lifting the degeneracy of the Raman active E modes [P1] as well as on the splitting of the ordinary refractive index [P2]. Due to the symmetry reduction under x and y strain, the crystal symmetry changes into the m point group with the mirror plane perpendicular to the y axis. The predicted reduction of a crystal from $3m$ to m point group symmetry under x and y strain is also in agreement with Ref. [182]. Also Mennel *et al.* have reported a symmetry reduction under mechanical strain in 2D crystals which is reflected in their resulting polarization-reflecting SHG patterns [192, 193]. When studying SHG under uniaxial stress in x and y direction, the symmetry reduction becomes evident by splitting the identical SHG components as shown in Figs. 5.12(a) and (b). For the m point group the SHG tensor has ten independent elements [24]. Indeed, the number of the independent elements is

Table 5.8: The relation between the uniaxial stress direction and the resulting crystal symmetry with its corresponding independent nonzero SHG and piezo-optic coefficients for $3m$ point group symmetry. The discussed tensor elements are represented as bold indices. All other tensor elements and identities are not discussed in this work but are expected to be nonzero. The nonlinear second-order susceptibility tensors for the m and $3m$ point group are expressed in detail in Appendix A.1.3.

Components of σ_m	Crystal symmetry	Nonzero components of $d_{i\ell}$	Nonzero components of $\pi_{i\ell m}$
1, 2	m	**22**, **21**, **23**, 24, **15**, **16**, **32**, **31**, **33**, 34	241 = **152**, 242 = **151**, **321** = **312**, **322** = **311**, **332** = **331**, **211** = −**212**, **221** = −**222**, **161** = −**162**, **231** = **232**, 341, 342
3	$3m$	**15** = 24, **31** = **32**, **33**, **22** = **21** = **16**	243 = **153**, **323** = **313**, **333**, **163** = **213** = **223**

increased as can be seen in Figs. 5.12(a) and (b). These are exactly the independent components which are expected for a crystal with m point group symmetry. The d_{24} and the d_{34} component are also expected to behave as independent components, but are not taken into account in the discussion.

In particular, the d_{23} component, which is vanishing at 0 GPa due to the crystal symmetry, appears under x and y stress. Both for compressive as well as tensile stress, the calculated d_{23} value increases linearly with roughly the same gradient. The appearing of d_{23} is also in agreement with the measurements which observe a non zero value for the d_{23} component (see Fig. 5.12(b)) confirming the symmetry reduction experimentally.

From previous studies, it is known that DWs in LN behave in first approximation as the compressed bulk [15, 18]. The SHG contrast at the DWs of LN has been investigated, as well [20, 26, 198]. Hence, from the results of SHG under stress conclusions can be drawn concerning the DWs in LN. Especially, it is expected that new tensor elements occur at the DWs due to symmetry reduction. This is in agreement with the appearing d_{23} component. From the comparison of the calculated slopes under x and y stress and in agreement with Ref. [182], the identities shown in Table 5.8 for $\pi_{i\ell 1}$ and $\pi_{i\ell 2}$ can be concluded as a property of the crystal symmetry, which reduces from the $3m$ to the m point group under x and y stress.

In Table 5.9 the calculated and measured independent nonlinear POCs derived from the linear fits in Fig. 5.12 are shown for an excitation wavelength of 933 nm and 950 nm, respectively. The calculated nonlinear POCs are close to the determined experimentally obtained values. Especially, the d_{22}, d_{31} and d_{23} components have the largest change under stress in y direction. In particular, the calculations show, that the π_{222} component

Table 5.9: Calculated and measured nonlinear POCs $\pi_{i\ell m}$ (in pmV^{-1}GPa^{-1}) for 933 nm and 950 nm obtained from the linear fit of Fig. 5.12. The experimental coefficients are normalized using Ref. [191]. Since d_{23} is zero in the unstressed case, the sign of π_{232} and π_{233} could not be experimentally determined and an alternative normalization procedure was performed. The corresponding values are marked with an asterisk.

$\pi_{i\ell m}$ [pmV^{-1}GPa^{-1}]	Theory	Exp.
π_{151}	0.54	–
π_{211}	-1.01	–
π_{161}	-0.83	–
π_{152}	-1.37	–
π_{332}	0.06	–
π_{312}	-1.17	–
π_{222}	-2.68	-1.7 ± 1.0
π_{232}	$-1.67/1.77$	$\pm 1.4^{*} \pm 1.1$
π_{322}	0.45	–
π_{153}	0.82	–
π_{223}	0.43	0.8 ± 0.5
π_{233}	0.00	$\pm 0.06^{*} \pm 0.08$
π_{323}	0.70	0.32 ± 0.15
π_{333}	-1.23	–

has the highest absolute value compared to all other components for y stress. Furthermore, the change of the d_{33} component, i.e. π_{333}, is the largest for uniaxial stress in z direction.

In the following, the calculated dispersion of the SHG and nonlinear POCs is discussed as they mirror the crystal symmetry as indicated in Table 5.8. As the spectra of d_{31} and d_{32} show many features under uniaxial stress, Fig. 5.13(a)-(c) shows exemplary the calculated dispersion of the d_{31} and d_{32} component for different stress values. As with Riefer *et al.* [183], the main features of unstrained LN are also in the range between 1.5 eV and 3 eV. The peaks of the SHG components and the ratios between each other, as well as the components in the visible range roughly correspond to those of Riefer *et al.* (see Fig. 5.13 and Appendix A.1.3). In particular, the d_{31} component of the unstrained LN has a peak at about 2 eV as in Ref. [183]. This peak is linearly blue-shifted and the intensity increased when LN is tensile stressed in z direction as can be seen in Fig. 5.13(c). To a similar amount, the peak is red-shifted and reduced in its intensity with compression in z direction. Since LN remains in the $3m$ point group under z stress, the dispersions of d_{31} and d_{32} are the same in Fig. 5.13(c). For the d_{31} component, the changes in the peaks are very high compared to the other components which are shown in Appendix A.1.3.

When the crystal is stressed along the x or y direction, the symmetry of LN is reduced to the m point group and, therefore, identical compenents as d_{31} and d_{32} are split as already mentioned above. The dispersion of the SHG components under uniaxial stress is shown in Figs. 5.13(a) and (b). Moreover, the identities of Table 5.8 hold also for

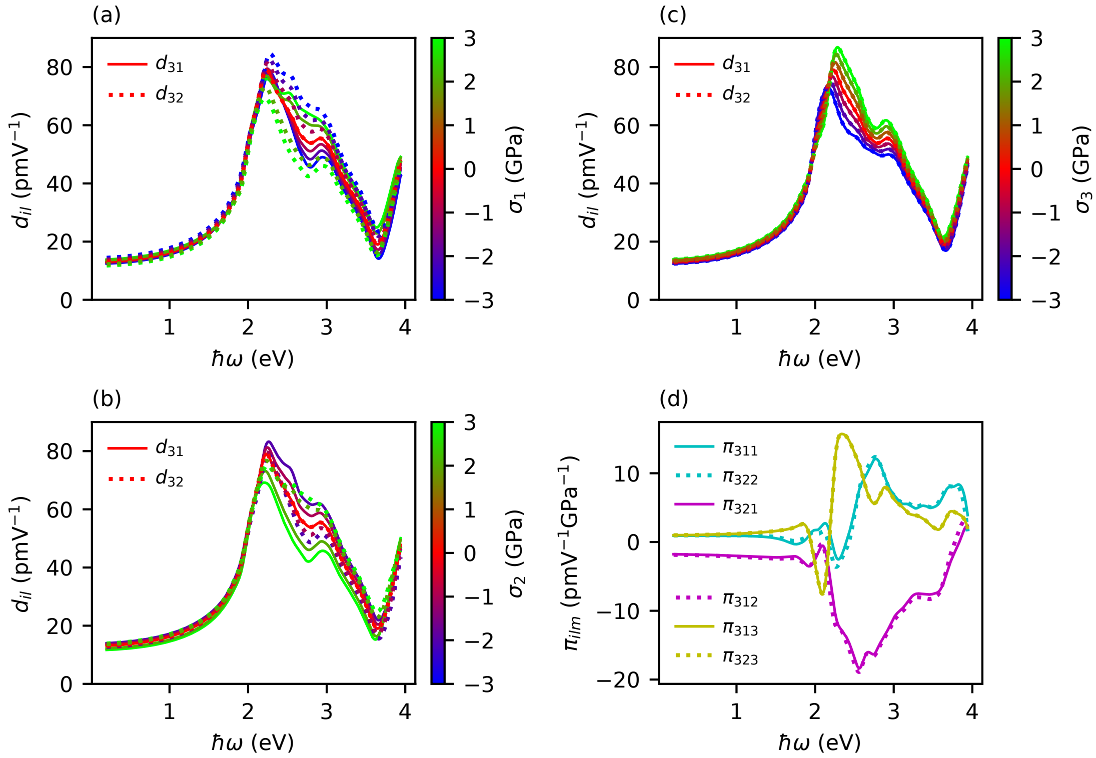

Figure 5.13: DFT computed dispersion of d_{31} and d_{32} under uniaxial stress in (a) x, (b) y and (c) z direction as well as (c) the dispersion of π_{311}, π_{322}, π_{321}, π_{312}, π_{313} and π_{321}.

the dispersion of the SHG components. From the dispersion of the SHG components under uniaxial stress, the dispersion of the nonlinear POCs can be concluded according to Eq. (5.18), as well. In Fig. 5.13(d) the dispersion of three independent POCs, derived from the dispersion of Figs. 5.13(a)-(c), are shown. Indeed, the identities of Table 5.8 hold except from some small deviations for example π_{311} and π_{322} at around 2 eV due to numerical issues. Up to 1.5 eV, which is the range of major technical relevance, the displayed coefficients are roughly constant. For z stress, the first peak of the d_{31} and d_{32} component changes the most. Due to the shift of this peak at around 2 eV, the maximum of the π_{313} and π_{323} for the corresponding excitation energy is obtained. The d_{32} and d_{31} component for x and y stress, respectively, have a growing local maximum at around 2.5 eV. As a result the π_{321} and π_{312} components yield a maximum for this excitacion energy. On the other hand, the local minimum at around 2.8 eV is shrinking for the d_{31} and d_{32} component under x and y stress, respectively. As a result, for π_{311} and π_{322} a maximum at around 2.8 eV can be derived. The dispersion of the other POCs is shown in the Appendix A.1.3.

5.6 Coherent anti-Stokes Raman spectroscopy

5.6.1 Theoretical background

In contrast to spontaneous Raman scattering, CARS is a third-order nonlinear optical process in which pump (ω_p) and Stokes (ω_s) fields coherently excite a vibrational mode ν at $\Omega_\nu \approx \omega_\mathrm{p} - \omega_\mathrm{s}$. A probe field at frequency ω_pr then scatters inelastically from this vibrational coherence, giving rise to anti-Stokes emission at [199, 200]:

$$\omega_\mathrm{as} = \omega_\mathrm{p} - \omega_\mathrm{s} + \omega_\mathrm{pr}. \tag{5.21}$$

Usually, the same laser is employed for the pump and probe fields, such that $\omega_\mathrm{p} = \omega_\mathrm{pr}$, and Eq. (5.21) reduces to $\omega_\mathrm{as} = 2\omega_\mathrm{p} - \omega_\mathrm{s}$ (see Fig. 5.14). The CARS spectral intensity can be written as [201]

$$\begin{aligned} I_\mathrm{CARS}(\omega) \propto \Big| \iiint \chi^{(3)}(\omega; \omega_\mathrm{p}, -\omega_\mathrm{s}, \omega_\mathrm{pr}) \mathcal{E}_\mathrm{p}(\omega_\mathrm{p})\, \mathcal{E}_\mathrm{s}^*(\omega_\mathrm{s})\, \mathcal{E}_\mathrm{pr}(\omega_\mathrm{pr}) \\ \cdot \delta(\omega - \omega_\mathrm{p} + \omega_\mathrm{s} - \omega_\mathrm{pr})\, \mathrm{d}\omega_\mathrm{p}\, \mathrm{d}\omega_\mathrm{s}\, \mathrm{d}\omega_\mathrm{pr} \Big|^2, \end{aligned} \tag{5.22}$$

where $\chi^{(3)}$ is the third-order susceptibility and $\mathcal{E}_\mathrm{p}$, $\mathcal{E}_\mathrm{s}$, and $\mathcal{E}_\mathrm{pr}$ are the spectral amplitudes of the pump, Stokes, and probe fields, respectively. Here, the Stokes field enters as a complex conjugate amplitude $\mathcal{E}_\mathrm{s}^*(\omega_\mathrm{s})$ because the CARS process annihilates a Stokes photon while creating pump, probe, and anti-Stokes photons (see Fig. 5.14). Equation (5.22) can be recast into a more compact form [201]:

$$I_\mathrm{CARS}(\omega) \propto \left| \{ C_\mathrm{st}(\omega)\, \chi^{(3)}(\omega) \} * \mathcal{E}_\mathrm{pr}(\omega) \right|^2, \tag{5.23}$$

where $*$ denotes convolution, and $C_\mathrm{st}(\omega) = [\mathcal{E}_\mathrm{s}(\omega) \star \mathcal{E}_\mathrm{p}(\omega)]$ is the coherent stimulation profile given by the cross-correlation $\star$ of the Stokes and pump spectra.

For a spectrally narrow probe and slowly varying instrumental response, the intensity can be approximated as

$$I_\mathrm{CARS}(\omega) \simeq |C(\omega)\, \chi^{(3)}(\omega)|^2, \tag{5.24}$$

where $C(\omega)$ is an effective instrumental factor that incorporates the coherent stimulation profile, the probe spectrum, and the frequency-dependent detection efficiency of the setup (e.g., optics, spectrometer, and detector response). In experiments, $C(\omega)$ must be determined or calibrated in order to obtain quantitative CARS spectra. In theoretical calculations, the instrumental factor is set $C(\omega) \equiv 1$.

It is convenient to separate the susceptibility into resonant and nonresonant parts [201]:

$$\chi^{(3)}(\omega) = \chi^{(3)}_\mathrm{R}(\omega) + \chi^{(3)}_\mathrm{NR}(\omega). \tag{5.25}$$

The resonant part $\chi^{(3)}_\mathrm{R}$ arises from vibrational Raman-active modes (see Fig. 5.14(b)). For a single mode ν of frequency Ω_ν and damping Γ_ν [199, 200]:

$$\chi^{(3)}_{ijkl,\mathrm{R}}(-\omega_\mathrm{as}; \omega_\mathrm{p}, -\omega_\mathrm{s}, \omega_\mathrm{pr}) = \sum_\nu \frac{N_\nu}{\Omega_\nu - (\omega_\mathrm{p} - \omega_\mathrm{s}) - i\Gamma_\nu} \left(\frac{\partial \alpha_{ij}}{\partial Q_\nu} \right) \left(\frac{\partial \alpha_{kl}}{\partial Q_\nu} \right), \tag{5.26}$$

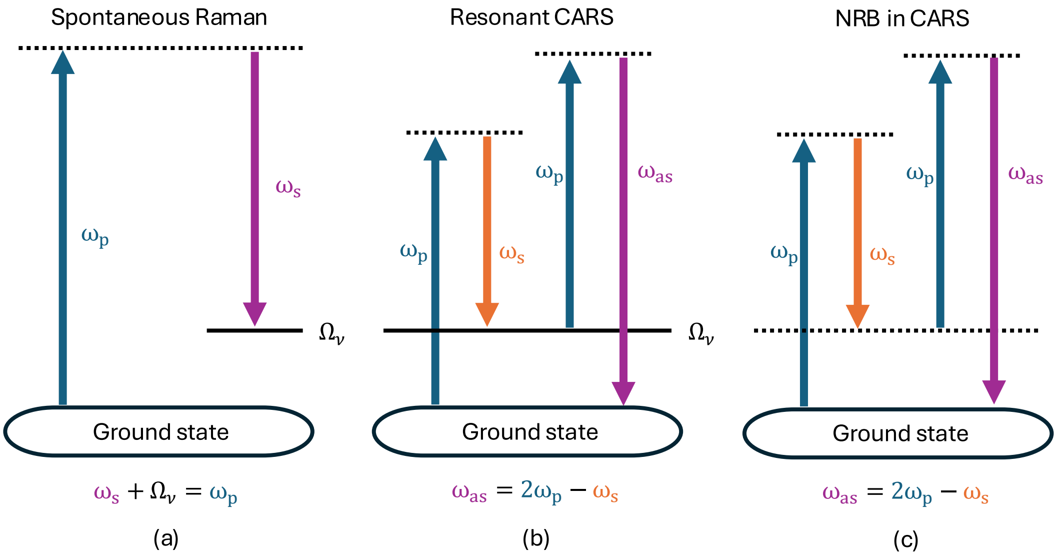

Figure 5.14: A schematic representation of: (a) spontaneous Raman, (b) resonant coherent anti-Stokes Raman scattering (CARS) and (c) nonresonant background (NRB) in CARS.

where Ω_ν and Γ_ν are frequency and damping of mode ν, N_ν is the oscillator density, Q_ν is the normal coordinate, and $\partial\alpha/\partial Q_\nu$ are the Raman tensor elements for mode ν. Compared to spontaneous Raman scattering, Eq. (5.26) contains the product of two Raman tensors because the vibrational coherence is both created by the pump-Stokes pair and read out by the probe field in a coherent four-wave-mixing process. In contrast, in spontaneous Raman the scattering intensity is proportional to the modulus square of a single Raman tensor. As a result, the resonant part can be calculated by determining the Raman tensor from first-principles approaches like the frozen-phonon method as presented in Sec. 2.6 or density functional perturbation theory (DFPT) [45, 46].
The nonresonant part $\chi^{(3)}_{\mathrm{NR}}$ originates from virtual electronic four-wave mixing pathways [199, 200] (see Fig. 5.14(c)). Far from electronic resonances, it is slowly varying with frequency [59]. Since the nonresonant part can be considered as a combination of different virtual processes like SFG and DFG, the approach of Ref. [P5] presented in Sec. 4 can be used to calculate the nonresonant part of the third-order susceptibility. For this purpose, the Fourier coefficients with $n = 2$ and $m = -1$ need to be determined from Eq. (4.14).
The interference between $\chi^{(3)}_{\mathrm{R}}$ and $\chi^{(3)}_{\mathrm{NR}}$ can be seen explicitly in $|\chi^{(3)}|^2 = |\chi^{(3)}_{\mathrm{NR}} + \chi^{(3)}_{\mathrm{R}}|^2 = |\chi^{(3)}_{\mathrm{NR}}|^2 + |\chi^{(3)}_{\mathrm{R}}|^2 + 2\,\mathrm{Re}[\chi^{(3)}_{\mathrm{NR}}{}^{*}\chi^{(3)}_{\mathrm{R}}]$. Far from electronic resonances $\chi^{(3)}_{\mathrm{NR}}$ is slowly varying and essentially real, so the cross term has a asymmetric line shape [65].
The labeling for the CARS polarization configurations follows the notation for spontaneous Raman scattering, where the first set of parentheses indicates the polarization of the incident fields (pump, probe, and Stokes) and the second set indicates the polarization of the detected anti-Stokes field. The propagation direction is indicated by the indices outside the parentheses. Since the theoretical models are independent of the propagation direction, only the polarization configurations are indicated for theoretical CARS spectra.

5.6.2 Computational details

The CARS spectra are computed by evaluating Eq. (5.26) for the resonant contribution and using the methodology described in Sec. 5.5.2 for the nonresonant part. For the resonant part, phonon eigenvectors and frequencies are obtained via DFPT as implemented in Quantum Espresso [45, 46], employing the same computational parameters and strained structures as in Sec. 5.5.2. Raman tensors are determined using finite displacement calculations, with atomic displacements of 0.01 Å along each Cartesian axis, and the same computational setup as previously described. The dielectric tensor is evaluated from the DFT wave functions and eigenvalues, considering 65 electronic states to ensure convergence within 1 %. This yields the Raman tensors for all phonon modes at the Γ point which can be inserted into Eq. (5.26) to obtain the resonant part of the third-order susceptibility. The phonon lifetimes Γ_ν and oscillator densities N_ν are not calculated in this work, and the resonant part is only known up to a scaling factor. For the resonant part, the Raman spectrum is drawn using Gaussian smearing with an arbitrary width of $10\,\mathrm{cm}^{-1}$ corresponding to a typical measured line-width.

For the nonresonant part, the approach described in Ref. [P5] is employed, where the Fourier coefficients with $n = 2$ and $m = -1$ are extracted from Eq. (4.14). The same computational parameters as in Sec. 5.5.2 are used, with a less dense $8 \times 8 \times 8$ k-point mesh to reduce computational cost for test calculations. As this work is a collaboration with experimental CARS measurements, the pump and probes energies are chosen at 1.165 eV to match the experimental conditions.

5.6.3 Results

The calculated nonresonant part of the third-order susceptibility component $\chi^{(3)}_{xxxx}$ of unstrained LN is shown in Fig. 5.15(a). The raw data (points) exhibit some numerical noise, which is smoothed using an exponential fit (solid lines) in the frequency range relevant for CARS measurements (0.541 eV to 1.652 eV). The real part of $\chi^{(3)}_{xxxx}$ is negative and decreases with increasing frequency, while the imaginary part is positive and increases with frequency. The nonresonant part is then combined with the resonant contribution, calculated using Eq. (5.26) and the Raman tensors obtained from DFPT. The resulting CARS spectrum for the (xxx, x) polarization configuration of stoichiometric LN is presented in Fig. 5.15(b), alongside experimental $y(xxx, x)y$ CARS data from congruent LN (R. Buschbeck, private communication, 2025). Since the derivative of the polarizability with respect to the normal coordinate is only known up to a scaling factor, and the oscillator density N_ν and lifetimes Γ_ν are not determined, the absolute magnitude of the resonant part is unknown. Therefore, both the resonant and nonresonant contributions are normalized to the experimental data. Since the square of the sum of the resonant and nonresonant part determines the CARS intensity, three terms contribute: the resonant part squared, the nonresonant part squared, and the interference term. The latter is responsible for the asymmetric line shapes as also discussed in Ref. [65]. Since the resonant part is proportional to the Raman tensor, it is expected that the relative intensities of the phonon modes in the calculated CARS spectrum correspond to those in the Raman spectrum. Indeed, the calculated CARS spectrum reproduces the main features of the $y(x, x)y$ spontaneous Raman spectrum from Ref. [164]. For this geometry

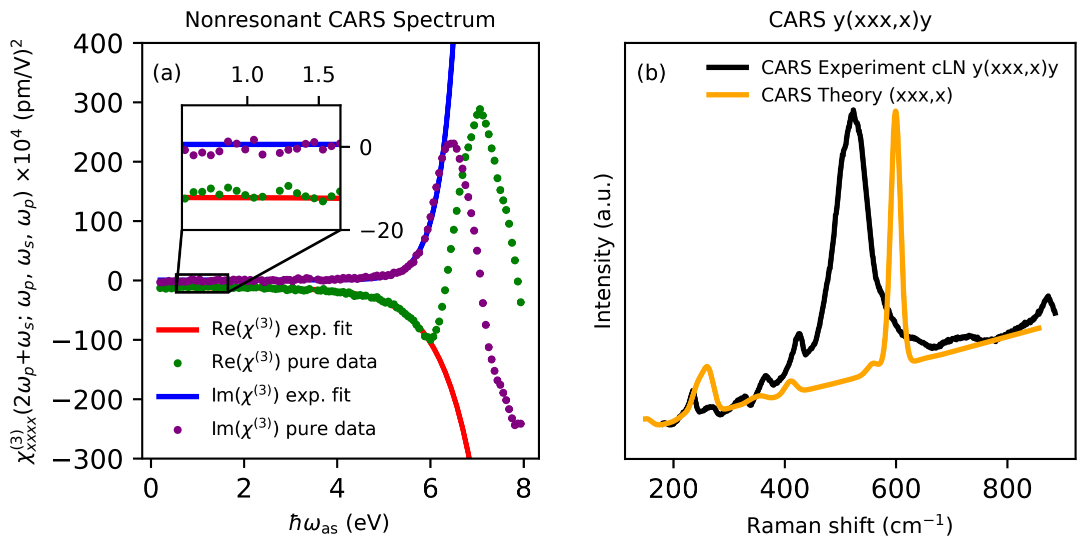

Figure 5.15: (a) Real and imaginary part of the susceptibility component $\chi^{(3)}_{xxxx}$ of NRB in CARS of unstrained LN calculated with the approach of Sec. 4. The points indicate the calculated raw values. The solid lines correspond to an exponential fit to smooth the data in the range between 0.541 eV and 1.652 eV where the CARS measurements are performed. (b) Calculated (xxx, x) CARS spectrum of stoichimetric LN in comparison with experimental $y(xxx, x)y$ CARS spectrum of congruent LN. The calculated CARS spectrum is obtained by the absolute square of the sum of the resonant and nonresonant part which is obtained from the fit in the inset of (a). Since the absolute value of the resonant part is not known, the resonant and nonresonant part are normalized to the experimental data.

A_1 TO and E LO modes are expected to be observed. However, LO-TO splitting is not captured since it is compuationally more expensive. As a result, only the A_1 TO modes are seen in the calculated CARS spectrum. Especially, the strong $A_1(TO_4)$ mode at 600 cm^{-1} and the weaker $A_1(TO_{1-3})$ modes between 240 cm^{-1} and 350 cm^{-1} are well reproduced in comparison the spontaneous Raman spectrum from Ref. [164]. Although the $A_1(TO_{1-3})$ modes are in a good agreement also with the experimental CARS spectrum, there is a dominating peak at around 520 cm^{-1} with a very large width in the experimental CARS spectrum which might be a LO mode corresponding to another polarization configuration mixed in the CARS spectrum due to slight misalignment of the sample. In accordance to Hempel *et al.* [65], the small shoulder at around 630 cm^{-1} can be assigned to the $A_1(TO_4)$ mode. Moreover, the last peak at around 870 cm^{-1} which can be classified as $E(LO_9)$ mode is missing in the calculated CARS spectrum. The calculated CARS spectrum shown in Fig. 5.15(b) represents the first attempt to theoretically model a CARS spectrum for a crystalline solid. Although many assumptions and approximation have to be made, the calcuated data is in good agreement with the experiment and allows fot the interpretation of the measured data. Since the calculation of the nonresonant part is very time consuming in relation to the resonant part and the peaks of the CARS spectrum are mainly determined by the resonant part, only the resonant part is calculated under strain in the following. It is assumed that strain does not significantly modify the nonresonant contribution, since $\chi^{(3)}_{\mathrm{NR}}$ is evaluated in the low-frequency, non-dispersive regime, far from electronic resonances. In this regime, strain is expected to affect at most the overall magnitude of $\chi^{(3)}_{\mathrm{NR}}$ (i.e., the slowly varying background), but not to introduce additional resonant features or new peaks in the CARS spectrum.

Due to the lack LO-TO splitting in the present calculations, there is only one configuration that can be properly compared with the experimental CARS data, namely the (zzz, z) configuration, where only A_1 TO modes are expected. The calculated resonant CARS spectra of stoichiometric LN under uniaxial stress between -2 % and 2 % in x, y and z direction are shown in Fig. 5.16, along with experimental $y(zzz, z)y$ CARS spectra from congruent LN off and on a x wall (R. Buschbeck, private communication, 2025). In the theoretical spectra, the $\mathrm{A}_1(\mathrm{TO}_1)$ mode at around 250 cm^{-1}, as well as the $\mathrm{A}_1(\mathrm{TO}_4)$ mode at around 600 cm^{-1}, are clearly visible. This is in agreement with the theoretical and experimental spontaneous Raman spectra from Ref. [164]. In the experimental CARS spectrum, small peaks between 240 cm^{-1} and 350 cm^{-1} are visible which can be assigned to the $\mathrm{A}_1(\mathrm{TO}_{1-3})$ modes and one large peak at around 520 cm^{-1} (which appears in all experimental spectra, see Appendix A.1.4), which seems to be the same as in the previous experimental CARS spectrum shown in Fig. 5.15(b). The fact that this peak appears in this configuration as well supports the assumption that this peak corresponds to another polarization configuration mixed in the CARS spectrum caused by a misalignment of the sample. The corresponding peak has a shoulder at around 630 cm^{-1} which is already assigned to the $\mathrm{A}_1(\mathrm{TO}_4)$ mode. On the DW the peak at around 520 cm^{-1} disappears and the shoulder at around 630 cm^{-1} becomes more pronounced. This result fits well to the calculated CARS spectra under strain, where the intensity of the $\mathrm{A}_1(\mathrm{TO}_4)$ mode is increasing under uniaxial tension in x or y direction. The calculated resonant CARS spectra of all other configurations under uniaxial stress in x, y and z direction are shown in Appendix A.1.4.

The attentive reader may ask: Why is the $y(zzz, z)y$ configuration the only one where only TO modes are expected? According to the selection rules shown in Table 5.3, there is also the $y(x, z)y$ or the $z(x, y)z$ configuration where only TO modes are expected. Are the selection rules of spontaneous Raman from Table 5.3 not transferable to CARS? The answer is yes and no: According to Eq. (5.26), the resonant part of the third-order susceptibility is proportional to the product of two Raman tensors, which, respectively, obey the selection rules of spontaneous Raman scattering. However, the product of two (in general different) Raman tensors can yield nonzero contributions in polarization configurations that are forbidden in spontaneous Raman scattering. For example, in the $y(xxx, z)y$ configuration, the resonant CARS signal arises from the product of Raman tensor elements α_{xx} and α_{xz}. As a consequence, different symmetry species can contribute simultaneously to a given polarization configuration, so that, for instance, both A_1 and E modes can overlap in the same spectral region. Hence, while the selection rules for spontaneous Raman provide a useful guideline, the actual polarization dependence of CARS can be more complex due to the involvement of multiple Raman tensor elements. Since the resonant part is proportional to the product of two Raman tensors, CARS is also not symmetric under exchange of the polarizations of the incident and scattered light, in contrast to spontaneous Raman scattering. For instance,

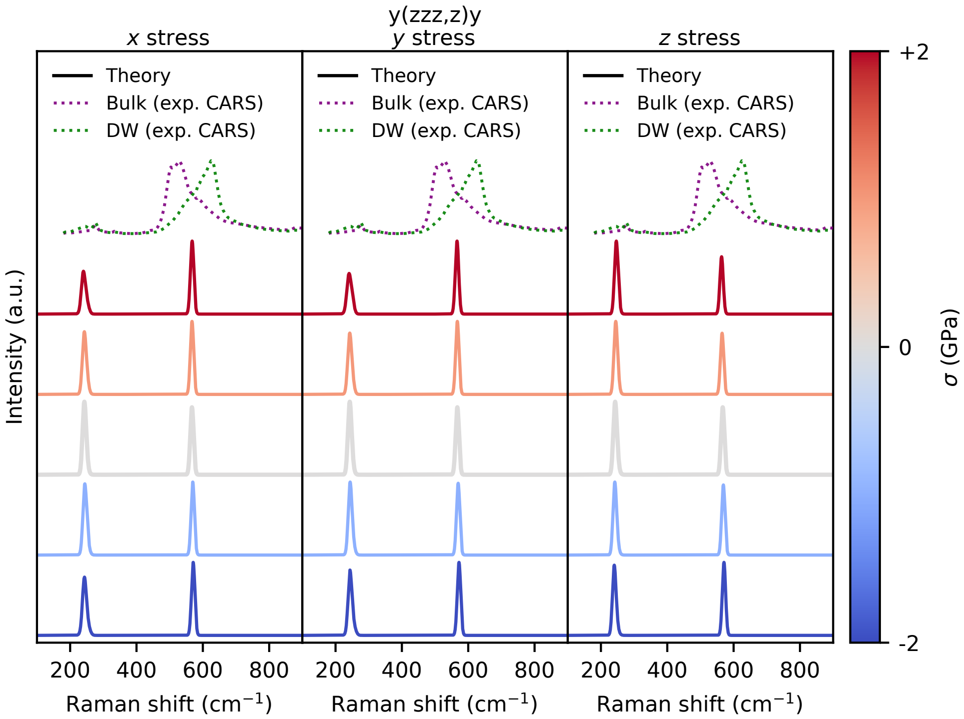

Figure 5.16: Calculated (zzz, z) resonant CARS spectrum of stoichiometric LN under uniaxial stress between -2 % and 2 % in x, y and z direction. The calculated intensities are drawn with an arbitrary Gaussian broadening of 10 cm^{-1}. The dotted lines indicate the $y(zzz, z)y$ experimental CARS spectrum of congruent LN off and on the domain wall (R. Buschbeck, private communication, 2025).

the $y(xxx, z)y$ configuration is not equivalent to the $y(zzz, x)y$ configuration, as can be seen in the calculated as well as measured CARS spectra in Appendix A.1.4.

As already seen in Fig. 5.16, the raw $y(xxx, z)y$ CARS spectrum exhibits a very broad and intense feature around 520 cm^{-1}, superimposed on the sharper phonon resonances. Additional insight can be gained by applying a phase-retrieval (PR) procedure to these experimental CARS data, following the approach of Camp *et al.* [201]. In the transformed $y(xxx, z)y$ spectrum (see Fig. 5.17), the peak positions and relative intensities of the phonon modes are in much better agreement with the calculated CARS spectrum, while the very broad feature around 520 cm^{-1} is strongly reduced and no longer appears as a distinct resonance. At the same time, the phonon modes between 200 cm^{-1} and 400 cm^{-1} become the dominant features. In this frequency range the calculated spectrum is governed by overlapping A$_1$ and E modes, and the transformed experimental spectrum reflects this behavior. A further key observation from the comparison between bulk and DW spectra is the emergence of a new, well-defined peak at approximately 630 cm^{-1} at the DW, which can be assigned to the A$_1$(TO4) mode and is essentially absent in the corresponding bulk response. This is fully consistent with the above considerations, mentioning that the shoulder at around 630 cm^{-1} becomes more pronounced at the DWs. The same trend is reproduced in the calculated spectra under strain, where the intensity of the A$_1$(TO4) peak at 630 cm^{-1} shows a pronounced and systematic dependence on the applied strain. Altogether, these findings indicate that the large, broad

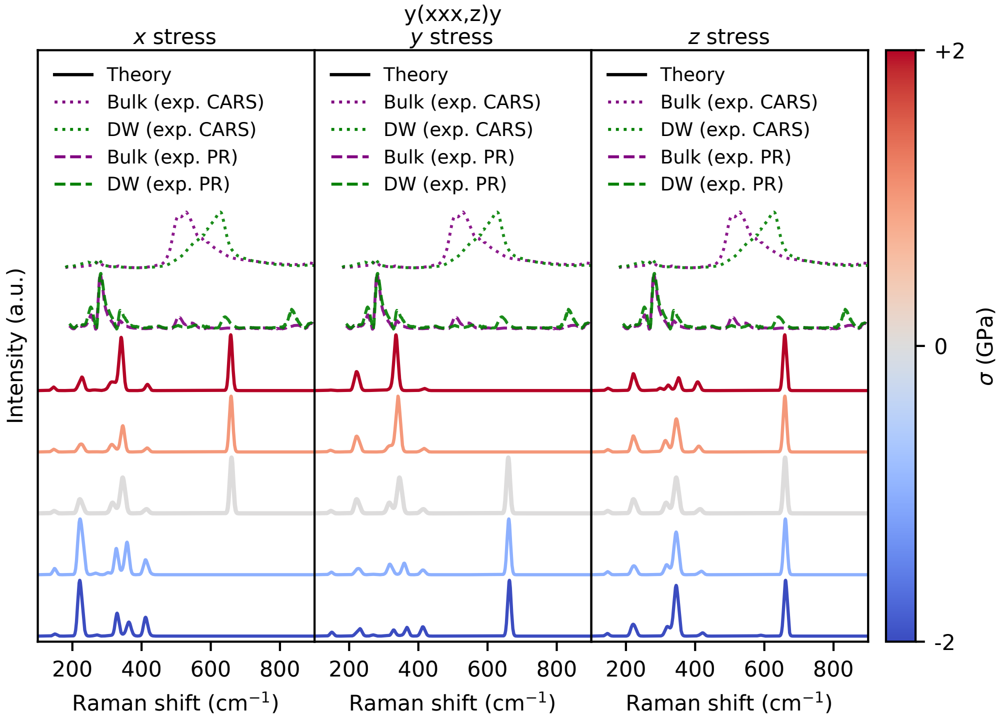

Figure 5.17: Calculated (xxx, z) resonant CARS spectrum of stoichiometric LN under uniaxial stress between -2 % and 2 % in x, y and z direction. The calculated intensities are drawn with an arbitrary Gaussian broadening of 10 cm^{-1}. The dotted lines indicate the $y(xxx, z)y$ experimental CARS spectrum of congruent LN off and on the domain wall. The dashed lines indicate the $y(xxx, z)y$ experimental phase-retrieval (PR) spectrum of congruent LN off and on the domain wall (R. Buschbeck, private communication, 2025).

peak at about 520 cm^{-1} in the raw CARS spectra of the bulk is neither of resonant nor of purely nonresonant vibrational origin, but is instead dominated by the experimental detector function $C(\omega)$, which includes, for instance, frequency-dependent detection efficiency and phase-matching effects. In the theoretical modeling this function is set to $C(\omega) \equiv 1$, such that these setup-specific contributions are absent and only the intrinsic vibrational contribution to $\chi^{(3)}$ is retained. However, the quantitative details of the PR spectrum inevitably depend on the choice of parameters entering the PR procedure (e.g., the specifics of the Kramers-Kronig implementation), as discussed in detail by Camp *et al.* [201]. The overall picture of a detector function-dominated feature around 520 cm^{-1} and dominant overlapping A$_1$ and E modes between 200 cm^{-1} and 400 cm^{-1} is thus robust, even though fine intensity ratios should be interpreted with appropriate caution, and the microscopic origin of the broad structure near 520 cm^{-1} cannot yet be regarded as completely and unambiguously resolved. All other comparisons of the theoretical resonant CARS spectra with the experimental PR spectra are shown in Appendix A.1.4. In addition, to the sepctrum shown in this section, the PR $z(xxx, y)z$ and $z(yyy, x)z$ spectra fit very well to the theoretical resonant CARS spectra. Thus, deeper knowledge of the interplay between resonant CARS, nonresonant background, and experimental setup is required for a better understanding of the experimental and theoretical CARS spectra.

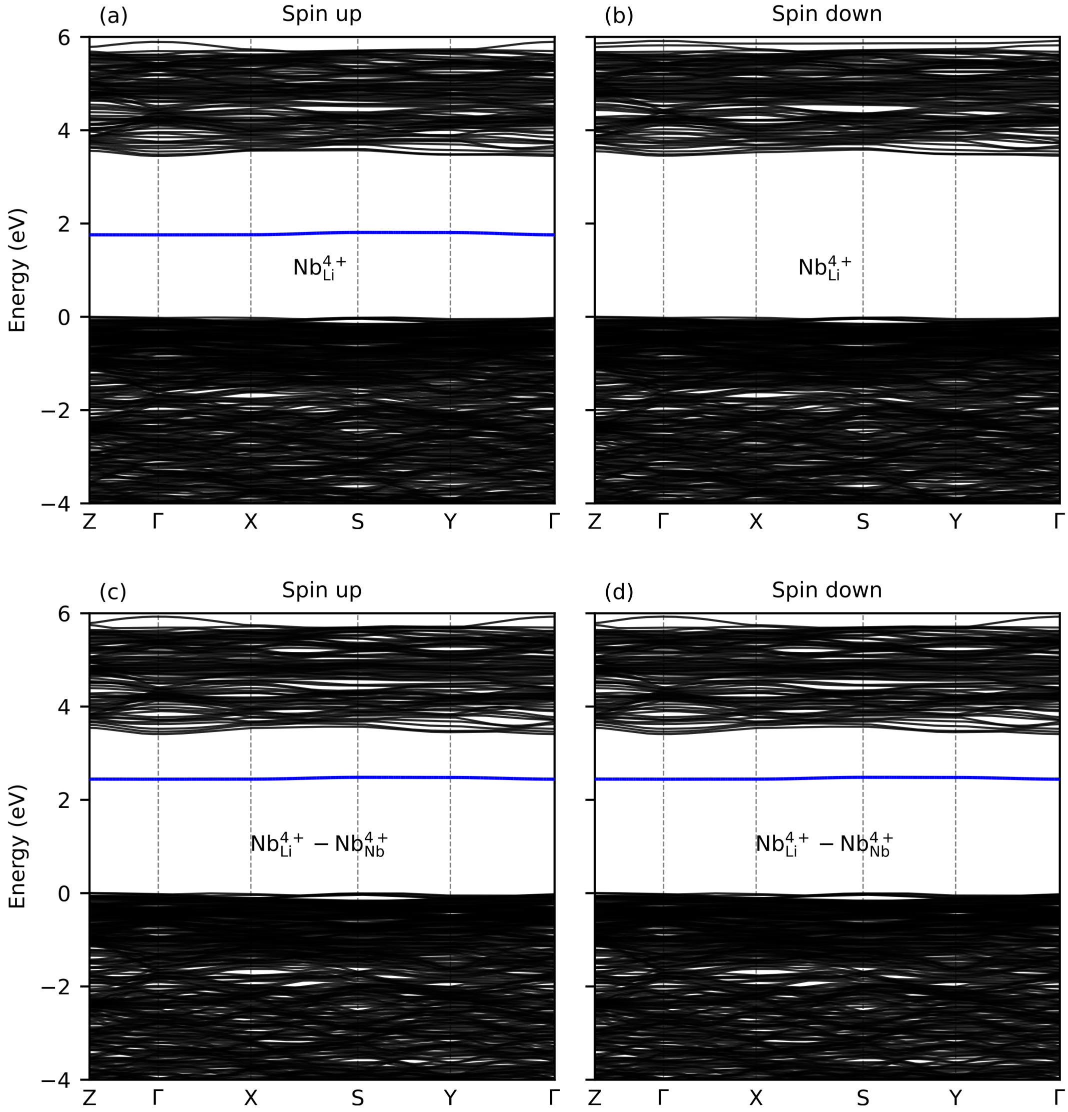

Figure 5.18: Electronic band structures in (a) and (b) of the $\mathrm{Nb}_{\mathrm{Li}}^{4+}(4d^1)$ small bound polaron and (c) and (d) of the $\mathrm{Nb}_{\mathrm{Li}}^{4+}$–$\mathrm{Nb}_{\mathrm{Nb}}^{4+}(4d^1 - 4d^1)$ bipolaron in LN. The localized electronic state related to the polaron is plotted in blue (spin up channel in (a) and spin up and down channel in (c) and (d)).

5.7 Polaronic properties

5.7.1 Theoretical background

In LN, excess electrons can become self-trapped through strong coupling to the surrounding lattice, forming small polarons. These play a crucial role in the electronic transport properties of the material. In particular, the occurrence of polaronic defects at ferroelectric CDWs might be a key mechanism responsible for the enhanced conductivity observed in these regions [37, 39, 202].

Especially, the $\mathrm{Nb_{Li}}$ antisite, where a niobium atom occupies a lithium site, is one of the dominant defects in LN and occurs in large concentrations in congruent LN, which is grown under Nb-rich conditions. This defect can occur in different charge and spin states depending on the electron occupation of the Nb $4d$ orbitals [37, 39, 202]:

- The neutral $\mathrm{Nb_{Li}^{5+}}$ defect with an empty $4d^0$ state,
- The $\mathrm{Nb_{Li}^{4+}}$ small bound polaron with one localized electron in the $4d^1$ state 5.18(a) and (b),
- And the $\mathrm{Nb_{Li}^{4+}}$–$\mathrm{Nb_{Nb}^{4+}}$ bipolaron, with two electrons in the $4d^1 - 4d^1$ shared between neighboring Nb ions 5.18(c) and (d).

On the one hand, the small bound polaron can appear with axial symmetry, where the electron is localized around the $\mathrm{Nb_{Li}}$ site in a shape of a dumbbell oriented along the z axis, reflecting the crystal symmetry of LN. One the other hand, the small bound polaron can relax to lower energy-tilted associated with a quasi-Jahn-Teller distortion, in which the local threefold rotational symmetry is broken (see Fig. 5.19(d)). This distortion leads to a further local lattice relaxation that stabilizes the polaronic state. The bipolaron is formed by a pair of bound electrons from the $\mathrm{Nb_{Li}}$ antisite defect and the regular neighboring $\mathrm{Nb_{Nb}}$ site, and retains its axial symmetry (see Fig. 5.19(e)) [39]. While the structure and energetics of these defects in unstrained LN are well established, their behavior under external strain is less understood. This is particularly relevant for CDWs, where strong internal strain fields and symmetry breaking might alter defect stabilities and affect polaron formation.

Therefore, the relative formation energies of the neutral $\mathrm{Nb_{Li}^{5+}}$, the small bound polaron $\mathrm{Nb_{Li}^{4+}}$, and the bipolaron $\mathrm{Nb_{Li}^{4+}}$–$\mathrm{Nb_{Nb}^{4+}}$ under uniaxial strain applied along the crystallographic x, y, and z directions are computed in this work. This serves as a first step toward understanding how strain influences the thermodynamic stability of polarons, and in turn, how such effects might enable charge transport along CDWs via polaron hopping mechanisms.

5.7.2 Computational details

Strain is modeled following the approach of Refs. [P1–P3]. Compressive strain is applied from 0 to 2.4 % in increments of 0.8 %. Calculations use a Γ-centered 4 × 6 × 4 k-point mesh and a 2 × 1 × 1 orthorhombic supercell containing 120 atoms, corresponding to a Li:Nb ratio of 92 %, which is close to the congruent composition. Previous studies by Nahm and Park [168] and Sanson *et al.* [169] have demonstrated that the DFT+U formalism of Cococcioni and de Gironcoli [92] accurately describes the strongly localized d electrons in Nb defects. Therefore, a DFT+U approach is employed with an empirical Hubbard parameter $U_{\text{eff}} = U - J = 4$ eV [168, 169] for the Nb d electrons. The defect formation energy E_f for a defect X in charge state q is calculated as [203, 204]:

$$E_f(X^q) = E^{\text{total}}(X^q) - E^{\text{total}}(\text{bulk}) + \sum_i n_i\mu_i + q(E_F + E_v + \Delta V) \tag{5.27}$$

where $E^{\text{total}}(X^q)$ and $E^{\text{total}}(\text{bulk})$ are the total energies of the supercell with and without the defect, and n_i and μ_i are the number and chemical potential of species i added

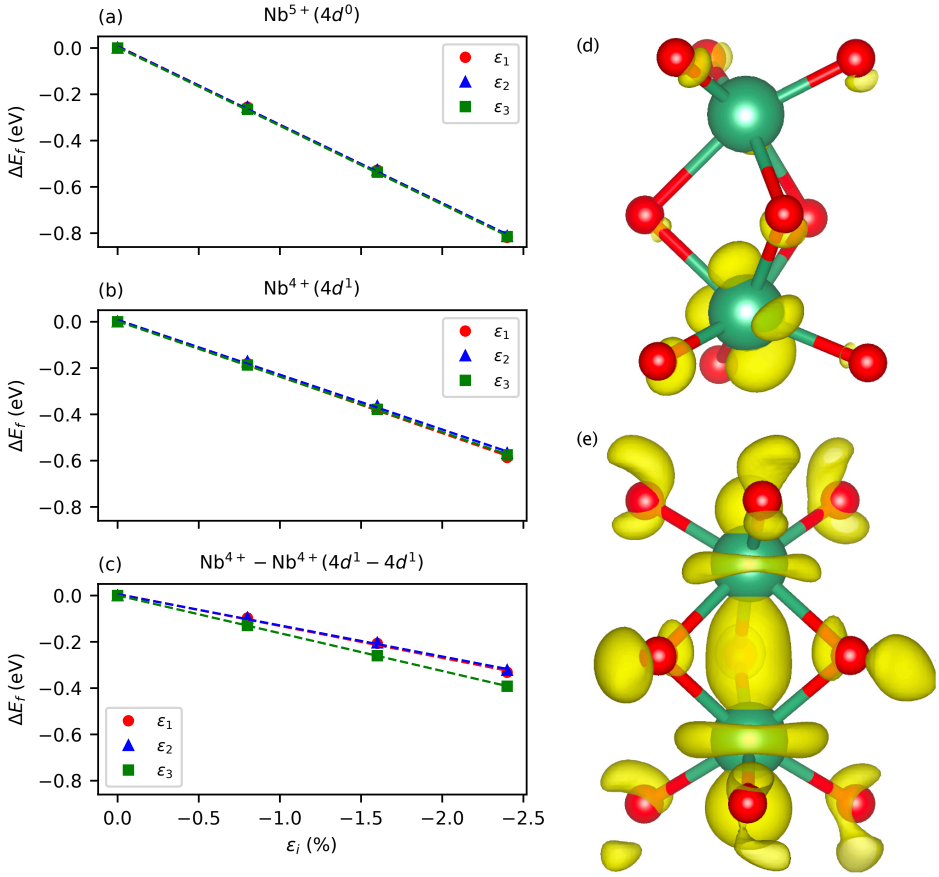

Figure 5.19: DFT calculated relative formation energy of the (a) Nb$_{\text{Li}}^{5+}$(4d^0), (b) Nb$_{\text{Li}}^{4+}$(4d^1) (c) Nb$_{\text{Li}}^{4+}$–Nb$_{\text{Nb}}^{4+}$(4$d^1 - 4d^1$) antisites of LN under uniaxial strain in x, y and z direction, respectively. The lines are drawn for the eyes. The electronic charge density associated with the (d) 4d^1 bound small polaron in the quasi-Jahn-Teller distortion and (e) 4$d^1 - 4d^1$ bipolaron. Green and red balls represent the niobium and oxygen atoms, respectively.

or removed to form the defect. E_F is the Fermi energy referenced to the valence band maximum E_v, and ΔV aligns the reference potential between the defect and bulk supercells [203]. Since the last two terms in Eq. (5.27) are constant under strain in a first approximation, it is sufficient to compute $E^{\text{total}}(X^q)$ and $E^{\text{total}}(\text{bulk})$ as a function of strain ϵ to determine the relative formation energy ΔE_f. In the following, the results of Ref. [P4] are shown.

5.7.3 Results

Figures 5.19(a)-(c) show the resulting relative formation energies of the investigated defects. In particular, Fig. 5.19(b) shows the relative formation energy as a function of uniaxial strain of the small bound polaron in the quasi-Jahn-Teller distortion as indicated in Fig. 5.19(d), which is known as the true ground state of the 4d^1 polaron [202].

Furthermore, the relative formation energy of the $4d^1 - 4d^1$ bipolaron is displayed in Fig. 5.19(c), which consists of a covalent bond between the antisites and its nearest Nb neighbor as shown in Fig. 5.19(e) [202]. The formation energies of the investigated antisites are decreasing roughly linearly with the applied stress as can be seen in Figs. 5.19(a)-(c). As a result, it can be concluded that the formation energy of these defects at the DWs is lowered, as well. This effect is less pronounced with decreasing charge of the antisites. The relative formation energy is the same for each strain direction except from the bipolaron whose formation energy shrinks even more for z strain. As the $\mathrm{Nb_{Li}} - \mathrm{Nb_{Nb}}$ bond is built along the z direction, a compression in the z direction results in a shortened, stronger bond.

5.8 Conclusions

In this chapter, a comprehensive theoretical and experimental investigation of the vibrational, optical, and polaronic properties of LN (and for the vibrational part LT) under uniaxial stress has been presented.

By doing so, the elastic properties of LN with the full set of elastic stiffness and compliance tensor components have been investigated from first principles. The calculated tensor quantities are consistent with experimental data [6]. Especially the PBEsol functional yields the best agreement with the experimental values. Subsequently, the elastic constants have been used to model uniaxial stress in LN crystals.

First, phonon frequencies as a function of strain have been computed for both LN and LT and compared to experimental data. All phonon modes exhibit sensitivity to strain. Theoretical and experimental findings consistently show an approximately linear dependence of the phonon frequencies on strain, which can be understood by examining the calculated eigenvectors. The observed linear slopes are in agreement with previous studies under hydrostatic pressure [21]. Both experimental and theoretical results indicate that x and y compressed LN exhibit especially large peak shifts for the $\mathrm{E(TO_{5/6})}$ modes, while z compressed LN shows pronounced shifts for the $\mathrm{A_1(TO_2)}$, $\mathrm{E(TO_7)}$, and $\mathrm{E(TO_8)}$ modes [21]. Furthermore, calculations have shown that the degeneracy of the E modes is lifted for x and y compression due to symmetry reduction. This splitting has also been observed experimentally when using different scattering geometries. Additionally, calculations have indicated that LT exhibits a strain response very similar to that of LN.

The full set of the linear piezo-optic and photoelastic tensors has been calculated as a function of excitation energy. As a result, the behavior of the refractive index as well as the birefringence under strain could be understood. In addition, the magnitude and sign of the piezo-optic and photoelastic coefficients, expressing the photoelastic properties, in Refs. [186, 187] have been confirmed by the calculations provided in this work.

In addition, the second-order nonlinear piezo-optic properties of LN have been investigated through comprehensive calculations of the SHG tensor under uniaxial stress and compared with thin-film LN measurements. This has enabled the determination of the nonlinear POCs, as defined in Refs. [181, 182], resulting in a three-dimensional strain map of the SHG response in LN. Notably, the splitting of identical SHG tensor elements and the appearance of new components are prominent signatures of symmetry reduction under x and y stress. This suggests that such new tensor elements should also be present at DWs, consistent with observations of SHG contrast at DWs [20, 26, 198]. Furthermore, the calculated dispersion of the nonlinear POCs allows reconstruction of SHG modifications under uniaxial stress for different laser wavelengths. Both, the investigation of the phonon frequencies of LN as well as its refractive and nonlinear optical nature under strain provides a set of references which may help to interpret, e.g. Raman signatures, of DWs or to improve the application of waveguides.

The CARS spectra have been calculated from first principles for the first time for solid crystals such as LN by combining the resonant contribution from Raman-active phonon modes with the nonresonant electronic contribution, computed using the first principles approach of Ref. [P5]. The calculated CARS spectrum for the (xxx, x) polarization configuration of stoichiometric LN show similarities to the main features of experimental CARS data from congruent LN, particularly the strong $\mathrm{A}_1(\mathrm{TO}_4)$ mode at 600 cm^{-1} and the weaker $\mathrm{A}_1(\mathrm{TO}_{1-3})$ modes between 240 cm^{-1} and 350 cm^{-1}. The relative intensities of the phonon modes in the calculated CARS spectrum correspond well to those in the spontaneous Raman spectrum of Ref. [164]. The analysis also highlights that the polarization dependence of CARS can be more complex than that of spontaneous Raman scattering due to the involvement of multiple Raman tensor elements, leading to nonzero contributions in configurations that are forbidden in spontaneous Raman scattering. The disentanglement of resonant and nonresonant contributions provides valuable insight into the microscopic origin of the measured CARS spectra. All experimental CARS spectra show a large broad peak at around 520 cm^{-1} which does not appear in the calculated resonant CARS spectra. Since the nonresonant part can be calculated from first principles as well, it can be concluded that this peak is neither of resonant nor of nonresonant vibrational origin. Instead, it is dominated by the experimental detector function $C(\omega)$, which includes, for instance, frequency-dependent detection efficiency and phase-matching effects. This is where the theoretical modeling can help to interpret the experimental data, since in the calculations this function is set to $C(\omega) \equiv 1$, such that these setup-specific contributions are absent and only the vibrational contribution and the NRB in $\chi^{(3)}$ is retained.

At the end, the relative formation energies of the $\mathrm{Nb}_{\mathrm{Li}}^{5+}$, $\mathrm{Nb}_{\mathrm{Li}}^{4+}$ small bound polaron and the $\mathrm{Nb}_{\mathrm{Li}}^{4+}$–$\mathrm{Nb}_{\mathrm{Nb}}^{4+}$ bipolaron have been calculated under uniaxial strain in x, y and z direction. The results show that the formation energy of all polarons associated with the antisite are reduced under compression, indicating that polarons are more likely to form at CDWs enhancing their conductivity.

Overall, the results presented in this chapter connect the elastic, vibrational, optical, and polaronic properties of LN under stress. These results not only reproduce experimental observations but also offer predictive insights into the behavior of strained LN and its DWs.

6 Summary & outlook

The work presented in this thesis has focused on modeling the response of ferroelectric and two-dimensional materials to external perturbations from first principles. Two main directions have been pursued.

In the first part of this work, a real-time formalism has been developed to simulate nonlinear frequency-mixing processes from first principles, based on the dynamical polarization, calculated within the modern theory of polarization. The method extends the real-time approach of Attaccalite and Grüning [49] to SHG by allowing the decomposition of the dynamical polarization into individual frequency components, making it applicable to SFG, DFG, and FI-SHG [P5]. The method has been implemented within the Yambo [47, 49] and YamboPy [P5, P6] codes. It has been validated for the IPA as well as TD-aGW [107], reducing to GW+BSE in the linear regime. The approach has been demonstrated on the prototypical two-dimensional crystals h-BN and MoS$_2$ monolayer, extending the understanding of their excitonic nature. This methodological development has provided the theoretical framework to model CARS.

The subsequent part of this thesis is dedicated to the application of the novel theoretical approach to the investigation of ferroelectric oxides under strain. Starting from the determination of the elastic properties [P2], the vibrational [P1] as well as refractive [P2] and nonlinear optical properties [P3] under uniaxial stress have been investigated for LN (the vibrational part for LT). The results provide a quantitative three-dimensional map of the vibrational and optical properties under stress. As DWs have been shown to behave as a strained bulk, the obtained results also allow for the interpretation of exciting physical phenomena occuring at DWs such as the SHG or Raman signal enhancement. The calculation of CARS has been established using the first principles approach of Ref. [P5]. The resulting phonon mode intensities in the computed CARS spectra closely match those observed in spontaneous Raman spectra of Ref. [164]. Furthermore, Nb$_{\mathrm{Li}}$ associated polarons under strain have been studied to gain deeper insight into the contributions of polarons to the enhanced conductivity at DWs [P4]. This investigation also implies that strain-engineered defect configurations could be used to tailor the electronic conductivity of ferroelectric oxides.

Looking forward, several extensions of this work are necessary. On the methodological side, the real-time approach to nonlinear optical processes can be combined with many-body perturbation theory at the GW+BSE level, allowing for a more accurate description of excitonic effects and optical dispersion when investigating LN under uniaxial stress. The inclusion of finite-temperature effects and electron-phonon coupling would enable realistic modeling of the temperature dependence of photoelastic properties. The maxima of the POCs can be related to the maximum values of the coefficient of the acousto-optic (AO) figure of merit [205, 206]. Since the calculation of this quantity requieres the POCs, the theoretical investigation of the AO figure of merit of LN can be a follow-up investigation, as well. From an application perspective, extending all these calculations to lithium niobate-tantalate solid solutions and other polar oxides would help optimize materials for integrated photonic [1–4] and acousto-optic devices [4, 7–14]. Combining the strain-dependent response maps established here with real-time CARS simulations opens the possibility of predictive modeling of strain- and defect-sensitive optical spectroscopies, enabling the quantitative interpretation of experiments on DWs. However, the resonant part of the CARS spectrum should be calculated in absolute values to enable quantitative comparisons with experimental data. As in the experiment the complete CARS spectrum without distinction between resonant and nonresonant part is visible, it is of particular interest to know the relative magnitude of the resonant and nonresonant parts. Nevertheless, a recent work of Hempel *et al.* [207] has shown that the nonresonant part as well as the phonon dephasing times can be extracted from time delayed, broadband CARS measurements, tested with SiO_2 and diamond. Hence, combining such experimental data with the present theoretical framework could allow for calculations of the absolute CARS values in future studies. Furthermore, the analysis of the theoretical CARS spectra under stress without considering LO modes is limited. Hence, the calculation of CARS under consideration of LO-TO splitting is an important next step. In addition, the investigation of polarons at DWs in the framework of Ginzburg-Landau-Devonshire theory as applied in Ref. [P4] is of high interest to better understand the formation of polarons at DWs as well as their influence on the conductivity.

Recent experimental investigations on bilayer MoS_2 have revealed two main features in optical absorption. First, a giant Stark splitting of bright interlayer excitons (IEs) into opposite, well-separated dipole branches that shift linearly with an out-of-plane field and strongly (weakly) hybridize with the intralayer B (A) exciton [208]. Secondly, the clean IE crossing turns under electron doping into stochastic hybridization, determined by the interlayer electron coherence whose strength increases with density and decreases with temperature [209]. The established real-time simulations of frequency-mixing processes can also be applied to bilayer MoS_2 for a theoretical description of these observed effects. Computing SFG and DFG maps and FI-SHG, as in Ref. [P5], across gate- and twist-tuned IE-A/B resonances might be useful to quantify the IE-B anticrossing and the linear dipole branch shifts in the nonlinear response, offering a quantitative complement to absorption measurements. In parallel, the real-time simulations can include electron doping to determine how electron coherence modifies the nonlinear response.

Methodologically, the real-time approach can also be extended and applied beyond optics to electric conductivity. Mao *et al.* [210] recently developed an *ab initio* method to calculate the shift current (SC) response in 2D materials. Using a real-time approach with a monochromatic electric field that couples in analogy to Ref. [49] through a dynamical Berry phase formulation describing a current:

$$\mathbf{J}(\omega) = \sigma^{(1)}(\omega)\boldsymbol{\mathcal{E}}(\omega) + \sum_{ij} \sigma^{(2)}(\omega_i, \omega_j)\boldsymbol{\mathcal{E}}(\omega_i)\boldsymbol{\mathcal{E}}(\omega_j) + O(\boldsymbol{\mathcal{E}}^3), \tag{6.1}$$

where $\sigma^{(1)}(\omega)$ is the linear conductivity tensor and $\sigma^{(2)}(\omega_i, \omega_j)$ is the second-order nonlinear conductivity tensor responsible for the bulk photovoltaic effect including SC. The SC response is calculated in its time-domain and can then be analyzed analogously to Ref. [P5]. This can be done at GW+BSE level including excitonic effects, which have been shown to strongly enhance the SC response in 2D materials [210]. This framework captures how inversion breaking, layer polarity, and exciton character tune the magnitude and sign of the SC in 2D materials. Hence, computing both the nonlinear response as well as the SC of MoS_2 bilayer one can predict gate- and twist-tailored modifications in IE and moiré trion formations, hybridizations, and energy-ordering.

Appendix

A.1 Ferroelectric oxides under strain

A.1.1 Elastic properties

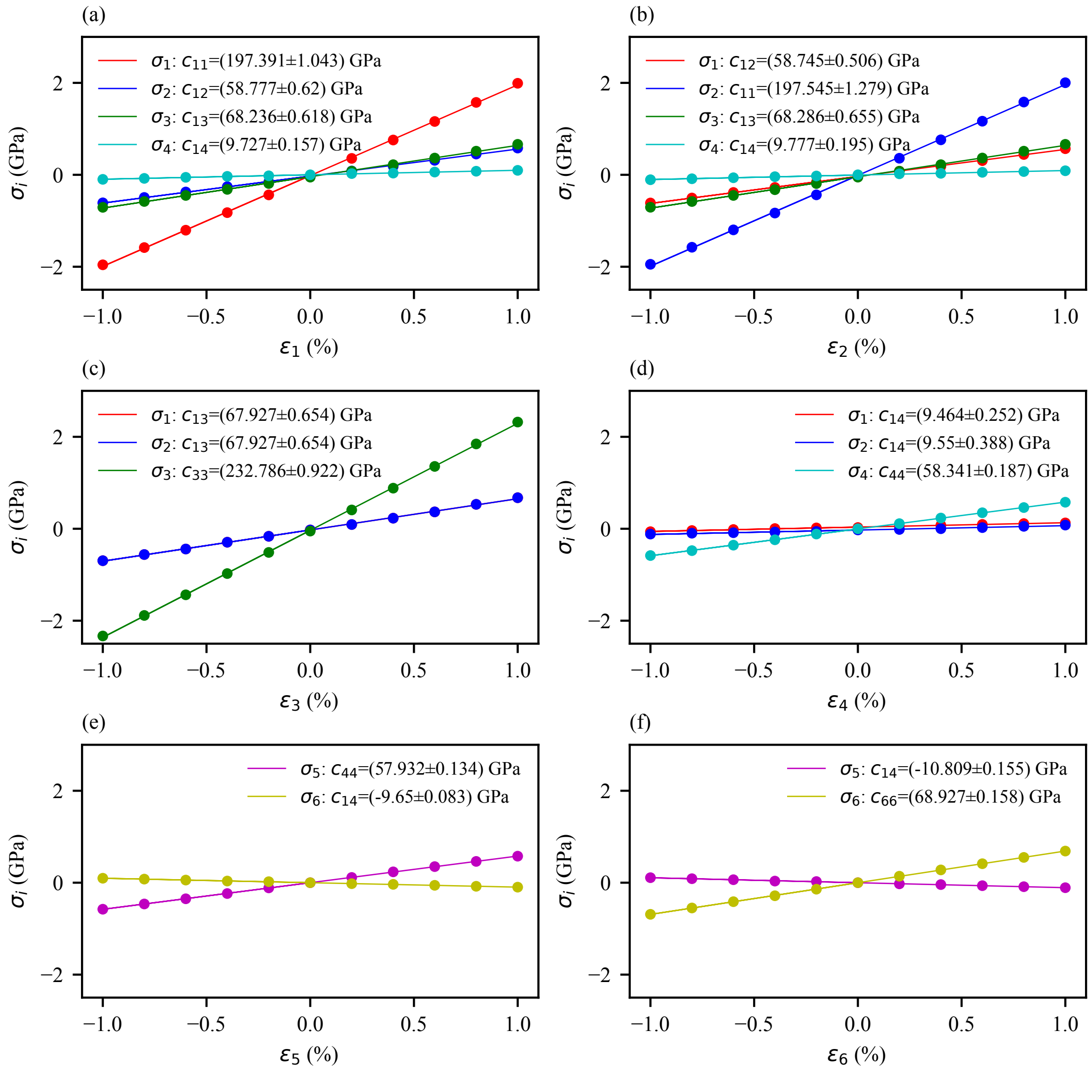

Figure A.1: The calculated stress tensor elements as a function of (a) ϵ_1, (b) ϵ_2, (c) ϵ_3, (d) ϵ_4, (e) ϵ_5 and (f) ϵ_6, while the rest of the strain tensor is set to zero in each case.

A.1.2 Vibrational properties

In order to compare the calculated phonon frequencies in unstrained LN and LT with Ref. [164], they are displayed in Table A.1 and A.2. In addition, Table A.3 and A.4 show all the slopes of LN and LT under uniaxial compressive and tensile strain.

Table A.1: Calculated frequencies of the Raman active phonon modes in unstrained LN in comparison with calculated and measured frequencies of Ref. [164].

Phonon mode	Theory [cm^{-1}]	Theory [cm^{-1}] [164]	Exp. [cm^{-1}] [164]
$A_1(TO_1)$	242	239	252–255
$A_1(TO_2)$	282	289	275–276
$A_1(TO_3)$	350	353	333–334
$A_1(TO_4)$	613	610	633
$E(TO_1)$	150	148	150–151
$E(TO_2)$	216	216	237
$E(TO_3)$	265	262	262–263
$E(TO_4)$	319	323	320–321
$E(TO_5)$	372	380	367–369
$E(TO_6)$	384	391	367–369
$E(TO_7)$	420	423	432
$E(TO_8)$	577	579	580–581
$E(TO_9)$	668	667	664

Table A.2: Calculated frequencies of the Raman active phonon modes in unstrained LT in comparison with calculated and measured frequencies of Ref. [164].

Phonon mode	Theory [cm^{-1}]	Theory [cm^{-1}] [164]	Exp. [cm^{-1}] [164]
$A_1(TO_1)$	200	209	209–210
$A_1(TO_2)$	255	286	256–257
$A_1(TO_3)$	369	376	359–360
$A_1(TO_4)$	578	591	600
$E(TO_1)$	139	144	143
$E(TO_2)$	193	199	210
$E(TO_3)$	247	253	254–257
$E(TO_4)$	313	319	315–317
$E(TO_5)$	370	409	383–384
$E(TO_6)$	384	420	383–384
$E(TO_7)$	452	459	460–465
$E(TO_8)$	579	590	592
$E(TO_9)$	658	669	661–662

Table A.3: Calculated slopes of transversal A_1 and E modes of LN under compressive and tensile strain in the x, y and z direction for strains in steps of 0.2 % in cm^{-1}/%. The slopes for strain are defined as $(\Delta\omega)/(|\Delta\epsilon|)$.

Phonon modes	Compressive strain (cm^{-1}/%)			Tensile strain (cm^{-1}/%)		
	x direction	y direction	z direction	x direction	y direction	z direction
$A_1(TO_1)$	0.22	-0.09	-2.97	-3.46	-4.49	-4.07
$A_1(TO_2)$	4.45	4.46	4.44	-3.03	-3.08	-5.20
$A_1(TO_3)$	4.82	4.13	0.65	-7.18	-6.48	-0.32
$A_1(TO_4)$	6.35	5.70	-4.91	-1.03	0.31	5.36
$E(TO_1)$	0.48/4.24	4.05/1.48	-0.61	-0.61/-2.81	-3.98/-0.39	0.30
$E(TO_2)$	1.74/-0.14	-1.30/2.55	-2.55	-2.11/-0.11	-1.23/-1.66	1.14
$E(TO_3)$	1.48/3.27	1.50/3.93	0.50	-3.67/-1.05	-2.68/-2.61	-0.53
$E(TO_4)$	4.28/-0.11	0.22/3.80	2.40	-4.49/-0.12	0.07/-4.78	-2.56
$E(TO_5)$	6.20/6.94	8.79/6.30	-0.68	-8.90/-13.24	-13.14/-11.82	1.29
$E(TO_6)$	12.80/11.03	11.51/10.08	-0.94	-7.62/-4.45	-2.19/-7.76	1.12
$E(TO_7)$	4.18/2.40	4.37/1.98	4.75	0.11/0.15	0.65/-0.13	-4.08
$E(TO_8)$	2.87/-0.55	-0.61/4.83	3.35	-7.08/0.70	-3.12/-5.20	-2.57
$E(TO_9)$	-0.67/7.06	7.18/-0.67	0.90	2.98/-7.02	-7.20/2.83	-0.52

Table A.4: Calculated slopes of transversal A_1 and E modes of LT under compressive and tensile strain in the x, y and z direction for strains in steps of 0.4 % in $cm^{-1}/\%$. The slopes for strain are defined as $(\Delta\omega)/(|\Delta\epsilon|)$.

Phonon modes	Compressive strain ($cm^{-1}/\%$)			Tensile strain ($cm^{-1}/\%$)		
	x direction	y direction	z direction	x direction	y direction	z direction
$A_1(TO_1)$	3.48	3.46	-2.72	-2.61	-2.74	2.75
$A_1(TO_2)$	5.34	5.33	3.89	-3.18	-3.05	-3.75
$A_1(TO_3)$	5.41	4.69	1.82	-12.73	-7.23	-1.78
$A_1(TO_4)$	5.53	3.74	-4.32	-4.37	-4.41	4.98
$E(TO_1)$	1.55/1.76	2.25/1.03	-0.45	-0.34/-2.38	-1.75/-0.99	0.48
$E(TO_2)$	3.12/1.05	0.46/3.59	-3.33	-3.76/-0.68	-1.47/-2.94	2.05
$E(TO_3)$	3.09/2.84	3.05/2.82	-1.29	-2.34/-4.33	-3.82/-2.92	1.24
$E(TO_4)$	3.17/2.33	2.58/2.90	1.65	-4.39/-2.99	-2.72/-4.42	-2.04
$E(TO_5)$	8.39/9.92	10.76/8.61	-0.24	-6.15/-16.13	-16.48/-11.86	0.22
$E(TO_6)$	14.80/6.43	13.64/14.27	-0.79	-10.70/-7.49	-6.11/-11.74	0.72
$E(TO_7)$	1.55/1.86	2.00/1.42	4.36	-0.68/-0.95	-0.74/-0.84	-4.68
$E(TO_8)$	5.04/2.27	5.30/3.25	5.35	-1.98/-1.77	-0.97/-2.92	-4.51
$E(TO_9)$	4.51/3.84	4.77/4.79	3.26	-2.38/-2.35	-2.80/-3.21	-2.80

A.1.3 Optical Properties

The second-order nonlinear susceptibility tensor for the 1, m and $3m$ point group has the following form

$$d_1 = \begin{pmatrix} d_{11} & d_{12} & d_{13} & d_{14} & d_{15} & d_{16} \\ d_{21} & d_{22} & d_{23} & d_{24} & d_{25} & d_{26} \\ d_{31} & d_{32} & d_{33} & d_{34} & d_{35} & d_{36} \end{pmatrix}, \tag{A.1}$$

$$d_m = \begin{pmatrix} 0 & 0 & 0 & 0 & d_{15} & d_{16} \\ d_{21} & d_{22} & d_{23} & d_{24} & 0 & 0 \\ d_{31} & d_{32} & d_{33} & d_{34} & 0 & 0 \end{pmatrix}, \tag{A.2}$$

$$d_{3m} = \begin{pmatrix} 0 & 0 & 0 & 0 & d_{15} & -d_{22} \\ -d_{22} & d_{22} & 0 & d_{15} & 0 & 0 \\ d_{31} & d_{31} & d_{33} & 0 & 0 & 0 \end{pmatrix}, \tag{A.3}$$

with the contracted notation $d_{il} = \frac{1}{2}\chi_{ijk}$ and

$$(ij) = \begin{pmatrix} 11 & 12 & 13 \\ 21 & 22 & 23 \\ 31 & 32 & 33 \end{pmatrix} = \begin{pmatrix} 1 & 6 & 5 \\ 6 & 2 & 4 \\ 5 & 4 & 3 \end{pmatrix} = (l). \tag{A.4}$$

A comparison between the SHG calculated from the real-time approach (Yambo) and the sum of the two-band contribution (VASP) of unstrained LN is shown in Fig. A.2. The wavefunctions are calculated in VASP within the GGA [172] in the formulation of PBE [89]. PAW [95] potentials have been used with projectors up to $\ell = 3$ for Nb, and $\ell = 2$ for Li and O. For a comparison with the spectra from the real-time approach the optimized lattice constants obtained from QUANTUM ESPRESSO have been applied. The plane-wave basis set is expanded up to a kinetic energy of 475 eV and the first Brillouin-zone corresponding to the rhombohedral unit cell is sampled using a $10\times10\times10$ k-point mesh, which is proved to be accurate enough [25]. For the calculation of Eq. 10, 135 bands have been considered. Due to inconsistent results regarding the crystal symmetry d_{34}, d_{35}, d_{36}, d_{32}, d_{25}, and d_{24} are not considered for the determination of the nonolinear piezo-optic properties.

In Figs. A.3, A.4 and A.5 the calculated dispersion of the SHG coefficients for different configurations of uniaxial stress in x, y and z direction are displayed, respectively. From the gradient of the SHG coefficients with the applied stress, the dispersion of the nonlinear POCs are determined and shown in Fig. A.6. Similar to Ref. [2], the nonlinear POCs have an increasing gradient close to the bandgap. These are caused by peak shifts of the SHG coefficients, e.g. in Fig. A.5(g) due to small changes of the bandgap under strain.

Table A.5: Calculated SHG components of unstrained LN for an excitation wavelength of 933 nm in comparison with experimental literature values. The d_{15} component is not explicitly mentioned in the literature since $d_{15} = d_{32}$ for the considered laser wavelength in accordance to Kleinman symmetry.

d_{il} [pm/V]	Theory	Exp. [191]	Exp. [194]	Exp. [195]	Exp. [196]	Exp. [197]
d_{22}	10.4	3	2.1	–	–	–
d_{32}	19.8	6	4.3	3.7–6.3	–	–
d_{15}	19.0	–	–	–	–	–
d_{33}	12.5	36	27	20–42	41.7	25

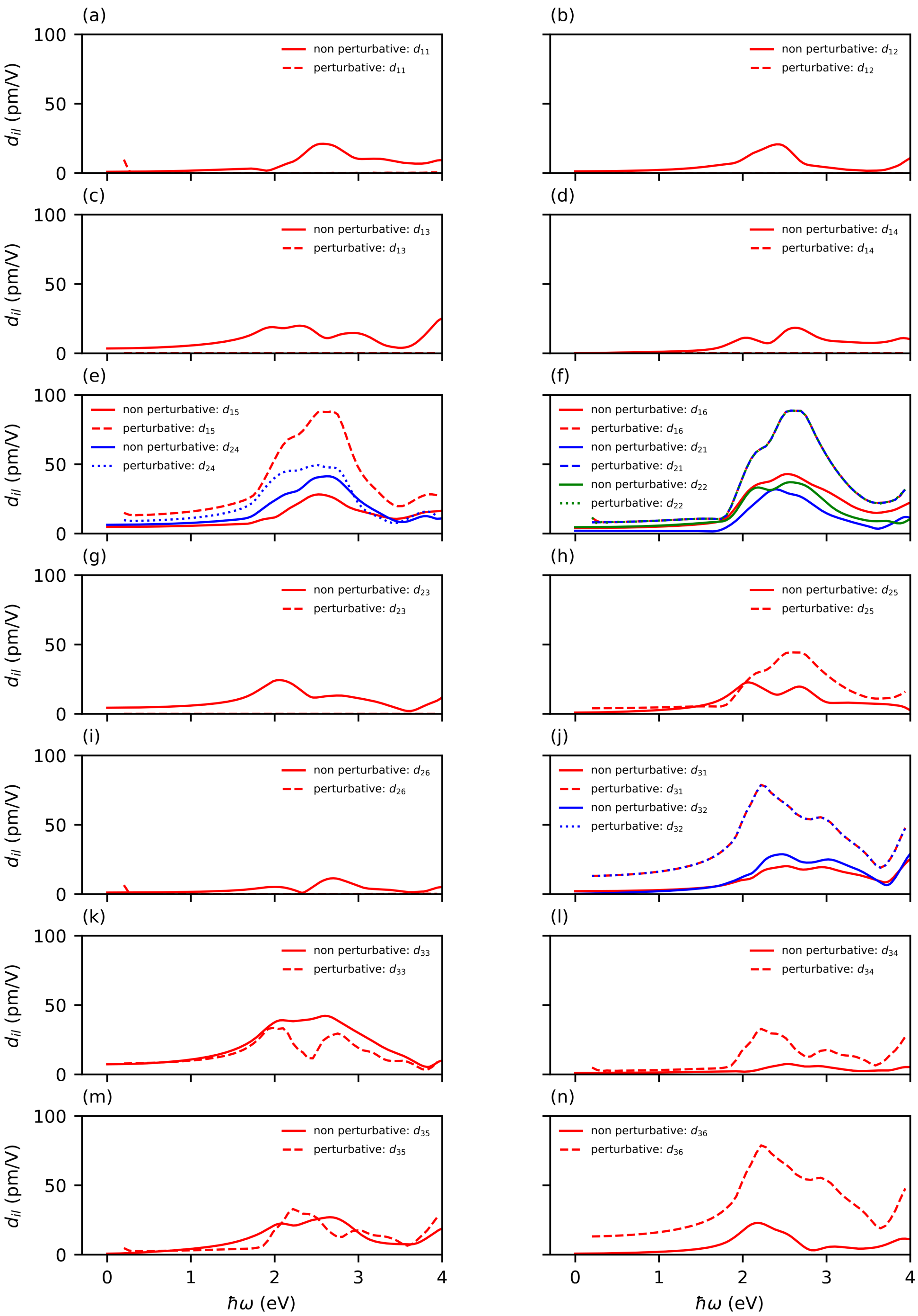

Figure A.2: Calculated SHG components of unstrained LN obtained with sum of two-bands contributions (non perturbative approach) and real-time approach (perturbative approach). For (a) d_{11}, (b) d_{12}, (c) d_{13}, (d) d_{14}, (g) d_{23} and (i) d_{26}, the results of both approaches are identical.

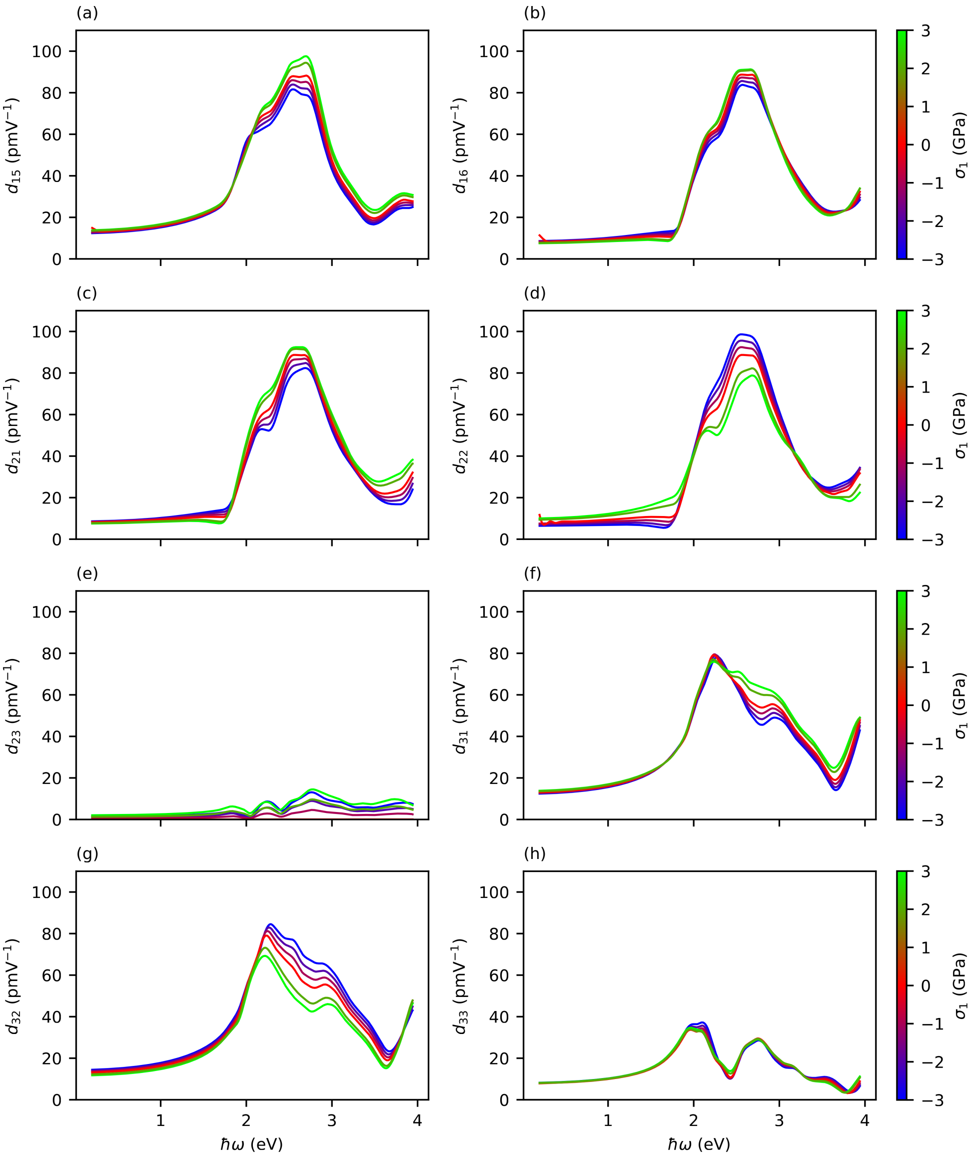

Figure A.3: Calculated SHG spectra of LN under uniaxial x stress between -3 and 3 GPa in steps of 1 GPa (1 GPa is omitted). Due to the symmetry reduction from $3m$ to m point group symmetry the d_{23} component appears (see (e)). The identities for the m point group symmetry from Table 5.8 apply to the SHG spectra under x stress.

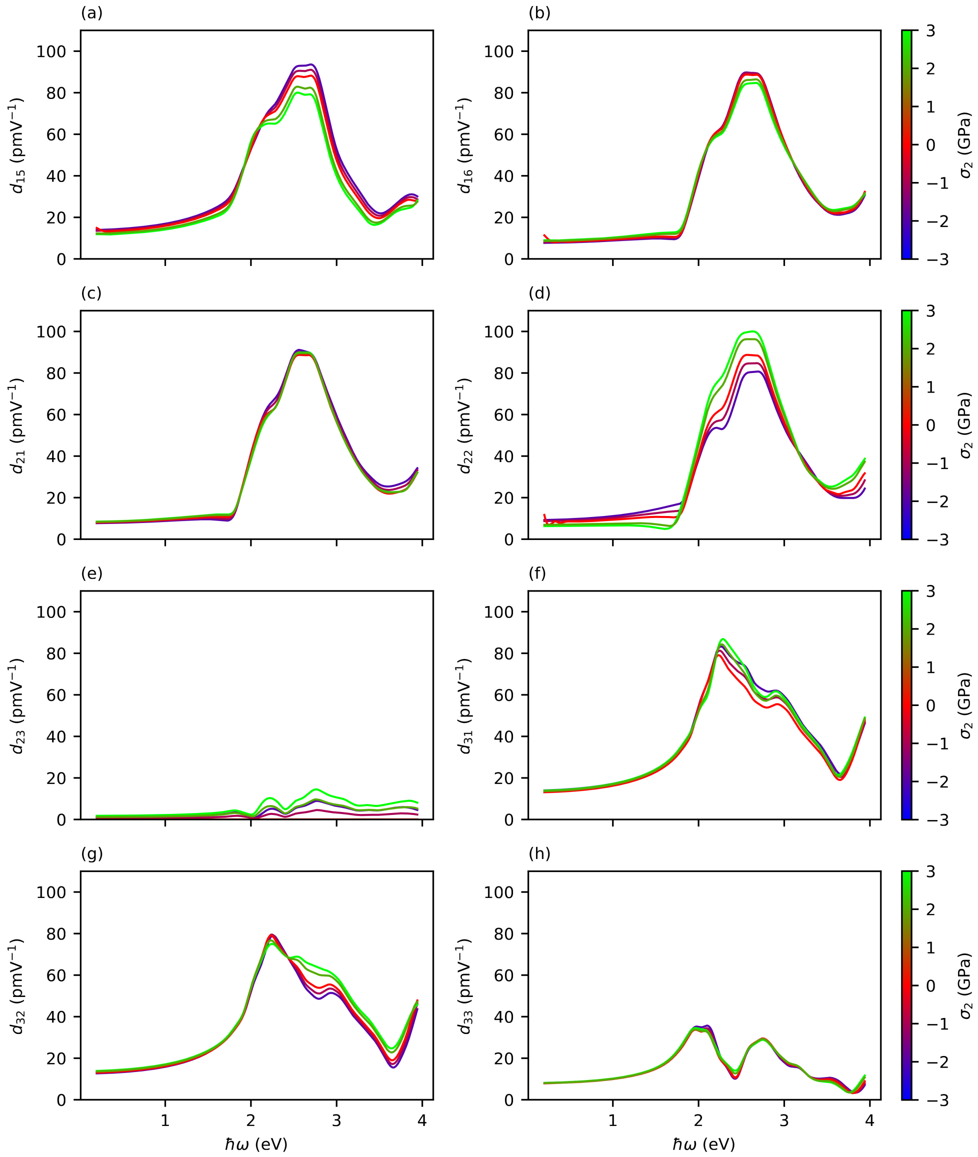

Figure A.4: Calculated SHG spectra of LN under uniaxial y stress between -3 and 3 GPa in steps of 1 GPa (-3 GPa and 1 GPa are omitted). Due to the symmetry reduction from $3m$ to m point group symmetry the d_{23} component appears (see (e)). The identities for the m point group symmetry from Table 5.8 apply to the SHG spectra under y stress.

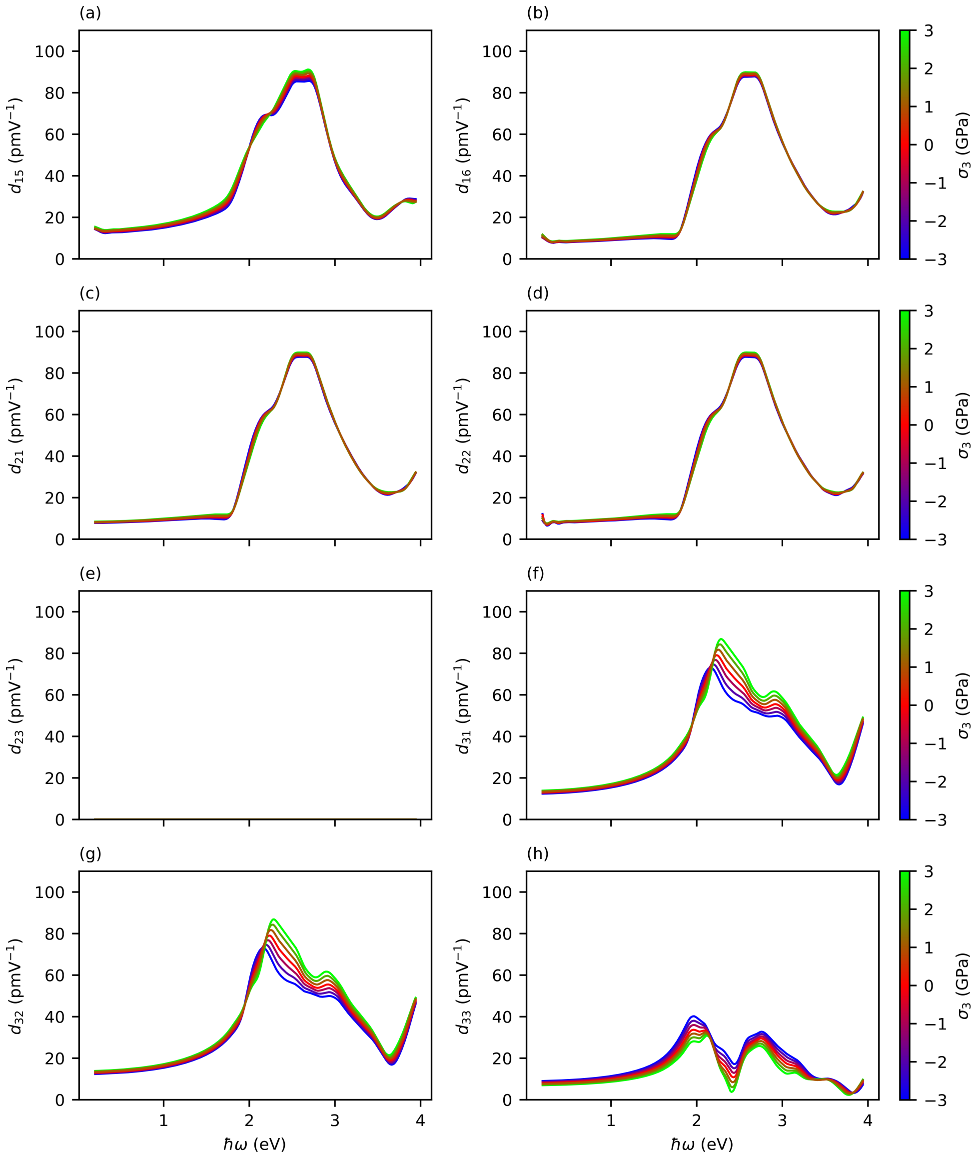

Figure A.5: Calculated SHG spectra of LN under uniaxial z stress between -3 and 3 GPa in steps of 1 GPa. Since the $3m$ point group symmetry is preserved uneder z stress, the d_{23} component is still zero (see (e)). The identities for the $3m$ point group symmetry from Table 5.8 apply to the SHG spectra under z stress.

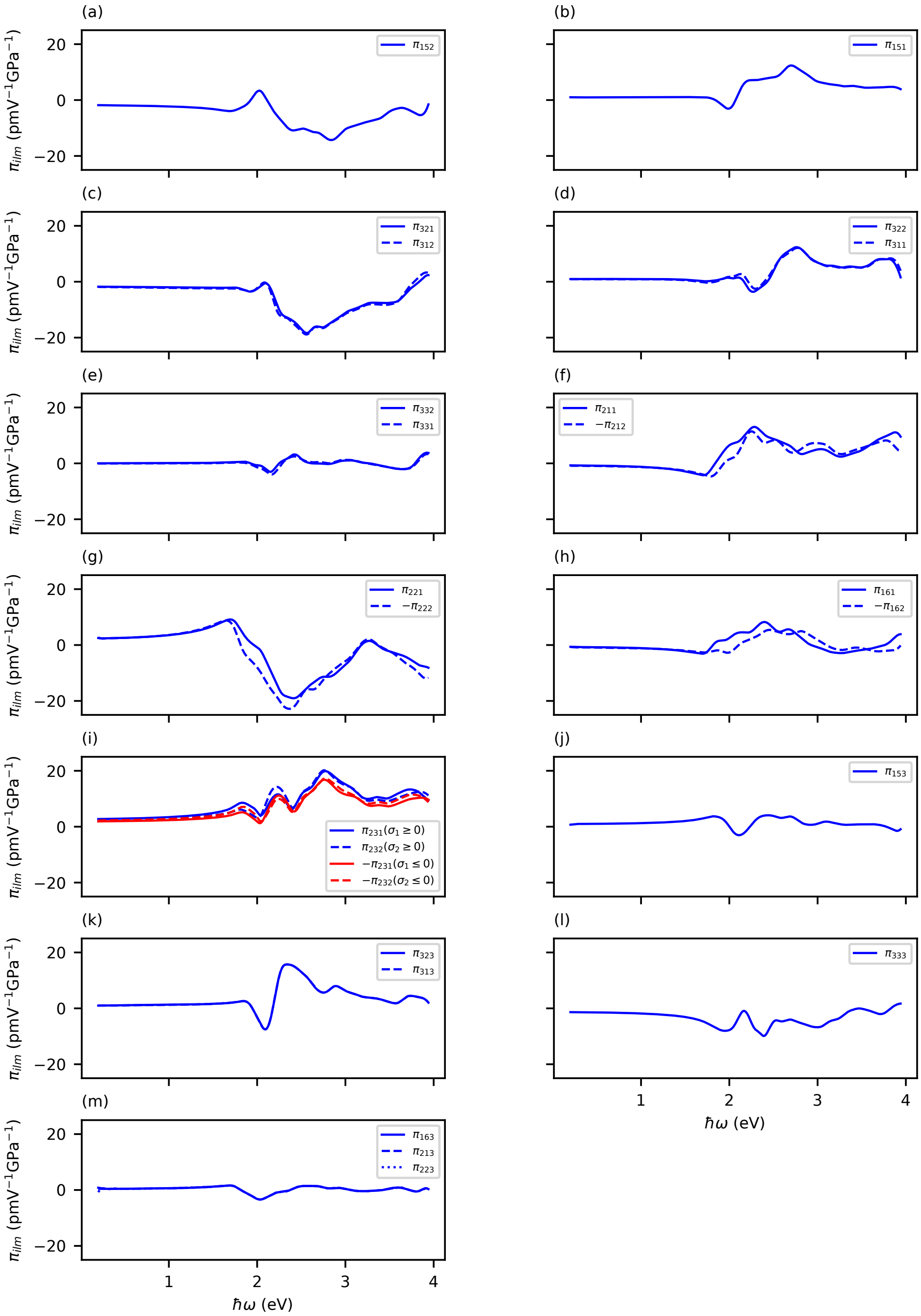

Figure A.6: Calculated spectra of the nonlinear piezo-optic coefficients of LN. Such coefficients, which are identical in the $3m$ point group, are shown together (see Table 5.8). Apart from minor deviations, the identies of Table 5.8 apply. Up to 1.5 eV the coefficients are nearly constant.

A.1.4 Coherent anti-Stokes Spectroscopy

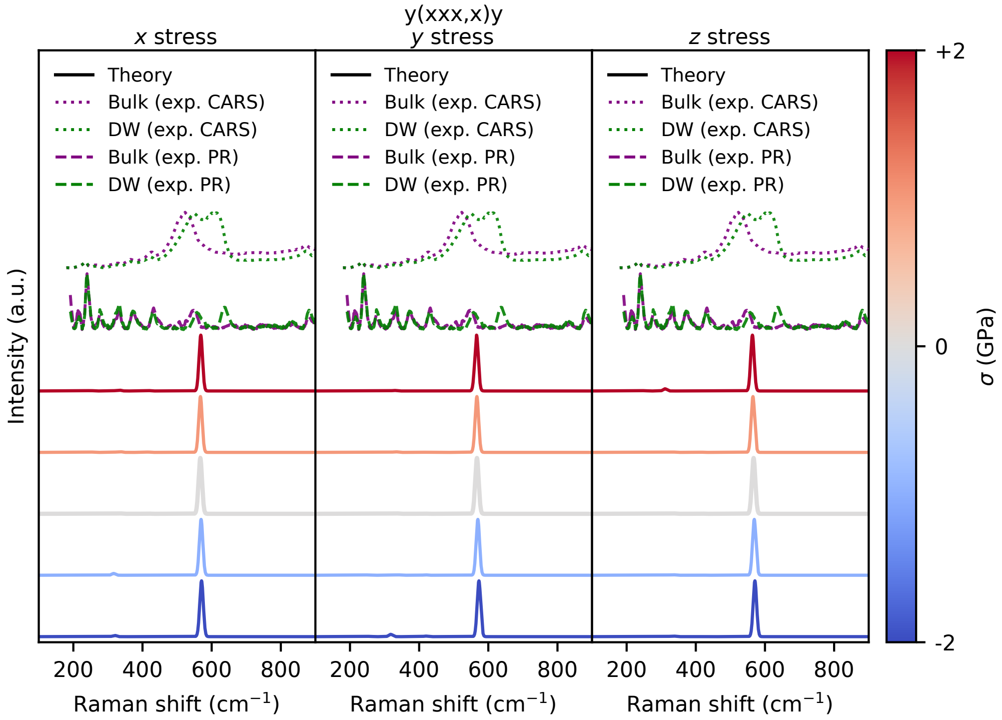

Figure A.7: Calculated (xxx, x) resonant CARS spectrum of stoichiometric LN under uniaxial stress between -2 % and 2 % in x, y and z direction. The calculated intensities are drawn with an arbitrary Gaussian broadening of 10 cm^{-1}. The dotted lines indicate the $y(xxx, x)y$ experimental CARS spectrum of congruent LN off and on the domain wall. The dashed lines indicate the $y(xxx, x)y$ experimental phase-retrieval (PR) spectrum of congruent LN off and on the domain wall (R. Buschbeck, private communication, 2025).

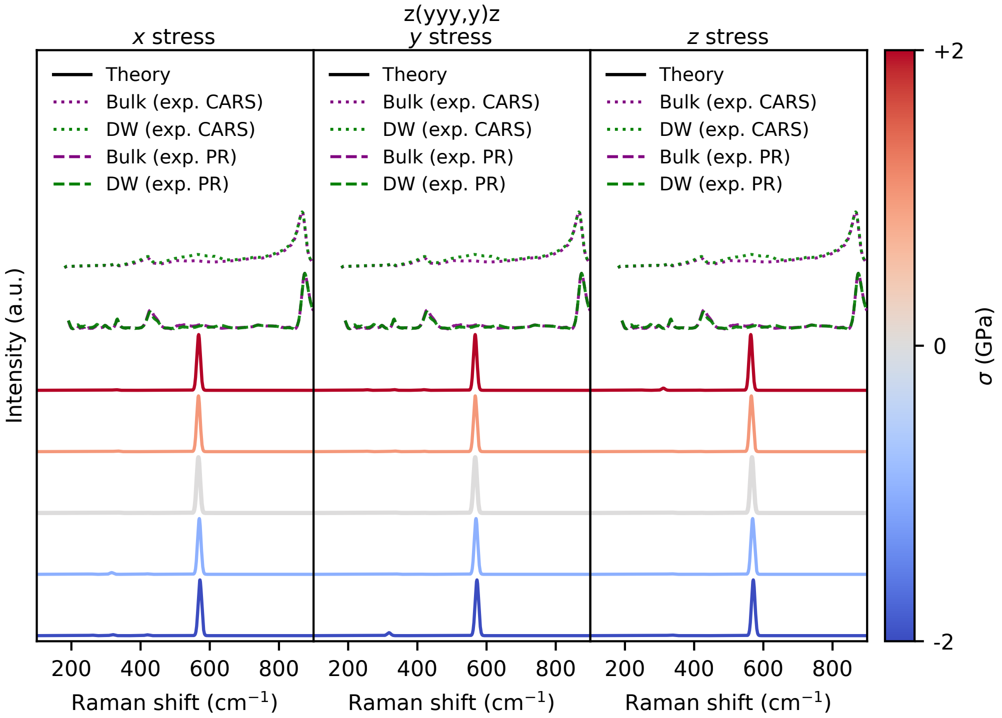

Figure A.8: Calculated (yyy, y) resonant CARS spectrum of stoichiometric LN under uniaxial stress between -2 % and 2 % in x, y and z direction. The calculated intensities are drawn with an arbitrary Gaussian broadening of 10 cm^{-1}. The dotted lines indicate the $z(yyy, y)z$ experimental CARS spectrum of congruent LN off and on the domain wall. The dashed lines indicate the $z(yyy, y)z$ experimental phase-retrieval (PR) spectrum of congruent LN off and on the domain wall (R. Buschbeck, private communication, 2025).

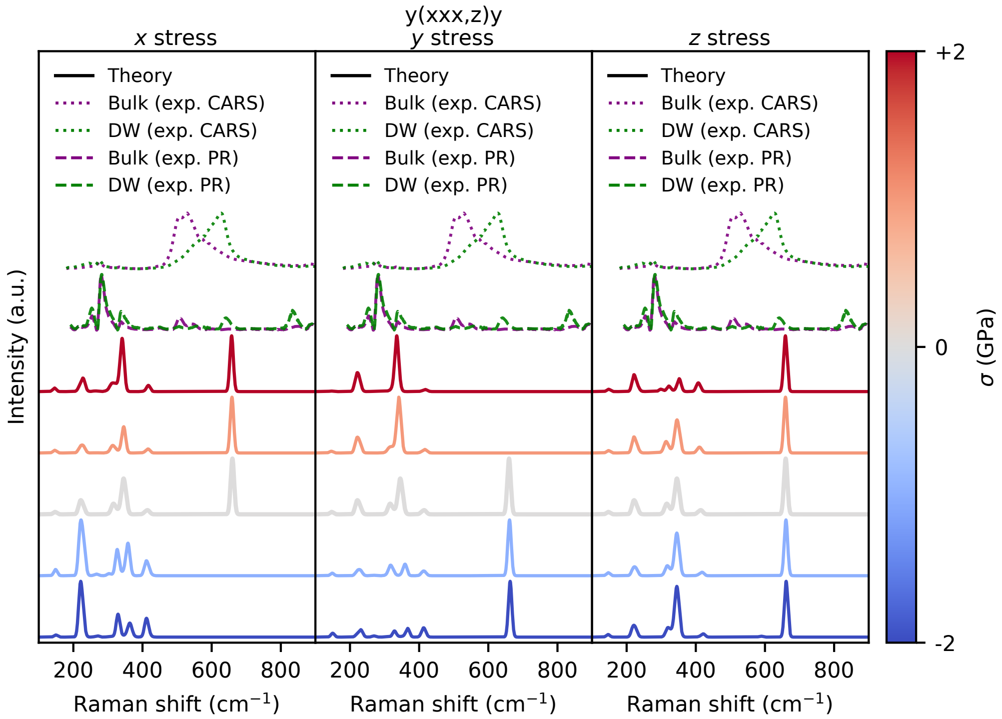

Figure A.9: Calculated (xxx, z) resonant CARS spectrum of stoichiometric LN under uniaxial stress between -2 % and 2 % in x, y and z direction. The calculated intensities are drawn with an arbitrary Gaussian broadening of 10 cm^{-1}. The dotted lines indicate the $y(xxx, z)y$ experimental CARS spectrum of congruent LN off and on the domain wall. The dashed lines indicate the $y(xxx, z)y$ experimental phase-retrieval (PR) spectrum of congruent LN off and on the domain wall (R. Buschbeck, private communication, 2025).

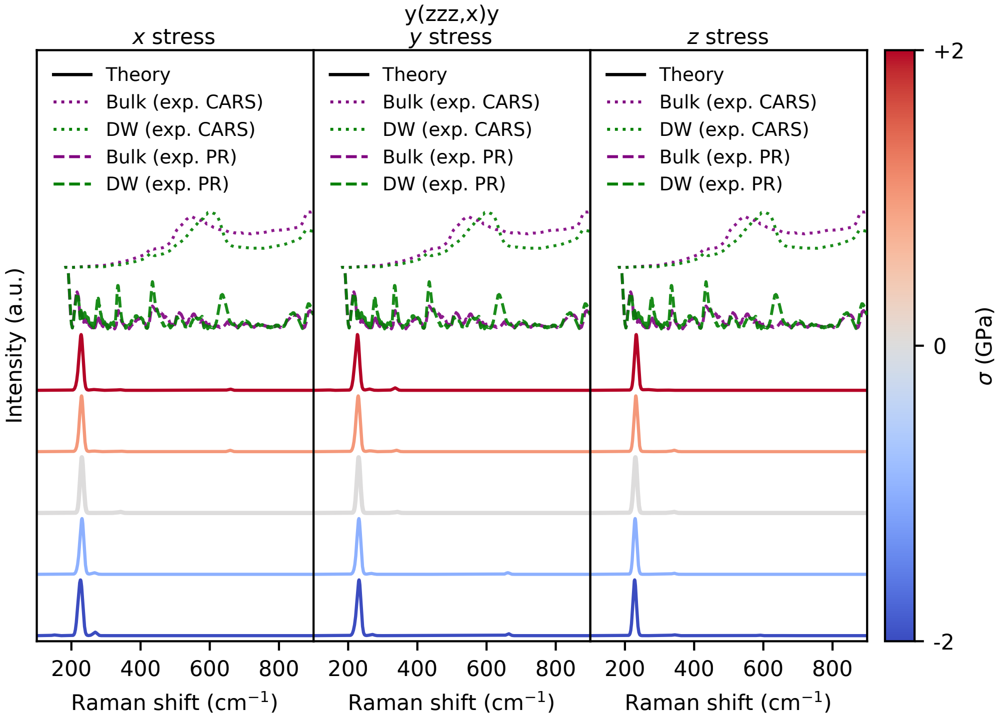

Figure A.10: Calculated (zzz, x) resonant CARS spectrum of stoichiometric LN under uniaxial stress between -2 % and 2 % in x, y and z direction. The calculated intensities are drawn with an arbitrary Gaussian broadening of 10 cm^{-1}. The dotted lines indicate the $y(zzz, x)y$ experimental CARS spectrum of congruent LN off and on the domain wall. The dashed lines indicate the $y(zzz, x)y$ experimental phase-retrieval (PR) spectrum of congruent LN off and on the domain wall (R. Buschbeck, private communication, 2025).

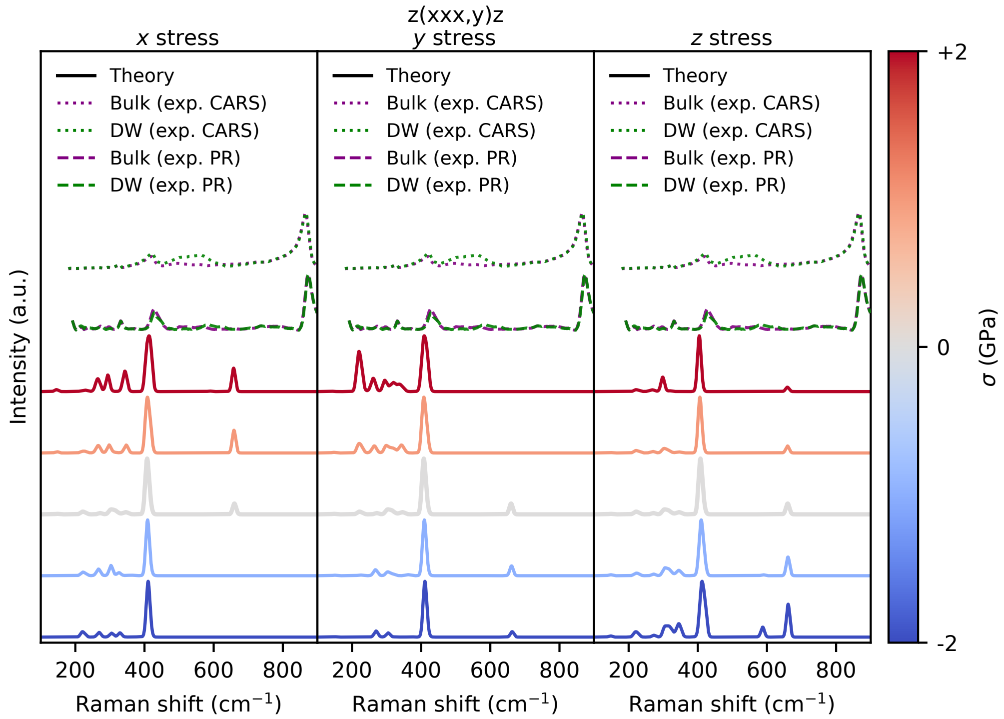

Figure A.11: Calculated (xxx, y) resonant CARS spectrum of stoichiometric LN under uniaxial stress between -2 % and 2 % in x, y and z direction. The calculated intensities are drawn with an arbitrary Gaussian broadening of 10 cm^{-1}. The dotted lines indicate the $z(xxx, y)z$ experimental CARS spectrum of congruent LN off and on the domain wall. The dashed lines indicate the $z(xxx, y)z$ experimental phase-retrieval (PR) spectrum of congruent LN off and on the domain wall (R. Buschbeck, private communication, 2025).

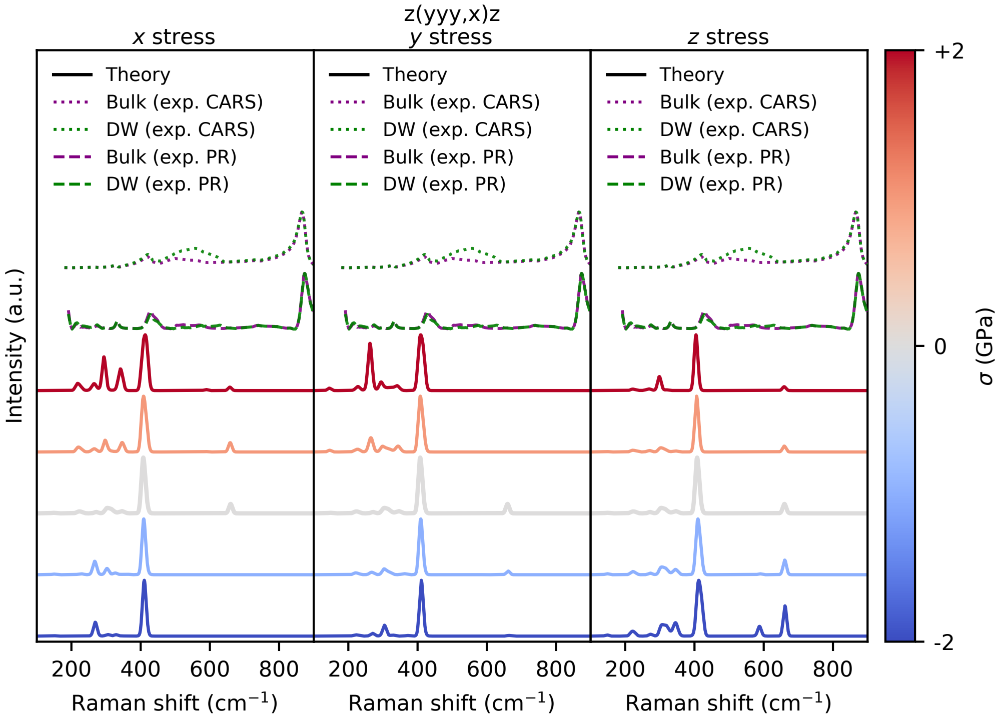

Figure A.12: Calculated (yyy, x) resonant CARS spectrum of stoichiometric LN under uniaxial stress between -2 % and 2 % in x, y and z direction. The calculated intensities are drawn with an arbitrary Gaussian broadening of 10 cm^{-1}. The dotted lines indicate the $z(yyy, x)z$ experimental CARS spectrum of congruent LN off and on the domain wall. The dashed lines indicate the $z(yyy, x)z$ experimental phase-retrieval (PR) spectrum of congruent LN off and on the domain wall (R. Buschbeck, private communication, 2025).

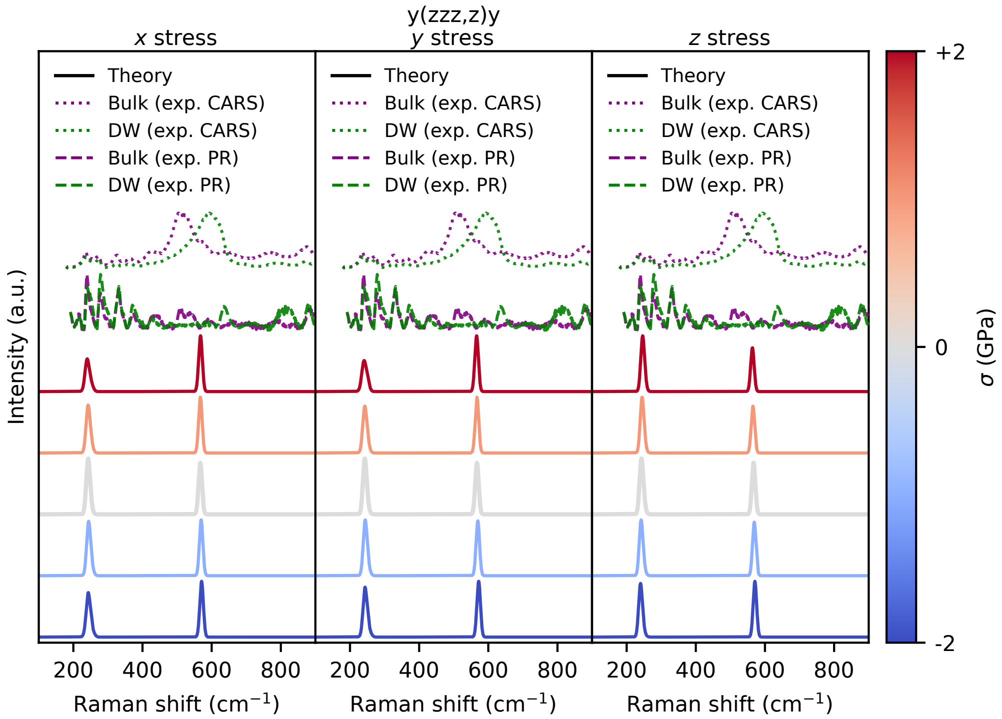

Figure A.13: Calculated (zzz, z) resonant CARS spectrum of stoichiometric LN under uniaxial stress between -2 % and 2 % in x, y and z direction. The calculated intensities are drawn with an arbitrary Gaussian broadening of 10 cm^{-1}. The dotted lines indicate the $y(zzz, z)y$ experimental CARS spectrum of congruent LN off and on the domain wall. The dashed lines indicate the $y(zzz, z)y$ experimental phase-retrieval (PR) spectrum of congruent LN off and on the domain wall (R. Buschbeck, private communication, 2025).

Bibliography

[1] L. Arizmendi, Photonic applications of lithium niobate crystals, Phys. Status Solidi (a) **201**, 253–283 (2004).

[2] M. Bazzan and C. Sada, Optical waveguides in lithium niobate: Recent developments and applications, Appl. Phys. Rev. **2**, 40603 (2015).

[3] E. L. Wooten, K. M. Kissa, A. Yi-Yan, E. J. Murphy, D. A. Lafaw, P. F. Hallemeier, D. Maack, D. V. Attanasio, D. J. Fritz, G. J. McBrien, and D. E. Bossi, A review of lithium niobate modulators for fiber-optic communications systems, IEEE J. Sel. Top. Quantum Electron. **6**, 69–82 (2000).

[4] M. Parfenov, P. Agruzov, I. Il'ichev, and A. Shamray, Simulation of Ti-indiffused lithium niobate waveguides and analysis of their mode structure, J. Phys. Conf. Ser. **741**, 12141 (2016).

[5] R. S. Weis and T. K. Gaylord, Lithium niobate: Summary of physical properties and crystal structure, Appl. Phys. A **37**, 191–203 (1985).

[6] A. W. Warner, M. Onoe, and G. A. Coquin, Determination of elastic and piezoelectric constants for crystals in class (3 m), J. Acoust. Soc. Am. **42**, 1223–1231 (1967).

[7] I. V. Il'ichev, A. S. Kozlov, P. V. Gaenko, and A. V. Shamray, Optimisation of the proton-exchange technology for fabricating channel waveguides in lithium niobate crystals, Quantum Electron. **39**, 98–104 (2009).

[8] M. Friedrich, W. G. Schmidt, A. Schindlmayr, and S. Sanna, Optical properties of titanium-doped lithium niobate from time-dependent density-functional theory, Phys. Rev. Mater. **1**, 034401 (2017).

[9] M. Rusing, P. O. Weigel, J. Zhao, and S. Mookherjea, Toward 3D integrated photonics including lithium niobate thin films: A bridge between electronics, radio frequency, and optical technology, IEEE Nanotechnol. Mag. **13**, 18–33 (2019).

[10] Q. Li, H. Zhang, H. Zhu, and H. Hu, Characterizations of single-crystal lithium niobate thin films, Crystals **12**, 667 (2022).

[11] S. Reitzig, M. Rüsing, J. Zhao, B. Kirbus, S. Mookherjea, and L. M. Eng, "Seeing is believing"—in-depth analysis by co-imaging of periodically-poled X-cut lithium niobate thin films, Crystals **11**, 288 (2021).

[12] T. Kämpfe, B. Wang, A. Haußmann, L.-Q. Chen, and L. M. Eng, Tunable non-volatile memory by conductive ferroelectric domain walls in lithium niobate thin films, Crystals **10**, 804 (2020).

[13] A. Honardoost, K. Abdelsalam, and S. Fathpour, Rejuvenating a versatile photonic material: Thin-film lithium niobate, Laser Photonics Rev. **14**, 2000088 (2020).

[14] D. Zhu, L. Shao, M. Yu, R. Cheng, B. Desiatov, C. J. Xin, Y. Hu, J. Holzgrafe, S. Ghosh, A. Shams-Ansari, *et al.*, Integrated photonics on thin-film lithium niobate, Adv. Opt. Photon. **13**, 242–352 (2021).

[15] T. Jach, S. Kim, V. Gopalan, S. Durbin, and D. Bright, Long-range strains and the effects of applied field at 180° ferroelectric domain walls in lithium niobate, Phys. Rev. B **69**, 064113 (2004).

[16] J. Padilla, W. Zhong, and D. Vanderbilt, First-principles investigation of 180° domain walls in $BaTiO_3$, Phys. Rev. B **53**, R5969–R5973 (1996).

[17] G. Berth, W. Hahn, V. Wiedemeier, A. Zrenner, S. Sanna, and W. G. Schmidt, Imaging of the ferroelectric domain structures by confocal Raman spectroscopy, Ferroelectrics **420**, 44–48 (2011).

[18] M. Rüsing, S. Neufeld, J. Brockmeier, C. Eigner, P. Mackwitz, K. Spychala, C. Silberhorn, W. G. Schmidt, G. Berth, A. Zrenner, and S. Sanna, Imaging of 180° ferroelectric domain walls in uniaxial ferroelectrics by confocal Raman spectroscopy: Unraveling the contrast mechanism, Phys. Rev. Mater. **2**, 103801 (2018).

[19] D. A. Scrymgeour, V. Gopalan, A. Itagi, A. Saxena, and P. J. Swart, Phenomenological theory of a single domain wall in uniaxial trigonal ferroelectrics: Lithium niobate and lithium tantalate, Phys. Rev. B **71**, 184110 (2005).

[20] U. Acevedo-Salas, B. Croes, Y. Zhang, O. Cregut, K. D. Dorkenoo, B. Kirbus, E. Singh, H. Beccard, M. Rüsing, L. M. Eng, *et al.*, Impact of 3D curvature on the polarization orientation in non-Ising domain walls, Nano Lett. **23**, 795–803 (2023).

[21] J. Mendes-Filho, V. Lemos, and F. Cerdelra, Pressure dependence of the Raman spectra of $LiNbO_3$ and $LiTaO_3$, J. Raman Spectrosc. **15**, 367–369 (1984).

[22] G. Stone, B. Knorr, V. Gopalan, and V. Dierolf, Frequency shift of Raman modes due to an applied electric field and domain inversion in $LiNbO_3$, Phys. Rev. B **84**, 134303 (2011).

[23] M. D. Fontana and P. Bourson, Microstructure and defects probed by Raman spectroscopy in lithium niobate crystals and devices, Appl. Phys. Rev. **2**, 040602 (2015).

[24] R. W. Boyd, *Nonlinear Optics*, 3rd ed. (Academic Press, 2008).

[25] C. Dues, M. J. Müller, S. Chatterjee, C. Attaccalite, and S. Sanna, Nonlinear optical response of ferroelectric oxides: First-principles calculations within the time and frequency domains, Phys. Rev. Mater. **6**, 065202 (2022).

[26] S. Cherifi-Hertel, H. Bulou, R. Hertel, G. Taupier, K. D. Dorkenoo, C. Andreas, J. Guyonnet, I. Gaponenko, K. Gallo, and P. Paruch, Non-Ising and chiral ferroelectric domain walls revealed by nonlinear optical microscopy, Nat. Commun. **8**, 15768 (2017).

[27] S. Cherifi-Hertel, C. Voulot, U. Acevedo-Salas, Y. Zhang, O. Crégut, K. D. Dorkenoo, and R. Hertel, Shedding light on non-Ising polar domain walls: Insight from second harmonic generation microscopy and polarimetry analysis, J. Appl. Phys. **129**, 081101 (2021).

[28] P. S. Bednyakov, B. I. Sturman, T. Sluka, A. K. Tagantsev, and P. V. Yudin, Physics and applications of charged domain walls, npj Comput. Mater. **4**, 65 (2018).

[29] C. S. Werner, S. J. Herr, K. Buse, B. Sturman, E. Soergel, C. Razzaghi, and I. Breunig, Large and accessible conductivity of charged domain walls in lithium niobate, Sci. Rep. **7**, 9862 (2017).

[30] M. Zahn, E. Beyreuther, I. Kiseleva, A. S. Lotfy, C. J. McCluskey, J. R. Maguire, A. Suna, M. Rüsing, J. M. Gregg, and L. M. Eng, Equivalent-circuit model that quantitatively describes domain-wall conductivity in ferroelectric $LiNbO_3$, Phys. Rev. Appl. **21**, 024007 (2024).

[31] L. Liu, K. Xu, Q. Li, J. Daniels, H. Zhou, J. Li, J. Zhu, J. Seidel, and J.-F. Li, Giant domain wall conductivity in self-assembled $BiFeO_3$ nanocrystals, Adv. Funct. Mater. **31**, 2005876 (2021).

[32] E. Singh, H. Beccard, Z. H. Amber, J. Ratzenberger, C. W. Hicks, M. Rüsing, and L. M. Eng, Tuning domain wall conductivity in bulk lithium niobate by uniaxial stress, Phys. Rev. B **106**, 144103 (2022).

[33] J. R. Whyte, R. G. P. McQuaid, P. Sharma, C. Canalias, J. F. Scott, A. Gruverman, and J. M. Gregg, Ferroelectric domain wall injection, Advanced Materials **26**, 293–298 (2014).

[34] G. Catalan, J. Seidel, R. Ramesh, and J. F. Scott, Domain wall nanoelectronics, Rev. Mod. Phys. **84**, 119–156 (2012).

[35] J. Wang, J. Ma, H. Huang, J. Ma, H. M. Jafri, Y. Fan, H. Yang, Y. Wang, M. Chen, D. Liu, *et al.*, Ferroelectric domain-wall logic units, Nat. Commun. **13**, 3255 (2022).

[36] G. F. Nataf, M. Guennou, J. M. Gregg, D. Meier, J. Hlinka, E. K. H. Salje, and J. Kreisel, Domain-wall engineering and topological defects in ferroelectric and ferroelastic materials, Nat. Rev. Phys. **2**, 634–648 (2020).

[37] S. Sanna, Bound electron polarons in lithium niobate, in *2015 Symposium on Piezoelectricity, Acoustic Waves, and Device Applications (SPAWDA)* (2015) pp. 523–527.

[38] A. Krampf, M. Imlau, Y. Suhak, H. Fritze, and S. Sanna, Evaluation of similarities and differences of $LiTaO_3$ and $LiNbO_3$ based on high-t-conductivity, nonlinear optical fs-spectroscopy and ab initio modeling of polaronic structures, New J. Phys. **23**, 033016 (2021).

[39] F. Schmidt, A. L. Kozub, U. Gerstmann, W. G. Schmidt, and A. Schindlmayr, Electron polarons in lithium niobate: Charge localization, lattice deformation, and optical response, Crystals **11**, 542 (2021).

[40] M. Krenz, U. Gerstmann, and W. G. Schmidt, Bound polaron formation in lithium niobate from ab initio molecular dynamics, Appl. Phys. A **128**, 480 (2022).

[41] M. Imlau, H. Badorreck, and C. Merschjann, Optical nonlinearities of small polarons in lithium niobate, Appl. Phys. Rev. **2** (2015).

[42] G. Kresse and J. Hafner, Ab initio molecular dynamics for liquid metals, Phys. Rev. B **47**, 558 (1993).

[43] G. Kresse and J. Furthmüller, Efficiency of ab-initio total energy calculations for metals and semiconductors using a plane-wave basis set, Comput. Mater. Sci. **6**, 15–50 (1996).

[44] G. Kresse and J. Furthmüller, Efficient iterative schemes for ab initio total-energy calculations using a plane-wave basis set, Phys. Rev. B **54**, 11169–11186 (1996).

[45] P. Giannozzi, S. Baroni, N. Bonini, M. Calandra, R. Car, C. Cavazzoni, D. Ceresoli, G. L. Chiarotti, M. Cococcioni, I. Dabo, *et al.*, Quantum espresso: a modular and open-source software project for quantum simulations of materials, J. Phys. Condens. Matter **21**, 395502 (2009).

[46] P. Giannozzi, O. Andreussi, T. Brumme, O. Bunau, M. B. Nardelli, M. Calandra, R. Car, C. Cavazzoni, D. Ceresoli, M. Cococcioni, *et al.*, Advanced capabilities for materials modelling with Quantum ESPRESSO, J. Phys. Condens. Matter **29**, 465901 (2017).

[47] D. Sangalli, A. Ferretti, H. Miranda, C. Attaccalite, I. Marri, E. Cannuccia, P. Melo, M. Marsili, F. Paleari, A. Marrazzo, *et al.*, Many-body perturbation theory calculations using the yambo code, J. Phys. Condens. Matter **31**, 325902 (2019).

[48] A. Marini, C. Hogan, M. Grüning, and D. Varsano, yambo: An ab initio tool for excited state calculations, Comput. Phys. Commun. **180**, 1392–1403 (2009).

[49] C. Attaccalite and M. Grüning, Nonlinear optics from an ab initio approach by means of the dynamical Berry phase: Application to second- and third-harmonic generation in semiconductors, Phys. Rev. B **88**, 235113 (2013).

[50] L. Zhou, H. Fu, T. Lv, C. Wang, H. Gao, D. Li, L. Deng, and W. Xiong, Nonlinear optical characterization of 2D materials, Nanomaterials **10** (2020).

[51] H. Lotem, R. T. Lynch, and N. Bloembergen, Interference between Raman resonances in four-wave difference mixing, Phys. Rev. A **14**, 1748–1755 (1976).

[52] C. L. Evans and X. S. Xie, Coherent anti-Stokes Raman scattering microscopy: Chemical imaging for biology and medicine, Annu. Rev. Anal. Chem. **1**, 883–909 (2008).

[53] C. Zhang, D. Zhang, and J.-X. Cheng, Coherent Raman scattering microscopy in biology and medicine, Annu. Rev. Biomed. Eng. **17**, 415–445 (2015).

[54] G. I. Petrov, R. Arora, and V. V. Yakovlev, Coherent anti-Stokes Raman scattering imaging of microcalcifications associated with breast cancer, Analyst **146**, 1253–1259 (2021).

[55] Q. Tang, B. Li, J. Wang, Y. Liu, I. Pinkas, H. Rigneault, D. Oron, and L. Ren, Electronic-resonance coherent anti-Stokes Raman scattering spectroscopy and microscopy, ACS Photonics **11**, 3467–3475 (2024).

[56] K. Ikeda and K. Uosaki, Coherent phonon dynamics in single-walled carbon nanotubes studied by time-frequency two-dimensional coherent anti-Stokes Raman scattering spectroscopy, Nano Lett. **9**, 1378–1381 (2009).

[57] G. Dovbeshko, O. Fesenko, A. Dementjev, R. Karpicz, V. Fedorov, and O. Y. Posudievsky, Coherent anti-Stokes Raman scattering enhancement of thymine adsorbed on graphene oxide, Nanoscale Res. Lett. **9**, 1–11 (2014).

[58] J. Koivistoinen, P. Myllyperkiö, and M. Pettersson, Time-resolved coherent anti-Stokes Raman scattering of graphene: Dephasing dynamics of optical phonon, J. Phys. Chem. Lett. **8**, 4108–4112 (2017).

[59] A. Virga, C. Ferrante, G. Batignani, D. De Fazio, A. Nunn, A. Ferrari, G. Cerullo, and T. Scopigno, Coherent anti-Stokes Raman spectroscopy of single and multilayer graphene, Nat. Commun. **10**, 3658 (2019).

[60] J. Ling, X. Miao, Y. Sun, Y. Feng, L. Zhang, Z. Sun, and M. Ji, Vibrational imaging and quantification of two-dimensional hexagonal boron nitride with stimulated Raman scattering, ACS Nano **13**, 14033–14040 (2019).

[61] A. Paddubskaya, D. Rutkauskas, R. Karpicz, G. Dovbeshko, N. Nebogatikova, I. Antonova, and A. Dementjev, Recognition of spatial distribution of CNT and graphene in hybrid structure by mapping with coherent anti-Stokes Raman microscopy, Nanoscale Res. Lett. **15**, 1–7 (2020).

[62] G. Lee, K. M. Jyothsna, J. Park, J. Lee, V. Raghunathan, and H. Kim, Confocal nonlinear optical imaging on hexagonal boron nitride nanosheets, PhotoniX **4**, 27 (2023).

[63] H. Dai, Y. Wang, J. Zhao, H. Liu, Z. Liu, and D. Liu, Enhanced double resonance Raman scattering in multilayer graphene with broadband coherent anti-Stokes Raman spectroscopy, Nanoscale **16**, 1247–1253 (2024).

[64] E. Lin, M. Scherman, A. Pierret, B. Attal-Tretout, A. Andrieux, L. Tailpied, T. Taniguchi, K. Watanabe, and A. Loiseau, Hyperspectral microscopy of boron nitride nanolayers using hybrid femto/picosecond coherent anti-Stokes Raman scattering, Opt. Lett. **49**, 2329–2332 (2024).

[65] F. Hempel, S. Reitzig, M. Rüsing, and L. M. Eng, Broadband coherent anti-Stokes Raman scattering for crystalline materials, Phys. Rev. B **104**, 224308 (2021).

[66] K. Niu and R. A. Marcus, Sum frequency generation, calculation of absolute intensities, comparison with experiments, and two-field relaxation-based derivation, PNAS **117**, 2805–2814 (2020).

[67] A. Morita, *Theory of sum frequency generation spectroscopy*, Vol. 97 (Springer, 2018).

[68] J. A. Maytorena, W. L. Mochán, and B. S. Mendoza, Hydrodynamic model for sum and difference frequency generation at metal surfaces, Phys. Rev. B **57**, 2580 (1998).

[69] D. Li, W. Xiong, L. Jiang, Z. Xiao, H. Rabiee Golgir, M. Wang, X. Huang, Y. Zhou, Z. Lin, J. Song, *et al.*, Multimodal nonlinear optical imaging of MoS_2 and MoS_2-based van der Waals heterostructures, ACS Nano **10**, 3766–3775 (2016).

[70] T. Yang, E. Pollmann, S. Sleziona, E. Hasselbrink, P. Kratzer, M. Schleberger, R. K. Campen, and Y. Tong, Interaction between a gold substrate and monolayer MoS_2: An azimuthal-dependent sum frequency generation study, Phys. Rev. B **107**, 155433 (2023).

[71] K. Yao, E. Yanev, H.-J. Chuang, M. R. Rosenberger, X. Xu, T. Darlington, K. M. McCreary, A. T. Hanbicki, K. Watanabe, T. Taniguchi, *et al.*, Continuous wave sum frequency generation and imaging of monolayer and heterobilayer two-dimensional semiconductors, ACS Nano **14**, 708–714 (2019).

[72] Y. Wang, M. Ghotbi, S. Das, Y. Dai, S. Li, X. Hu, X. Gan, J. Zhao, and Z. Sun, Difference frequency generation in monolayer MoS_2, Nanoscale **12**, 19638–19643 (2020).

[73] Y. Kim, H. Kim, H. Jang, J.-H. Ahn, and J. Lee, Dual resonant sum frequency generations from two-dimensional materials, Nano Lett. **20**, 4530–4536 (2020).

[74] D. Sangalli, M. D'Alessandro, and C. Attaccalite, Exciton-exciton transitions involving strongly bound excitons: An ab initio approach, Phys. Rev. B **107**, 205203 (2023).

[75] V. A. Margulis, E. E. Muryumin, and E. A. Gaiduk, Spectral characteristics of the sum-frequency generation from atomically thin hexagonal crystals lacking center-of-inversion symmetry, J. Opt. **17**, 065502 (2015).

[76] I. Souza, J. Íñiguez, and D. Vanderbilt, Dynamics of Berry-phase polarization in time-dependent electric fields, Phys. Rev. B **69**, 085106 (2004).

[77] M. Grüning and C. Attaccalite, Second harmonic generation in h-BN and MoS_2 monolayers: Role of electron-hole interaction, Phys. Rev. B **89**, 081102 (2014).

[78] M. Reid, I. V. Cravetchi, and R. Fedosejevs, Terahertz radiation and second-harmonic generation from inas: Bulk versus surface electric-field-induced contributions, Phys. Rev. B **72**, 035201 (2005).

[79] Y. Ding, Y. Zeng, X. Yu, Z. Liu, J. Qian, Y. Li, Y. Peng, L. Song, Y. Tian, Y. Leng, *et al.*, Terahertz-assisted even harmonics generation in silicon, Iscience **25** (2022).

[80] S. Grillo, E. Cannuccia, M. Palummo, O. Pulci, and C. Attaccalite, Tunable second harmonic generation in 2D materials: Comparison of different strategies, SciPost Phys. Core **7**, 081 (2024).

[81] G. Czycholl, *Theoretische Festkörperphysik - Von den klassischen Modellen zu modernen Forschungsthemen*, 3rd ed. (Springer-Verlag, 2007).

[82] F. Jensen, *An Introduction to Computational Chemistry*, Vol. 3 (John Wiley & Sons, Ltd, 2017).

[83] M. Born and R. Oppenheimer, Zur Quantentheorie der Molekeln, Ann. Phys. **379**, 1 – 31 (1924).

[84] P. Hohenberg and W. Kohn, Inhomogeneous electron gas, Phys. Rev. **136**, B864–B871 (1964).

[85] W. Kohn and L. J. Sham, Self-consistent equations including exchange and correlation effects, Phys. Rev. **140**, A1133–A1138 (1965).

[86] W. Kohn, Nobel lecture: Electronic structure of matter—wave functions and density functionals, Rev. Mod. Phys. **71**, 1253–1266 (1999).

[87] J. P. Perdew, Generalized gradient approximations for exchange and correlation: A look backward and forward, Physica B: Physics of Condensed Matter **172**, 1–6 (1991).

[88] J. P. Perdew, J. A. Chevary, S. H. Vosko, K. A. Jackson, M. R. Pederson, D. J. Singh, and C. Fiolhais, Atoms, molecules, solids, and surfaces: Applications of the generalized gradient approximation for exchange and correlation, Phys. Rev. B **46**, 6671–6687 (1992).

[89] J. P. Perdew, K. Burke, and M. Ernzerhof, Generalized gradient approximation made simple, Phys. Rev. Lett. **77**, 3865–3868 (1996).

[90] J. P. Perdew, A. Ruzsinszky, G. I. Csonka, O. A. Vydrov, G. E. Scuseria, L. A. Constantin, X. Zhou, and K. Burke, Restoring the density-gradient expansion for exchange in solids and surfaces, Phys. Rev. Lett. **100**, 136406 (2008).

[91] V. I. Anisimov and O. Gunnarsson, Density-functional calculation of effective coulomb interactions in metals, Phys. Rev. B **43**, 7570–7574 (1991).

[92] M. Cococcioni and S. de Gironcoli, Linear response approach to the calculation of the effective interaction parameters in the LDA + U method, Phys. Rev. B **71**, 35105 (2005).

[93] H. Monkhorst and J. Pack, Special points for Brillouin zone integrations, Phys. Rev. B **13**, 5188 (1976).

[94] D. Vanderbilt, Soft self-consistent pseudopotentials in a generalized eigenvalue formalism, Phys. Rev. B **41**, 7892–7895 (1990).

[95] P. E. Blöchl, Projector augmented-wave method, Phys. Rev. B **50**, 17953–17979 (1994).

[96] R. P. Feynman, Forces in molecules, Phys. Rev. **56**, 340–343 (1939).

[97] P. A. Franken, A. E. Hill, C. W. Peters, and G. Weinreich, Generation of optical harmonics, Phys. Rev. Lett. **7**, 118–119 (1961).

[98] R. Leitsmann, W. G. Schmidt, P. H. Hahn, and F. Bechstedt, Second-harmonic polarizability including electron-hole attraction from band-structure theory, Phys. Rev. B **71**, 195209 (2005).

[99] D. Vanderbilt and R. D. King-Smith, Electric polarization as a bulk quantity and its relation to surface charge, Phys. Rev. B **48**, 4442–4455 (1993).

[100] R. D. King-Smith and D. Vanderbilt, Theory of polarization of crystalline solids, Phys. Rev. B **47**, 1651–1654 (1993).

[101] M. V. Berry, Quantal phase factors accompanying adiabatic changes, Proc. R. Soc. A **392**, 45–57 (1984).

[102] C. Attaccalite, Non-linear response in extended systems: a real-time approach (2017), arXiv:1609.09639 [cond-mat.mtrl-sci] .

[103] F. Bloch, Über die Quantenmechanik der Elektronen in Kristallgittern, Z. Physik **52**, 555–600 (1929).

[104] R. Resta, Macroscopic polarization in crystalline dielectrics: the geometric phase approach, Rev. Mod. Phys. **66**, 899–915 (1994).

[105] R. Resta, Quantum-mechanical position operator in extended systems, Phys. Rev. Lett. **80**, 1800–1803 (1998).

[106] R. Resta and S. Sorella, Electron localization in the insulating state, Phys. Rev. Lett. **82**, 370–373 (1999).

[107] C. Attaccalite, M. Grüning, and A. Marini, Real-time approach to the optical properties of solids and nanostructures: Time-dependent Bethe-Salpeter equation, Phys. Rev. B **84**, 245110 (2011).

[108] F. Aryasetiawan and O. Gunnarsson, The GW method, Rep. Prog. Phys. **61**, 237 (1998).

[109] D. Kremp, M. Schlanges, and W.-D. Kraeft, *Quantum statistics of nonideal plasmas* (Springer, 2005).

[110] L. P. Kadanoff, *Quantum statistical mechanics* (CRC Press, 2018).

[111] B. Farid, R. Daling, D. Lenstra, and W. van Haeringen, GW approach to the calculation of electron self-energies in semiconductors, Phys. Rev. B **38**, 7530–7534 (1988).

[112] G. Onida, L. Reining, and A. Rubio, Electronic excitations: density-functional versus many-body Green's-function approaches, Rev. Mod. Phys. **74**, 601–659 (2002).

[113] G. Strinati, Application of the Green's functions method to the study of the optical properties of semiconductors, Riv. Nuovo Cim. **11**, 1–86 (1988).

[114] G. Pal, Y. Pavlyukh, W. Hübner, and H. C. Schneider, Optical absorption spectra of finite systems from a conserving Bethe-Salpeter equation approach, Eur. Phys. J. B **79**, 327–334 (2011).

[115] N.-H. Kwong and M. Bonitz, Real-time kadanoff-baym approach to plasma oscillations in a correlated electron gas, Phys. Rev. Lett. **84**, 1768–1771 (2000).

[116] C. Runge, Über die numerische Auflösung von Differentialgleichungen, Math. Ann. **46**, 167–178 (1895).

[117] S. Schmitt-Rink, D. S. Chemla, and H. Haug, Nonequilibrium theory of the optical stark effect and spectral hole burning in semiconductors, Phys. Rev. B **37**, 941–955 (1988).

[118] M. G. Stanford, P. D. Rack, and D. Jariwala, Emerging nanofabrication and quantum confinement techniques for 2D materials beyond graphene, npj 2D Mater. Appl. **2**, 1–15 (2018).

[119] G. Kim, B. Huet, C. E. Stevens, K. Jo, J.-Y. Tsai, S. Bachu, M. Leger, S. Song, M. Rahaman, K. Y. Ma, *et al.*, Confinement of excited states in two-dimensional, in-plane, quantum heterostructures, Nat. Commun. **15**, 6361 (2024).

[120] G. Cassabois, P. Valvin, and B. Gil, Hexagonal boron nitride is an indirect bandgap semiconductor, Nat. Photonics **10**, 262–266 (2016).

[121] A. Splendiani, L. Sun, Y. Zhang, T. Li, J. Kim, C.-Y. Chim, G. Galli, and F. Wang, Emerging photoluminescence in monolayer $\mathrm{MoS_2}$, Nano Lett. **10**, 1271–1275 (2010).

[122] K. F. Mak, C. Lee, J. Hone, J. Shan, and T. F. Heinz, Atomically thin $\mathrm{MoS_2}$: A new direct-gap semiconductor, Phys. Rev. Lett. **105**, 136805 (2010).

[123] K. S. Novoselov, D. Jiang, F. Schedin, T. Booth, V. Khotkevich, S. Morozov, and A. K. Geim, Two-dimensional atomic crystals, Proc. Natl. Acad. Sci. U.S.A. **102**, 10451–10453 (2005).

[124] Y. Wang, Z. Nie, and F. Wang, Modulation of photocarrier relaxation dynamics in two-dimensional semiconductors, Light Sci. Appl. **9**, 192 (2020).

[125] L. Wirtz, A. Marini, and A. Rubio, Excitons in boron nitride nanotubes: dimensionality effects, Phys. Rev. Lett. **96**, 126104 (2006).

[126] C.-J. Kim, L. Brown, M. W. Graham, R. Hovden, R. W. Havener, P. L. McEuen, D. A. Muller, and J. Park, Stacking order dependent second harmonic generation and topological defects in h-BN bilayers, Nano Lett. **13**, 5660–5665 (2013).

[127] D. Kim, Y. Lee, A. Chacón, and D.-E. Kim, Effect of interlayer coupling and symmetry on high-order harmonic generation from monolayer and bilayer hexagonal boron nitride, Symmetry **14**, 84 (2022).

[128] K. Yao, N. R. Finney, J. Zhang, S. L. Moore, L. Xian, N. Tancogne-Dejean, F. Liu, J. Ardelean, X. Xu, D. Halbertal, *et al.*, Enhanced tunable second harmonic generation from twistable interfaces and vertical superlattices in boron nitride homostructures, Sci. Adv. **7**, eabe8691 (2021).

[129] F. Paleari, T. Galvani, H. Amara, F. Ducastelle, A. Molina-Sánchez, and L. Wirtz, Excitons in few-layer hexagonal boron nitride: Davydov splitting and surface localization, 2D Materials **5**, 045017 (2018).

[130] D. Y. Qiu, F. H. da Jornada, and S. G. Louie, Optical spectrum of $\mathrm{MoS_2}$: Many-body effects and diversity of exciton states, Phys. Rev. Lett. **111**, 216805 (2013).

[131] G. Wang, A. Chernikov, M. M. Glazov, T. F. Heinz, X. Marie, T. Amand, and B. Urbaszek, Colloquium: Excitons in atomically thin transition metal dichalcogenides, Rev. Mod. Phys. **90**, 021001 (2018).

[132] K. F. Mak, K. He, J. Shan, and T. F. Heinz, Control of valley polarization in monolayer $\mathrm{MoS_2}$ by optical helicity, Nat. Nanotechnol. **7**, 494–498 (2012).

[133] H. Zeng, J. Dai, W. Yao, D. Xiao, and X. Cui, Valley polarization in $\mathrm{MoS_2}$ monolayers by optical pumping, Nat. Nanotechnol. **7**, 490–493 (2012).

[134] T. Cao, G. Wang, W. Han, H. Ye, C. Zhu, J. Shi, Q. Niu, P. Tan, E. Wang, B. Liu, *et al.*, Valley-selective circular dichroism of monolayer molybdenum disulphide, Nat. Commun. **3**, 887 (2012).

[135] D. Xiao, G.-B. Liu, W. Feng, X. Xu, and W. Yao, Coupled spin and valley physics in monolayers of $\mathrm{mos_2}$ and other group-VI dichalcogenides, Phys. Rev. Lett. **108**, 196802 (2012).

[136] W. Zhang, K. Tanaka, Y. Hasegawa, K. Shinokita, K. Matsuda, and Y. Miyauchi, Bright and highly valley polarized trions in chemically doped monolayer $\mathrm{MoS_2}$, Appl. Phys. Express **13**, 035002 (2020).

[137] A. Ramasubramaniam, Large excitonic effects in monolayers of molybdenum and tungsten dichalcogenides, Phys. Rev. B **86**, 115409 (2012).

[138] A. Kormányos, G. Burkard, M. Gmitra, J. Fabian, V. Zólyomi, N. D. Drummond, and V. Fal'ko, k · p theory for two-dimensional transition metal dichalcogenide semiconductors, 2D Materials **2**, 022001 (2015).

[139] Z. Y. Zhu, Y. C. Cheng, and U. Schwingenschlögl, Giant spin-orbit-induced spin splitting in two-dimensional transition-metal dichalcogenide semiconductors, Phys. Rev. B **84**, 153402 (2011).

[140] G.-B. Liu, W.-Y. Shan, Y. Yao, W. Yao, and D. Xiao, Three-band tight-binding model for monolayers of group-VIB transition metal dichalcogenides, Phys. Rev. B **88**, 085433 (2013).

[141] E. S. Kadantsev and P. Hawrylak, Electronic structure of a single MoS_2 monolayer, Solid state communications **152**, 909–913 (2012).

[142] A. Kormányos, V. Zólyomi, N. D. Drummond, and G. Burkard, Spin-orbit coupling, quantum dots, and qubits in monolayer transition metal dichalcogenides, Phys. Rev. X **4**, 011034 (2014).

[143] A. Molina-Sánchez, D. Sangalli, K. Hummer, A. Marini, and L. Wirtz, Effect of spin-orbit interaction on the optical spectra of single-layer, double-layer, and bulk MoS_2, Phys. Rev. B **88**, 045412 (2013).

[144] L. M. Malard, T. V. Alencar, A. P. M. Barboza, K. F. Mak, and A. M. de Paula, Observation of intense second harmonic generation from MoS_2 atomic crystals, Phys. Rev. B **87**, 201401(R) (2013).

[145] J. Ruan, Y.-H. Chan, and S. G. Louie, Exciton enhanced nonlinear optical responses in monolayer h-BN and MoS_2: Insight from first-principles exciton-state coupling formalism and calculations, Nano Lett. **24**, 15533–15539 (2024).

[146] A. Ono, Extracting nonlinear dynamical response functions from time evolution, Phys. Rev. Lett. **135**, 026401 (2025).

[147] A. Riefer and W. Schmidt, Solving the Bethe-Salpeter equation for the second-harmonic generation in Zn chalcogenides, Phys. Rev. B **96**, 235206 (2017).

[148] E. H. Moore, On the reciprocal of the general algebraic matrix, Bull. Am. Math. Soc. **26**, 294–295 (1920).

[149] R. Penrose, A generalized inverse for matrices, Math. Proc. Camb. Philos. Soc. **51**, 406–413 (1955).

[150] P. Virtanen, R. Gommers, T. E. Oliphant, M. Haberland, T. Reddy, D. Cournapeau, E. Burovski, P. Peterson, W. Weckesser, J. Bright, *et al.*, SciPy 1.0: Fundamental algorithms for scientific computing in Python, Nat. Methods **17**, 261–272 (2020).

[151] M. van Setten, M. Giantomassi, E. Bousquet, M. Verstraete, D. Hamann, X. Gonze, and G.-M. Rignanese, The PseudoDojo: Training and grading a 85 element optimized norm-conserving pseudopotential table, Comput. Phys. Commun. **226**, 39 – 54 (2018).

[152] P. Rivero, V. Manuel García-Suárez, D. Pereñiguez, K. Utt, Y. Yang, L. Bellaiche, K. Park, J. Ferrer, and S. Barraza-Lopez, Systematic pseudopotentials from reference eigenvalue sets for DFT calculations: Pseudopotential files, Data Br. **3**, 21–23 (2015).

[153] Y. Li, Y. Rao, K. F. Mak, Y. You, S. Wang, C. R. Dean, and T. F. Heinz, Probing symmetry properties of few-layer MoS_2 and h-BN by optical second-harmonic generation, Nano Lett. **13**, 3329–3333 (2013).

[154] M. L. Trolle, G. Seifert, and T. G. Pedersen, Theory of excitonic second-harmonic generation in monolayer MoS_2, Phys. Rev. B **89**, 235410 (2014).

[155] K. Beach, M. C. Lucking, and H. Terrones, Strain dependence of second harmonic generation in transition metal dichalcogenide monolayers and the fine structure of the c exciton, Phys. Rev. B **101**, 155431 (2020).

[156] T. Yang, S. Sleziona, E. Pollmann, E. Hasselbrink, P. Kratzer, M. Schleberger, R. K. Campen, and Y. Tong, Isolating the optical response of a MoS_2 monolayer under extreme screening of a metal substrate, Phys. Rev. B **109**, L161402 (2024).

[157] H. Jang, K. P. Dhakal, K.-I. Joo, W. S. Yun, S. M. Shinde, X. Chen, S. M. Jeong, S. W. Lee, Z. Lee, J. Lee, *et al.*, Transient SHG imaging on ultrafast carrier dynamics of MoS_2 nanosheets, Adv. Mater. **30**, 1705190 (2018).

[158] J. Chen, P. Han, and X.-C. Zhang, Terahertz-field-induced second-harmonic generation in a beta barium borate crystal and its application in terahertz detection, Appl. Phys. Lett. **95** (2009).

[159] T. Elsaesser, K. Reimann, and M. Woerner, Nonlinear terahertz spectroscopy of solids, in *Concepts and Applications of Nonlinear Terahertz Spectroscopy, Second Edition*, 2053-2563 (IOP Publishing, 2024) pp. 5–1 to 5–54.

[160] Y. Gillet, M. Giantomassi, and X. Gonze, First-principles study of excitonic effects in raman intensities, Phys. Rev. B **88**, 094305 (2013).

[161] H. P. Miranda, S. Reichardt, G. Froehlicher, A. Molina-Sánchez, S. Berciaud, and L. Wirtz, Quantum interference effects in resonant Raman spectroscopy of single- and triple-layer $MoTe_2$ from first-principles, Nano Lett. **17**, 2381–2388 (2017).

[162] S. Sanna and W. G. Schmidt, Lithium niobate X-cut, Y-cut, and Z-cut surfaces from ab initio theory, Phys. Rev. B **81**, 214116 (2010).

[163] S. Sanna and W. G. Schmidt, $LiNbO_3$ surfaces from a microscopic perspective, J. Phys. Condens. Matter **29**, 413001 (2017).

[164] S. Sanna, S. Neufeld, M. Rüsing, G. Berth, A. Zrenner, and W. G. Schmidt, Raman scattering efficiency in $LiTaO_3$ and $LiNbO_3$ crystals, Phys. Rev. B **91**, 224302 (2015).

[165] R. E. Newnham, *Properties of Materials* (Oxford University Press, 2004).

[166] W. L. Bond, The mathematics of the physical properties of crystals, Bell Syst. Tech. J. **22**, 1–72 (1943).

[167] D. R. Hamann, Optimized norm-conserving Vanderbilt pseudopotentials, Phys. Rev. B **88**, 85117 (2013).

[168] H. H. Nahm and C. H. Park, First-principles study of microscopic properties of the Nb antisite in $LiNbO_3$: Comparison to phenomenological polaron theory, Phys. Rev. B **78**, 184108 (2008).

[169] A. Sanson, A. Zaltron, N. Argiolas, C. Sada, M. Bazzan, W. G. Schmidt, and S. Sanna, Polaronic deformation at the $Fe^{2+/3+}$ impurity site in Fe:$LiNbO_3$ crystals, Phys. Rev. B **91**, 94109 (2015).

[170] P. F. Weck and E. Kim, Assessing Hubbard-corrected AM05+U and PBEsol+U density functionals for strongly correlated oxides CeO_2 and Ce_2O_3, Phys. Chem. Chem. Phys. **18**, 26816–26826 (2016).

[171] R. Schaufele and M. Weber, Raman scattering by lithium niobate, Phys. Rev. **152**, 705 (1966).

[172] J. P. Perdew, J. A. Chevary, S. H. Vosko, K. A. Jackson, M. R. Pederson, D. J. Singh, and C. Fiolhais, Erratum: Atoms, molecules, solids, and surfaces: Applications of the generalized gradient approximation for exchange and correlation, Phys. Rev. B **48**, 4978–4978 (1993).

[173] M. Rüsing, S. Sanna, S. Neufeld, G. Berth, W. G. Schmidt, A. Zrenner, H. Yu, Y. Wang, and H. Zhang, Vibrational properties of $LiNb_{1-x}Ta_xO_3$ mixed crystals, Phys. Rev. B **93**, 184305 (2016).

[174] W. G. Schmidt, F. Bechstedt, and G. P. Srivastava, III-V(110) surface dynamics from an ab initio frozen-phonon approach, Phys. Rev. B **52**, 2001–2007 (1995).

[175] P. Hermet, M. Veithen, and P. Ghosez, First-principles calculations of the nonlinear optical susceptibilities and Raman scattering spectra of lithium niobate, J. Phys. Condens. Matter **19**, 456202 (2007).

[176] D. Doratotaj, J. R. Simpson, and J.-A. Yan, Probing the uniaxial strains in MoS_2 using polarized Raman spectroscopy: A first-principles study, Phys. Rev. B **93**, 075401 (2016).

[177] M. Huang, H. Yan, C. Chen, D. Song, T. F. Heinz, and J. Hone, Phonon softening and crystallographic orientation of strained graphene studied by Raman spectroscopy, Proc. Natl. Acad. Sci. U.S.A. **106**, 7304–7308 (2009).

[178] S. Pak, J. Lee, Y.-W. Lee, A.-R. Jang, S. Ahn, K. Y. Ma, Y. Cho, J. Hong, S. Lee, H. Y. Jeong, *et al.*, Strain-mediated interlayer coupling effects on the excitonic behaviors in an epitaxially grown MoS_2/WS_2 van der Waals heterobilayer, Nano Lett. **17**, 5634–5640 (2017).

[179] B. G. Oliveira, A. Zabardasti, H. Goudarziafshar, and M. Salehnassaj, The electronic mechanism ruling the dihydrogen bonds and halogen bonds in weakly bound systems of $H_3SiH---HOX$ and $H_3SiH---XOH$ (X = F, Cl, and Br), J. Mol. Model. **21**, 77 (2015).

[180] B. Mytsyk, N. Demyanyshyn, A. Andrushchak, and O. Buryy, Photoelastic properties of trigonal crystals, Crystals **11** (2021).

[181] I. L. Lyubchanskii, N. N. Dadoenkova, M. I. Lyubchanskii, T. Rasing, J.-W. Jeong, and S.-C. Shin, Second-harmonic generation from realistic film–substrate interfaces: The effects of strain, Appl. Phys. Lett. **76**, 1848–1850 (2000).

[182] J.-W. Jeong, S.-C. Shin, I. L. Lyubchanskii, and V. N. Varyukhin, Strain-induced three-photon effects, Phys. Rev. B **62**, 13455–13463 (2000).

[183] A. Riefer, S. Sanna, A. Schindlmayr, and W. G. Schmidt, Optical response of stoichiometric and congruent lithium niobate from first-principles calculations, Phys. Rev. B **87**, 195208 (2013).

[184] J. L. P. Hughes and J. E. Sipe, Calculation of second-order optical response in semiconductors, Phys. Rev. B **53**, 10751–10763 (1996).

[185] D. E. Aspnes, Energy-band theory of the second-order nonlinear optical susceptibility of crystals of zinc-blende symmetry, Phys. Rev. B **6**, 4648–4659 (1972).

[186] B. G. Mytsyk, A. S. Andrushchak, N. M. Demyanyshyn, Y. P. Kost', A. V. Kityk, P. Mandracci, and W. Schranz, Piezo-optic coefficients of MgO $LiNbO_3$ crystals, Appl. Opt. **48**, 1904–1911 (2009).

[187] B. G. Mytsyk, Y. A. V. Pryris, and A. S. Andrushchak, The lithium niobate piezooptical features, Cryst. Res. Technol. **26**, 931–940 (1991).

[188] B. H. Mytsyk, N. M. Demyanyshyn, and Y. P. Kost', Signs of elastooptic coefficients in low-symmetry materials, Mater. Sci. **50**, 762–770 (2015).

[189] R. W. Dixon, Photoelastic properties of selected materials and their relevance for applications to acoustic light modulators and scanners, J. Appl. Phys. **38**, 5149–5153 (1967).

[190] R. W. Dixon and M. G. Cohen, A new technique for measuring magnitudes of photoelastic tensors and its application to lithium niobate, Appl. Phys. Lett. **8**, 205–207 (1966).

[191] Z. H. Amber, B. Kirbus, L. M. Eng, and M. Rüsing, Quantifying the coherent interaction length of second-harmonic microscopy in lithium niobate confined nanostructures, J. Appl. Phys. **130**, 133102 (2021).

[192] L. Mennel, M. Paur, and T. Mueller, Second harmonic generation in strained transition metal dichalcogenide monolayers: MoS_2, $MoSe_2$, WS_2, and WSe_2, APL Photonics **4**, 034404 (2019).

[193] L. Mennel, M. M. Furchi, S. Wachter, M. Paur, D. K. Polyushkin, and T. Mueller, Optical imaging of strain in two-dimensional crystals, Nat. Commun. **9**, 516 (2018).

[194] D. Roberts, Simplified characterization of uniaxial and biaxial nonlinear optical crystals: a plea for standardization of nomenclature and conventions, IEEE J. Quantum Electron. **28**, 2057–2074 (1992).

[195] I. Shoji, T. Kondo, A. Kitamoto, M. Shirane, and R. Ito, Absolute scale of second-order nonlinear-optical coefficients, J. Opt. Soc. Am. B **14**, 2268–2294 (1997).

[196] Z. Hao, L. Zhang, W. Mao, A. Gao, X. Gao, F. Gao, F. Bo, G. Zhang, and J. Xu, Second-harmonic generation using d_{33} in periodically poled lithium niobate microdisk resonators, Photon. Res. **8**, 311–317 (2020).

[197] R. Kremer, A. Boudrioua, P. Moretti, and J. Loulergue, Measurements of the non-linear d_{33} coefficients of light-ion implanted lithium niobate by second harmonic generation in total reflection geometry, Opt. Commun. **219**, 389–393 (2003).

[198] K. J. Spychala, P. Mackwitz, M. Rüsing, A. Widhalm, G. Berth, C. Silberhorn, and A. Zrenner, Nonlinear focal mapping of ferroelectric domain walls in $LiNbO_3$: Analysis of the SHG microscopy contrast mechanism, J. Appl. Phys. **128**, 234102 (2020).

[199] M. D. Levenson, C. Flytzanis, and N. Bloembergen, Interference of resonant and nonresonant three-wave mixing in diamond, Phys. Rev. B **6**, 3962–3965 (1972).

[200] M. D. Levenson and N. Bloembergen, Dispersion of the nonlinear optical susceptibility tensor in centrosymmetric media, Phys. Rev. B **10**, 4447–4463 (1974).

[201] C. H. Camp Jr, Y. J. Lee, and M. T. Cicerone, Quantitative, comparable coherent anti-Stokes Raman scattering (CARS) spectroscopy: correcting errors in phase retrieval, J. Raman Spectrosc. **47**, 408–415 (2016).

[202] F. Schmidt, A. L. Kozub, T. Biktagirov, C. Eigner, C. Silberhorn, A. Schindlmayr, W. G. Schmidt, and U. Gerstmann, Free and defect-bound (bi)polarons in $LiNbO_3$: Atomic structure and spectroscopic signatures from ab initio calculations, Phys. Rev. Res. **2**, 043002 (2020).

[203] C. G. Van de Walle and J. Neugebauer, First-principles calculations for defects and impurities: Applications to iii-nitrides, J. Appl. Phys. **95**, 3851–3879 (2004).

[204] S. Lany and A. Zunger, Assessment of correction methods for the band-gap problem and for finite-size effects in supercell defect calculations: Case studies for zno and gaas, Phys. Rev. B **78**, 235104 (2008).

[205] O. Buryy, N. M. Demyanyshyn, B. G. Mytsyk, A. S. Andrushchak, and D. Sugak, Acousto-optic interaction in LGS and CTGS crystals, Opt. Continuum **1**, 1314–1323 (2022).

[206] B. Mytsyk, A. Erba, J. Maul, N. Demyanyshyn, P. Shchepanskyi, and O. Syrotynsky, Photoelasticity of CNGS crystals, Appl. Opt. **62**, 7952–7959 (2023).

[207] F. Hempel, M. Rüsing, F. Vernuccio, K. J. Spychala, R. Buschbeck, G. Cerullo, D. Polli, and L. M. Eng, Phonon dephasing times determined with time-delayed broadband coherent anti-stokes raman scattering, Phys. Rev. B **112**, 224106 (2025).

[208] N. Leisgang, S. Shree, I. Paradisanos, L. Sponfeldner, C. Robert, D. Lagarde, A. Balocchi, K. Watanabe, T. Taniguchi, X. Marie, *et al.*, Giant stark splitting of an exciton in bilayer $\mathrm{MoS_2}$, Nat. Nanotechnol. **15**, 901–907 (2020).

[209] X. Liu, N. Leisgang, P. E. Dolgirev, A. A. Zibrov, J. Sung, J. Wang, T. Taniguchi, K. Watanabe, V. Walther, H. Park, *et al.*, Optical signatures of interlayer electron coherence in a bilayer semiconductor, Nat. Phys. , 1–7 (2025).

[210] Y. Mao, J. Zhou, M. Grüning, and C. Attaccalite, Shift current in two-dimensional janus transition-metal dichalcogenides: The role of excitons, Phys. Rev. Mater. **9**, 124002 (2025)

Publication list

[P1] E. Singh, M. N. Pionteck, S. Reitzig, M. Lange, M. Rüsing, L. M. Eng, and S. Sanna, Vibrational properties of $LiNbO_3$ and $LiTaO_3$ under uniaxial stress, Phys. Rev. Mater. **7**, 24420 (2023).

[P2] M. N. Pionteck and S. Sanna, Photoelastic properties of stoichiometric lithium niobate from first-principles calculations, Phys. Status Solidi (a) , 2300970 (2024).

[P3] M. N. Pionteck, M. Roeper, B. Koppitz, S. D. Seddon, M. Rüsing, L. Padberg, C. Eigner, C. Silberhorn, S. Sanna, and L. M. Eng, Second-order nonlinear piezo-optic properties of single crystal lithium niobate thin films, Phys. Rev. B **111**, 064109 (2025).

[P4] L. M. Verhoff, M. N. Pionteck, M. Rüsing, H. Fritze, L. M. Eng, and S. Sanna, Two-dimensional electronic conductivity in insulating ferroelectrics: Peculiar properties of domain walls, Phys. Rev. Res. **6**, L042015 (2024).

[P5] M. N. Pionteck, M. Grüning, S. Sanna, and C. Attaccalite, A real-time approach to frequency-mixing spectroscopies: Application to sum and difference frequency generation in two-dimensional crystals, SciPost Physics **19**, 129 (2025).

[P6] F. Paleari, A. Molina-Sánchez, M. Nalabothula, R. Reho, M. Bonacci, J. Castelo, J. Cervantes-Villanueva, M. Pionteck, M. Silvetti, C. Attaccalite, and H. Pereira Coutada Miranda, YamboPy: a pre/post-processor tool for Yambo and QuantumEspresso written in Python., Zenodo (2025).

[P7] C. Kofahl, J. Uhlendorf, B. A. Muscutt, M. N. Pionteck, S. Sanna, H. Fritze, S. Ganschow, and H. Schmidt, Oxygen diffusion in Li(Nb, Ta)O_3 single crystals, Phys. Status Solidi (a) **222**, 2300959 (2025).

[P8] A. Cammarata, M. Pruneda, R. Poloni, J. Carrete, P. García-Fernández, M. Grüning, X. He, M. Pionteck, N. Protik, M. Todorovic, A. Togo, X. Wang, and Z. Zanolli, Software interoperability in atomistic simulations of materials, submitted to Comput. Mater. Sci. (2025).

[P9] M. N. Pionteck and S. Sanna, $LiNbO_3$(0001) surfaces: Raman spectra from first principles, in preparation.

[P10] R. Buschbeck, M. N. Pionteck, N. Fugal, M. Rüsing, S. Kehr, S. Sanna, and L. M. Eng, Understanding and utilizing the B-CARS contrast mechanism of lithium niobate domain walls, in preparation.

[P11] K. Holtgrewe, F. Ziese, J. Bilk, M. N. Pionteck, K. Eberheim, F. Bernhardt, C. Dues, and S. Sanna, Tuning the conductivity of metallic nanowires by hydrogen adsorption, in *High Performance Computing in Science and Engineering '20*, edited by W. E. Nagel, D. H. Kröner, and M. M. Resch (Springer International Publishing, Cham, 2021) pp. 133–146.

[P12] M. N. Pionteck, F. Bernhardt, J. Bilk, C. Dues, K. Eberheim, C. Fink, K. Holtgrewe, N. Jöckel, B. Muscutt, F. A. Pfeiffer, F. Ziese, and S. Sanna, Dynamical properties of the Si(553)-Au nanowire system, in *High Performance Computing in Science and Engineering '21*, edited by W. E. Nagel, D. H. Kröner, and M. M. Resch (Springer International Publishing, Cham, 2023) pp. 97–111.

[P13] M. N. Pionteck, F. Bernhardt, C. Dues, K. Eberheim, C. Fink, K. Holtgrewe, F. A. Pfeiffer, N. A. Schäfer, L. M. Verhoff, F. Ziese, and S. Sanna, Hyperpolarizabilities of $LiNbO_3$, $LiTaO_3$ and $KNbO_3$ calculated from first principles, in *High Performance Computing in Science and Engineering '22*, edited by W. E. Nagel, D. H. Kröner, and M. M. Resch (Springer Nature Switzerland, Cham, 2024) pp. 129–143.

[P14] M. N. Pionteck, F. Bernhardt, K. Eberheim, C. Fink, F. A. Pfeiffer, N. A. Schäfer, L. M. Verhoff, F. Ziese, and S. Sanna, First principles investigation of the $LiNbO_3$ and $LiTaO_3$ lattice dynamics under uniaxial stress, in *High Performance Computing in Science and Engineering '23*, edited by W. E. Nagel, D. H. Kröner, and M. M. Resch (Springer Nature Switzerland, Cham, 2024) accepted.

[P15] M. N. Pionteck, F. Bernhardt, K. Eberheim, C. Fink, F. A. Pfeiffer, N. A. Schäfer, L. M. Verhoff, F. Ziese, and S. Sanna, Effect of Mg doping on the $LiNbO_3$ ferroelectric phase transition, in *High Performance Computing in Science and Engineering '24*, edited by W. E. Nagel, D. H. Kröner, and M. M. Resch (Springer Nature Switzerland, Cham, 2025) accepted